General Disclaimer

One or more of the Following Statements may affect this Document
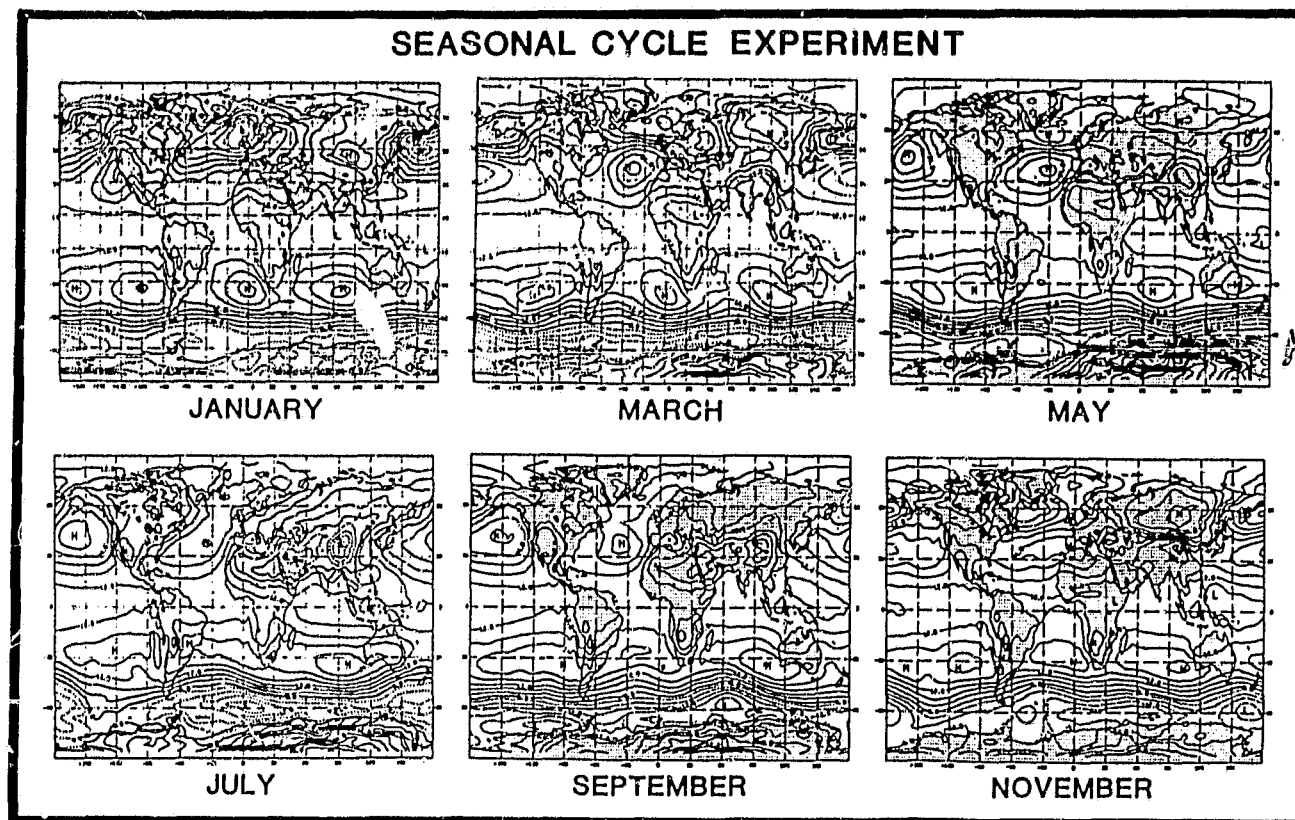
- This document has been reproduced from the best copy furnished by the organizational source. It is being released in the interest of making available as much information as possible.

- This document may contain data, which exceeds the sheet parameters. It was furnished in this condition by the organizational source and is the best copy available.

- This document may contain tone-on-tone or color graphs, charts and/or pictures, which have been reproduced in black and white.

- This document is paginated as submitted by the original source.

- Portions of this document are not fully legible due to the historical nature of some of the material. However, it is the best reproduction available from the original submission.

NASA

Technical Memorandum 84983

RESEARCH REVIEW-1982

SEASONAL CYCLE EXPERIMENT

JANUARY   MARCH   MAY

JULY   SEPTEMBER   NOVEMBER

GLOBAL MODELING AND SIMULATION BRANCH

LABORATORY FOR ATMOSPHERIC SCIENCES

JANUARY 1983

National Aeronautics and
Space Administration

Goddard Space Flight Center
Greenbelt, Maryland 20771

MAY 1983
RECEIVED
NASA STI FAC
ACCESS.

RESEARCH REVIEW - 1982

GLOBAL MODELING AND SIMULATION BRANCH
LABORATORY FOR ATMOSPHERIC SCIENCES

JANUARY 1983

NASA GODDARD SPACE FLIGHT CENTER
GREENBELT, MARYLAND 20771

TABLE OF CONTENTS

I.   INTRODUCTION

II.   GLOBAL WEATHER/OBSERVING SYSTEMS

   A.   Analysis and Forecast Studies

   B.   Satellite Observing Systems

I. INTRODUCTION

I.   I N T R O D U C T I O N

The Global Modeling and Simulation Branch (GMSB) of the Laboratory for Atmospheric Sciences (GLAS) is engaged in general circulation modeling studies related to global atmospheric and oceanographic research. The research activities are organized into two disciplines: Global Weather/Observing Systems and Climate/ Ocean-Air Interactions.

The Global Weather activities are grouped in four areas: 1) Analysis and Forecast Studies, 2) Satellite Temperature and Wind Retrievals, 3) Analysis and Model Development, 4) Atmospheric Dynamics and Diagnostic Studies.

The GLAS Analysis/Forecast/Retrieval System was applied to the FGGE Special Observing periods 1 and 2 (5 Jan - 5 March and 1 June - 31 July 1979) respectively. The resulting analyses have already been used in a large number of theoretical studies of atmospheric dynamics, forecast impact studies and development of new or improved algorithms for the utilization of satellite data. The results obtained with the GLAS temperature retrieval system are particularly noteworthy: not only are the atmospheric temperature soundings quite accurate, but as a by- product, remarkably accurate determinations of land and sea surface temperatures, cloud cover, height and temperatures, and snow and ice extent have been obtained from operational TIROS-N sounders.

The focus of the climate research is to understand the variability of the climate on the monthly to seasonal time scale. In support of this goal, studies are carried out in the three areas of: 1) Data Analysis, 2) Climate Modeling, and 3) Sensitivity Experiments. The analysis of observational data to formulate and validate hypotheses for short-term climate change has been and continues to be an integral part of the climate research effort. Extensive studies have been completed which establish the physical basis for the prediction of monthly and seasonal climate changes through the use of anomalies in sea surface temperature and other space observed boundary conditions. In conjunction with these studies, existing general circulation/climate models are being extended and improved substantially. A 24-month simulation carried out in the presence of a seasonal cycle indicates that the current model can simulate the winter to summer climate change. Currently, the models are being extended to include much of the stratosphere.

Ocean/air interaction studies are concentrated on the development of models for the prediction of upper ocean currents, temperatures, sea state, mixed- layer depths, and upwelling zones, and on studies of the interaction of the atmospheric and oceanic circulation systems on time scales of a month or more.

This research review contains a synopsis of extended abstracts in the Global Weather/Observing System studies, and Climate/Ocean-Air Interaction studies conducted at the Modeling and Simulation Branch for 1982-83 (Sections 2 and 3). Abstracts of the Summer Lecture Series, jointly sponsored by GMSB and the University of Maryland, are present in Section IV. Section V lists the recent publications by the GMSB and visiting scientists.

II. GLOBAL WEATHER/OBSERVING SYSTEMS

A. ANALYSIS AND FORECAST STUDIES

EMPIRICAL CORRECTION OF THE LARGE SCALE FORECAST BIAS OF A GLOBAL NWP MODEL

R. N. Hoffman and J. Firestone

The most satisfying solution to the problem of large scale forecast errors would be to find and correct their root causes. The least satisfying solution would be to remove the observed bias at each forecast time, as an _a posteriori_ statistical filter as suggested by Leith (1974a). We would like to propose, as an intermediate solution, the _empirical_ correction of the large scale forecast bias _within_ a NWP model.

The general topic of the empirical correction of NWP models has been discussed extensively by Leith (1974b, 1978) and by Faller and his collaborators (Faller and Lee, 1975; Faller and Schemm, 1977; Schemm and Faller, 1977; Schemm et. al. 1981). Leith has theoretically solved the complete problem of preserving the climate mean and single-time covariance by adding constant and linear terms to the equations of motion. Leith's solution is not practical because estimates of the climate statistics are based on relatively small samples, and Leith's plan involves estimating $O(N^2)$ parameters, where N is the number of model variables. If we simplify Leith's scheme to only eliminate the model's bias we need only estimate $O(N)$ parameters. But even N is much greater than our effective sample size.

Both Leith and Faller suggest making corrections locally in grid point space because the corrections are presumably needed to account for subgrid scale processes which have been parameterized and truncation errors which primarily effect the small scales. Unfortunately, from the practical viewpoint the small scales are not well observed and without a good estimate of the error we cannot correct it. Therefore we plan to make corrections in the normal mode representation of the model, correcting only the largest spatial scales and longest time scales. There are several advantages to this approach:

(a) The number of parameters to be estimated is greatly reduced, avoiding in part the sampling problem.

(b) By excluding from consideration those normal modes of essentially computational or gravity wave nature we avoid estimating those parameters which we are unable to observe.

(c) Restricting the corrections to Rossby modes is also an advantage when applying the corrections. If we correct the governing equations then we avoid adding a forcing term to the gravity wave modes. If we correct the model state at intervals the shocks to the system do not directly change the fast modes, although they may excite gravity waves indirectly.

(d) A good deal of the bias appears to be large scale.

An interesting connection between empirical bias corrections and the specification of topography is noted. Since topography appears in the horizontal momentum equation at all levels as a single constant the "barotropic" component of the corrections to the horizontal momentum equations may be interpreted in terms of a topographic correction. Interestingly it turns out that this "barotropic" component of the wind errors is insignificant compared to

the wind errors at any one sigma level.

We have been trying to identify and plan to remove the model bias by examining the perceived forecast error observed during the assimilation cycle, i.e. the analysis minus the 6 hour first guess, of the GLAS Analysis/Forecast system (Halem et al., 1982) for the FGGE SOP-1. The particular analysis cycle we are examining (2453) is a "full FGGE" experiment, i.e., all data sources are included (Baker et al., 1981a). This experiment makes use of the thoroughly edited FGGE II-b data set (Baker et al., 1981b).

The results to date are intriguing; some error statistics are presented in the figures. These results are for 5 January through 5 March. Many of the small isolated features in these figures are probably due to station biases, but quite a few are associated with geographic factors which plausibly could cause some of the parameterizations used in the model to be in error. In Fig. 1 we see that surface pressure is forecast high over Greenland, the Rockies and east central Alaska. In the wind field at sigma level 8 a distinctive southeastly flow is seen in the error field over the North Atlantic (Fig. 2a), while at sigma level 3 a very well defined anticyclonic flow is seen in the error field off the West Coast (Fig. 2b). In Fig. 3 we see that the model is too warm over Greenland and too cold around the southern boundaries of Greenland. This feature is seen from sigma level 9 up to sigma level 5 with litle change in shape. Figure 4 shows the rms temperature errors over all sigma levels and all times in the sample. The feature centered over the foothills of the Himalayas indicates the model is regularly making poor 6 h forecasts here. The greatest part of this feature is due to errors in the lowest layers.

We are currently working on methods of filtering the observed bias; we are hopeful that we can separate the model bias from the station biases.

REFERENCES

Baker, W., D. Edelmann, M. Iredell, D. Han and S. Jakkempudi, 1981a: Objective analysis of observational data from the FGGE observing systems. NASA Tech. Memo. 82062.

Baker, W., D. Edelmann and H. Carus, 1981b: The GLAS editing procedures for the FGGE Level II-b data collected during SOP-1 and 2. NASA Tech. Memo. 83811.

Faller, A. J., and D. K. Lee, 1975: Statistical corrections to numerical prediction equations. Mon. Wea. Rev., 103, 845-855.

Faller, A. J., and C. E., 1977: Statistical corrections to numerical prediction equations. II. Mon. Wea. Rev. 105, 37-56.

Halem, M., E. Kalnay, W. E. Baker and R. Atlas, 1982: An assessment of the FGGE satellite observing system during SOP-1. Bull. Am. Meteor. Soc., 63, 407-426.

Leith, C. E., 1974b: Spectral statistical-dynamical forecast experiments. *Report of the International Symposium on Spectral Methods in Numerical Weather Prediction.* Copenhagen, 12-16 August 1974, GARP Working Group on Numerical Experimentation, Rep. No. 7, 445-467.

Leith, C. E., 1974a: Theoretical skill of Monte Carlo forecasts. *Mon. Wea. Rev.*, 102, 409-418.

Leith, C. E., 1978a: Objective methods for weather prediction. *Annual Review of Fluid Mechanics*, Vol. 10, Academic Press, 107-128.

Schemm, C. E., and A. J. Faller, 1977: A note on the statistical correction of prediction equations. *Mon. Wea. Rev.*, 105, 1473-1477.

Schemm, C. E., D. A. Unger and A. J. Faller, 1981: Statistical corrections to numerical weather predictions III. *Mon. Wea. Rev.*, 109, 96-109.
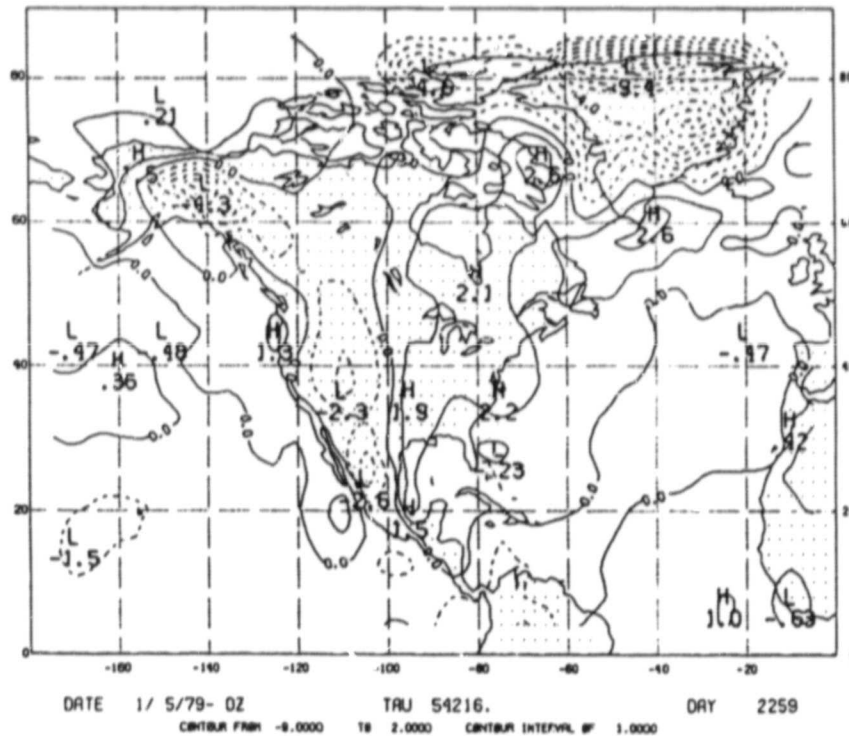
Fig. 1. Average 6 h surface pressure forecast error (mb). Sixty day sample every 6 h. (Note: error = analysis - forecast).

10

ANALYSIS - FIRST GUESS MEAN 60 DAYS EVERY 6.0 HOURS

σ(8)   WINDS   (M/SEC)

DATE 1/ 5/79- 0Z   TAU 54216.   DAY 2259
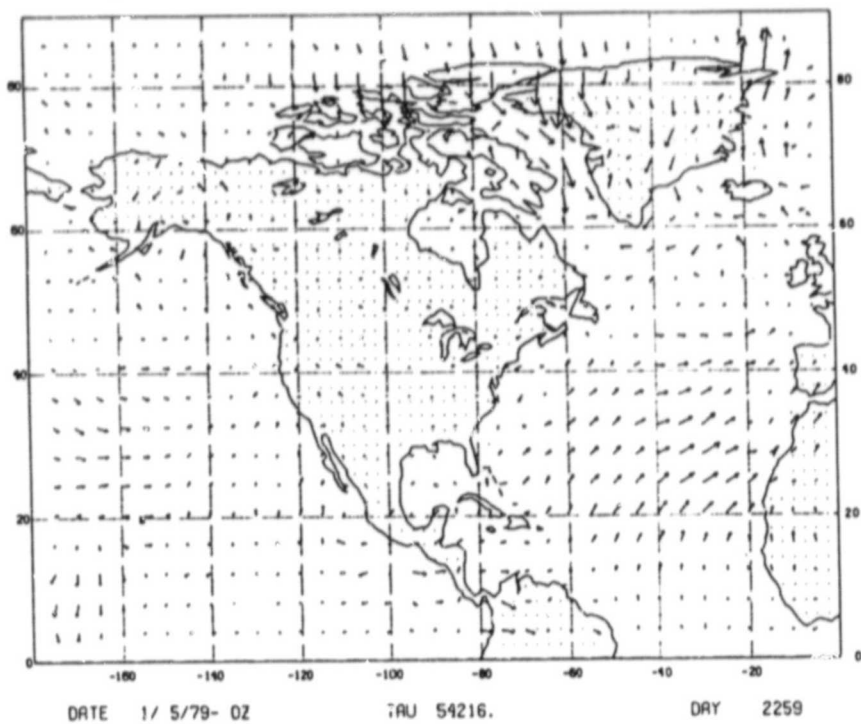
20.
MAXIMUM VECTOR

ANALYSIS - FIRST GUESS MEAN 60 DAY

σ(3)   WINDS   (M/SEC)

DATE 1/ 5/79- 0Z   TAU 54216.   DAY 2259
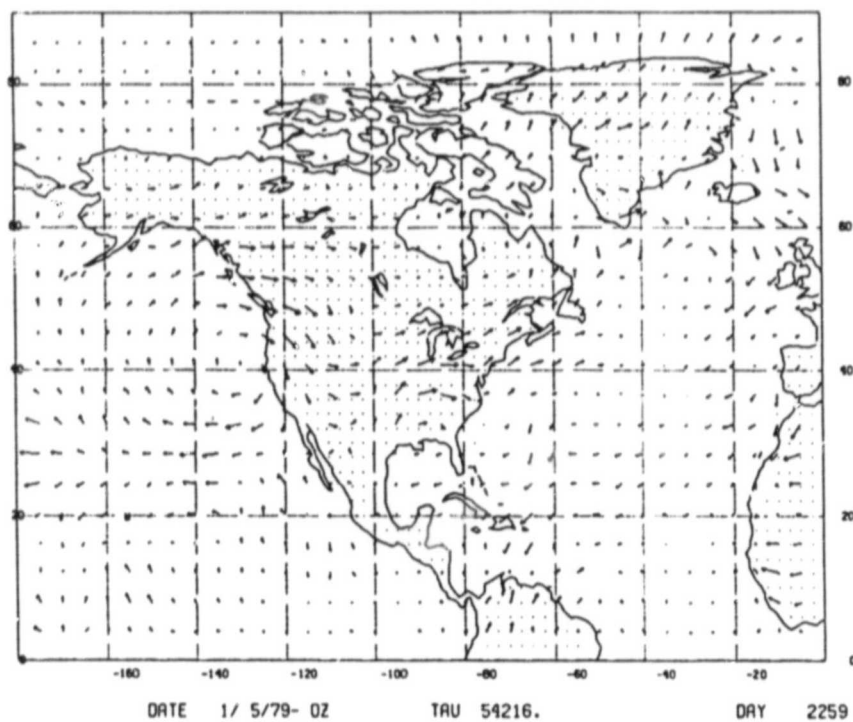
20.
MAXIMUM VECTOR

Fig. 2.   Average 6 h wind forecast error at sigma levels 8(a) and 3(b).   (Scale a lower right is a 20 m/s wind vector).

ANALYSIS - FIRST GUESS MEAN 60 DAYS EVERY 6.0 HOURS

$\sigma(7)$ TEMPERATURE   (K)

DATE 1/ 5/79- 0Z   TAU 54216.   DAY 2259
CONTOUR FROM -1.5000 TO 2.5000 CONTOUR INTERVAL OF .50000
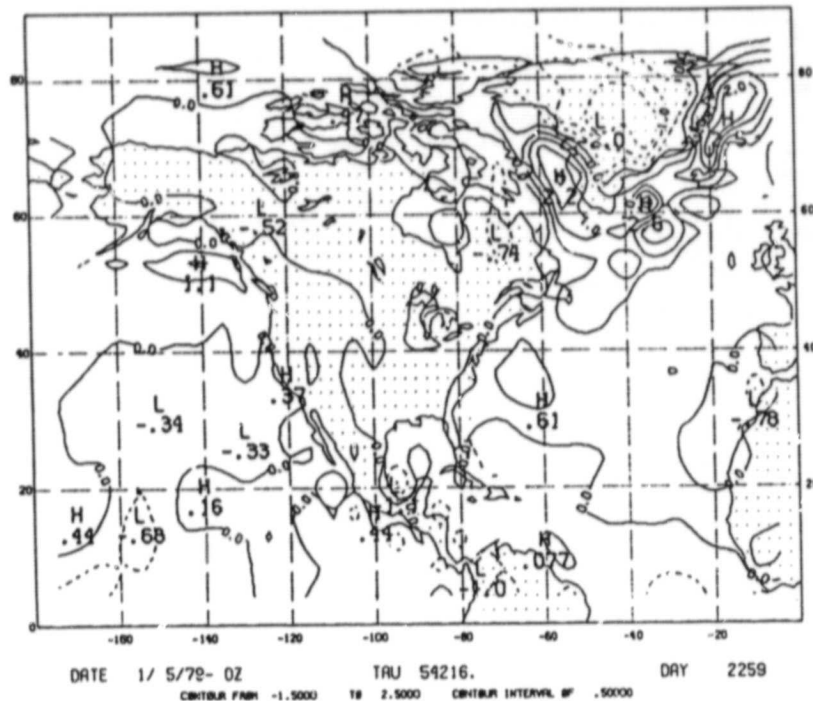
Fig. 3. Average 6 h temperature forecast error at sigma level 7. (°C, contours
every 0.5°C).

ANALYSIS - FIRST GUESS RMS 60 DAY EVERY 6.0 HRS (9 LAYER RMS AVG)

$\sigma(*)$ TEMPERATURE   (K)

DATE 1/ 5/79- 0Z   TAU 54216.   DAY 2259
CONTOUR FROM 1.0000 TO 4.5000 CONTOUR INTERVAL OF .50000
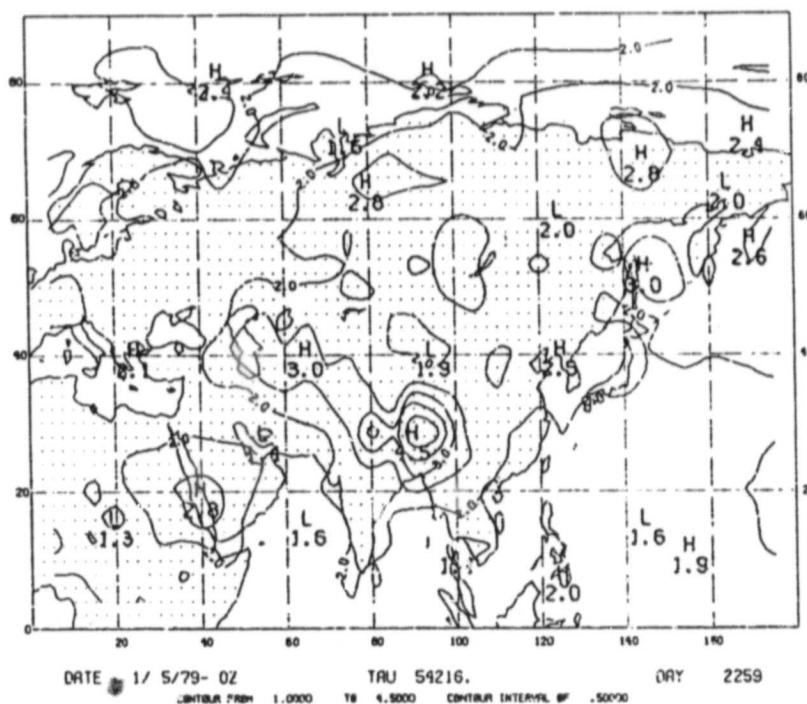
Fig. 4. Rms over all times and all sigma levels of 6 h temperature forecast
errors. (°C, contours every 0.5°C, first contour is 1.0°C).

CASE STUDIES OF COASTAL CYCLOGENESIS

R. Atlas and R. Rosenberg

A series of forecast experiments was conducted to assess the accuracy of the GLAS Model's prediction of two cases of coastal cyclogenesis and to determine the importance of large-scale dynamical processes and diabatic heating to the cyclone development. The model used in the assimilation and to generate the forecasts is the fourth order global atmospheric model described by Kalnay-Rivas et al. (1977), Kalnay-Rivas and Hoitsma (1979) and Halem et al. (1982), with nine vertical layers, equally spaced in sigma, and a coarse horizontal resolution of 4° latitude by 5° longitude, which is compensated by the use of accurate horizontal differences.

The first case studied was the "President's Day Cyclone" which developed along the east coast of the United States on February 18-19, 1979, and produced very heavy snowfall from Virginia to southeast New York. This storm was significant because of the severity of the weather it produced and the failure of the operational models in use at the National Meteorological Center (NMC) to adequately predict the intensity of cyclogenesis. For example, the Limited-Area Fine Mesh (LFM-II) model's 12, 24, 36 and 48 h forecasts which verified at 1200 GMT 19 February 1979 all displayed serious errors in the prediction of this cyclone and associated heavy precipitation. The 12 h forecast predicted the low to be too weak and south of its observed position; the 24 h forecast predicted a much weaker low; and the 36 h forecast indicated only a trough with no closed cyclone center.

The GLAS model 36 h forecast from the GLAS analysis at 0000 GMT 18 February correctly predicted intense coastal cyclogenesis and heavy precipitation (Fig. 1a). When this forecast was repeated without surface heat and moisture fluxes, only an inverted trough developed along the east coast (Fig. 1b), while an experiment without surface heat and moisture fluxes failed to predict any cyclonic development (Fig. 1c). An extended-range forecast from 0000 GMT 16 February as well as a forecast from the NMC analysis as a forecast from the NMC analysis at 0000 GMT 18 February interpolated to the GLAS grid (not shown) predicted weak coastal low development.

Detailed examination of these forecasts (Atlas and Rosenberg, 1982) showed that diabatic heating resulting from oceanic fluxes significantly contributed to the generation of low level cyclonic vorticity and the intensification and slow rate movement of an upper level ridge over the western Atlantic. As an upper level short-wave trough approached this ridge, diabatic heating associated with the release of latent heat intensified, and the gradient of vorticity, vorticity advection, upper level divergence, and upward vertical motion (Fig. 2) in advance of the trough were greatly increased, providing strong large-scale forcing for the surface cyclogenesis.

The second case studied was the intense cyclone which developed along the east coast of the United States on 6-7 February 1978. This storm, which also produced record-breaking snowfall accumulations, was accurately predicted by NMC's operational forecast models (Brown and Olson, 1978; Cressman, 1978).

Fig. 3a shows the GLAS model 36 h forecast generated from the NMC analysis at 1200 GMT February 1978 while the corresponding forecasts with surface moisture fluxes withheld and surface heat and moisture fluxes withheld are shown in Figs. 3b and c, respectively. Comparison of these forecasts shows some weakening of the predicted cyclone intensity resulting from the exclusion of surface fluxes. However, the effect of these fluxes is significantly smaller than in the President's Day cyclogenesis.

REFERENCES

Atlas, R., and R. Rosenberg, 1982: Numerical prediction of the Mid-Atlantic states cyclone of 18-19 February 1979. NASA Tech. Memo. 83992, 53 pp.

Brown, H. E., and D. A. Olsen, 1978: Performance of NMC in forecasting a record-breaking winter storm, 6-7 February 1978. Bull. Amer. Meteor. Soc., 59, 562-575.

Cressman, G. P., 1978: A notable forecasting achievement. Bull. Amer. Meteor. Soc., 59, 370.

Halem, M., E. Kalnay-Rivas, W. E. Baker, and R. Atlas, 1982: An assessment of the FGGE satellite observing system during SOP-1. Accepted by Bull. Amer. Meteor. Soc.

Kalnay-Rivas, E., A. Bayliss, and J. Storch, 1977: The 4th order GISS model of the global atmosphere. Beitr. Phys. Atmos., 50, 299-311.

Kalnay-Rivas, E., and D. Hoitsma, 1979: The effect of accuracy, conservation and filtering on numerical weather forecasting. Preprints Fourth Conf. on Numerical Weather Prediction, Silver Spring, Maryland, Amer. Meteor. Soc., 302-312.
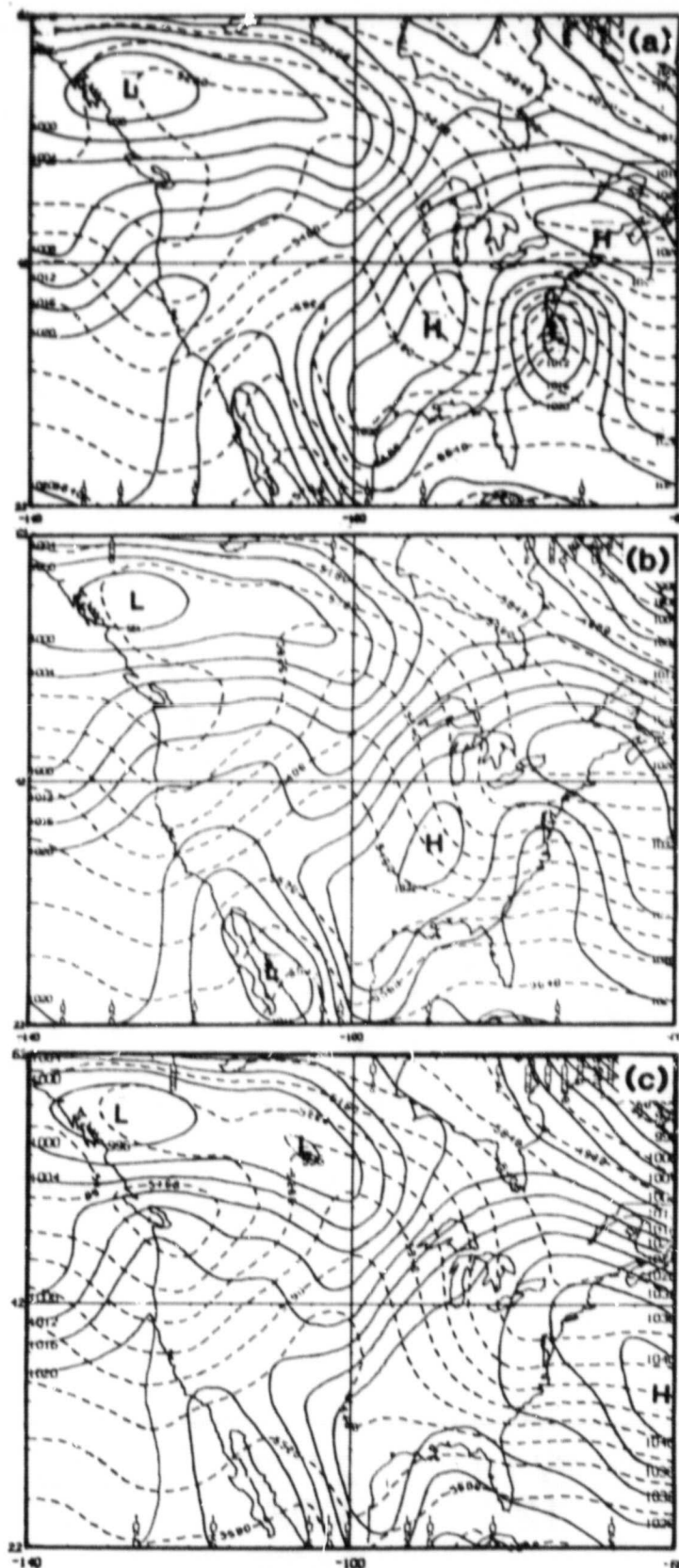
Fig. 1.   GLAS model 36h sea level pressure (solid lines) and 1000-500 mb thickness
          (dashed lines) forecasts valid 1200 GMT 19 February 1979 with full physics
          (a), no surface moisture flux (b), and no surface heat or moisture fluxes
          (c).
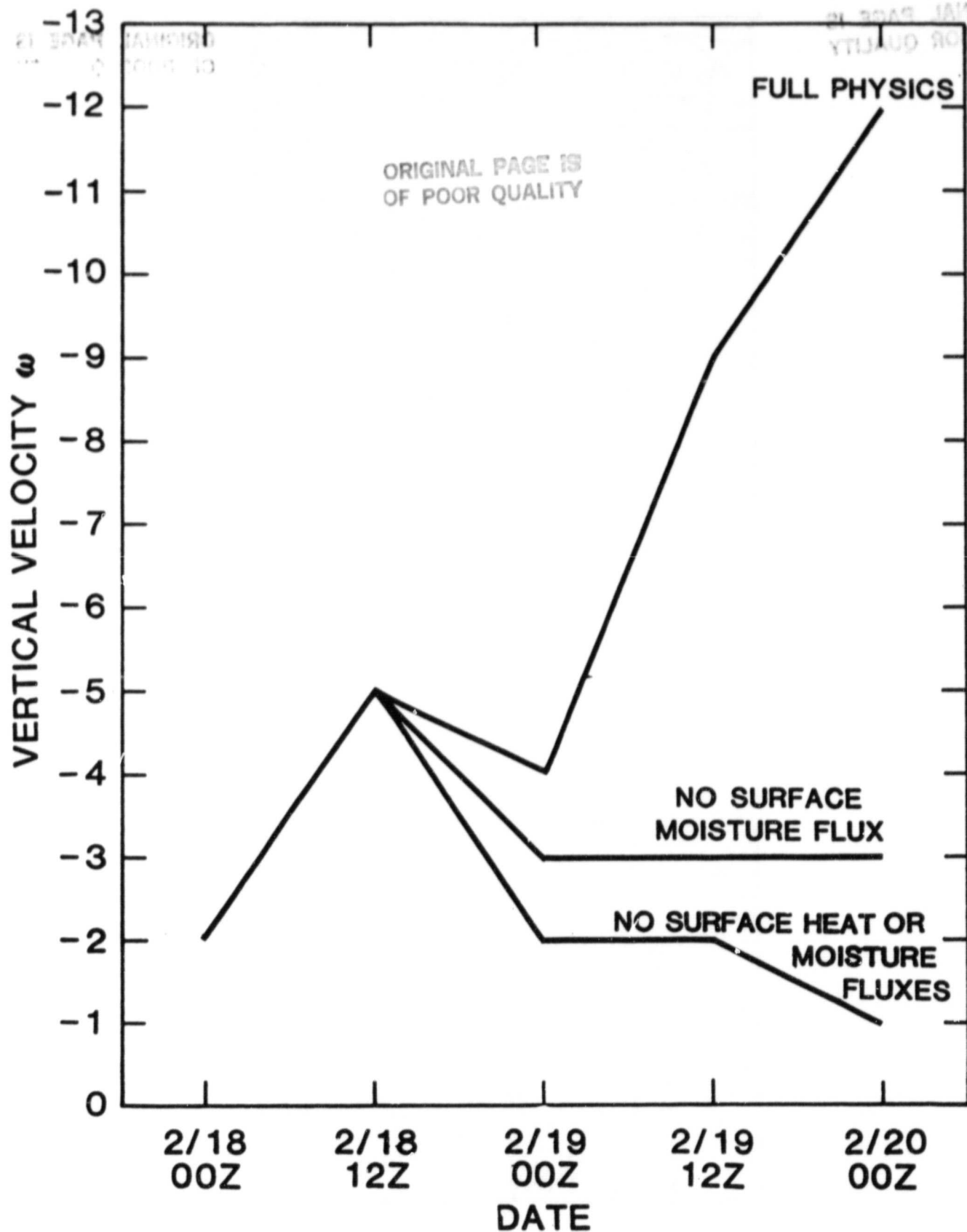
Fig. 2. Change in 500 mb vertical velocity in advance of the upper level trough.
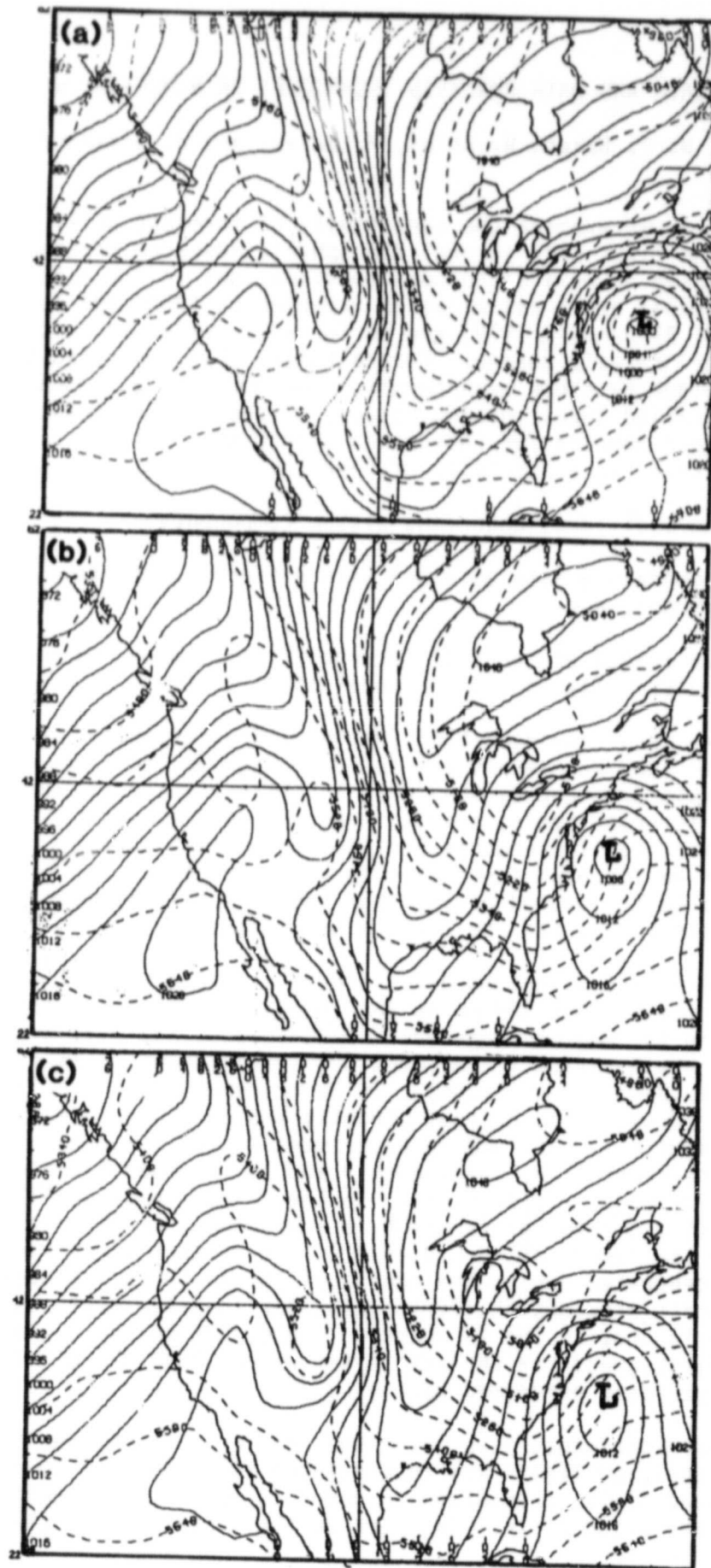
Fig. 3. Same as Fig. 1 for 36h forecasts valid 0000 GMT 7 February 1978.

THE EFFECT OF DATA AND DATA ANALYSIS TECHNIQUES ON NUMERICAL WEATHER FORECASTS

W. E. Baker, R. Atlas, M. Halem, and J. Susskind

In this study we examine the sensitivity of forecast skill to individual components of the First GARP (Global Atmospheric Research Program) Global Experiment database as well as to some modifications in the data analysis techniques. Several short assimilation experiments (0000 GMT 18 January 1979 through 0000 GMT 21 January 1979) are performed in order to test the effects of each database or analysis change. Forecasts are then generated from the initial conditions provided by these experiments. The 0000 GMT 21 January 1979 case is chosen for a detailed investigation because of the poor forecast skill obtained earlier over North America for that particular case. Specifically, we conduct experiments to test the sensitivity of forecast skill to:

1) the individual observing system components,

2) temperature data obtained with different satellite retrieval methods, and

3) the method of vertical interpolation between the mandatory pressure analysis levels and the model sigma levels.

For the one case examined, NESS (National Environmental Satellite Service) TIROS-N infrared land retrievals are found to degrade the forecast, while TIROS-N retrievals produced by GLAS with a physical inversion method, as part of an analysis forecast cycle, result in an improved forecast. The use of oceanic VTPR (Vertical Temperature Profile Radiometer) satellite retrievals also results in an improved forecast over North America. The forecast is found to be sensitive to the method of vertical interpolation between the mandatory pressure analysis levels and the model sigma levels.

These results are illustrated for the S_1 score in Figs. 1 and 2 for the sea level pressure and 500 mb height forecasts verified against the ECMWF (European Centre for Medium Range Weather Forecasts) analysis over North America. In the control assimilation (Experiment 3), (rawinsondes, pibals, aircraft, surface and ship data are utilized). In Experiments 4 and 5 NESS TIROS-N retrievals are added to the control globally and only over oceans, respectively. VTPR data are similarly utilized in Experiment 7 over the oceans. GLAS retrievals are added to the control in Experiments 9 and 10 in a non-interactive mode and in an interactive mode, respectively. In the former, the satellite temperature retrievals utilize a first guess which is independent of the analysis/forecast cycle in which the retrievals are used. In the latter, satellite temperature soundings are generated during the course of the analysis/forecast cycle. The model 6 h forecast provides the first guess for the retrievals as in the non-interactive cycle, but in the interactive cycle, the current model 6 h forecast provides the first guess for the retrievals rather than the 6 h forecast from the control experiment performed earlier.

In the experiments just described, differences between the model first guess and the analyzed fields are interpolated from pressure to sigma rather than the analyzed fields themselves in order to reduce interpolation errors during the assimilation cycle. In order to test this change, the analyzed

wind and temperature fields are interpolated in Experiment 11. Otherwise, Experiment 11 is identical to the control. As may be seen in Fig. 2, Experiment 11 is poorer than Experiment 3.
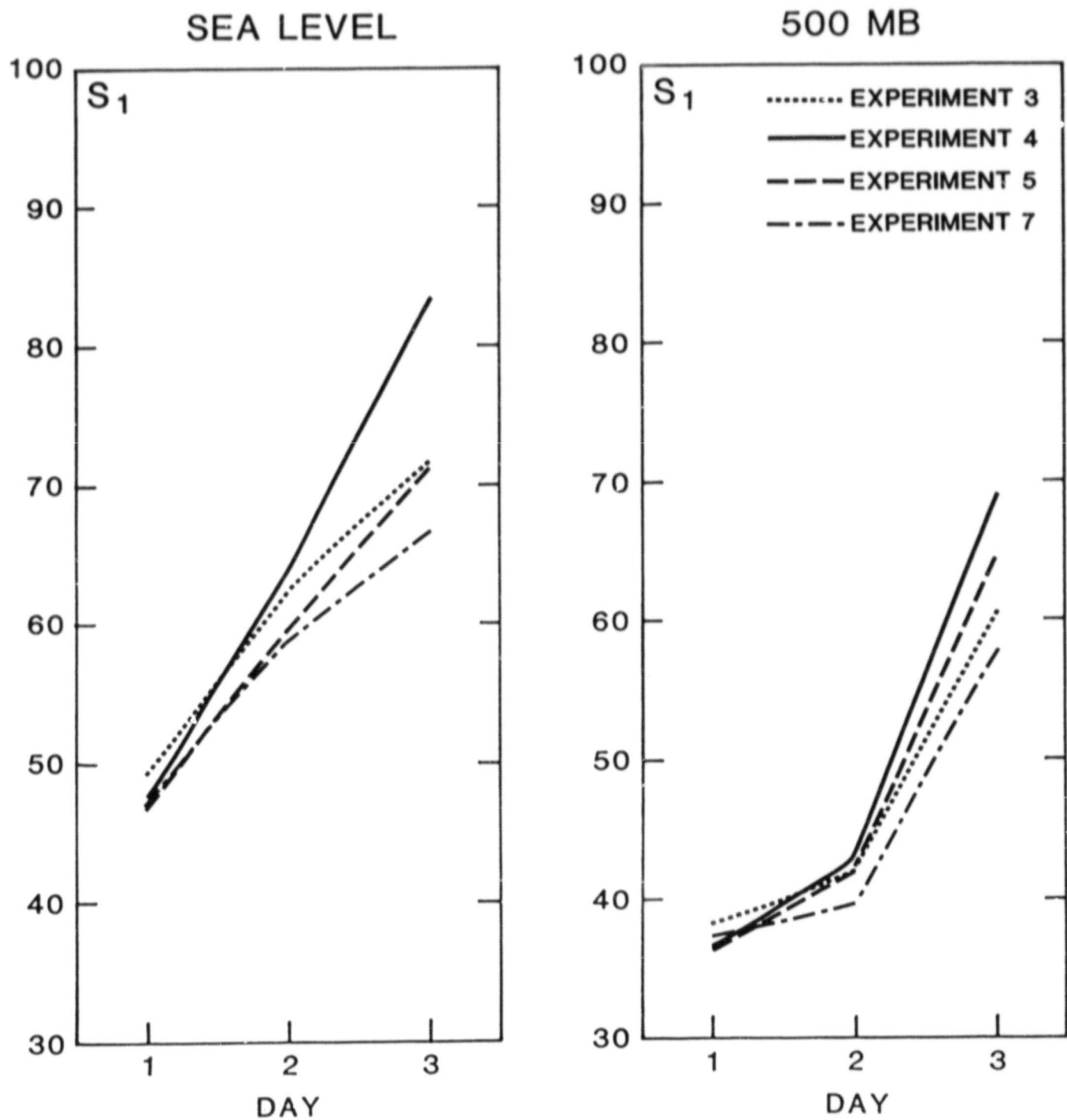
Fig. 1. See text for details.
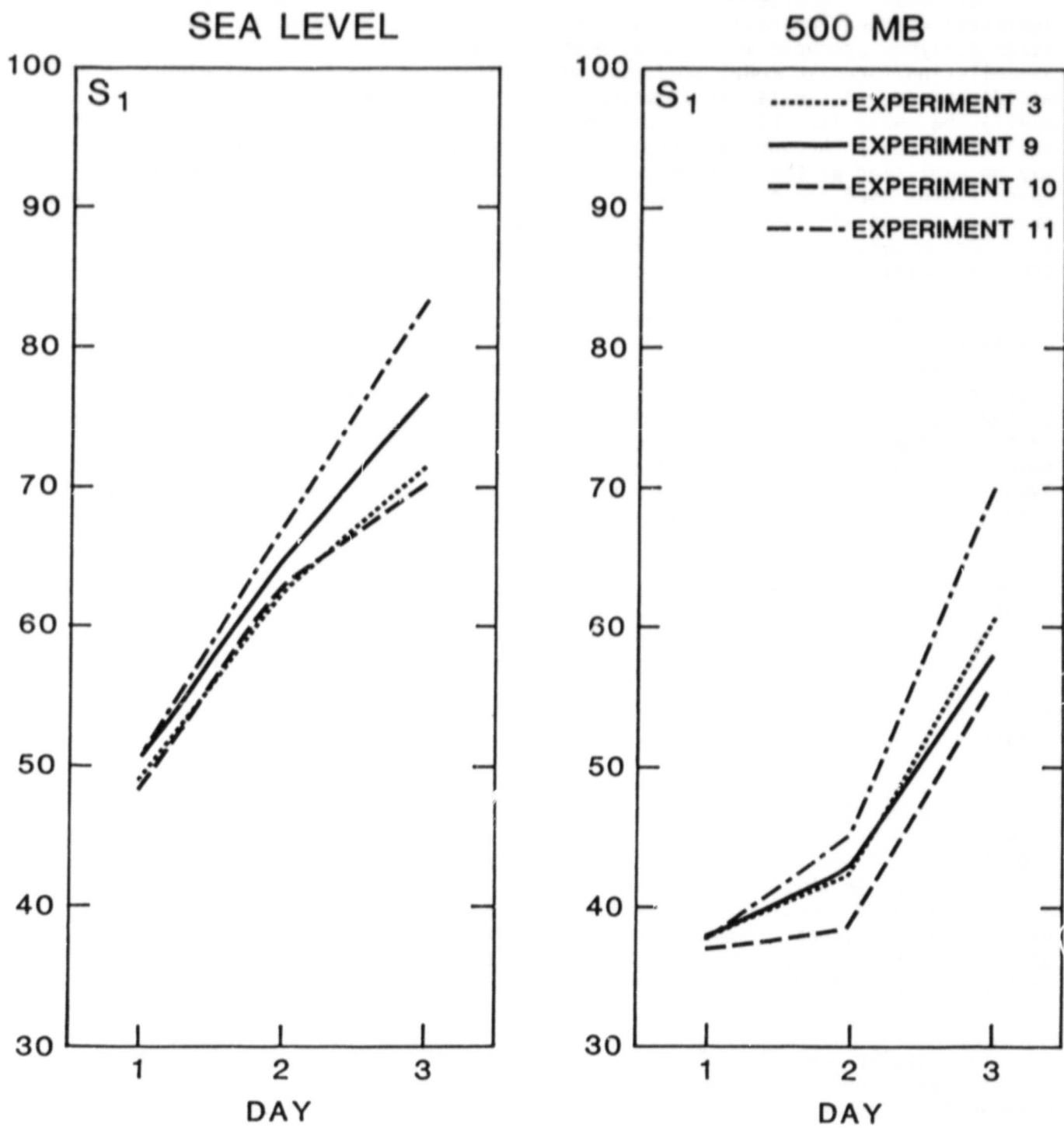
Fig. 2.   See text for details.

MODEL SENSITIVITY TO LOW-LEVEL WIND SPECIFICATION

R. Atlas and A. Pursch

For Seasat-A scatterometer (SASS) data to have a significant impact on numerical weather forecasting, substantial differences between the atmospheric state analyses produced with and without SASS data must occur, and the assimilation/forecast model used must be sensitive to the low level wind modifications. Assimilation of scatterometer data can work in two ways to modify the analysis. First, it can modify the wind field directly and the mass field indirectly through geostrophic adjustments. Second, these differences may be amplified at the next analysis time due to their effects on the first guess fields used for that analysis. Thus, the differences in objective analyses produced by the assimilation of scatterometer data can grow until a statistical equilibrium value is reached. This depends on the model's climatology and on the availability of conventional data.

Preliminary assimilation/forecast experiments with SASS data utilizing the coarse 4° latitude x 5° longitude GLAS Fourth-Order Forecast Model (Kalnay-Rivas et al., 1977 and Kalnay-Rivas and Hoitsma (1979) have shown a generally small effect of the SASS data on both analyses and forecasts. This may be due to the quality of the dealiased SASS winds, the assimilation methodology used in the preliminary impact experiments, model insensitivity to the SASS winds resulting from coarse resolution and the lack of a detailed planetary boundary layer formulation, or the SASS winds may be largely redundant to existing conventional observations and satellite temperature soundings.

Experiments have been conducted to investigate the sensitivity of the GLAS Fourth Order Forecast Model to low level wind specification. In the experiments, model forecasts were generated from initial conditions in which the correct 1000 mb or 1000 and 850 mb wind fields were replaced by the corresponding fields from 24 hours earlier. This has the effect of inserting large spatially coherent errors into the initial low level wind fields without disturbing the low level mass field or the upper level mass and wind fields, and allows the model sensitivity to these errors to be examined.

Fig. 1 shows the initial sea level pressure field for a forecast from 0000 GMT 9 September 1978, the 1000 mb wind field valid at this time, and the 1000 mb wind field valid at 0000 GMT 8 September. Fig. 2 shows the 36 hour forecasts from 0000 GMT 9 September which utilized these 1000 mb wind fields as well as a third forecast in which both the 1000 mb and 850 mb wind analyses from 0000 GMT 8 September were used. Comparison of these forecasts shows the forecasts to be similar in most areas. However substantial differences in the intensity of pressure systems (particularly in the North Atlantic) are evident and these differences are enhanced where the initial wind errors extended to the 850 mb level.

The results presented above are typical of other cases and indicate that the forecast model can be sensitive to surface wind data and the effect of such data would be enhanced if higher levels were also affected in the analysis.

22
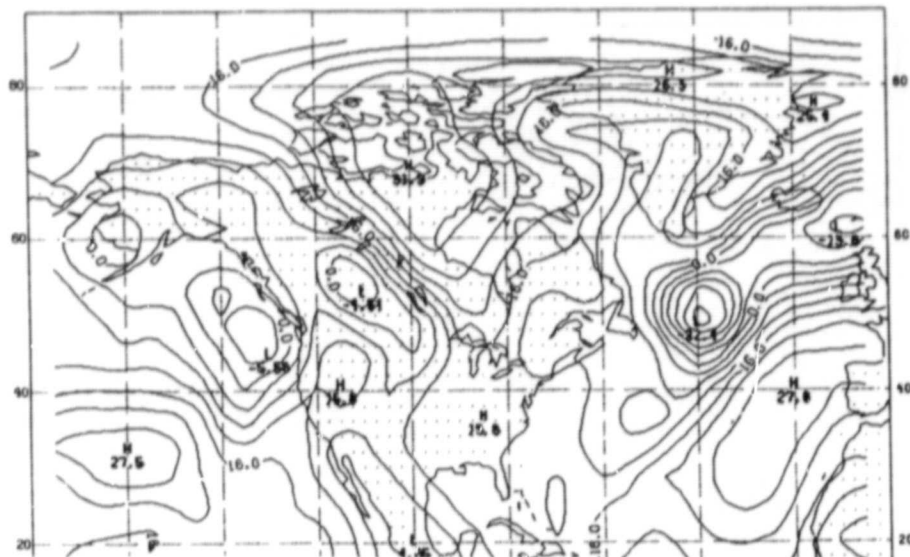
SEA LEVEL PRESSURE (MB)
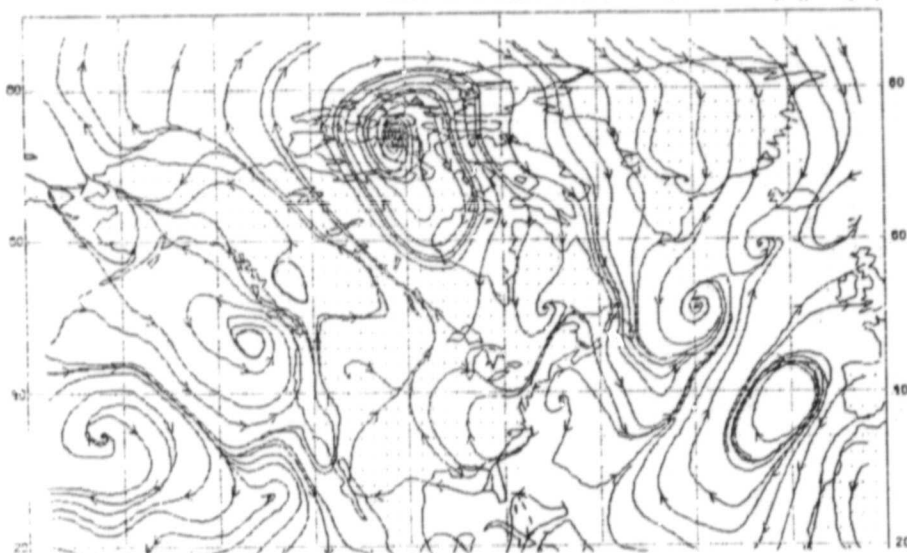
1000 MB STREAMLINE ANALYSIS
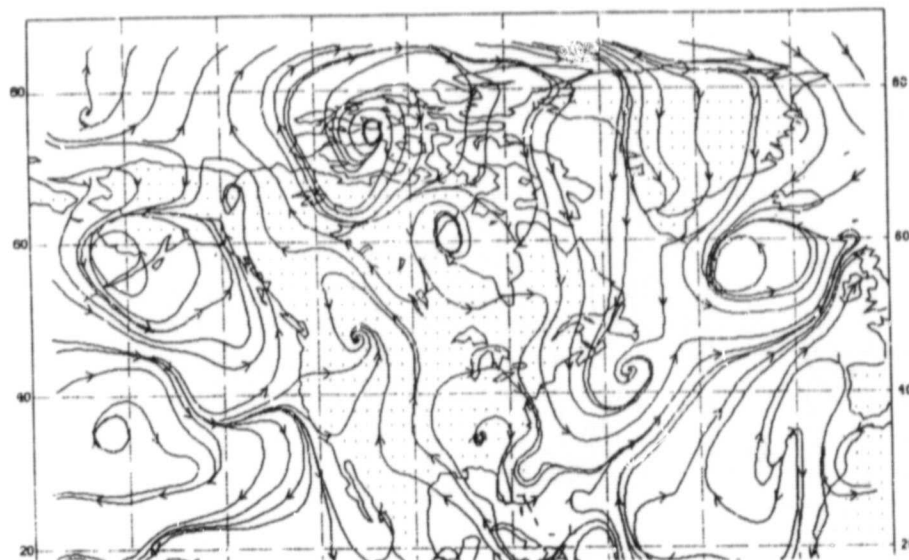
Fig. 1.   a) Sea level pressure analysis for 0000 GMT 9 September 1978.
          b) 1000 mb wind analysis for 0000 GMT 9 September 1978.
          c) 1000 mb wind analysis for 0000 GMT 8 September 1978.

SEA LEVEL PRESSURE (MB)
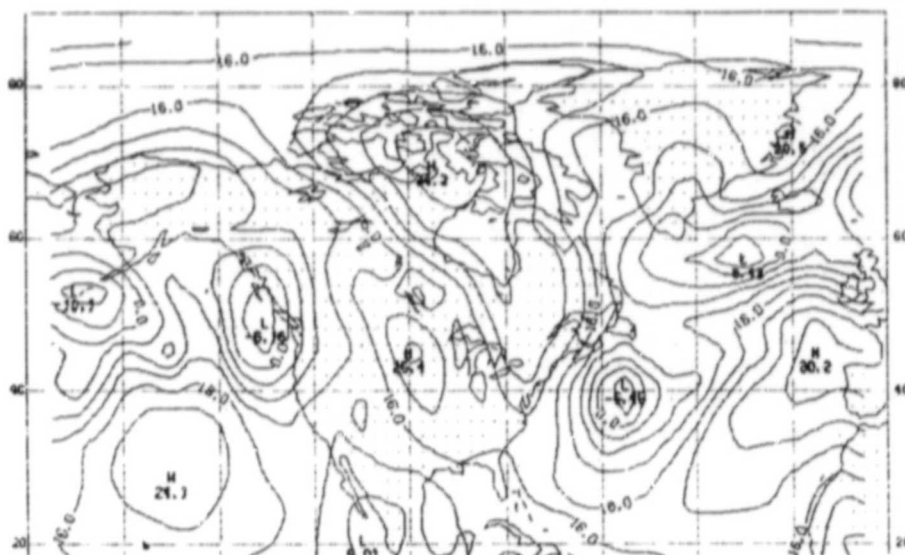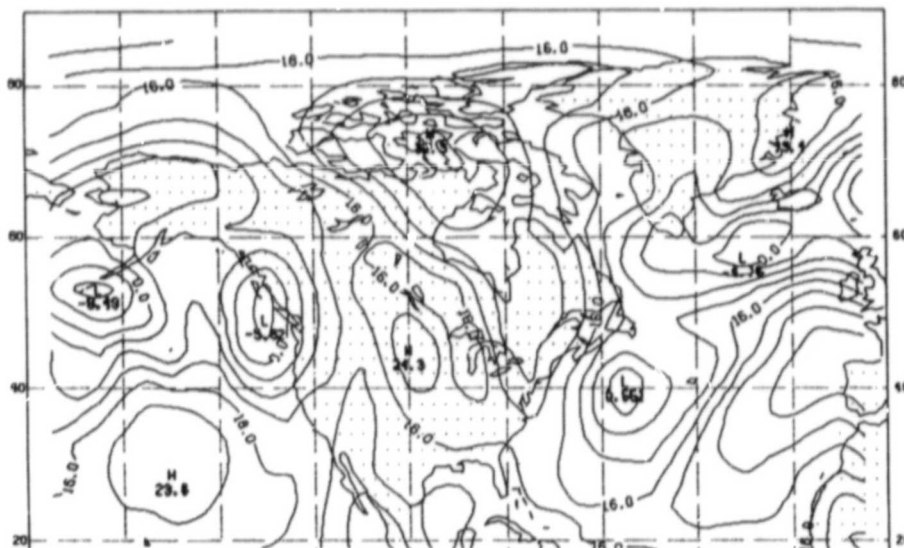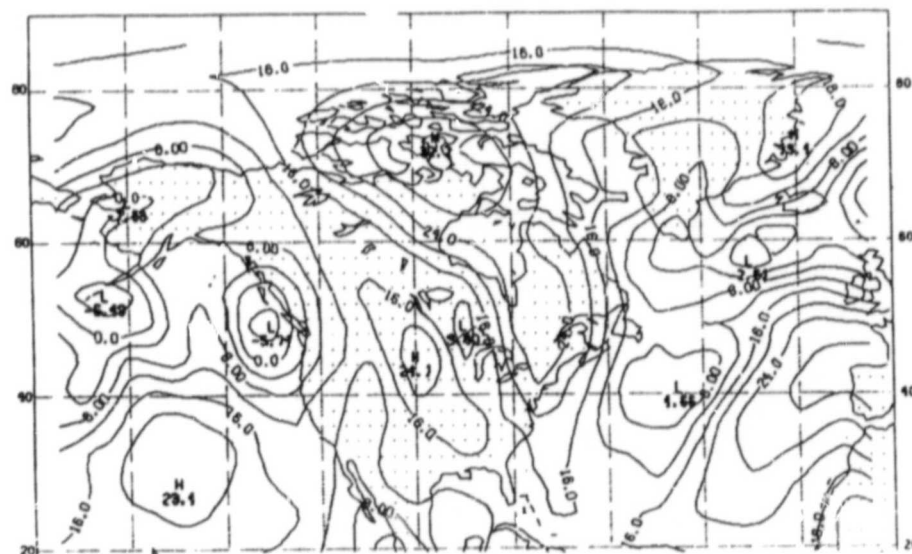
Fig. 2. 36h sea level pressure forecasts from 0000 GMT 9 September 1978
   a) with correct winds
   b) with incorrect 1000 mb winds (from 0000 GMT 8 September)
   c) with incorrect 1000 mb and 850 mb winds (from 0000 GMT 8 September)

SEASAT-A IMPACT EXPERIMENTS

R. Atlas, W. E. Baker, M. Halem and E. Kalnay

A study is being conducted to assess the impact of Seasat-A scatterometer (SASS) wind data on GLAS model analyses and forecasts. The SASS wind data fields, utilized in this study, were obtained from the Atmospheric Environment Service (AES) of Canada, courtesy of Dr. S. Peteherych. The inferred SASS winds contain a directional ambiguity with up to four possible directions associated with each report. Consequently, this directional ambiguity or "aliases" must be removed or accounted for when used in objective analysis.

The GLAS system employs a three-pass "iterative" procedure to objectively dealias the SASS wind field. Subjective dealiasing and subjective enhancement of objectively dealiased winds are also being performed in collaboration with Mr. P. Woiceshyn (JPL), Dr. M. Wurtele (UCLA) and Dr. S. Peteherych (AES).

A preliminary series of assimilation/forecast experiments have been performed with the GLAS analysis/forecast system (previously used for FGGE experiments). Four assimilation experiments were conducted from 0000 GMT 7 September 1978 to 0000 GMT 15 September 1978 which differed only with respect to the inclusion or exclusion of objectively dealiased SASS wind data or satellite temperatures from the available Vertical Temperature Profile Radiometer (VTPR) on board the NOAA-4 satellite. A total of sixteen forecasts (four from each assimilation) were generated from initial conditions at 0000 GMT 9 September, 1200 GMT 10 September, 0000 GMT 12 September and 1200 GMT 13 September 1978, respectively.

The SASS data impact is evaluated by means of pressure and wind field comparisons, objective measures of forecast accuracy and subjective comparisons of prognostic charts. Preliminary results indicate a negligible impact of the SASS data in the Northern Hemisphere and a small positive impact in the Southern Hemisphere. However, a larger impact is obtained in the Southern Hemisphere if the VTPR data are excluded from the system indicating some redundancy between the two systems.

B. SATELLITE OBSERVING SYSTEMS

APPLICATIONS OF A GLOBAL SPECTRAL ANALYSIS METHOD

M. Halem and E. Kalnay

Current four dimensional analysis (e.g. Rutherford, 1972) combine model forecasts with observations of mass and wind fields. In these schemes, the model provides an estimate of the fields in regions with data gaps. However, the dense coverage afforded by the satellite soundings allows useful estimates of not only temperatures but of thermal winds [Petersen and Horn, 1977; Broderick, 1981]. Thus, the uniform coverage afforded by satellite sounders suggests that for the first time it may be possible to produce daily global analyses of heights and winds without the use of a model. Although such analyses may not be optimal, their errors are uncorrelated with model errors, which could prove useful in validating results from four dimensional analysis schemes.

In this work we produce global spectral analyses of height and geostrophic winds employing the regularization method of Tyknonov (1963, 1964), in a form similar to that of Wahba and Wandelberger (1981). The method is well suited for satellite data but can be used also with other types of data. An optimal analysis based on cross-validation, using estimates of observational errors is obtained. For simplicity, the method is applied first along latitude circles, and then 2-dimensional analyses are obtained by expansion in spherical harmonics.

The global analysis scheme is shown to be (i) numerically stable and convergent in data sparse regions, i.e., it minimizes errors of interpolation, (ii) easy to implement since it avoids the need for solving the partial differential equations of mixed type that results in variational analysis schemes [Sasaki, 1960].

Fig. 1a and 1b show the global height field obtained from the NESS and GLAS soundings and in Fig. 1c we show the analysis produced from the gridded level III-b GLAS analysis from 00Z Jan. 5, 1979, all subjected to the same spherical harmonic truncation (T-15). In the southern hemisphere, the three analyses are very similar with differences occuring mainly on the Antartic continent edge. In the northern hemisphere, the largest differences appear in the orientation of the trough over Hudson's Bay, where the GLAS data produced a tilt to the NNE while in the NESS system there is a much stronger NE orientation. Both systems over Europe are in very good agreement with the FGGE analysis.

This method of analysis ought to be particularly applicable to the stratosphere where currently analyses are produced without the benefit of an accurate first guess forecast field and where satellites are the major data source. It is also a region that does not require high horizontal wave resolution, allowing for better fidelity of the harmonic analysis. Figs 2 and 3 compare the 10 mb height analysis from NESS soundings with the operational analyses of the United Kingdom Meteorological Office (UKMO) and NOAA for two different wavenumber regimes. Again, we find these analyses to be in good agreement except near the pole. It should be noted that no NESS data were available at 10 mb poleward of 75°N during the SOP-1.

Among the potential applications of this analysis scheme, we mention:

1) It provides estimates of the state of the atmosphere without the use of a numerical model, so that no spurious waves can be introduced by the model during an analysis cycle. This is particularly important in observational studies of atmospheric wave propagation, where free waves excited in the model may contaminate the four-dimensional analysis results (Lindzen, Straus and Katz, 1983).

2) It provides estimates of geostrophic winds without making use of the statistical assumptions commonly introduced in optimal interpolation, which can be grossly in error (Balgovind et al., 1983).

3) It can be used to obtain 3-dimensional satellite temperature retrievals. Current satellite temperature retrievals are one-dimensional, with a column by column approach. This does not take advantage of the strong redundancy present in current radiance observations which are made with a horizontal resolution of the order of 10 km, much smaller than even subsynoptic atmospheric scales. Clear column radiances should be functions of temperature and moisture, and therefore have smooth spatial structure. The present analysis scheme can be combined with temperature retrieval methods in the following way: Cloud filtering schemes are applied on the radiances to produce a first estimate of clear column radiances. The variational analysis is then applied horizontally to the clear column radiances. This has two major effects: small scale noise can be significantly reduced, and clear column radiances can be estimated even for those spots and channels where excessive cloudiness makes cloud filtering impossible. The standard vertical column temperature retrievals are then applied on the analysed clear column radiances at a regular or irregular grid. The whole procedure can be performed iteratively. The net result of this method should be to reduce both observational noise and data gaps.

4) The method can be applied to four-dimensional spectral analysis. Halem and Kalnay (1983) indicate that "off-line" global spectral analysis can be used as observational input to four-dimensional spectral analysis. They showe that under certain assumptions (i.e., that observational and forecast error statistics are horizontally homogeneous, and that in the computation of the error covariances, the wave-to-wave interactions can be neglected), four-dimensional Kalman filtering can be drastically simplified. Their analysis shows that with these assumptions the formulation of Kalman filtering by Ghil et al. (1982) reduces to a system of scalar equations, one for each wavenumber.

REFERENCES

Balgovind, R., A. Dalcher, M. Ghil, and E. Kalnay, 1983: A stochastic-dynamic model for the spatial structure of forecast error statistics. Mon. Wea. Rev., in press.

Broderick, H. J., 1981: The impact of TIROS-N soundings of the analysis of a cyclone in the Gulf of Alaska. Oct. 21-22, 1979, Fifth Conference on Numerical Weather Prediction, November 2-6, 1981, Monterey, California, American Meteorological Society.

Ghil, M., S. E. Cohn, and A. Dalcher, 1982: Sequential estimation, data assimilation and initialization. July 12-16, 1982, <u>Fourteenth Stanstead Seminar Bishop's University</u>, Quebec, Canada.

Lindzen, R., B. Katz, and D. Straus, 1982: An observational study of large-scale atmospheric Rossby waves. Submitted to <u>J. Atmos. Sci</u>.

Petersen, R. A., and L. H. Horn, 1977: An evaluation of 500 mb height and geostrophic wind fields from Nimbus 6 soundings. <u>Bull. Amer. Met. Soc.</u>, <u>58</u>, 1197-1201.

Tykhonov, A. N., and V. B. Glasko, 1964: Approximate solution of Fredholm integral equations of first kind USSR Comp. Math and Math Phys., <u>4</u>, 236-247.

Wahba, G., and J. Wendelberger, 1980: Some new mathematical methods for variational objective analysis using splines and cross-validation. <u>Mon. Wea. Rev.</u>, <u>108</u>, 36-57.
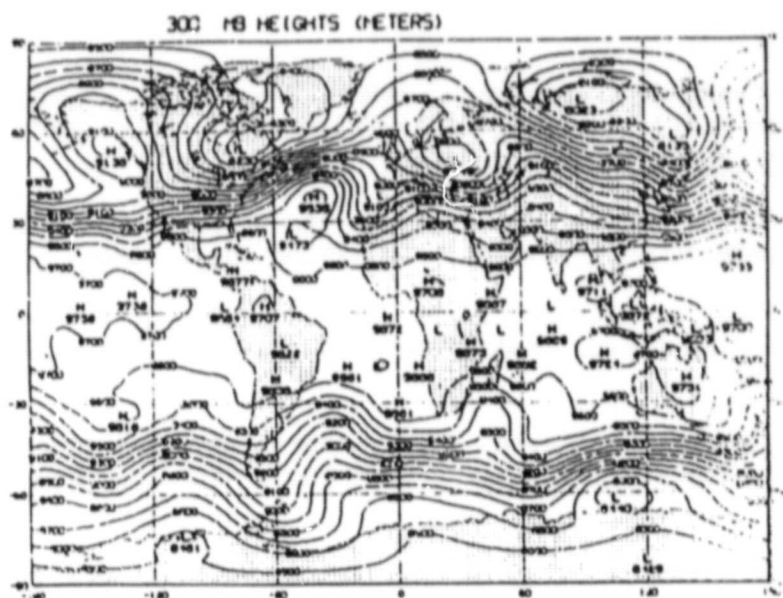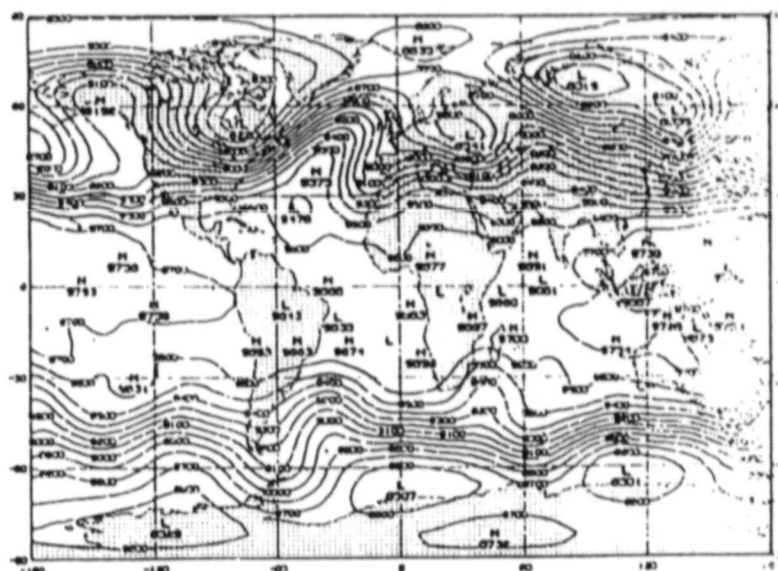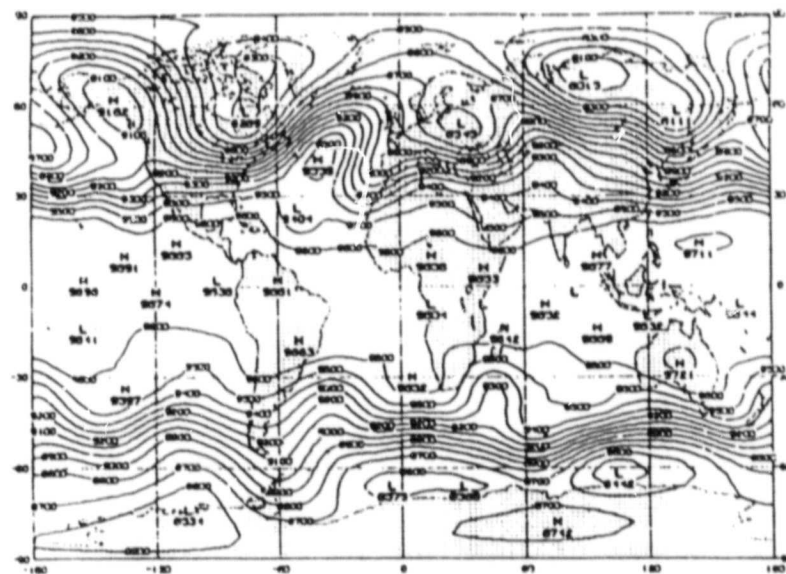
Fig. 1. Spherical harmonic analysis (T-15) of 300 mb geopotential heights at
0Z 5 January 1979. (a) NESS soundings, (b) GLAS soundings, and
(c) Full FGGE analysis.
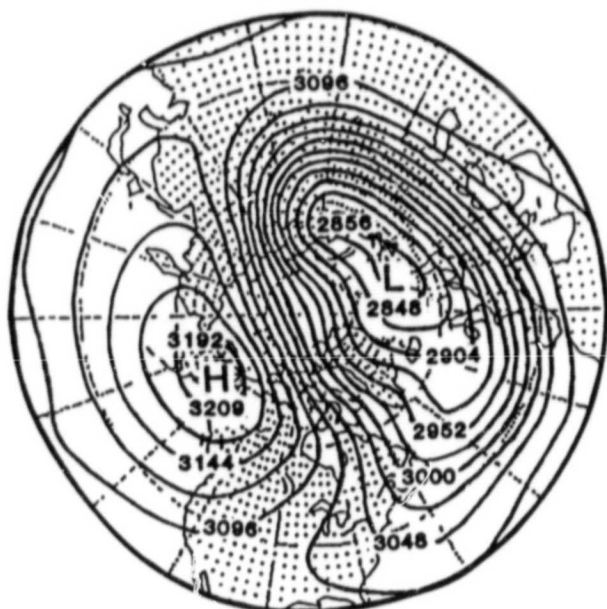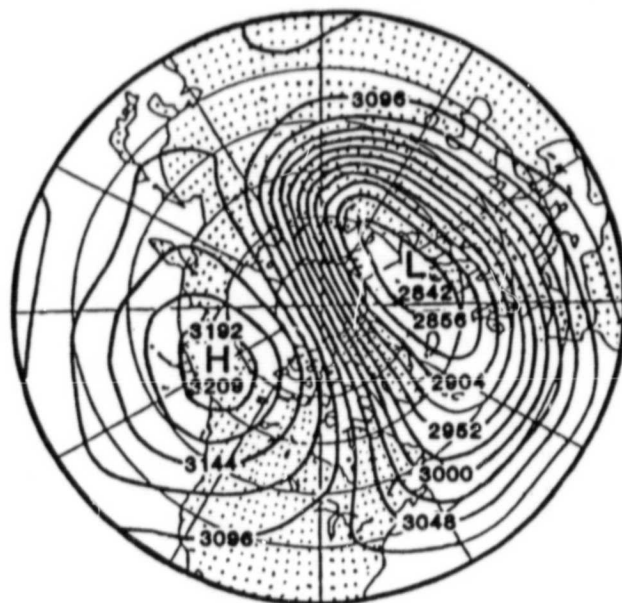
Fig. 2

10 MB HEIGHTS (DECAMETERS)

27 January 1979-0000 GMT ±6 H

GLAS   NOAA
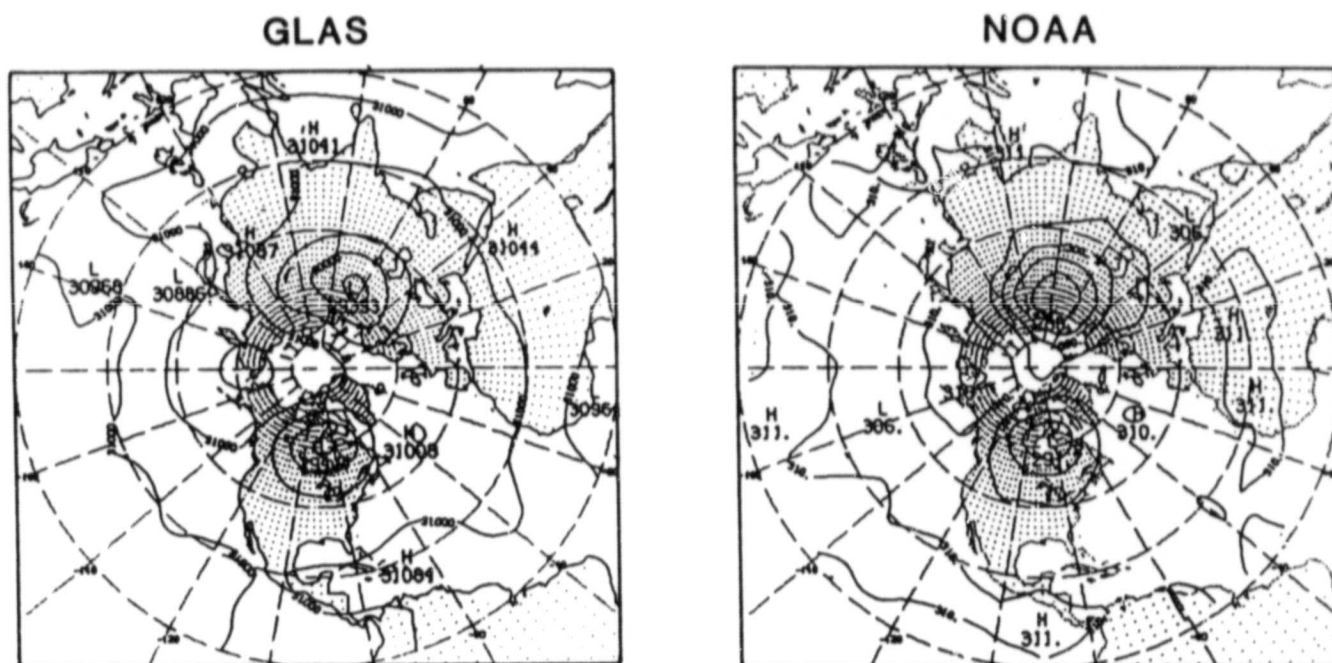
Fig. 3

10 MB HEIGHTS (METERS)

21 FEBRUARY 1979-1200 GMT $\pm$6 H

APPROXIMATE CALCULATIONS OF GREAT CIRCLE DISTANCES

R. Hoffman

For many objective analysis applications it is necessary to calculate the distance between a great many pairs of points on the earth's surface. These distances are great circle distances if the approximation that the earth as a sphere is used. (Airlines often follow great circle routes because great circles are the shortest path between two points on a sphere along its surface.) It is the purpose of this note to describe some approximations for calculating great circle distances when the two points are nearby. This is usually the case in objective analysis. It is assumed that the coordinate system is latitude and longitude. Because of the singularity at the poles in this coordinate system there is not one single best solution to the problem.

A great circle of a sphere is the intersection of any plane which passes through the center of the sphere with the surface of the sphere. This plane is shown in Fig. 1; it includes the two points, P_1 and P_2, the great circle and the center of the sphere, O. If distances are measured in units of the radius, R, of the sphere then the great circle distance g is also the angle P_1OP_2 measured in radians. Then by drawing the radius which bisects this angle and considering the right triangle which results, we see that

(1) $\sin(g/2) = d/2$

where $\underline{d}$ is the distance (in Cartesian space) between the two points. That is,

$$d^2 = (x_1 - x_2)^2 + (y_1 - y_2)^2 + (z_1 - z_2)^2$$

where (x_i, y_i, z_i) are the Cartesian coordinates of the ith point. The orientation and placement of this coordinate system is arbitrary. By transforming latitude and longitude to any convenient Cartesian coordinate system it is tedious but not too hard to show that

(2) $(d/2)^2 = \sin^2\phi - \sin^2\lambda\ (\sin^2\phi - \cos^2\bar{\phi})$

where

$\phi = (\phi_1 - \phi_2)/2$

$\lambda = (\lambda_1 - \lambda_2 + 2n\pi)/2$

$\bar{\phi} = (\phi_1 + \phi_2)/2$

where (ϕ_i, λ_i) are the latitude and longitude of the ith point. n may be zero or any integer here, but in what follows it should be chosen so that $|\lambda| \leq \pi/2$. Solving (1) and (2) for q is relatively expensive as there are five special function calls (two sines, a cosine, a square root and an arcsine).

To get approximations for small q expressions are found for d of the form

(3) $\quad (d/2)^2 = r^2[1 + a + b + O(s^6)]$

where $a = O(s^2)$, $b = O(s^4)$, $r = O(s)$ and s is a small parameter. Then by using the asymptotic expansions for $(1 + x)^{1/2}$ and $\sin^{-1}(x)$ it is found that

(4) $\quad q = 2r[1 + \{(a + r^2/3)/2\} + \{(b + a(r^2 - a/2)/2 + 3r^4/20)/2\} + O(s^6)]$

Note that the first term in $\{\ \}$ is $O(s^2)$ and the second is $O(s^4)$. Three cases are considered below for approximations valid away from the pole, near the pole and over the whole sphere. The first two cases require two special function calls while the third case requires three special function calls; this additional call is the cost of a uniformly valid approximation.

Case 1. Away from the pole both ϕ and λ are always small if q is small so everything but $\cos \phi = \alpha$ may be expanded. The result is

$r^2 = \phi^2 + \alpha^2\lambda^2$

$s^2 = \phi^2 + \lambda^2$

$a = -(s^2 + (2 - \alpha^2)\lambda^2\phi^2/r^2)/3$

$b = (2(s^4 - \lambda^2\phi^2) + (13 - 2\alpha^2)s^2\lambda^2\phi^2/r^2)/45$

For this case, the leading order behavior, i.e., neglecting terms of $O(s^2)$ in (4), is the approximation given by Schlatter (1975). In Eq. 4 the more terms retained the more accurate the solution as s^2 approaches zero but for finite s^2 neglecting terms of $O(s^4)$ gave the best results in numerical tests.

Case 2. Near the pole λ may be large even though the two points are close together. ϕ is still small and $|\phi|$ must be close to $\pi/2$. Let $\eta = \pi/2 - |\phi|$ so that $\cos \phi = \sin \eta$. Then everything may be expanded but $\sin \lambda = \mu$ and

$r^2 = \mu^2\phi^2 + (1 - \mu^2)\eta^2$

$s^2 = \phi^2 + \eta^2$

$$a = -(\mu^2\phi^4 + (1 - \mu^2)n^4)/3r^2$$

$$b = 2(\mu^2\phi^6 + (1 - \mu^2)n^6)/45r^2$$

Case 3. For a globally valid approximation neither $\cos \overline{\phi} = \alpha$ or $\sin \lambda = \mu$ may be expanded, resulting in

$$r^2 = (1 - \mu^2)\phi^2 + \alpha^2\mu^2$$

$$s^2 = \phi^2$$

$$a = -(1 - \mu^2)\phi^4/3r^2$$

$$b = 2(1 - \mu^2)\phi^6/45r^2$$

In all cases great care must be taken in programming to obtain efficient programs; all unnecessary arithmetic and logic must be eliminated. Note that when $r^2 = 0$ the two points are identical and $g = 0$. When the approximations for cases 1 and 3 neglecting terms of $O(s^4)$ were tested against the exact solution the relative errors were smaller than 1% for $\underline{g}$ as large as 1.

Finally, we note that for some applications it may be necessary to calculate great circle distances between a central point and many other points. In such a case one could also make use of the fact that $\phi = \phi_1 - \phi$ is small in calculating

$$\alpha^2 = \cos^2\phi_1 + 2(\cos \phi_1 \sin \phi_1) \phi + (\sin^2\phi_1 - \cos^2\phi_1) \phi^2$$

$$- 4/3 (\cos \phi_1 \sin \phi_1) \phi^3 - 1/3 (\sin^2\phi_1 - \cos^2\phi_1) \phi^4 + \ldots\ldots$$

Reference:

Schlatter, T. W., 1975: Some experiments with a multivariate statistical objective analysis scheme. Mon. Weather Rev., 103, 246-257.
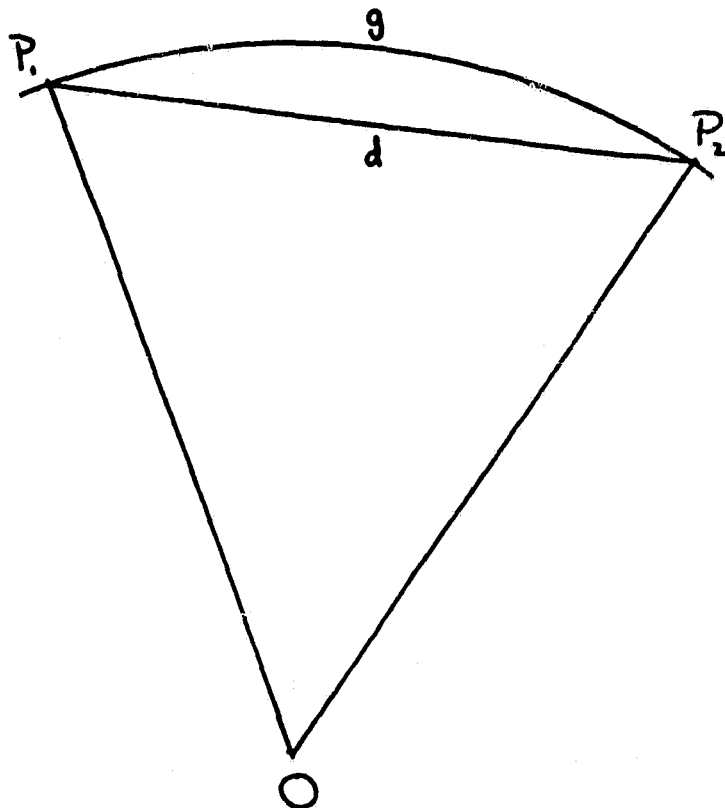
Fig. 1. The great circle distance, g, is the length of arc P_1P_2, d is the distance from P_1 to P_2 and $OP_1 = OP_2 = R$ is the radius of the sphere.

IMPROVEMENT OF MSU TEMPERATURE RETRIEVALS BY USE OF TROPOPAUSE HEIGHTS DERIVED FROM TOMS OZONE MEASUREMENTS

M.-J. Munteanu, E. R. Westwater, and N. C. Grody

The purpose of the paper is to use the high correlation between TOMS total ozone data and tropopause height to improve the MSU temperature retrievals.

The implementation of the tropopause height information is done in the context of stratified regression.

As discussed by Munteanu (companion paper) tropopause pressure can be derived from TOMS measurements of the total amount of ozone. Measurements of tropopause height obtained by a completely different technique, namely a ground-based VHF radar, led to dramatic improvement of temperature retrievals obtained from a ground-based microwave radiometer (Westwater et al., 1983). It would be of large practical importance if similar improvement could be obtained in satellite temperature retrievals from a satellite-based instrument which measures tropopause height.

We present here two case studies in which temperature profiles are derived from simulated MSU brightness temperatures, with and without the ozone-derived tropopause heigh information. We show that the accuracy and resolution of the derived profiles is considerably improved, especially in the region of the tropopause.

Our results are based on high spatial correlation between total ozone maxima and minima and the troughs and ridges in the tropopause field obtained by M.-J. Munteanu in a previous paper.

The conclusions of the above mentioned paper are the following:

1. The sample correlation was found to be .94 and .96, and as a result of this high correlation the rms error in the prediction of the tropopause height from total ozone was found to be 15 mb. In the prediction procedure the regression has been used in a manner equivalent to cross-validation.

2. Correlation between tropopause height and total ozone is the highest among all the other correlations with variables such as: brightness temperatures from microwave channels, ratio and differences of these quantities, latitude, mean layer temperatures, surface temperatures or surface pressure.

3. The high ozone values are associated with lows in 500 mb and 300 mb analysis and low ozone values with corresponding highs in the heights analysis.

4. In the MSU regression retrievals in the low tropopause cases there is a large bias and a significant residual error. The tropopause is mislocated by 100 - 200 mb.

5. The total rms error in the MSU regression retrievals is rather large in the region of the tropopause in comparison with the rest of the retrieval.

RETRIEVAL RESULTS

The results of our simulation study will be shown in three complementary ways. The first is simply to show typical retrieval results for the three coefficient sets (see Fig. 1, 2). All the sets of retrieval coefficients used in this study are derived using linear regression.

The first set is derived from an ensemble of 400 mid-latitudinal profiles with 0.5 K noise. We call the regression retrieval obtained global regression. The second set was derived from a collection of about 2000 profiles for the period February-March-April 1972-1977 for Denver, CO. The regression retrieval obtained is called here local regression. The third and most relevant sets of retrieval coefficients for this paper were calculated for ensembles containing profiles stratified by tropopause pressure within 40 mb thick class intervals. The data base for the tropopause stratification was all profiles 1972-1977, Denver, CO.

CONCLUSIONS

As is seen from the Figs. (1, 2) a substantial improvement in accuracy occurs around the tropopause region when stratified coefficients are used. In all of our cases, no degradation of retrievals occured when tropopause stratified coefficients were used, and in a substantial fraction cases, a dramatic improvement in accuracy and resolution was apparent.

Sometimes even in the lower tropopause region the accuracy of the retrieval is improved.

The general improvement in accuracy obtained by using ozone data is quite apparent in the statisical sense. In Table 1, we present at mandatory pressure levels the rms errors of the three sets of retrievals for the April 15, 1979 and the April 25, 1979 cases. The performance of the two climatological retrievals is bettered at almost all levels by the tropopause stratified retrievals, with improvements ranging from 1 to 2 K rms.

As a final illustration of the retrieval improvement offered by the utilization of ozone data, we present two-dimensional fields of tropopause height as derived from (a) radiosondes (ground truth), (b) local climatological retrievals, (c) global climatological retrievals, and (d) tropopause stratified retrievals. It is apparent that both climatological retrievals result in tropopause height fields that bear little resemblance to the actual ones. However, the thermal fields derived from the combined MSU and ozone contain several, but not all, of the features of the original field. These results strongly suggest that tropopause height information is, at best, only weakly contained in the MSU radiances.

As a general conclusion the results presented strongly suggest that a substantial improvement in, at least, MSU thermal retrieval accuracy can be obtained by utilizing TOMS measurements of total ozone content and its subsequent relationship to tropopause height. These results are totally consistent with earlier efforts incorporating radar tropopause height measurements with passive soundings (Westwater et al., 1983).

RMS by Levels

	APRIL 15				APRIL 25	
Pressure in mb	Local Clim	Strat Trop	AMSU		Global Clim	Strat Trop
1000	-	-	3.024		5.889	-
850	-	-	4.174		2.276	-
700	4.321	4.311	3.044		2.721	3.324
500	4.035	2.514	3.364		3.278	1.885
400	2.900	2.797	2.297		3.809	2.060
300	4.543	1.828	4.079		2.096	1.880
250	3.475	2.213	5.242		2.418	1.823
200	3.539	2.453	5.727		4.064	1.979
150	2.361	2.570	3.627		2.687	2.112
100	1.687	1.760	1.516		2.753	1.840
70	2.118	2.090	-		1.061	1.742
50	1.867	1.844	-		2.086	2.014
nr. of profiles	38	38	38		42	42

Table 1
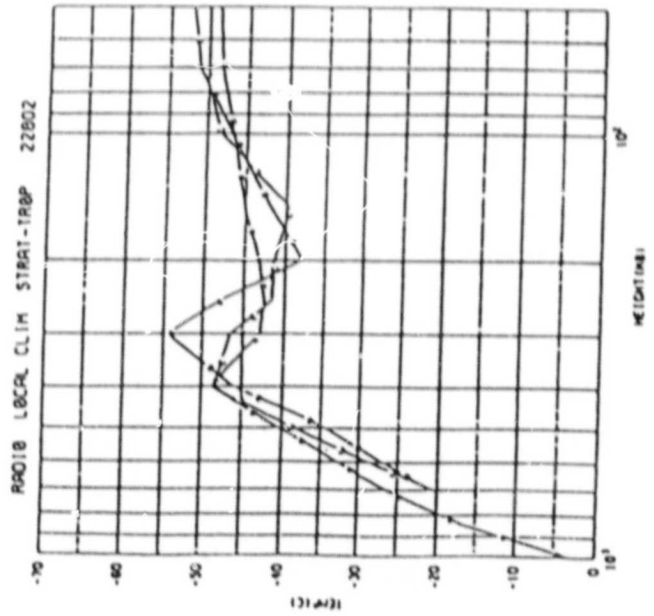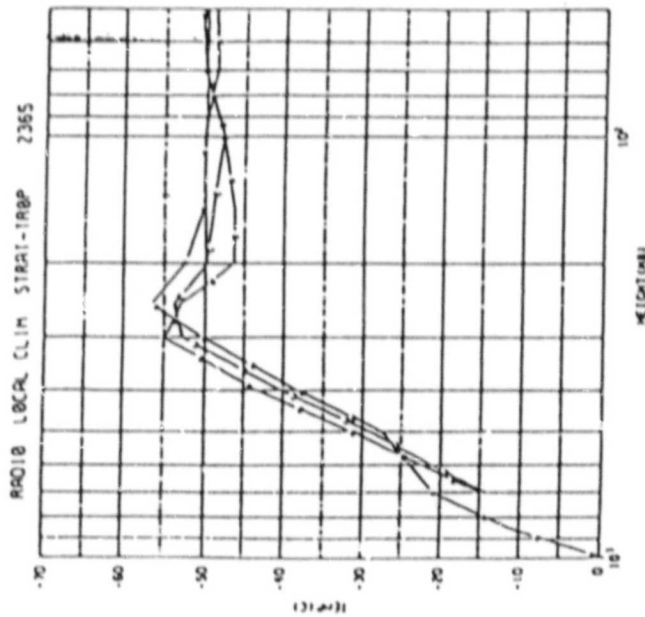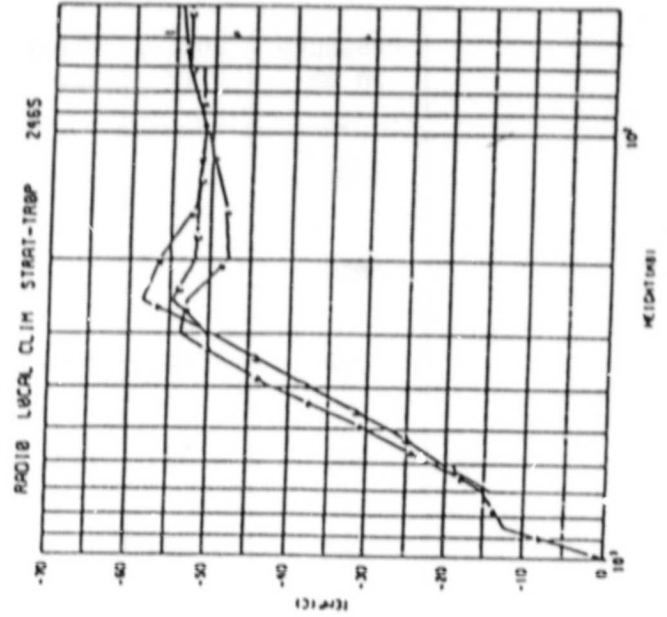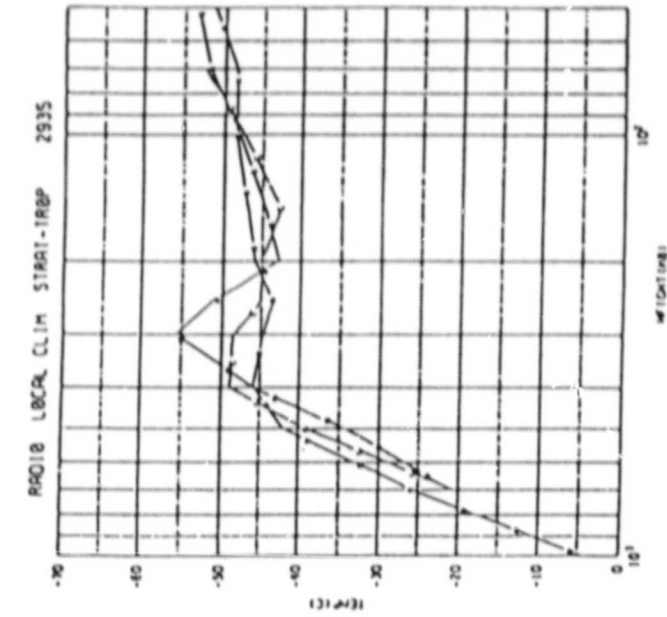
41
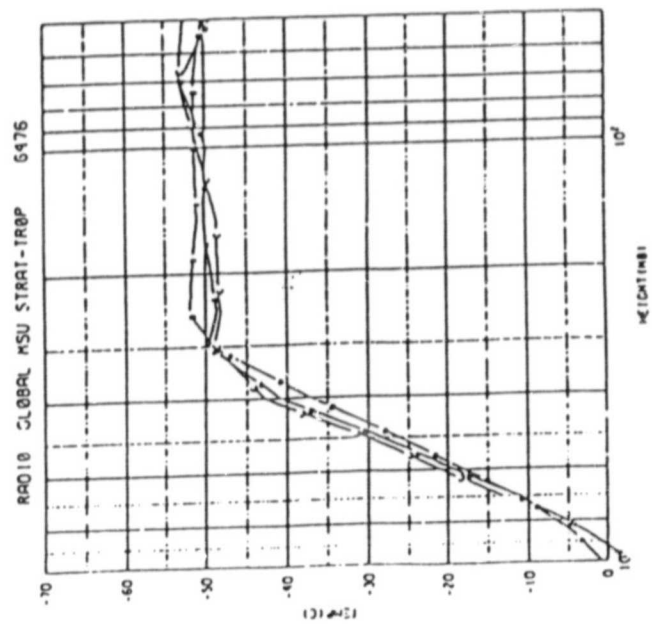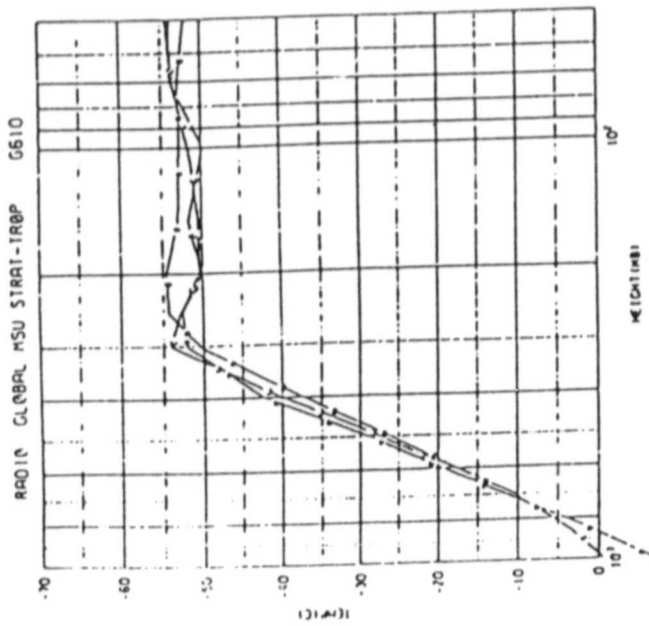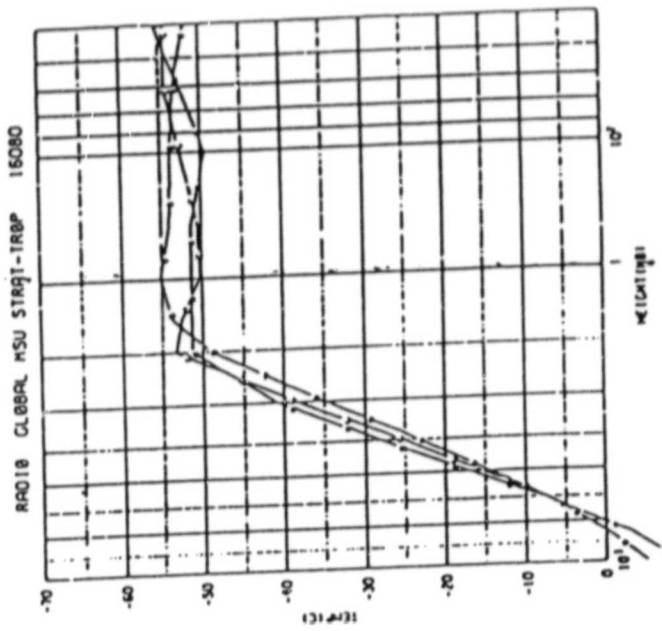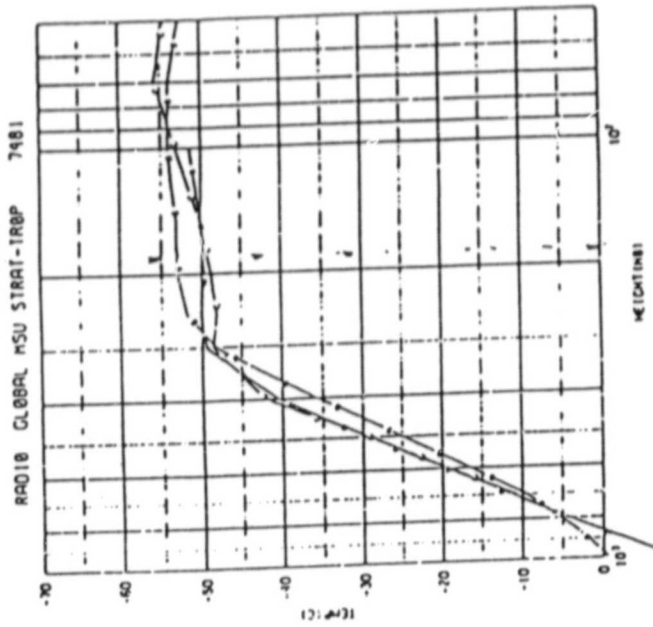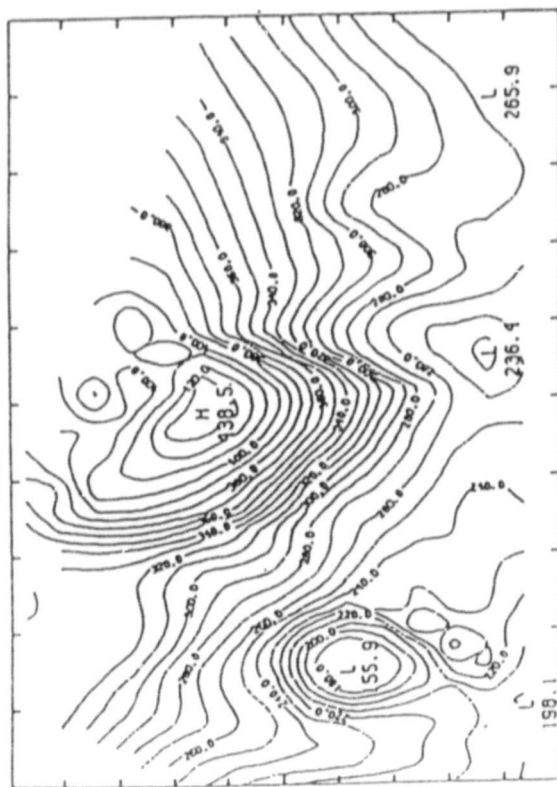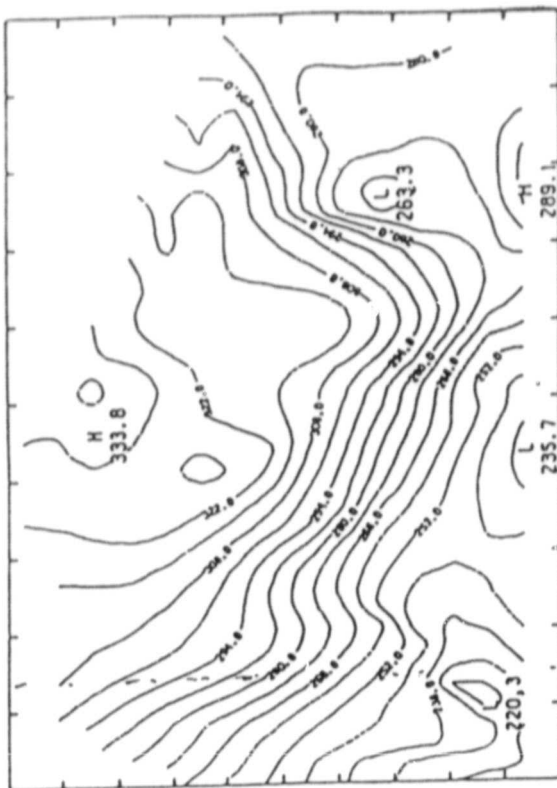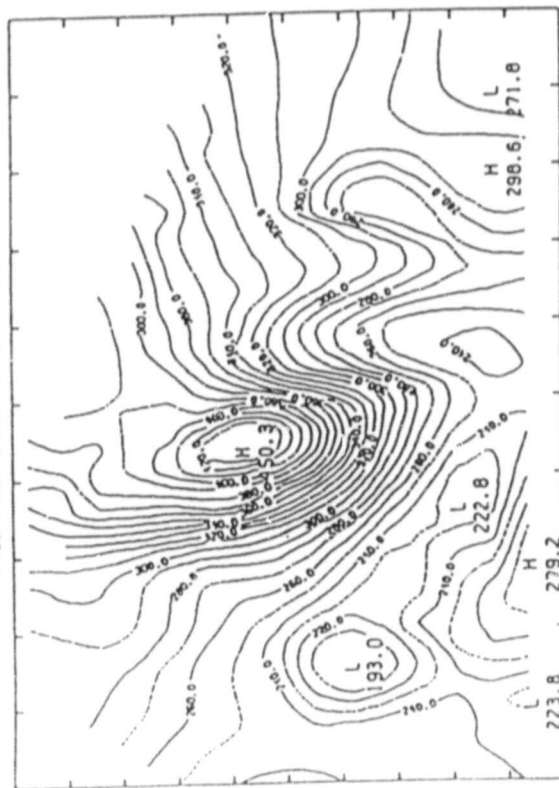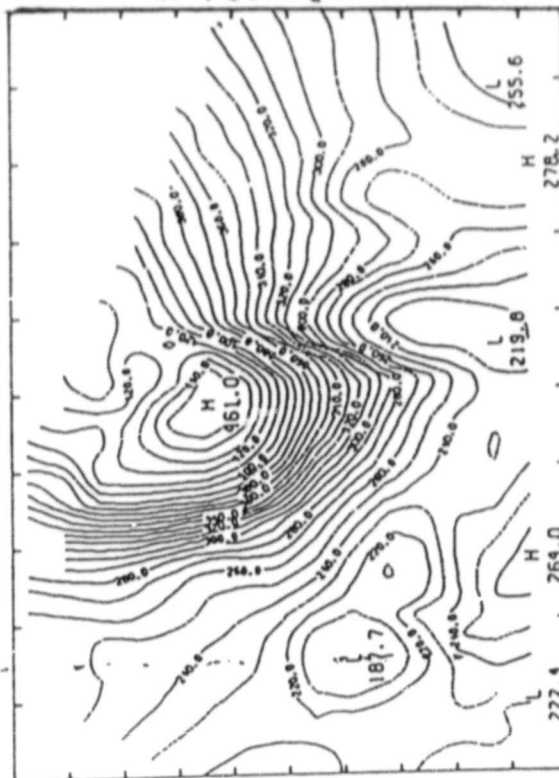
Figure 1
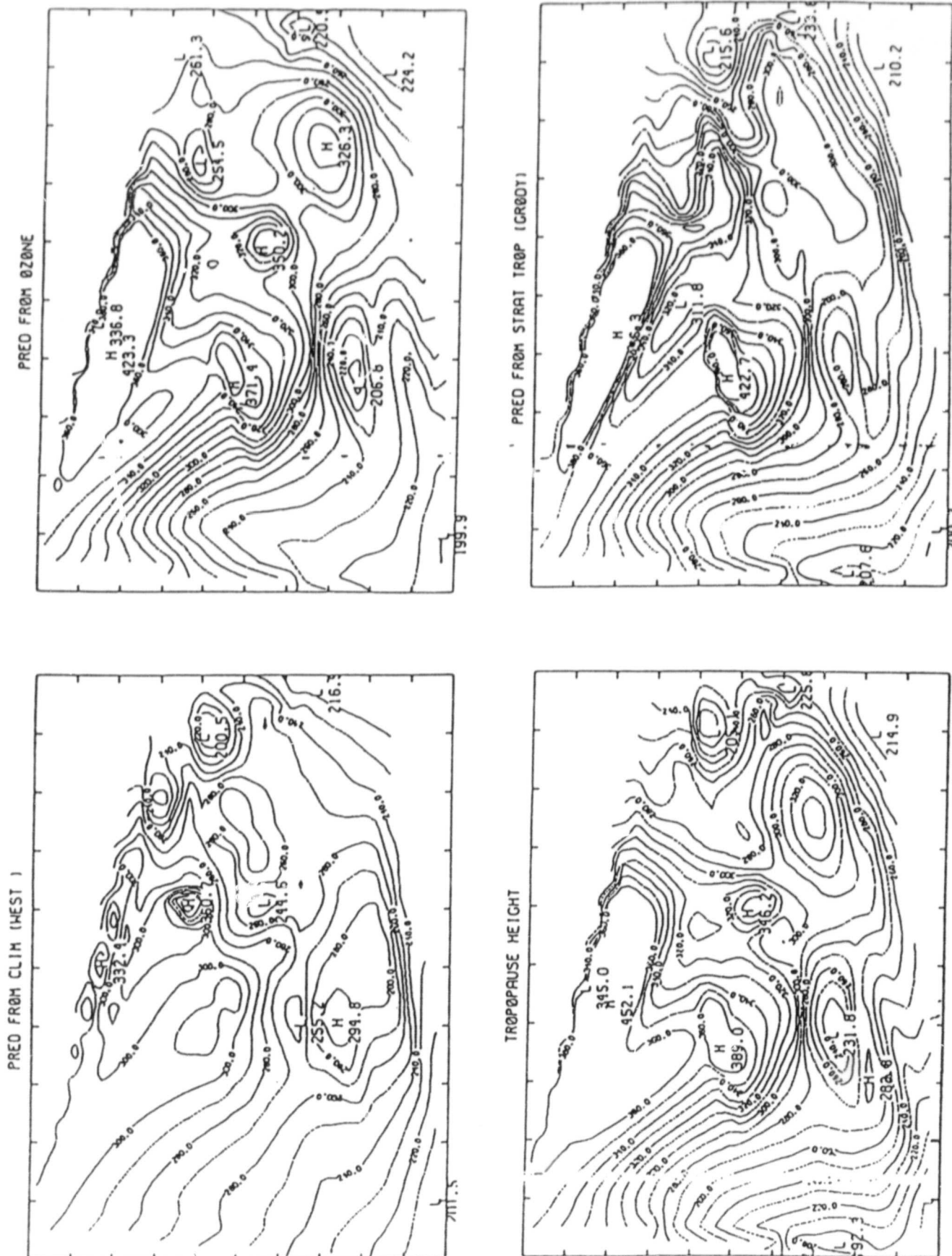
Figure 2

Figure 3

Figure 4

STUDY OF TROPOPAUSE HEIGHT ESTIMATE FROM TOMS TOTAL OZONE DATA FROM NIMBUS-7 AND FROM THE MICROWAVE REGRESSION TEMPERATURE RETRIEVAL OF SIMULATED BRIGHTNESS TEMPERATURES

M-J. Munteanu

A well known characteristic of satellite soundings is the fact that they exhibit very large errors in the region of the tropopause due to poor vertical resolution (N. Phillips et al., 1981, Schlatter, 1973, NESS group, 1982, Susskind et al., M. Halem et al., 1981).

This study pursues the idea of investigating the potential use of TOMS total ozone from NIMBUS-7 satellite in order to improve the satellite retrievals in the region of tropopause.

We have concentrated our research in the following four areas:

(i)   Determination of the tropopause using TOMS data.

(ii) Impact of tropopause errors in microwave MSU retrievals.

(iii) Impact of tropopause errors in the future AMSU retrievals.

(iv) Use of air-mass to stratify regression retrievals.

(i) Determination of the tropopause height using TOMS data.

The first step has been the investigation of whether an accurate estimation of the tropopause height can be obtained using total ozone remotely sensed from NIMBUS-7 satellite. For this purpose we have studied the correlation between TOMS total ozone and tropopause height from radiosonde data over Europe for two areas of interest.

I   Northern Europe: 10°E - 50°E and 50°N-65°N Date: April 15, 1979

II Western Europe: 10°W-20°E and 30°N-65°N Date: April 25, 1979

The data consisted of NIMBUS-7 TOMS total ozone data colocated in time and space with radiosonde measurements of temperature and humidity and NMC geopotential heights analysis. The conclusions from this study are:

1. The sample correlation between tropopause height and total ozone data were found to be .94 and 0.96 which corresponds to an rms error of about 15 mb. For comparison the prediction of the tropopause height from radar measurements has an rms error of 30 mb. In the prediction procedure the regression has been used on the manner equivalent to cross-validation.

2. Correlations between tropopause height and total ozone is the highest compared with all other correlations with variables such as: brightness temperatures from microwave channels, ratic of differences of these quantities, latitude, mean layer temperatures, surface temperatures or surface pressure.

3. Experiments correlating tropopause data with mean layer derived directly from radiosonde data showed that even predictions of tropopause height from exact mean layer temperatures were inferior than those derived from total ozone.

4. The folding of the tropopause should be taken into account because it is associated with the highest gradient on the ozone field. We should give different weights to the prediction in those regions where the folding of the tropopause is likely to occur.

5. The high ozone values are associated with lows in the 500 mb analysis and the low ozone values with corresponding highs in the heights analysis (see Fig. [1]).

(ii) Impact of tropopause errors in the MSU retrievals.

To study the impact of the lack of resolution at the tropopause levels we have performed simulation of microwave radiation measured with three MSU channels existing on TIROS-N and then performed local regression retrievals with Westwater's formulas for April 15, 1979 and global regression retrievals with Grody's formulas for April 25, 1979.

The conclusions are:

1. In the low tropopause cases there is a large bias and large residual error (Figure [2]).

2. The low tropopause cases produce very poor temperature retrievals. The overall rms is large in the region of the tropopause (Figure [2], Figure [6]).

3. The tropopause is mislocated by 100-200 mb in the regression microwave retrievals in the extreme cases. In one example the tropopause is estimated at 300 mb and it is actually observed at 490 mb. In another case the tropopause is observed at 450 mb, 419 mb, 412 mb, 415 mb, and estimated in all these cases at 300 mb (Figure [2]).

Two dimensional fields of: ozone, tropopause height, predicted tropopause height from total ozone, tropopause height calculated from climatology regression retrieval are presented in Figure [3] and Figure [4] for the 15th and 25th respectively.

4. As it is observed the MSU regression temperature retrieval damps almost entirely the trough in the two dimensional field of the tropopause height for April 15 and in general does not contain all of the highs and lows for April 25.

(iii) Impact of tropopause errors in the future AMSU retrievals

Experiments involving microwave simulation of radiosonde data with 5 of the AMSU channels and a comparison with MSU simulation have been performed. The conclusions are the following:

1. The location of the tropopause is not improved with respect to the MSU in

the low tropopause cases (see Figure [2]).

2. The retrievals based on the 5 AMSU channels generally perform better in the average tropopause height cases.

3. The general conclusion of these experiments could be described by saying that the resolution in the region of the tropopause is not improved by the additional AMSU channels, especially in the cases of low tropopause.

(iv) Use of air-mass to stratify regression temperature retrievals

The correlation between the tropopause height and the difference between the brightness temperatures of the two MSU channels situated in the region of the tropopause is greater than with any other combination of individual channels. This leads to the natural idea of using the difference between the two MSU channels as a stratifier for regression temperature retrieval formulas.

The main conclusion is:

1. Experiments using stratified temperature retrieval formulas indicated that they perform better in the region of the tropopause (see Fig. [5]).

500 MB HEIGHTS 12Z 15 APRIL 1979

TOTAL OZONE 15 APRIL 1979

Fig. 1

Fig. 2
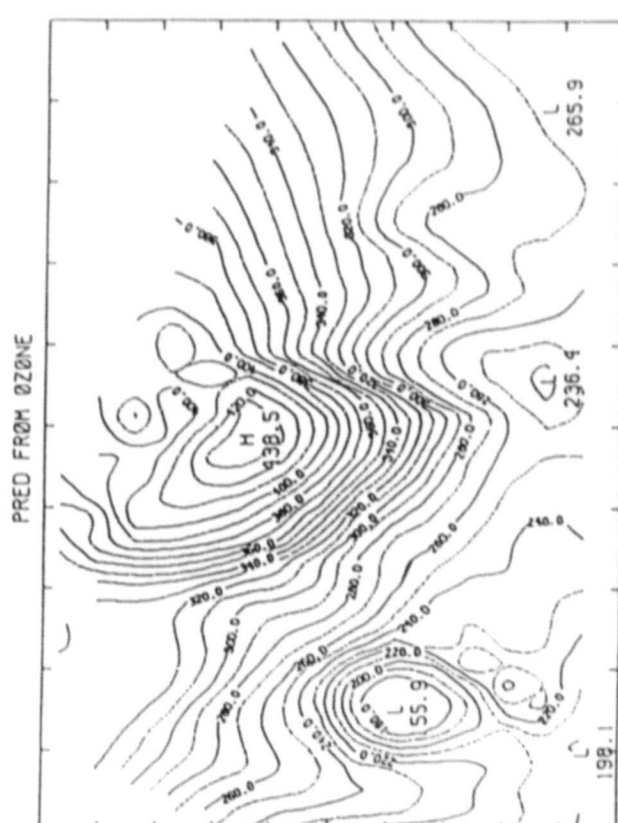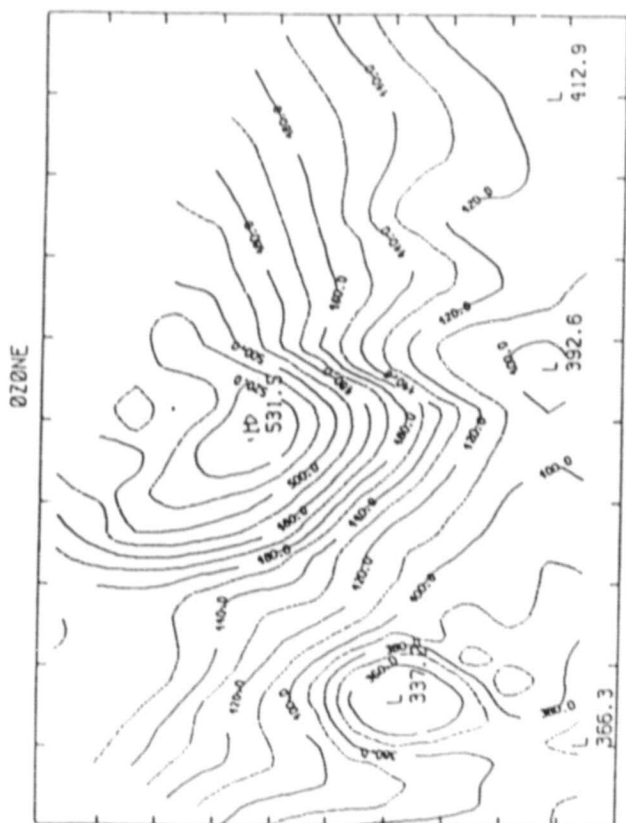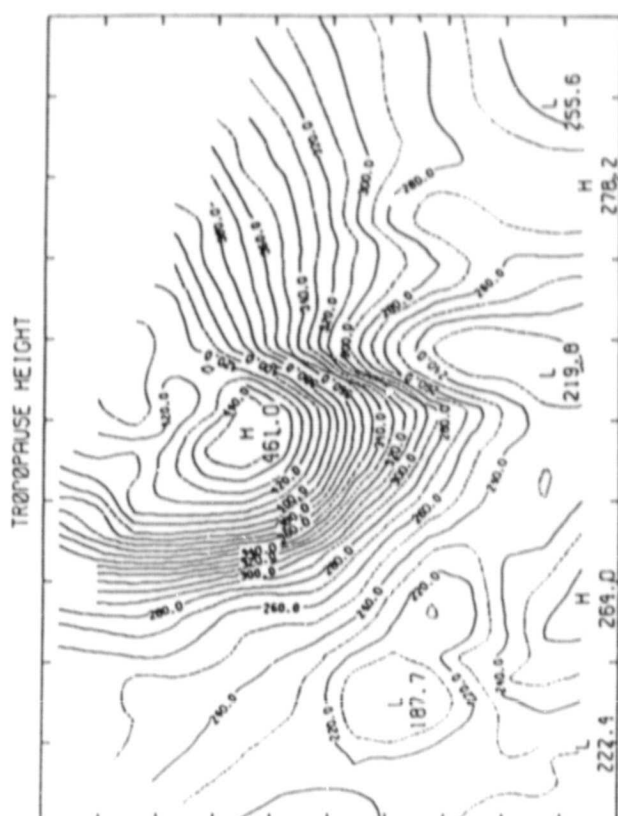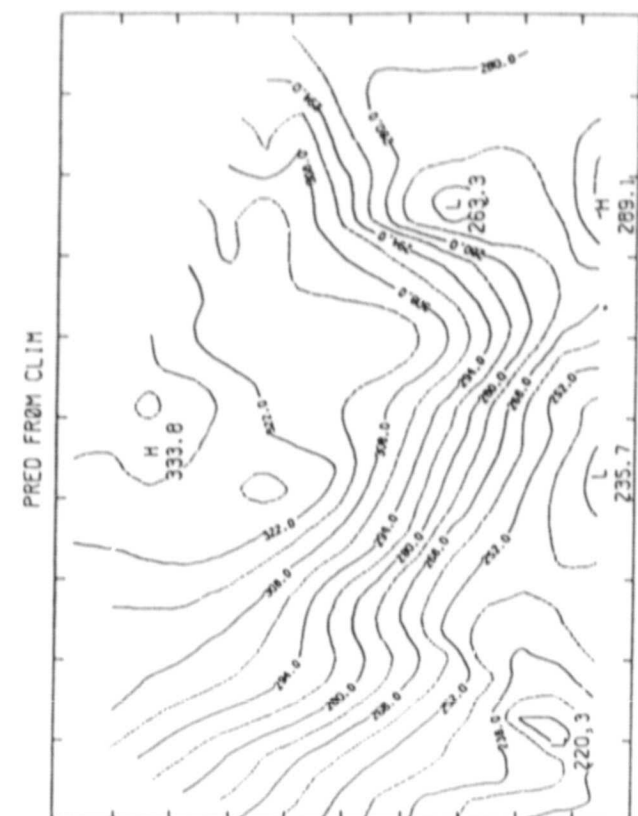
Fig. 3
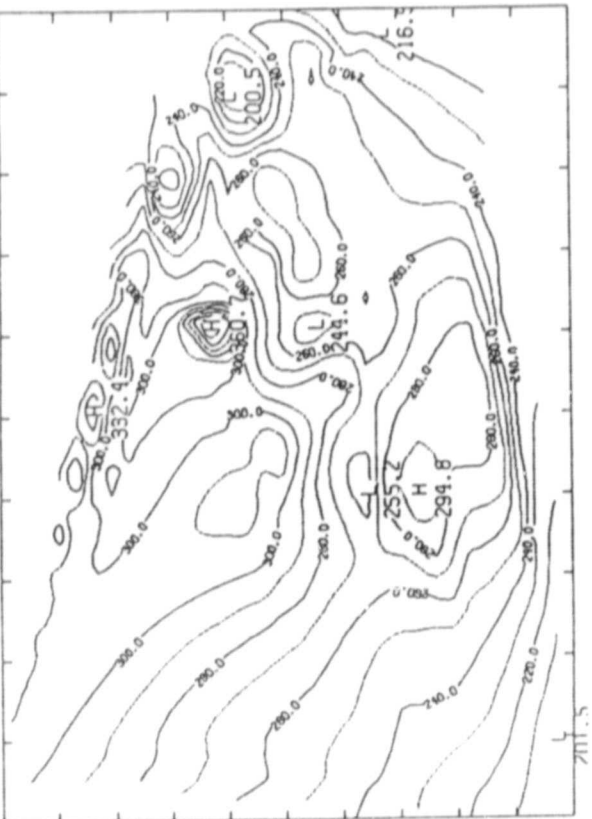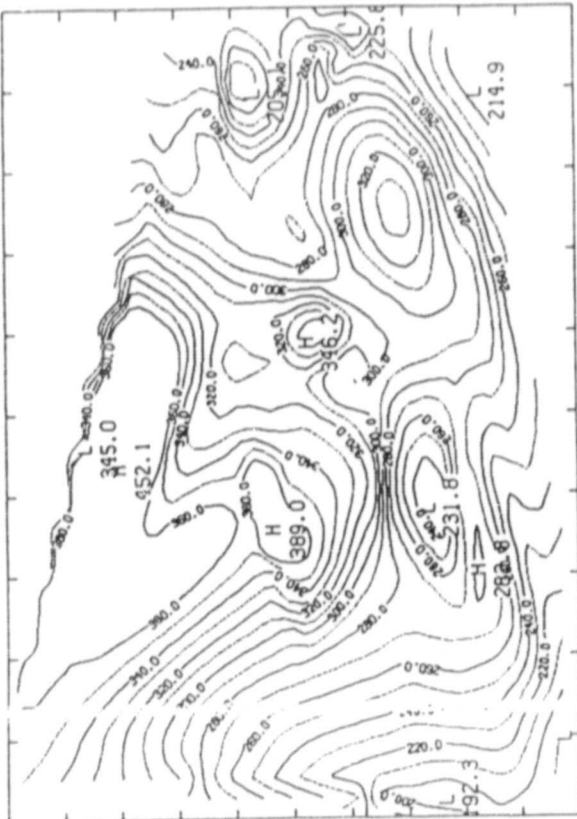
Fig. 4
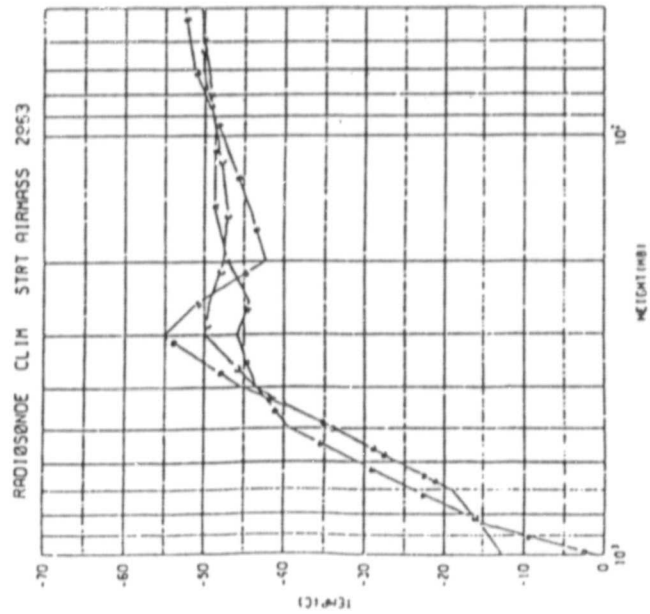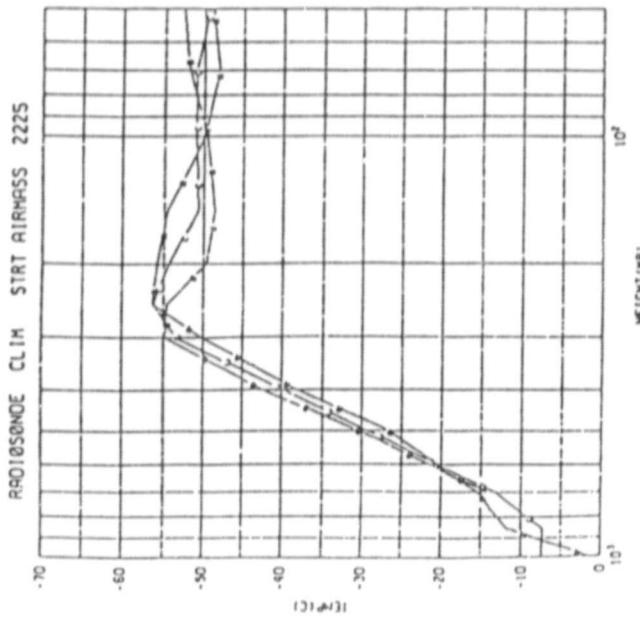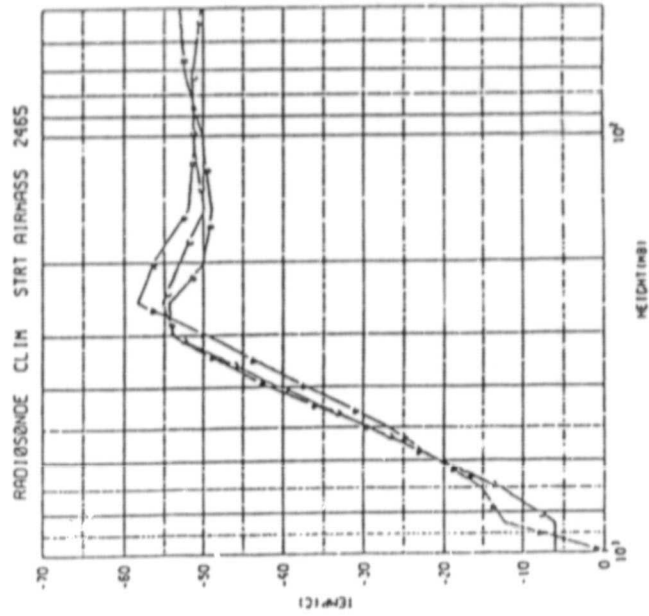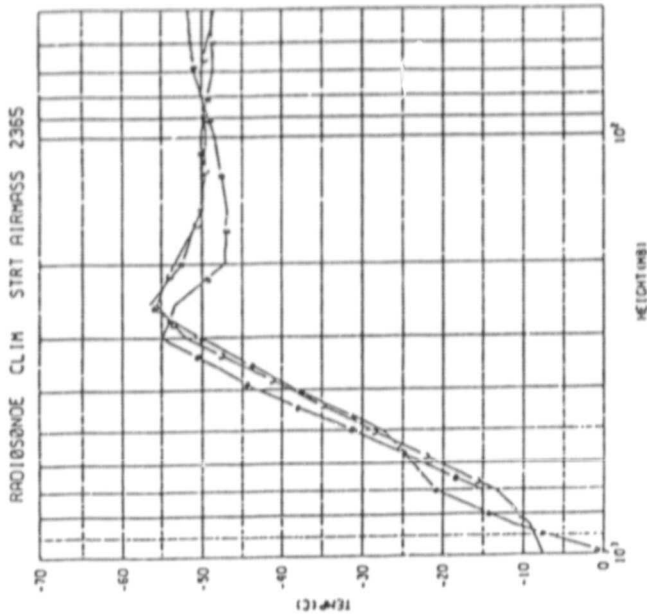
Fig. 5

RMS by Levels

| Pressure in mb | APRIL 15 | | | | | APRIL 25 |
	Local Clim	AMSU	Strat BT	Local Clim		Global Clim
1000	-	3.024	-	-		5.889
850	-	4.174	3.224	-		2.276
700	4.321	3.044	6.625	5.847		2.721
500	4.035	3.364	4.753	6.347		3.278
400	2.900	2.297	2.788	3.485		3.809
300	4.543	4.079	4.709	7.640		2.096
250	3.475	5.242	3.302	4.954		2.418
200	3.539	5.727	3.469	5.110		4.064
150	2.361	3.627	3.055	3.885		2.687
100	1.687	1.516	1.785	2.515		2.753
70	2.118	-	1.957	2.569		1.461
50	1.807	-	2.871	2.640		2.086
nr. of profiles	38	38	14	14		42

Fig. 6

THREE DIMENSIONAL INVERSION OF SATELLITE OBSERVED BRIGHTNESS TEMPERATURES

R. N. Hoffman

We propose here to obtain fully three dimensional fields of temperature from observed satellite brightness temperatures by using some of the variational techniques championed by Wahba and collaborators (Wahba and Wendelberger, 1980; and references therein). We recognize from the start that radiances or the equivalent brightness temperatures are not tropospheric temperatures but only proxies for these temperatures and that our results will depend upon what a priori information the inversion process utilizes. This being said it follows that the best combination of all a priori information should be used. The variational procedure allows in a natural way a variety of different information to contribute to the inversion process. In calculating three dimensional retrievals we can fully use our a priori knowledge that horizontally the temperature field is smooth to obtain maximum vertical resolution, filter cloud effects, minimize the effects of instrument noise and obtain horizontally coherent retrievals.

It has often been remarked that satellite observed radiances contain more information about temperature gradients than information about temperature. Because it acts as a spatial filter, there are several reasons to expect that the variational analysis method (VAM) will result in better and more useful retrievals. First, the retrieved temperature field will be horizontally coherent. The effect of random instrument noise and small scale meteorological features which are not really resolvable by the instrument will not be present in the retrievals. Second, by combining information from many spots (that is observation points or satellite footprints) the maximum amount of information about the vertical structure of the atmosphere may be extracted. This includes cloud structure; the VAM has the potential to act as a very powerful cloud filter retrieving cloud amounts, heights and other properties (such as emissivity). Third, the VAM is very flexible in allowing additional sources of information such as a 6 h forecast or the conventional radiosonde data to influence the retrieved temperatures. In addition the VAM may be fully integrated with a NWP model to provide what might be termed four dimensional retrievals. Fourth, the above points also apply to retrieved surface quantities such as temperature and emissivity.

Notwithstanding the above observations, every retrieval system attempted to date has been essentially one dimensional. (By one dimensional we mean that the clear column radiances for each spot are processed independently of each other spot. Of course, for IR retrievals, neighboring spots are used to remove cloud effects and thus reduce the 'raw' radiances to clear column radiances). One might suppose that if the one dimensional problem is difficult the three dimensional problem will be more difficult and should not be attempted until the one dimensional problem is solved. It is certainly true that the three dimensional problem is very complicated and difficult computationally. However the three dimensional problem may be better posed in the sense of uniqueness and stability.

The basic problem of three dimensional retrievals, common to many inverse problems (geophysical, medical, etc.), is that there is a finite number of observations of some parameters which depend on the continuous distribution of

some properties of the system under observation. In the present case we observe brightness temperatures

$$T_B(\nu_i, R_n) \qquad i = 1,\ldots.I; \quad n = 1,\ldots.N$$

at a number of viewing geometries (R_n) in a set of channels (ν_i), and these brightness temperatures depend on among other things, mixing ratios of the absorbing gases and the temperature all along the path followed by the radiation through the atmosphere. The result is that the problem of retrieving the system properties from the observations is grossly underdetermined and to a large extent the solution depends on what other information is added by the investigator (Backus and Gilbert, 1967). In many cases it is possible to avoid this problem simply by limiting the resolution of the solution, that is to use a relatively coarse grid to represent the system. This presupposes that the system properties vary smoothly. This assumption is in fact additional information. In the atmosphere temperature is very smooth, the mixing ratio of water is smooth but less so and cloud amount is sometimes not smooth at all on the length scale of the observing cell.

The difference between the length scales for temperature and cloud amount is the crux of the three dimensional retrieval problem. In general we can classify a system property as either ragged (resp. smooth) if its length scale is the order of or smaller than (resp. greater than) the observing cell size of the instrument. For properties which are ragged, like cloud amounts, we may be able to infer some sort of average value over each particular observing cell but it is impossible to retrieve point values. Smooth properties on the other hand should be retrievable at points either within or between the observing cells. It is important to note that while cloud amounts are ragged, cloud properties (such as emissivity) are smooth if we allow their definition where there are no clouds (Fig. 1). This is the basis of the multiple fields of view cloud filtering methods (Chahine, 1977; and references therein). The properties of the earth's surface are also in general ragged because the length scale for soil types and land use is relatively small.

The intuition behind our strategy is therefore the following: We expect to use one channel for each ragged property needed for the forward problem. Then the remaining channels will be pooled geographically by the smoothness constraints acting on the smooth parameters to yield optimal estimates. Of course the better we know the smooth properties the better we can estimate the ragged properties and vice versa. Within the variational formulation the retrieval of all quantities occurs simultaneously and this beneficial interaction between knowledge of the various variables will occur naturally.

To generalize the variational problem of Wahba to take all relevant parameters into account let us symbolically write the solution to the forward problem as

$$T_C(\nu_i, R_n) = f_i \left(\rho_1(R_n), \rho_2(R_n)\ldots\rho_r(R_n), \sigma_1(R_n)\ldots\sigma_s(R_n) \right)$$

where $\rho_i(R_n)$ represents the value(s) of the $\underline{i}$tn rough variable entering the

forward problem evaluated for viewing geometry R_n; similarly $\sigma_j(R_n)$ represents the value(s) of the jth smooth variable entering the forward problem. Some of these variables are 2-dimensional such as surface emissivity, while others are 3-dimensional like air temperature. In general some of the ρ_j will be cloud amounts for each of several cloud types and some of the σ_j will be the corresponding cloud top pressures, emissivites, etc. Now we wish to minimize

$$(1) \quad S = \sum_{i,n} w_{in} \, (T_B(\nu_i, R_n) - T_C(\nu_i, R_n))^2$$

$$+ \sum_{j=1}^{s} \lambda_j \, J_{m_j}(\sigma_j)$$

where

$$J_m(\theta) = \sum_{\alpha_1 + \alpha_2 + \alpha_3 = m} \left(\frac{m!}{\alpha_1! \alpha_2! \alpha_3!} \right) \iiint \left(\frac{\partial^m \theta}{\partial x^{\alpha_1} \partial y^{\alpha_2} \partial p^{\alpha_3}} \right)^2 dx\,dy\,dp$$

During the minimization m and λ are held fixed. We must still specify f, the solution of the forward problem, the spatial representation of θ and the remaining free parameters (m, λ, w_{in}) to complete the problem. Note that a different way of measuring the smoothness of each of σ-variables is possible and that there is no penalty if the ρ-variables are not smooth. Also there is a λ weight for each σ-variable to balance the tradeoff between the various constraints. One could, and probably will, append to the end of (1) a variety of other constraints, such as climatological information, 'first-guess' information, radiosonde data, etc. Although the mathematical machinery developed by Wahba applies directly only to linear functionals, the general method has already been applied to large nonlinear problems (Hoffman, 1982).

REFERENCES

Backus, G. E. and J. F. Gilbert, 1967: Numerical application of a formalism for geophysical inverse problems. Geophys. J. R. Astronom. Soc., 13, 247-276.

Chahine, M. T., 1977: Remote sounding of cloudy atmospheres II. Multiple cloud formations. J. Atmos. Sci., 34, 744-757.

Hoffman, R., 1982: SASS wind ambiguity removal by direct minimization. Mon. Wea. Rev., 110, 434-445.

Wahba, G., and J. Wendelberger, 1980: Some new mathematical methods for variational analysis using splines and cross-validation. Mon. Wea. Rev., 108, 1122-1143.
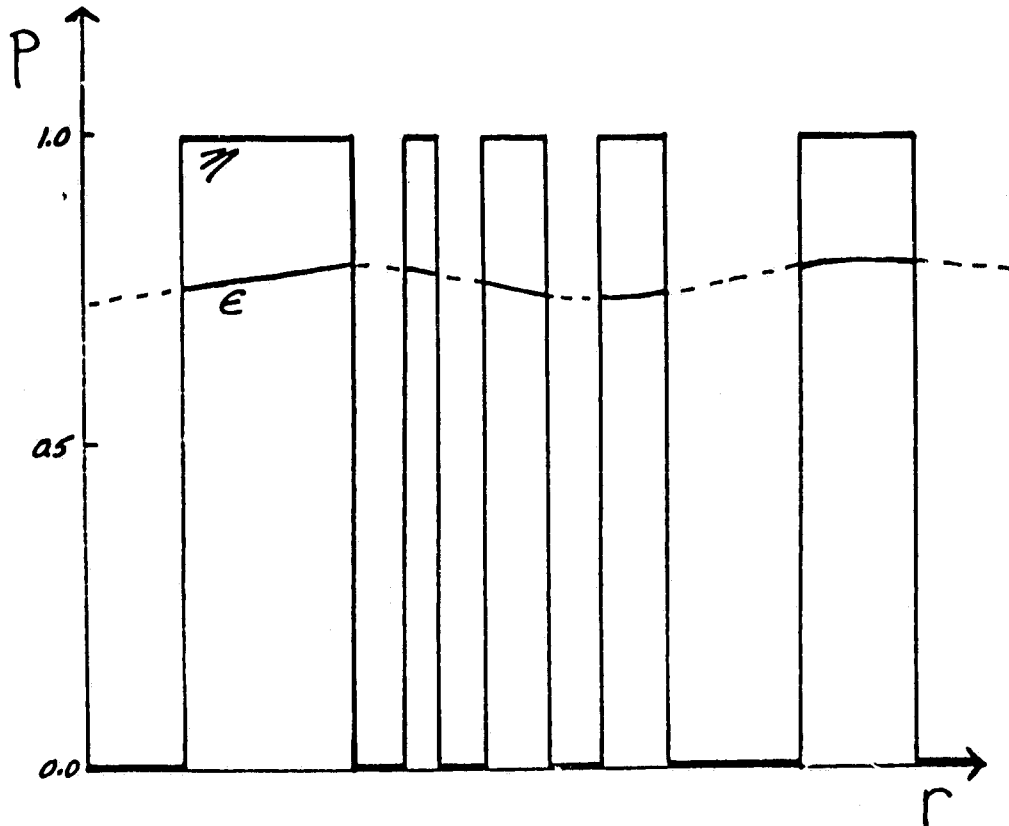
Fig. 1. Cloud parameter (p) versus position (r). Cloud
amount (η) is ragged and Boolean. Cloud emissi-
vity (ϵ) is smooth within clouds and may be
defined smoothly between clouds.

SIMULATION COMPARISON STUDY OF THE AMTS AND HIRS2 SOUNDERS

J. Susskind, D. Reuter and A. Dalcher

The Advanced Moisture and Temperature Sounders (AMTS) is a proposed high spectral resolution passive infra-red sounder designed to produce higher vertical resolution soundings of temperature and humidity than currently available [Kaplan et al., 1977]. In addition, the channels are chosen so as to essentially eliminate any dependence of the signals on extraneous variables, i.e., H_2O and O_3 distribution in the case of temperature sounding channels.

The simulation study is part of a joint study between NASA, NOAA, and the University of Denver to assess the sounding capabilities of the AMTS as compared to the HIRS2 instrument currently flying on the TIROS-NOAA series operational satellites. Radiances for both instruments were simulated by the University of Denver for a set of profiles containing information of the ground temperature, atmospheric temperature-humidity-ozone profiles, reflected solar radiation off the ground, and satellite zenith angle of observation. In one portion of the test, radiances were simulated for a large sample of cloud free conditions. In a second portion, more detailed simulations were made involving radiance fields computed as a function of multi-layer cloud fields, thermal gradients, and the scan pattern of the instrument. Only the clear test is considered in this write-up. The cloudy portion is discussed in Dennis Reuter's section in this report.

In the clear test, radiances were simulated by the University of Denver for 1600 profiles, selected from 3 week periods in each the winter and summer. The radiances for both instruments, together with colocated radiosonde information, were sent to both NOAA and NASA. Each group analyzed data for each instrument according to their preferred method of analysis, regression analysis in the case of NOAA, and a physical inversion method by NASA. The test then compared both methods and instruments. The colocated data was to be used for any purpose i.e., generation of regression coefficients for NOAA and generation of empirical tuning coefficients to minimize systematic differences between radiances calculated by the University of Denver and by NASA for the same profiles. The actual test was based on radiances simulated from radiosonde data in the subsequent 2 week period. These profiles were not made known to the participants. Here, we briefly show the GLAS method of analysis and indicate results based on the original sample of 1600 cases, in which half the radiosonde information was withheld in the generation of coefficients and that sample used as the test data set.

The method of analysis was very similar to that used by GLAS in analysis of TIROS-N HIRS2/MSU data [Susskind et al., 1982]. The procedures used in the test differ from those used in analysis of TIROS-N for two reasons:

1) A 6 hour forecast guess of temperature and humidity is available in analysis of TIROS-N data but is not available in the test.

2) The noise levels in the test are realistic assessments of instrumental noise but do not include the effects of scene noise.

As a result of these differences, the first guess used in the analysis was based on a regression relationship between observed brightness temperatures and radiosonde temperature profiles. Also, the form of iterative relaxation equation was modified so as to decrease the smoothing applied to the solution and a correction was applied to the climatological humidity as a first guess profile.

In order to generate an initial guess temperature profile based on regression relationships between observed brightness temperatures and atmospheric temperature profiles, it is desirable to remove to first order the angle dependance of the satellite brightness temperatures. To do this, observed satellite brightness temperatures at angle θ, $T_B(\theta)$, are corrected to $T_B(0)$, their estimate values if the observations were at nadir.

TABLE 1

CHANNELS USED IN DIFFERENT STEPS

	HIRS	AMTS
ANGLE CORRECTION	1-8, 13-16	3-10, 20-26
REGRESSION GUESS	1-8, 13-16	3-10, 20-26
TUNING	1-7, 13-16	1-10, 20-26
GROUND TEMPERATURE	18, 19	26-28
HUMIDITY CORRECTION	8	11
TEMPERATURE PROFILE	1-4, 13-15	4-10, 20-24

TABLE 2

ASSIGNED PRESSURES FOR CHANNELS USED IN THE TEMPERATURE RELAXATION SCHEME

AMTS				HIRS		
CHANNEL	P_ℓ	$P_L - P_U$		CHANNEL	P_ℓ	$P_L - P_U$
9	3	-		1	10	-
10	15	-		2	-	30-90
8	-	30-90		3	-	90-200
7	-	30-80		4	-	200-380
6	-	50-150		15	-	380-625
5	-	100-220		14	-	625-875
4	-	200-400		13	-	875-1000
20	-	300-500				
21	-	400-600				
22	-	600-775				
23	-	775-1000				
24	-	925-1000				

We use the equation

$$T_B^S(0) = T_B^S(\theta) + A \; \frac{\sec \theta - 1}{\sec 50 - 1} \; T_B^S(\theta) \qquad (1)$$

The superscript S means simulated data. A is 15 x 15 for AMTS and 12 x 12 for HIRS2 as shown in table 1. A separate A matrix was constructed for winter and summer. The coefficients of A were determined from simulated radiances for the 800 profiles at a 50° zenith angle and at nadir.

Once the Goldman data were corrected to zero zenith angle by equation (1) regression equations of the form

$$T(P) = \overline{T}(P) + B[T^G(0) - \overline{T}_B(0)] \qquad (2)$$

were constructed for each of eight zones, (land/water), (tropics/extratropics), and (summer/winter). $T_B(0)$ is the vector of brightness temperatures for the N_R channels used for regression constructed by angle correcting the data provided by the University of Denver for the particular profile to 0° according to equation (1). $\overline{T_B(0)}$ is the mean vector of all the resulting $T_B(0)$ in the data set. N_R = 15 for AMTS and 12 for HIRS with the channels shown in table 1. All humidity sounding channels and most window channels have been excluded from the regression for both instruments so as not to use humidity as a predictor for temperature.

Possible systematic computational differences are minimized by comparing a set of "observed" brightness temperatures T_B, with those simulated by GLAS, T_B^S, and finding C and D which best fit the relation

$$T_B^S = C \; T_B + D \tag{3}$$

where C is an $N_T \times N_T$ matrix for the N_T channels tuned and D is a $N_T \times 1$ vector. Once C and D are obtained from analysis of a dependent set, the observed brightness temperatures T_B in the independent set are modified according to

$$\tilde{T}_B = C \; T_B + D \tag{4}$$

so as to best match the brightness temperatures we would compute under the same conditions.

Retrievals are performed using $\tilde{T}_B$ as data rather than T_B. We now compare the modified observed brightness temperatures for the temperature sounding channels $\tilde{T}_{B,i}$, with the computed brightness temperatures from the Nth guess, $T_{B,i}^N$, and modify the guess to produce an N+1th iterative temperature profile. Twelve temperature sounding channels are used for the AMTS and seven are used for HIRS2 as shown in Table 1.

The relaxation equations used are almost identical to those described in Susskind et al. [1982]. Temperatures at pressures between 30 and 1000 mb are treated differently than temperatures at pressures lower than 30 mb. The basis of the relaxation method lies in the approximation that small a constant shift in the temperature profile will produce an almost identical change in the brightness temperature computed for a sounding channel. Moreover, if the shift is applied only in the region of the atmosphere where the radiance of the channel is most sensitive to atmospheric temperature, a similar change in computed brightness temperatures will occur.

For channels sensitive to temperatures at pressures greater to 30 mb, we assign an atmospheric layer, P_{iL} to P_{iU}, which is considered to be the layer in which the radiances of the channel are most sensitive to atmospheric temperature change. P_{iL} and P_{iU}, representing the lower and upper pressure boundaries for sounding channel i, are shown in Table 2 for the sounding channels of AMTS and HIRS used in the analysis. Channels primarily sensitive to temperature changes above 30 mb are treated as representative of temperature changes at a specific

pressure, rather than in a layer. This pressure, P_{il} is indicated in Table 2 for the appropriate channels.

For pressures greater than 30 mb, we write the relaxation equation

$$T_i^{N+1} = T_i^N + \tilde{T}_{B,i} - T_{B,i}^N \tag{5}$$

where $\overline{T}_i^N$ is the average temperature of the Nth iterative guess temperature profile in the atmospheric layer corresponding to channel i

$$\overline{T}_i^N = \int_{P_{iL}}^{P_{iU}} T^N(P) \, d\ell nP \quad /\ell n \quad \frac{P_{iU}}{P_{iL}} \tag{6}$$

and $\overline{T}_i^{N+1}$ is the new estimate of the layer mean temperature in the appropriate atmospheric layer. In order to determine a $N+1^{th}$ iterative temperature profile at pressure P_l from estimates of layer mean temperatures, we constrain the solution to be given by

$$T^{N+1}(P_k) = T^0(P_k) + \sum A_j^{N+1} F_j(P_k) \tag{7}$$

where $T^0(P_k)$ is the initial guess, $F_j(P_k)$ are empirical orthogonal functions of temperature, given by the eigenvectors, with largest eigenvalues, of the covariance matrix of a set of global radiosonde profiles, sampled at the 52 pressure levels between 1000 and 30 mb, which are a subset of the 64 pressure levels used in the calculation, and A^{N+1} are the iterative coefficients which, together with the initial guess, completely determine the solution.

The coefficients, A^{N+1}, are solved for according

$$A^{N+1} = [\overline{F}'\overline{F} + \sigma H]^{-1} \overline{F}' [\overline{T}^{N+1} - \overline{T}^0] \tag{8}$$

where F represents the matrix of layer averaged empirical orthogonal functions

$$\overline{F}_{ij} = \int_{P_{iL}}^{P_{iU}} F_j(P) \, d\ell nP \quad /\ell n \quad \frac{P_{iU}}{P_{iL}} \quad , \tag{9}$$

F' is the transpose of F, H is a diagonal matrix with H_{jj} being the inverse of the fraction of the total variance arising from eigenvector j, and σ is a constant. The term σH is added to $F'F$ in order to stabilize the solution, as in Susskind et al. [1982].

63

For AMTS, 10 mean layer temperatures, shown in Table 2, are used to estimate coefficients of 9 empirical orthogonal function, with $\sigma = 1 \times 10^{-3}$. For HIRS2, 6 mean layer temperatures are used to estimate coefficients of 5 empirical orthogonal functions with $\sigma = 5 \times 10^{-4}$.

Figs. 1 and 2 show the RMS errors of the regression generated guess are the retrieved temperature profiles obtained from both the AMTS and HIRS data for the independent sample. Separate statistics are shown for the winter and summer cases. Only levels which were interpolated from radiosonde reports are included in the statistics. Under clear conditions, the RMS errors of the physical retrievals for both AMTS and HIRS are .1° - .2° better than their regression guess beneath about 300 mb. Above 300 mb, the physical retrieval is of comparable quality to the guess for the AMTS and somewhat worse for the HIRS2. The AMTS results show significant improvement over the HIRS2 results, relatively independent of the method used. Improvements are the order of .3° below 300 mb and .7° above 300 mb. Improvements in the lowest atmospheric level, from 880-1000 mb, are the order of .5°.

Figure 3 shows similar statistics for the single zone land-mid-latitude winter, characterized by large inversions in the lower troposphere. Under these conditions, the physical retrieval method shows larger improvements over regression in the lower troposphere and likewise, the improvements in the retrieval actuary obtained from the higher vertical resolution of AMTS over HIRS are more significant.

REFERENCES

Susskind, J., J. Rosenfield, D. Reuter, and M. T. Chahine, 1982: The GLAS physical inversion method for analysis of HIRS2/MSU sounding data. NASA Tech. Memo. 84936.

LAYER MEAN TEMPERATURE RMS ERRORS
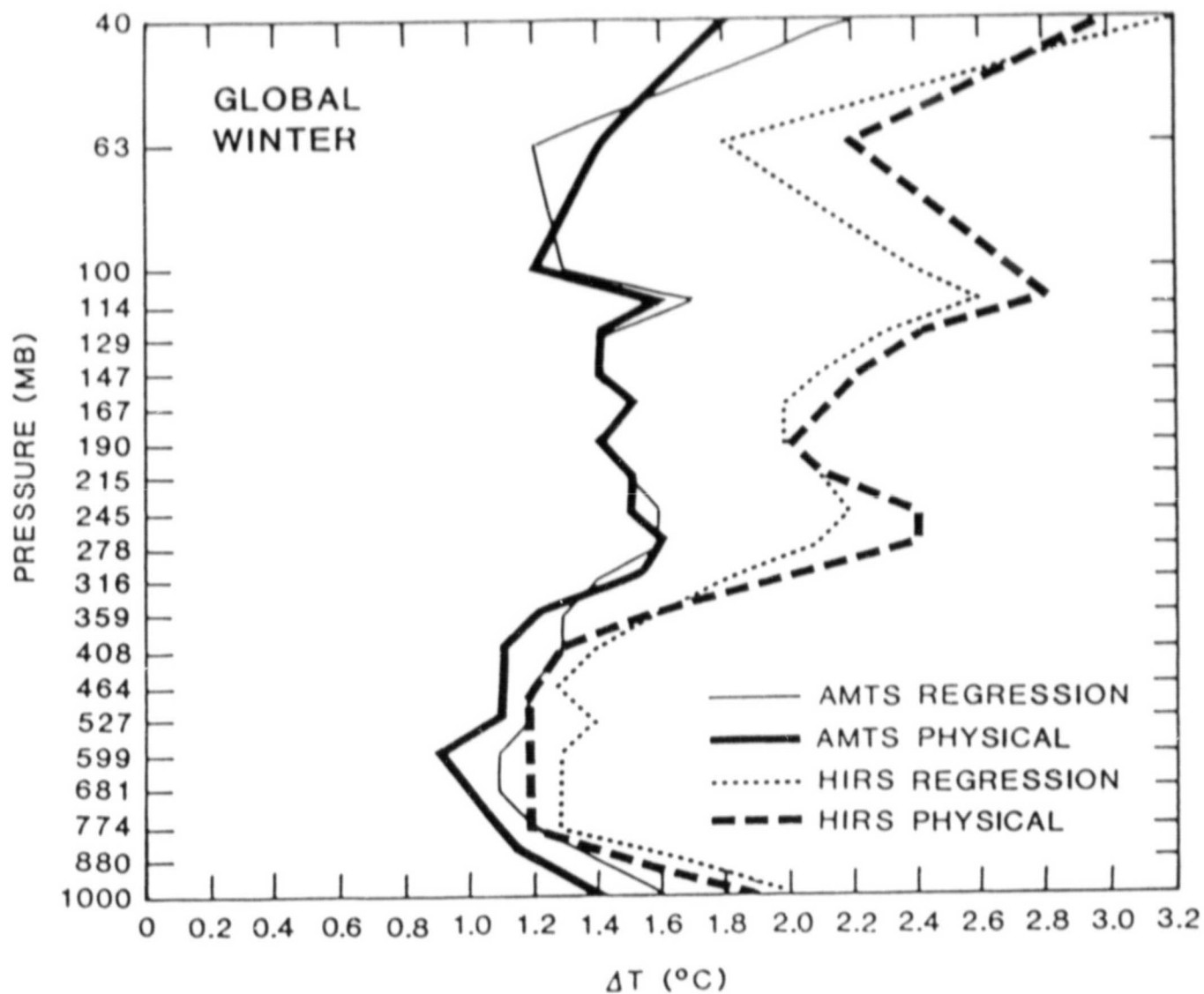
Figure 1. Results of analysis by GLAS of 400 sets of radiances from the clear winter dependent set using information from the other 400 profiles. The errors plotted are of the layer-mean temperatures with layers shown in the figure. In each case, the error for the layer is plotted at the lower boundary of the layer.

LAYER MEAN TEMPERATURE RMS ERRORS
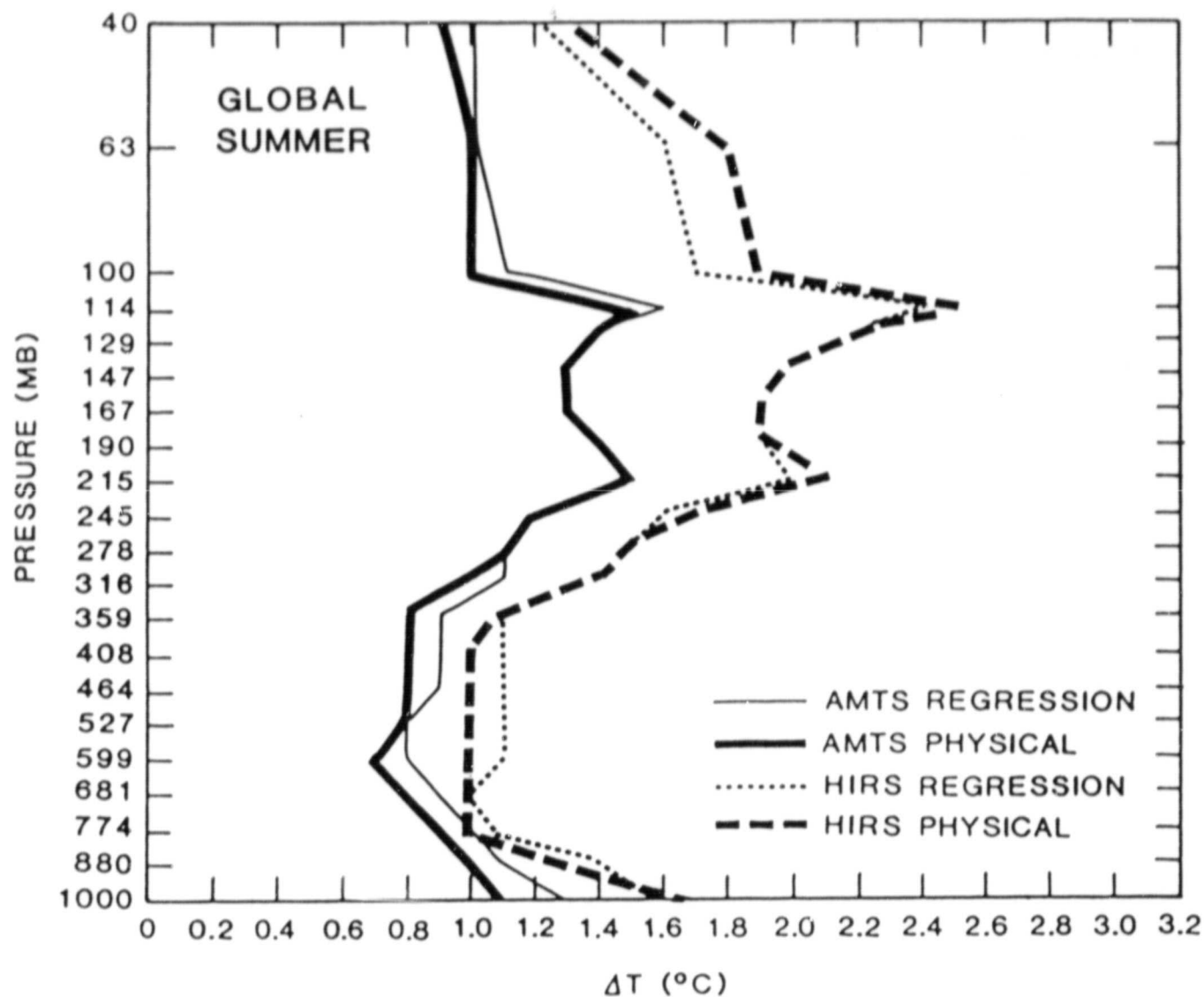
Figure 2. As in Figure 1 but for the clear summer profiles.
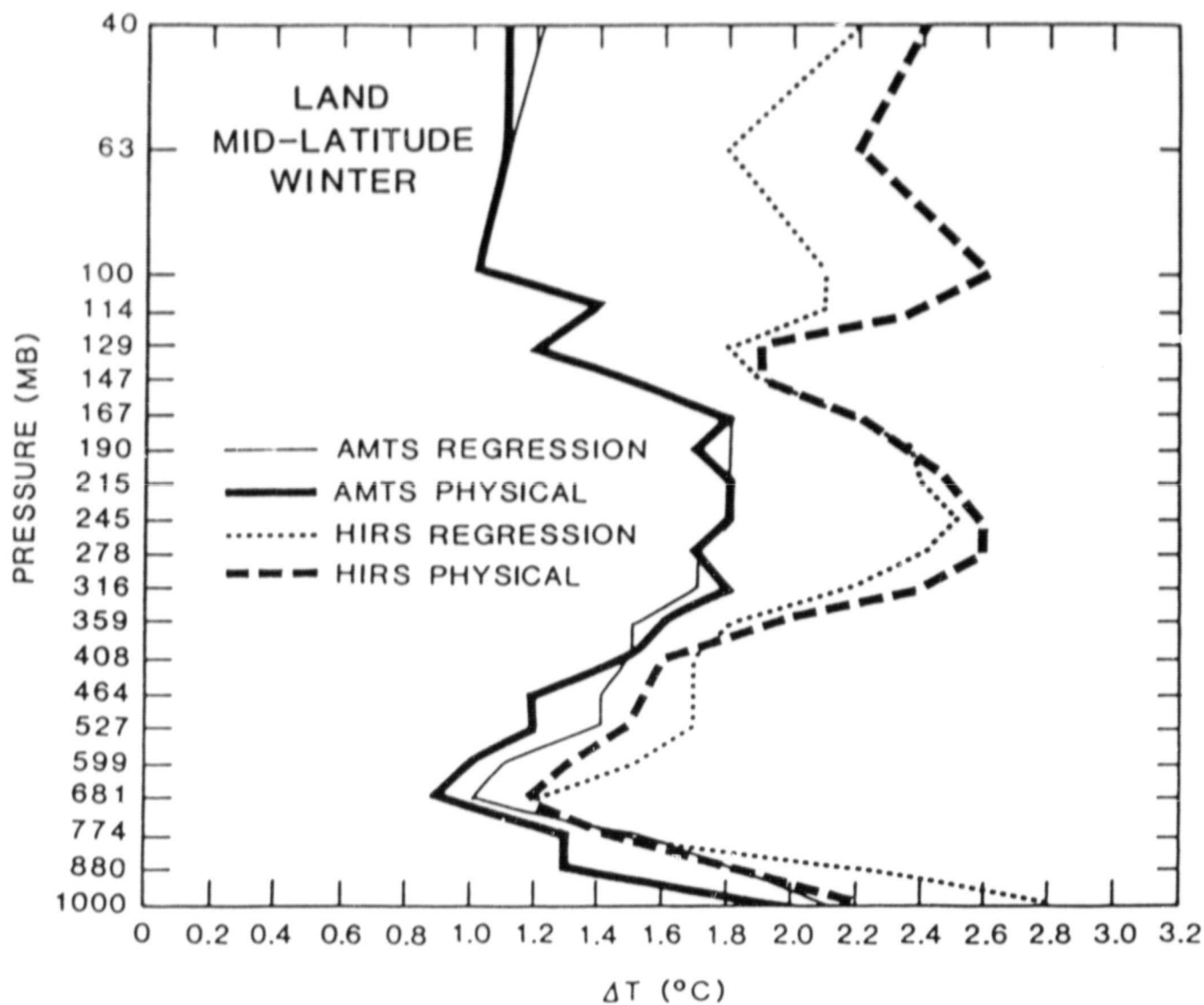
Figure 3. As in Figure 1 but for the clear winter land mid-latitude profiles only.

SIMULATION STUDIES OF THE HIRS2/MSU AND AMTS/MSU SATELLITE SOUNDING UNITS: CLOUDY CONDITIONS

D. Reuter, J. Susskind and A. Dalcher

Currently, a joint NOAA/NESS - NASA simulation study is under way to compare the accuracies of atmospheric temperature profiles retrievals as produced from the currently operational HIRS/MSU sounding system and the proposed AMTS/MSU sounding system. This study is proceeding in two phases. In the first phase, which has already been completed, synthetic satellite radiances are calculated from realistic atmospheric temperature, water vapor, and ozone profiles, with the effects of surface temperatures, satellite viewing angle, and reflected solar radiation also taken into account. These simulated radiances are then used as input data for the statistically based temperature retrieval algorithm at NOAA/NESS and for the physically based retrieval system at GLAS. This first phase is described elsewhere in this report (see Susskind et al.) and will not be discussed here.

In the second phase of the test, the simulated radiances are contaminated by the effects of realistic cloud fields. In order to prepare for this phase of the test and, at the same time, to develop and test various methods for use with real data, we at GLAS have carried out simulation studies employing cloud contaminated radiances generated here. It is the purpose of this note to describe these studies.

For the purpose of these simulation studies, and in fact for the joint test, the clear column radiances are calculated according to a truncated version of the radiative transfer equation:

$$R_i = B_i[T_S]\tau_{iS}(P_S,\theta) + \int_{\ell nP_S}^{\ell n\bar{P}} B_i[T(P)] \frac{d\tau_i(P,\theta)}{d\ell nP} \tag{1}$$

where R_i is the frequency averaged radiance in sounding channel i, $B_i[T]$ is the Planck function evaluated at frequency ν_i and temperature T, $\tau_i(P,\theta)$ is the channel averaged transmittance from pressure P to the satellite pressure P at angle θ, and the subscript S stands for surface. This form of the equation neglects effects of reflected solar and downwelling thermal radiation but preserves most of the dependence of the radiances on atmospheric and surface properties and viewing angle.

In the presence of clouds, which are essentially opaque to infrared radiation, the radiance observed by the satellite, $\tilde{R}_i$, becomes a function of the cloud top pressures P_j, and fractional amounts α_j:

$$\tilde{R}_i = (1 - \sum_j \alpha_j) R_i^{CLR} + \sum_j \alpha_j R_{ji}^{CLD} \tag{2}$$

where R_i^{CLR} is the radiance which would be observed in the absence of clouds

and R_{ij}^{CLD} is the radiance which would be observed if the field of view of the sounder were obscured by a cloud with a cloud top pressure of P_j. Equation 2 is valid for any value of the emissivity of the clouds, however for the purposes of this test the emissivities were taken to be .1 (i.e. the clouds are taken to be perfect black body emitters). Note that the cloud fractions α_j are effective cloud fractions in the sense that if a high cloud obscures a lower cloud, then only that part of the lower cloud which is not obscured will contribute to the radiance.

If the set of radiances $\tilde{R}_i$ is used to determine the surface and atmospheric properties the results will be grossly in error. Therefore some method must be used to account for effects of clouds. At GLAS we use a method whereby the radiance which would be observed in the absence of clouds is reconstructed from observed radiances in several nearby fields of view.

An iterative estimate of the clear column radiance, $R_i^{CLR(N)}$, may be obtained from two fields of view as:

$$R_i^{CLR(N)} = \tilde{R}_{i,1} + \eta^{(N)} (\tilde{R}_{i,1} - \tilde{R}_{i,2}) \tag{3}$$

where $\tilde{R}_{i,j}$ is the observed radiance for channel i in field of view j and $\eta^{(N)}$ is a channel independent cloud filtering parameter which is equal to $\alpha_1/(\alpha_1 - \alpha_2)$ where α_1 and α_2 are the effective cloud fractions in field of view 1 and 2 respectively.

In the GLAS physical inversion method we always have an estimate of $R_i^{CLR(N)}$ from the Nth iterative atmospheric and surface properties. Therefore on any iteration $\eta^{(N)}$ may be estimated as:

$$\eta^{(N)} = \frac{R_i^{CALC(N)} - \tilde{R}_{i,1}}{\tilde{R}_{i,1} - \tilde{R}_{i,2}} \tag{4}$$

Since it is not expected that, at the beginning of the iterative temperature retrieval procedure, the Nth solution profile is in fact the correct atmospheric temperature profile, this method will tend to give erroneous results. To remove, at least to first order, any biases in $R_i^{CALC(N)}$; microwave channel 2, which is not affected by the presence of clouds, is used to obtain a corrected clear column radiance $R_i^{CC(N)}$:

$$R_i^{CC(N)} = B_i[T_i^{CALC(N)} + (T_{M2} - T_{M2}^{(N)})] \tag{5}$$

where $T_i^{CALC(N)}$ is the black body temperature for $R_i^{CALC(N)}$, $T_{M2}^{(N)}$ is the Nth iterative brightness temperature of microwave channel 2 and T_{M2} is the observed microwave channel 2 brightness temperature. Brightness temperatures are used because the radiances are extremely frequency dependent. This value for $R_i^{CC(N)}$ may be substituted for $R_i^{CALC(N)}$ in equation 4 to find $\eta^{(N)}$ which

may then be used in equation 3 to obtain the reconstructed clear column radiance $R_i^{CLR(N)}$. Since η is channel independent all infrared radiances may be corrected by the same η.

This procedure is quite adequate for accounting for one cloud level and therefore one degree of vertical inhomogeneity, however, in the simulation test described above multiple cloud levels are to be used and therefore multiple degress of inhomogeneity must be accounted for. We have therefore attempted to use three fields of view to account for at least two degrees of inhomegeneity. To determine the two cloud filtering parameters $\eta_1^{(N)}$ and $\eta_2^{(N)}$ channels 7 and 6, are used for the HIRS instrument while channels 1 and 2 are used for the AMTS. The observations are sorted into warm, intermediate and cold fields of view (F_1, F_2, F_3) according to the brightness temperatures in the window channels 8 for HIRS and 11 for AMTS. For three fields of view equation (3) may be expanded to:

$$R_i^{CLR(N)} = \tilde{R}_{i,1} + \eta_1^{(N)} (\tilde{R}_{i,1} - \tilde{R}_{i,3}) + \eta_2^{(N)} (\tilde{R}_{i,1} - \tilde{R}_{i,2}). \tag{6}$$

Note that $\eta_1^{(N)}$ is being used to describe most of the inhomegeniety since,

by the field of view sorting given above $(\tilde{R}_{i,1} - \tilde{R}_{i,3}) \geq (\tilde{R}_{i,1} - \tilde{R}_{i,2})$.

We will describe the determination of $\eta_1^{(N)}$ and $\eta_2^{(N)}$ by referring to the HIRS instrument. If only channel 7 were used to determine η_1 we would use equation 4 to obtain:

$$\eta_{1,7}^{(N)} = \frac{R_7^{CC(N)} - \tilde{R}_{7,1}}{\tilde{R}_{7,1} - \tilde{R}_{7,3}}. \tag{7}$$

A similar equation would be used to obtain η_1 if only channel 6 were used. We shall take $\eta_1^{(N)}$ to be a weighted average of $\eta_{1,7}^{(N)}$ and $\eta_{1,6}^{(N)}$:

$$\eta_1^{(N)} = \frac{\eta_{1,7}^{(N)} (\tilde{R}_{7,1} - \tilde{R}_{7,3})^2 + \eta_{1,6}^{(N)} (\tilde{R}_{6,2} - \tilde{R}_{6,3})^2}{(\tilde{R}_{7,1} - \tilde{R}_{7,3})^2 + (\tilde{R}_{6,2} - \tilde{R}_{6,3})^2 + \delta} \tag{8}$$

where δ is a damping parameter on the order of the microwave noise which is analogous to the ridge parameter in ridge regression. This equation is the least squares solution for $\eta_1^{(N)}$ if equation 6 is used to obtain the best estimate of $\eta_1^{(N)}$ based on channels 6 and 7. In other words $\eta_{1,7}^{(N)}$ and $\eta_{1,6}^{(N)}$ are weighted by the amount of signal in channels 7 and 6 respectively.

To determine n_2 a similar procedure is followed except that part of the inhomogeniety described by n_1 is removed from the signal, for example:

$$n_{2,7}^{(N)} = \frac{(R_7^{CC(N)} - \tilde{R}_{7,1}) - n_1^{(N)}(\tilde{R}_{7,1} - \tilde{R}_{7,3})}{(\tilde{R}_{7,1} - \tilde{R}_{7,2})} \qquad (9)$$

$$n_2^{(N)} = \frac{n_{2,7}^{(N)}(\tilde{R}_{7,1} - \tilde{R}_{7,2})^2 + n_{2,6}^{(N)}(\tilde{R}_{6,1} - \tilde{R}_{6,2})^2}{(\tilde{R}_{7,1} - \tilde{R}_{7,2})^2 + (\tilde{R}_{6,1} - \tilde{R}_{6,2})^2 + \delta} \qquad (10)$$

If the denominator of equation 10 is found to be on the order of the expected combined infrared and microwave instrumental noise n_2 is set to zero. Similarly if the denominator of equation 8 is on the order of the expected noise n_1 is set to zero. If $n_1^{(N)}$ is found to be less then zero $n_1^{(N)}$ is set to zero, in which case $n_2^{(N)}$ is set to zero since $n_1^{(N)}$ should contain most

of the cloud information. If either $[(\tilde{T}_{7,1} - \tilde{T}_{7,3}) + (\tilde{T}_{6,1} - \tilde{T}_{6,3})]/2 \leq 1°$ or

$[(\tilde{T}_{7,1} - \tilde{T}_{7,2}) + (\tilde{T}_{6,1} - \tilde{T}_{6,2})]/2 < 1°$ it is assumed that field of view 1 is clear and therefore n_1 and n_2 are both set to zero. In this case a further check is made to determine if the scene is completely overcast. If $(T_7^{CC} - \tilde{T}_{7,1}) \geq 5°$ the scene is assumed to have complete cloud cover and no retrievals are done. Finally, if $[(n_1^2 + n_2^2)]^{1/2} \geq 4$ the scene is assumed to be too cloudy to perform a retrieval.

The simulation retrieval studies to be described below were carried out using cloudy radiances simulated at GLAS. Retrievals were carried out using radiances simulated from radiosonde atmospheric temperature profiles at various satellite viewing angles. The surface temperature was taken to be randomly distributed about the surface air temperature with a standard deviation of three degrees. Equation 2 was used to construct cloud radiances for two cloud layers randomly distributed between 300 and 700 mb. For each radiosonde three fields of view were simulated. The two cloud top heights were taken to be the same for all three fields of view, however the cloud fractions for the two cloud heights varied randomly for the three fields of view. The average total cloud fraction for the three fields of view were $\bar{\alpha}_1 = 0.2$, $\bar{\alpha}_2 = 0.5$, $\bar{\alpha}_3 = 0.75$. Thus the cloudy radiance simulations produced, on the average, very cloud contaminated radiances. These simulated cloudy radiances were contaminated by reasonable instrumental noise and then used as observations for the GLAS physical retrieval scheme. The retrieval system then procedes by the steps:

1) Calculate clear column radiances based on a climatological first guess

2) Use equation 7, 8 and 10 to calculate $n_1^{(1)}$ and $n_2^{(1)}$

3) Reconstruct clear column radiances using equation 6

71

4) Obtain a ground temperature

5) Use the new ground temperture to recalulate the clear column radiances and use steps 2 and 3 to reconstruct clear column radiances

6) Perform a regression to obtain an improved temperature profile

7) Recalculate the ground temperature

8) Reconstruct clear column radiances

9) Perform a physical retrieval step and check differences between calculated clear column brighness temperatures and reconstructed clear column brightness temperatures for convergence

10) Obtain a new ground temperature

11) Iterate steps 8, 9, 10 until convergence is achieved (step 10 is only done 3 times no matter how may iteration are done for steps 8 and 9)

12) Check rejection criteria and flag the retrieval if it should be rejected (i.e., if the RMS difference between the computed and reconstructed brightness temperatures is greater than 1° or if the calculated and observed values of MW channel 2 differ by more then, 1°, or 1.5° if both n_1 and $n_2 = 0$)

Figure 1 shows a comparison of the results of the retrieval for the HIRS2 and AMTS sounders. Also shown in this figure are the results obtained from the regression analysis performed in step 6. The regression matrices were obtained from clear column brightness temperatures obtained from calculations using radiosondes not used in this study and thus these profiles represent an independent set of regression results. As may be seen from this figure the AMTS improves the HIRS results throughout the atmosphere. Furthermore the physical retrieval method shows much improvement over the regression results. In this connection it should be noted that attempts to improve the regression results by iterating the regression (i.e., by substituting step 6 for step 9) gave rise to some improvement of the regression results, but they were still inferior to the results from the physical retrieval.

Figure 2 compares the results obtained from these cloudy radiances with results obtained when the same radiosondes were used to simulate radiances with no clouds. As may be seen from this figure the degradation of the results in the presence of heavy clouds is not very severe.

Finally, to indicate the relevance of these results to the joint NOAA/NESS-NASA Simulation Test, Figure 3 compares the results of retrievals performed in the clear column portion of this test using radiances generated at the University of Denver and the results for the same profiles using clear column radiances simulated by the model used in the GLAS simulations. As may be seen from this figure the results obtained using radiances based on the GLAS simulation model are quite similar to the results obtained from radiances based on the model to be used in the actual test.

As a final note it might be asked what relation, if any, this simulation

72

study bears to what might be expected from an operational sounder sensing the true atmosphere. Since the GLAS physical inversion method relies quite heavily on the ability to calculate the radiances which would be observed at the satellite given the true atmospheric and surface conditions, the errors in this calculation will very probably be the limiting factor in determining the applicability of these results to real data sounding. However, it has been shown (Susskind et al., 1982) that the model used in this study quite accurately reproduces satellite observation when the relevant parameters are known. Therefore, we feel that we may transfer results obtained from this work to the problem of actual meteorological parameter sensing. In particular the current analysis system used at GLAS for the HIRS2 sounder uses a two field of view single cloud layer cloud filtering algorithm (i.e., equation 3, 4, and 5 in the text). Based on this study we found that the multiple layer cloud filtering algorithm showed significant improvement over the single cloud layer system. Therefore we are currently in the process of modifying our operational system to test whether this result holds true for real data analysis.

REFERENCES

Susskind, J., D. Reuter, A. Dalcher, 1983: Simulation comparison study of the AMTS and HIRS sounder. NASA Tech. Memo. 84983.

Susskind, J., J. Rosenfield, D. Reuter, and M. T. Chahine, 1983: The GLAS physical inversion method for analysis of HIRS/MSU sounding data. NASA Tech. Memo. 84936.
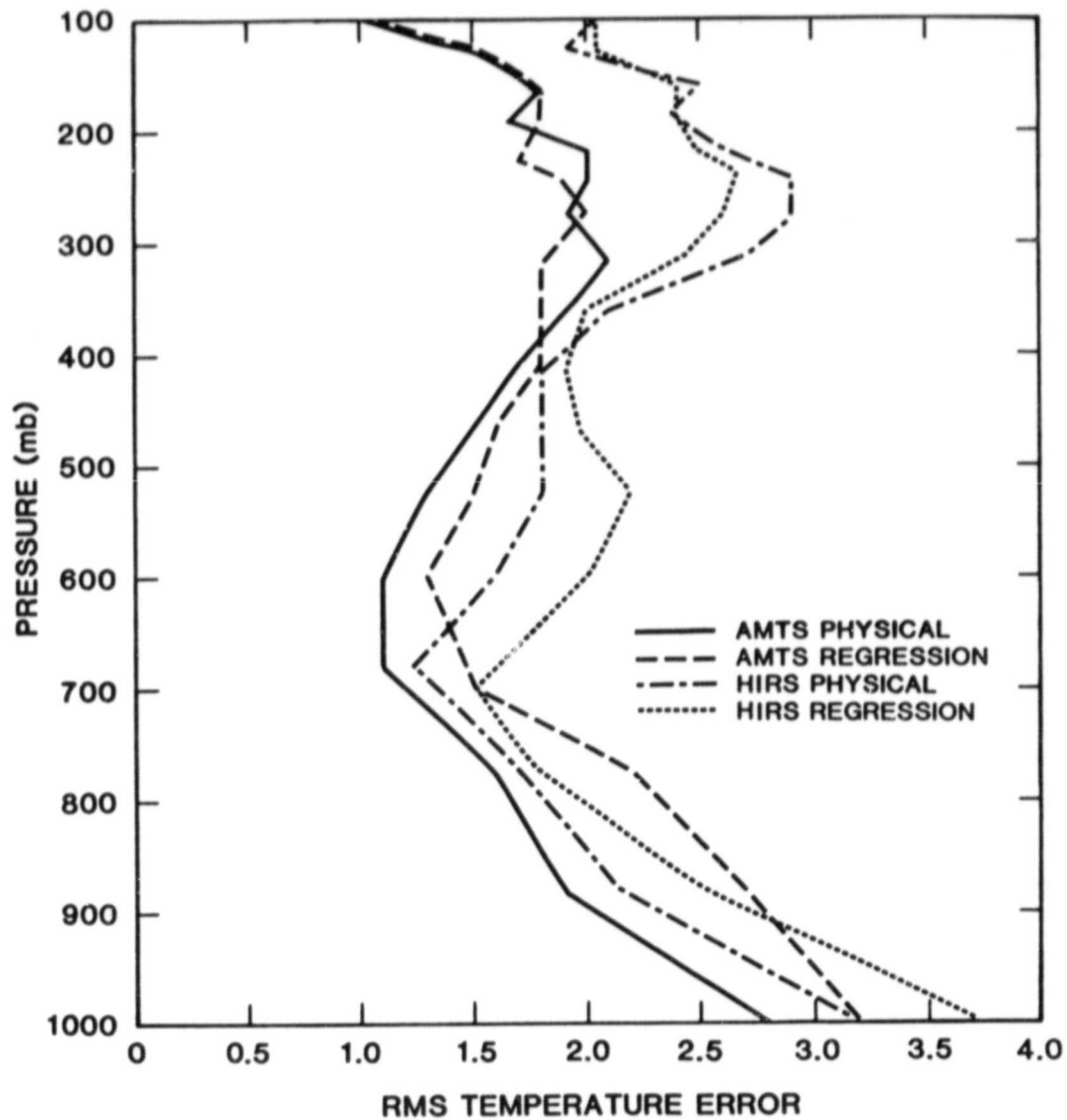
Figure 1. RMS temperature errors for AMTS and HIRS sounders (physical retrieval scheme and regression).
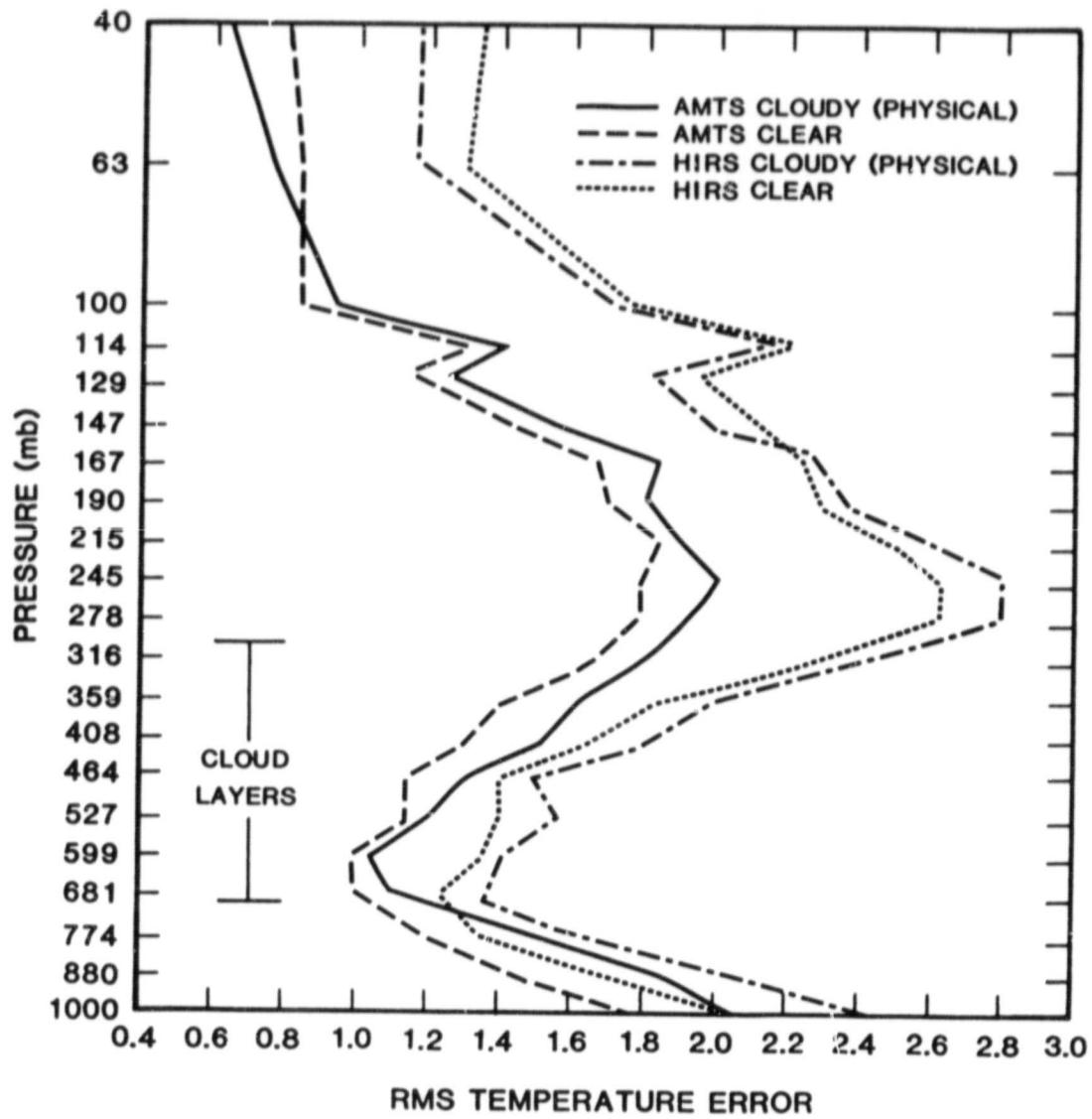
Figure 2. Comparison of clear and cloudy physical retrievals (RMS temperature errors).
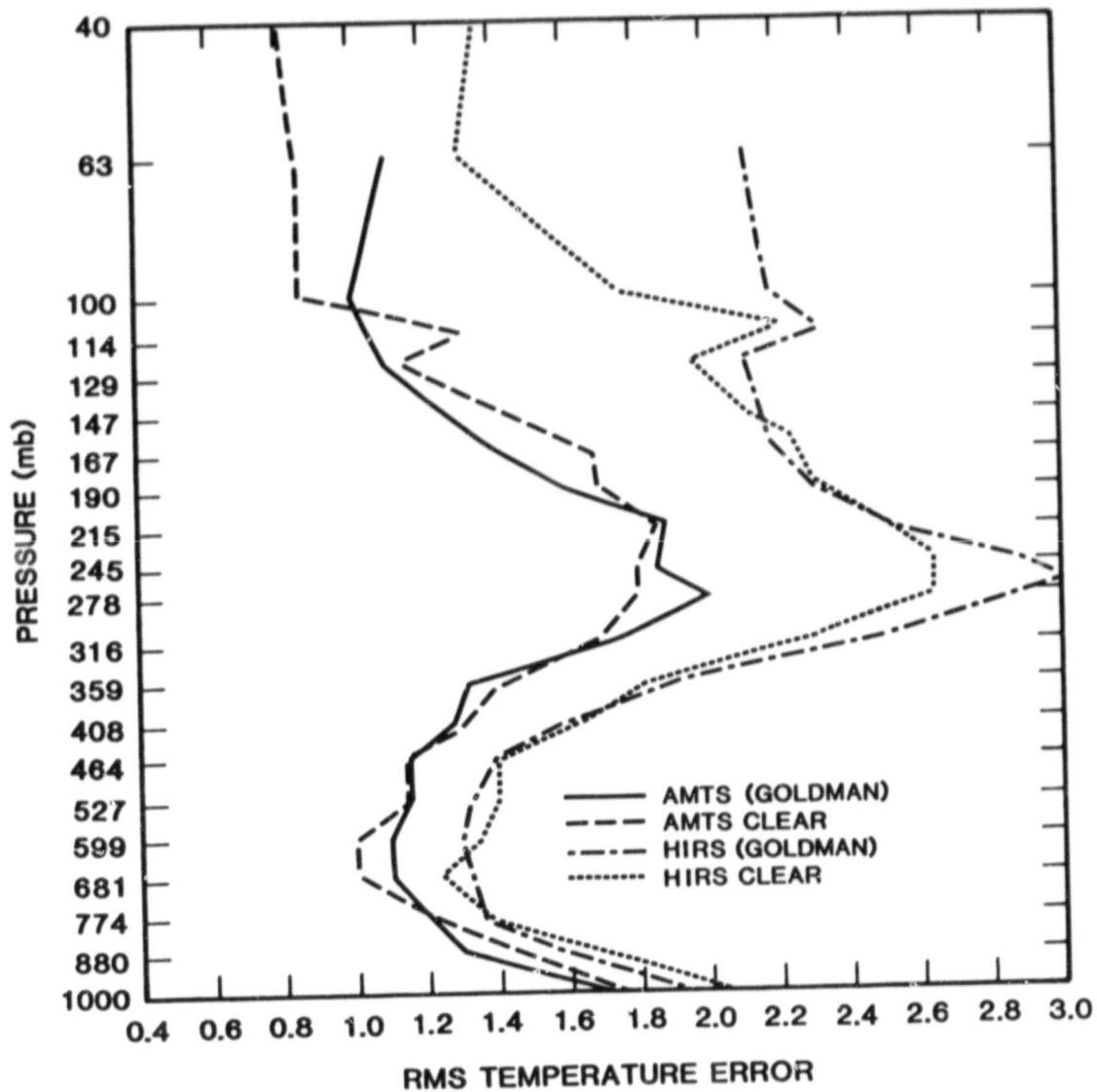
Figure 3. Comparison of retrievals based on clear column radiances simulated by Goldmann at the Unversity of Denver and retrievals based on clear column radiances simulated at GLAS (RMS temperature errors).

WATER VAPOR PROFILE RETRIEVALS FROM THE HIRS/MSU SOUNDER: CLEAR AND CLOUDY SIMULATION STUDIES

D. Reuter and J. Susskind

Currently, the GLAS physical retrieval scheme is capable of producing accurate atmospheric and surface temperature retrievals and accurate measures of cloud fields from radiances measured by the HIRS/MSU sounding unit (Susskind et al., 1982). Since the presence of water vapor could contaminate these radiances only those infrared and microwave channels which are quite insensitive to the amount of water vapor are used to determine the temperature and cloud fields in the analysis. However water vapor is, in itself, a variable of meteorological interest and the HIRS instrument has a number of channels which are quite sensitive to the presence of water vapor; specifically the surface and lower tropospheric channels 8 and 10 and the mid and upper tropospheric channels 11 and 12. In order to determine if these channels contain any useful water vapor information we have carried out studies in which water vapor retrievals were performed, based on simulated clear and cloudy radiances and retrieved atmospheric and surface temperatures. The method used for simulating the clear and clody radiances has been described previously in this report (Reuter et al.) and thus no further detail will be given here.

The water vapor retrieval scheme is based on considerations similar to those used in the retrieval of temperature information. Specifically, for two atmospheric profiles which have the same temperature structure, but whose water vapor contents are different by a small amount $\delta\mu(P)$ it may be shown that:

$$T_i[\mu(P) + \delta\mu(P)] - T_i[\mu(P)] = \int_{P_S}^{\overline{P}} W_i(P)\, \delta\mu(P)\, d\ell np \tag{1}$$

where T_i is the equivalent black body temperature for radiance R_i in channel i, $\overline{P}$ is the satellite pressure, P_S is the surface pressure and W_i is a water vapor sensitivity function for channel i given as

$$W_i(P) = \left(\frac{d\, \dfrac{d\tau_i(P,\theta)}{d\ell np}}{d\mu(P)} \right)_{\mu(P)}. \tag{2}$$

In equation 2 $\tau_i(P,\theta)$ is the frequency averaged transmittance in channel i from pressure P to $\overline{P}$ at angle θ.

In this very preliminary work two somewhat drastic, but not unreasonable assumptions were made to simplify the problem. The first assumption arises because each channels is primarily sensitive to changes to water in specific pressure intervals and thus what is determined in not $\delta\mu(P)$ but rather a mean layer change $\overline{\delta}$. The second assumption is that $\int_{P_S}^{\overline{P}} W_i(P)\, d\ell np$ is essentially a constant $\overline{W}$ for each channel for the profiles studied. Under these assumptions

equation (1) becomes:

$$T_i[\mu(P) + \delta\mu(P)] - \overline{T_i[\overline{\mu}(P)]} = \overline{W}\,\overline{\delta}. \tag{3}$$

This equation suggests that a regression treatment may be used to find $\overline{W}$ as a function of $\overline{\delta}$ and brightness temperature differences. The method of analysis is, then, as follows:

1) Simulated radiances (T_i^{OBS}) are used as input to the GLAS temperature scheme and retrieved temperature profiles are produced.

2) These retrieved temperature profiles are used to simulate brightness temperatures (T_i^{CALC}) in channels 8, 10, 11, and 12 using climatological water vapor profiles (μ^{CLIM}).

3) The data is divided into two sets, the first to generate the regression relationship and the second set to use as verification. The regression equation is then solved to find the regression matrix A.

$$(\mu^{TRUE} - \mu^{CLIM}) = A(T_i^{OBS} - T_i^{CALC}) \tag{4}$$

where

$$A = (\Delta T^T \Delta T + \gamma)^{-1} \Delta\mu \Delta T^T \tag{5}$$

and $\Delta T = (T_i^{OBS} - T_i^{CALC})$, $\Delta\mu = (\mu^{TRUE} - \mu^{CLIM})$ and γ is a ridge parameter.

4) This regression relation is used on the second set of data to generate retrieval statistics.

Note that the retrieved temperatures are used in the calculation of T_i^{CALC}. Equations (1) thru (3) are most nearly true if there is no difference in the temperature profiles giving rise to T_i^{OBS} and T_i^{CALC}. However, in the processing of real data, we would only have the retrieved temperature profiles, thus to attempt an accurate assessment of the ability of the HIRS instrument to retrieve water vapor profiles, we have included this source of noise in the simulation procedure.

The results of this study are given in figure 1 in terms of the percent error of the retrieved water vapor column densities in the pressure regions 1000-700 mb, 700-500 mb and 500-300 mb. Also given in this figure are the percent errors of the climatological guess. Results for two cases are shown: case S_1 is for a very moist summer ocean tropical zone, and case W_1 is for a dry winter land mid-latitude zone. For case S_1 results are presented for simulated clear and cloudy conditions. Note that the presence of clouds does not degrade the results significantly. The lines are only used to connect the points and do not indicate accuracies in the regions between points. Table 1 presents the absolute accuracies of the retrievals in terms of rms column densities for the pressure levels specified above. From this table it may be seen that even though the precent errors for W_1 are much worse than those for

S_1, the absolute accuracies are somewhat better.

Based on the results of this study it appears that there is usable water vapor information contained in the HIRS water vapor channels. We are presently in the process of refining this technique in the hope that we may impliment water vapor retrievals as part of the real data analysis scheme.

Table 1

RMS errors of retreived water vapor column densities (g/cm^2) (independent set)

P(mb)	S_1(clear)	S_1(cloudy)	W_1(clear)
300-500	0.029	0.028	0.012
500-700	0.14	0.16	0.063
700-1000	0.50	0.58	0.41
1-1000	0.51	0.65	0.43

REFERENCES

Reuter, D., J. Susskind, and A. Dalcher, 1983: Simulation studies of the HIRS2/MSU and AMTS/MSU satellite sounding units: cloudy conditions. NASA Tech. Memo. 84983.

Susskind, J., J. Rosenfield, D. Reuter, and M. T. Chahine, 1983: The GLAS physical inversion method for analysis of HIRS2/MSU sounding data. NASA Tech. Memo. 84936.
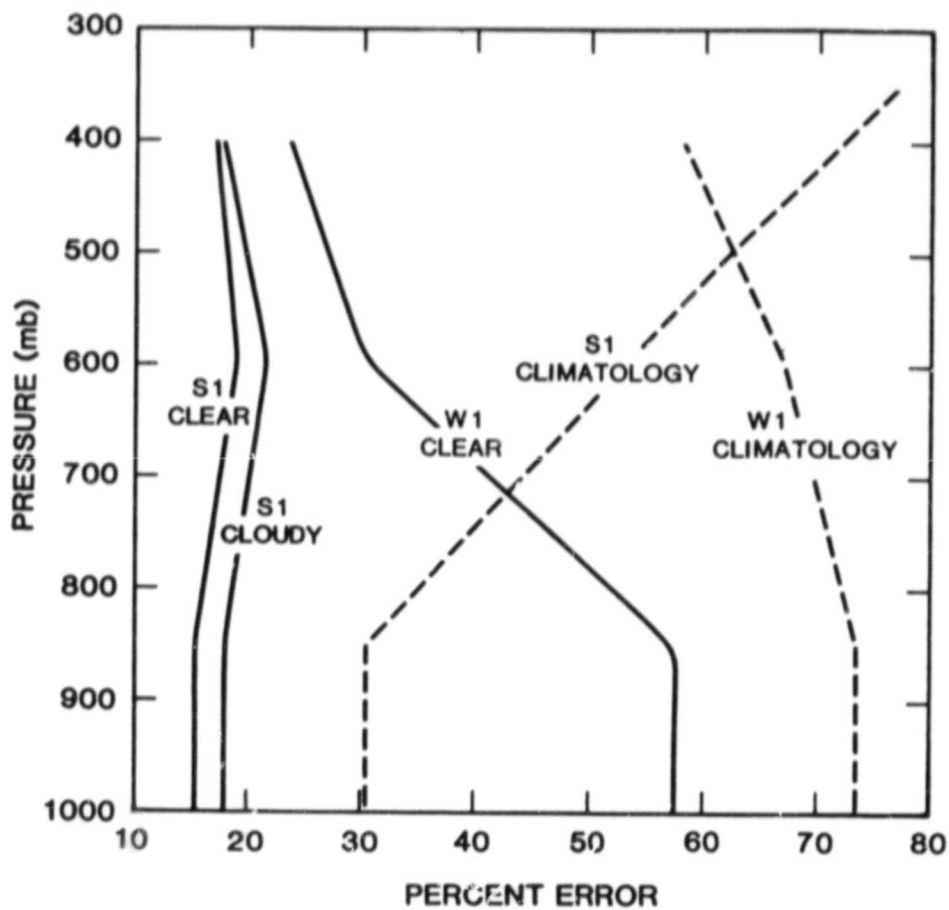
Figure 1. Percent errors of water vapor retrievals and climatologies: points
lie in the middle of the mean pressure regions. The lowest point
is extended vertically to 1000 mb.

C. ANALYSIS AND MODEL DEVELOPMENT

A LEVEL 2.4 SECOND-ORDER CLOSURE MODEL FOR THE PREDICTION OF TURBULENCE

H. M. Helfand and J. C. Labraga

Mellor and Yamada (1974) and Yamada (1977) have developed a hierarchy of second-order closure models for the prediction of atmospheric turbulence. These models range from the simple level 2 model, which consists of a system of purely algebraic equations, to the more complicated, expensive and accurate level 4 model, which consists of ten prognostic equations for the second order turbulent moments.

Yamada (1977) has proposed a level 2.5 model as a good compromise between the simplicity of the level 2 model and the accuracy of the level 4 model. This model has only one prognostic equation, that for the turbulent kinetic energy,

$$1/2 \ q^2 = 1/2 \ (\overline{u^2} + \overline{v^2} + \overline{w^2}). \tag{1}$$

We have analyzed the model, however, and we have found that it is ill-defined and singular when it predicts a value of $1/2 \ q^2$ significantly smaller than that predicted by the level 2 model. Accordingly, we have created a new second-order closure model which combines the best features of the level 2 model and the level 2.5 model. We have labeled this the level 2.4 model.

Both the level 2 and the level 2.5 models define turbulent transport coefficients for momentum and heat according to

$$K_m = q \ell \widetilde{S}_m \tag{2}$$

and

$$K_n = q \ell \widetilde{S}_h, \tag{3}$$

where q is the turbulent velocity scale defined in (1), ℓ is a turbulent length scale, and $\widetilde{S}_m$ and $\widetilde{S}_h$ represent the dimensionless parts of the coefficients. $\widetilde{S}_m$ and $\widetilde{S}_h$ are functions of the dimensionless shear,

$$S = \ell/q \ |U_z|, \tag{4}$$

and of the dimensionless Brunt-Vaisalla frequency,

$$M = \ell/q \ (g\Theta_z/\Theta_0)^{1/2} . \tag{5}$$

One can also express the anisotropy,

$$C_w = \overline{w^2}/(1/3 \ q^2) , \tag{6}$$

as a function of S and M. C_w is the ratio of the actual turbulent kinetic energy

in the vertical mode to that energy which would be in the vertical mode if the flow were isotropic. Physical reality demands that C_W should be well within the limits,

$$0 < C_W < 3. \tag{7}$$

Isotropy occurs when $C_W = 1$.

The level 2 model determines q as a function of the mean state of the atmosphere according to

$$q^2 = B_1 \ell^2 |U_z|^2 (\tilde{S}_m - Ri\ \tilde{S}_h), \tag{8}$$

where Ri is the gradient Richardson number,

$$Ri = g\Theta_z / \Theta_0 |U_z|^2, \tag{9}$$

and where B_1 is a constant. Eq. (8) tells us that S and M are functions of Ri in the level 2 model. $\tilde{S}_m$, $\tilde{S}_h$ and C_W therefore are also functions of Ri, and, as one can see in Fig. 1, they are well behaved. C_W, for instance, is well within the bounds of (7) and it decreases slowly with increasing atmospheric stability.

The level 2.5 model has an extra degree of freedom in comparison to the level 2 model. In the level 2.5 model, q is a prognostic variable and S and M must now be expressed as functions of Ri and q. Thus $\tilde{S}_m$, $\tilde{S}_h$ and C_W, which depend on S and M exactly as they do in the level 2 model, are also functions of both Ri and q.

While Eq. (8) does not necessarily hold for the level 2.5 model, it does hold whenever q reaches its equilibrium value of $q_e(Ri)$. Thus, the level 2 model is a special case of the level 2.5 model, and Fig. 1 represents the Ri dependence of $\tilde{S}_m$, $\tilde{S}_h$ and C_W for the level 2.5 model for the special case $q = q_e(Ri)$.

Fig. 2 represents the behavior of these functions for the case $q = 1.4 q_e(Ri)$ or the case where the turbulent kinetic energy is double its equilibrium value. Here $\tilde{S}_m$, $\tilde{S}_h$ and C_W behave quite smoothly, and, in fact, are less sensitive to Ri than they were in the level 2 model.

When $q = .7 q_e(Ri)$ or the turbulent kinetic energy is half of its equilibrium value, on the other hand, the behavior of $\tilde{S}_m$, $\tilde{S}_h$ and C_W is singular. Fig. 3 demonstrates that these functions approach plus infinity as the Richardson number decreases to -.68 and then they increase from minus infinity to negative finite values. This behavior is nonphysical, and the condition (7) is clearly violated for Ri < -.55. The level 2.5 model is basically an equilibrium model for turbulence

84

but when $1/2\ q^2$ is significantly smaller than its equilibrium value one cannot assume that the other turbulent quantities are in an equilibrium state.

To remedy the problem with the level 2.5 model for $q < q_e$, we have proposed the following model which we term the level 2.4 model. Define K_m and K_h according to (2) and (3) but take

$$\tilde{S}_m = \tilde{S}_m\ (Ri)$$
$$\tilde{S}_h = \tilde{S}_h\ (Ri) \tag{10}$$

from the level 2 model for $q < q_e$ (Ri), and take

$$\tilde{S}_m = \tilde{S}_m\ (Ri,\ q)\ ,$$
$$\tilde{S}_h = \tilde{S}_h\ (Ri,\ q)\ , \tag{11}$$

from the level 2.5 model for $q \geq q_e$ (Ri). The value of q in (4) and (5) is the prognostic one in either case. This model has the advantage of allowing K_m and K_h to be proportional to a prognostically determined turbulent velocity scale yet it assures one that the Richardson number dependence of these coefficients will be reasonable. It also allows turbulence to exist when Ri exceeds its critical value, as does the level 2.5 model, for in that case, q_e (Ri) = 0 and $q > 0$ implies that the model is identical to the level 2.5 model.

REFERENCES

Mellor, G. L., and T. Yamada, 1974: A hierarchy of turbulence closure models for planetary boundary layers. J. Atmos. Sci., 31, 1791-1806.

Yamada, T., 1977: A numerical simulation of pollutant dispersion in a horizontally homogeneous atmospheric boundary layer. Atmos. Environ., 11, 1015-1024.
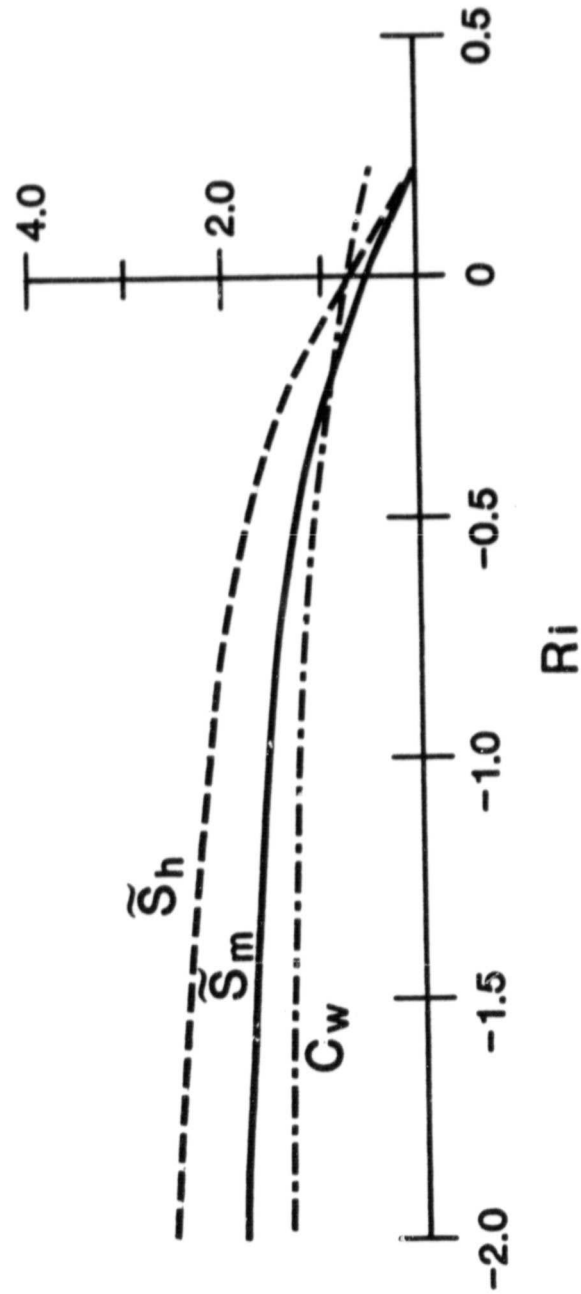
Fig. 1. Dependence of $\tilde{S}_m$ (solid line), $\tilde{S}_h$ (dashed line) and C_w (dash-dotted line) on Richardson number for the level 2 model.
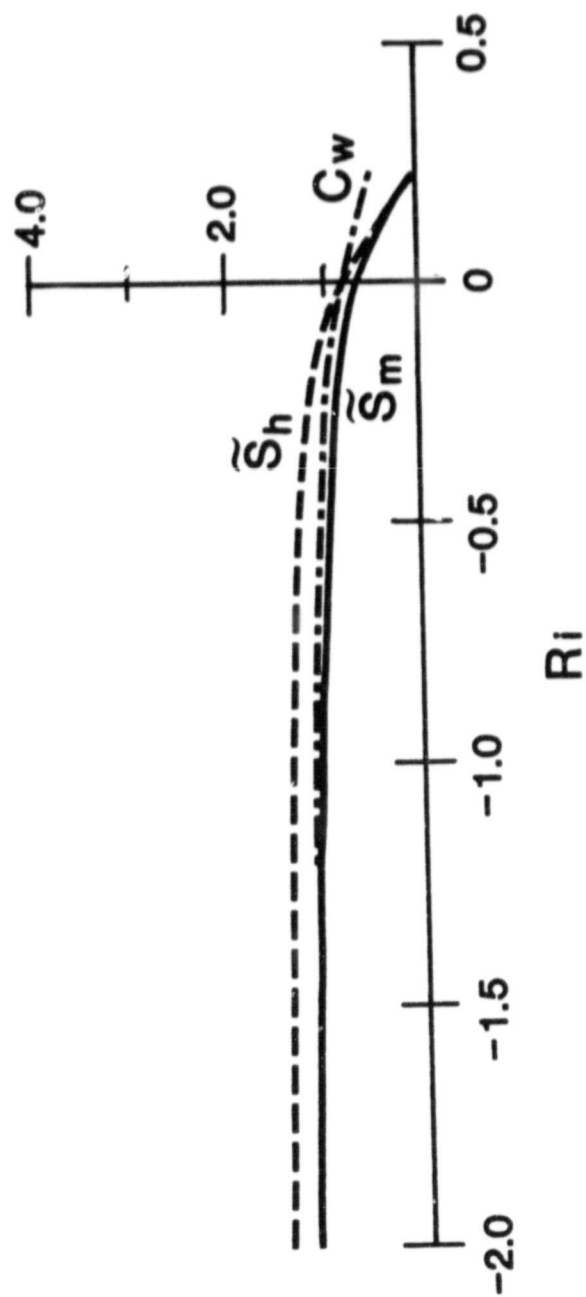
Fig. 2. Dependence of $\tilde{S}_m$, $\tilde{S}_h$ and C_w on Richardson number for the level 2.5 model when the turbulent kinetic energy is double its equilibrium value. Notation is that of Fig. 1.
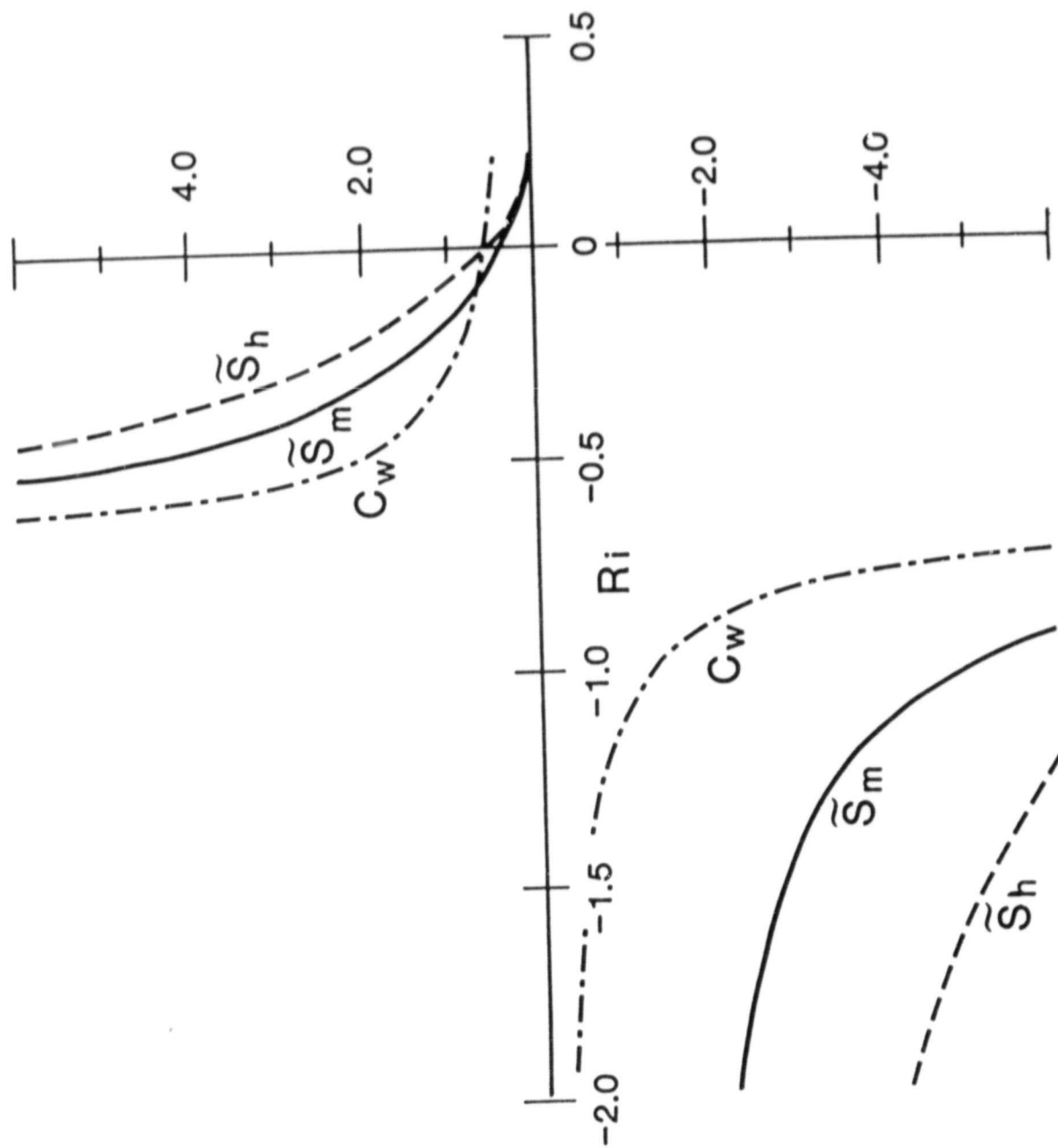
Fig. 3. Dependence of $\widetilde{S}_m$, S_h and C_w on Richardson number for the level 2.5 model when the turbulent kinetic energy is half its equilibrium value. Notation is that of Fig. 1.

SELECTION OF A BEST CANDIDATE HIGHER-ORDER CLOSURE SCHEME
FOR TURBULENCE IN THE GLAS FOURTH ORDER GCM

J. C. Labraga and H. M. Helfand

Mellor and Yamada (1974) have presented a hierarchy of second-order closure models for turbulence ranging from the complete level 4 model, with ten prognostic equations, to the simple level 2 model, which is a fully algebraic system of equations. On the basis of a set of Wangara simulations, they concluded that an intermediate member of the hierarchy, the level 3 model with two prognostic equations and eight diagnostic equations, was the optimum compromise between expense and accuracy for geophysical applications.

Later, Yamada (1977) introduced a yet simpler compromise between the level 3 and the level 2 models. His level 2.5 model carried turbulent kinetic energy as its only prognostic variable with the remaining seven variables determined prognostically. Miyakoda and Sirutis (1977) have selected this level 2.5 model to represent the vertical turbulent fluxes of heat, momentum and moisture in the planetary boundary layer (PBL) and in the free atmosphere in the GFDL General Circulation Model (GCM).

Elsewhere in this volume, Helfand and Labraga have demonstrated that the level 2.5 model is ill-defined and singular. In its stead, they have developed a level 2.4 model which incorporates the best features of the level 2.5 and level 2 models and yet is not singular.

We have tested the level 2.4 model by repeating a 48 hour simulation of the Wangara experiment carried out by Yamada and Mellor (1975) with the level 3 model. Our model had 31 layers progressively concentrated near the ground so as to have vertical resolution similar to that used by Yamada and Mellor. We also repeated our simulation with a simpler level 2 model so as to see where the level 2.4 simulation fell between those by its simpler and more complicated cousins.

We discovered that the level 2.4 model gave results remarkably similar to those of the level 3 model (see, for example, Fig. 1). We also saw, to our surprise, that the simulation by the level 2 model was virtually identical to that by the level 2.4 model.

To examine the feasibility of using the level 2.4 scheme in the GLAS Fourth Order GCM (Kalnay-Rivas et al., 1977), we repeated the Wangara simulation at a drastically reduced vertical resolution. In this experiment, the PBL was resolved by only four grid points, only three of which were located within 2 km of the ground. The layers were chosen as those of the PBL-simulating version of the GLAS Fourth Order Model. The surface flux parameterization was also taken from that model. This parameterization uses an extended Monin-Obukhov similarity scheme to predict surface fluxes on the basis of the temperature and wind gradients over the lowest 150 m of the atmosphere.

Fig. 2 shows that even at this drastically reduced vertical resolution, the level 2.4 model gives a good qualitative simulation of the diurnal cycle. Fig. 3 shows that the level 2.4 model, together with the surface flux parameterization does an excellent job at predicting surface fluxes at the coarse resolution.

The results of the experiment demonstrate the suitability of the level 2.4 model together with the surface flux scheme for use in the GLAS model.

The experiment was repeated with the level 2 model, and the results were again indistinguishable from those of the level 2.4 model. The level 2 model is cheaper to run than the level 2.4 model because it requires fewer computations, it is less subject to numerical instability, and it does not require storage of a turbulent kinetic energy field for prognostic purposes. Its accuracy is apparently identical to that of the level 2.4 model, and therefore, on the basis of the present study, the level 2 model is the best candidate for use in the GLAS Fourth Order GCM.

REFERENCES

Kalnay-Rivas, E., A. Bayliss and J. Storch, 1977: The 4th order GISS model of the global atmosphere. Contrib. Atmos. Phys., 50, 306-311.

Mellor, G. L., and T. Yamada, 1974: A hierarchy of turbulence closure models for planetary boundary layers. J. Atmos. Sci., 31, 1791-1806.

Yamada, T., 1977: A numerical simulation of pollutant dispersion in a horizontally homogeneous atmospheric boundary layer. Atmos. Environ., 11, 1015-1024.

Yamada, T., and G. L. Mellor, 1975: A simulation of the Wangara atmospheric boundary layer data. J. Atmos. Sci., 32, 2309-2329.

FIGURE CAPTIONS

Fig. 1.   Time and space variation of the virtual potential temperature Θ_v in units of degrees C for the observations (a) and for the simulation by the level 3 model (b) and in units of degrees K for the simulation by the level 2.4 model (c) and by the level 2 model (d).

Fig. 2.   Virtual potential temperature Θ_v profiles at 1200, day 33 to 0900, day 34 from the observations (a), from the simulation by the 31-layer model (b) and from the simulation by the 4-layer model (c).

Fig. 3.   Hourly variation of the surface heat flux from observations (triangles), from the simulation by the 31-layer model (solid line) and from the simulation by the 4-layer model (dashed line). The units are m s^{-1} K.
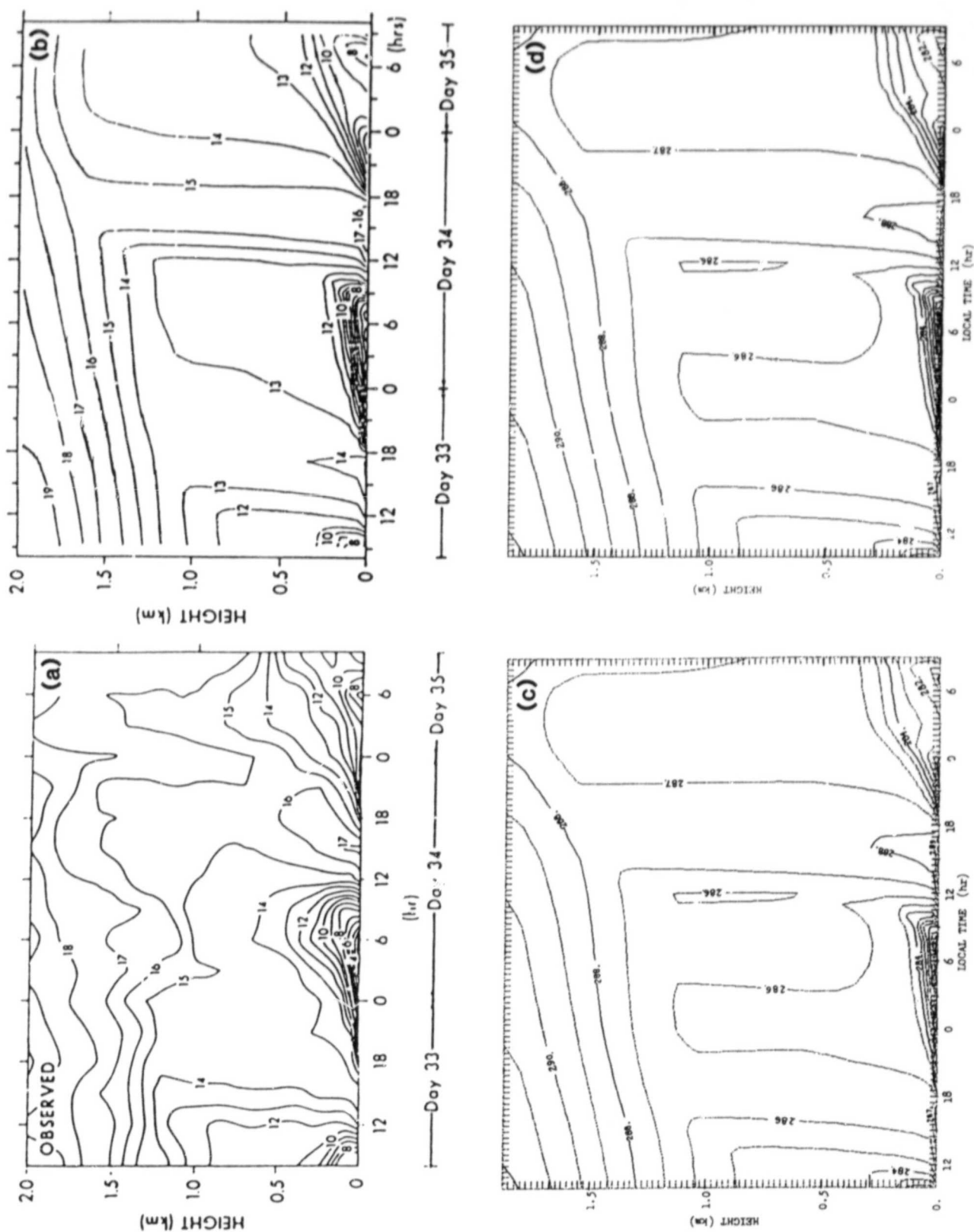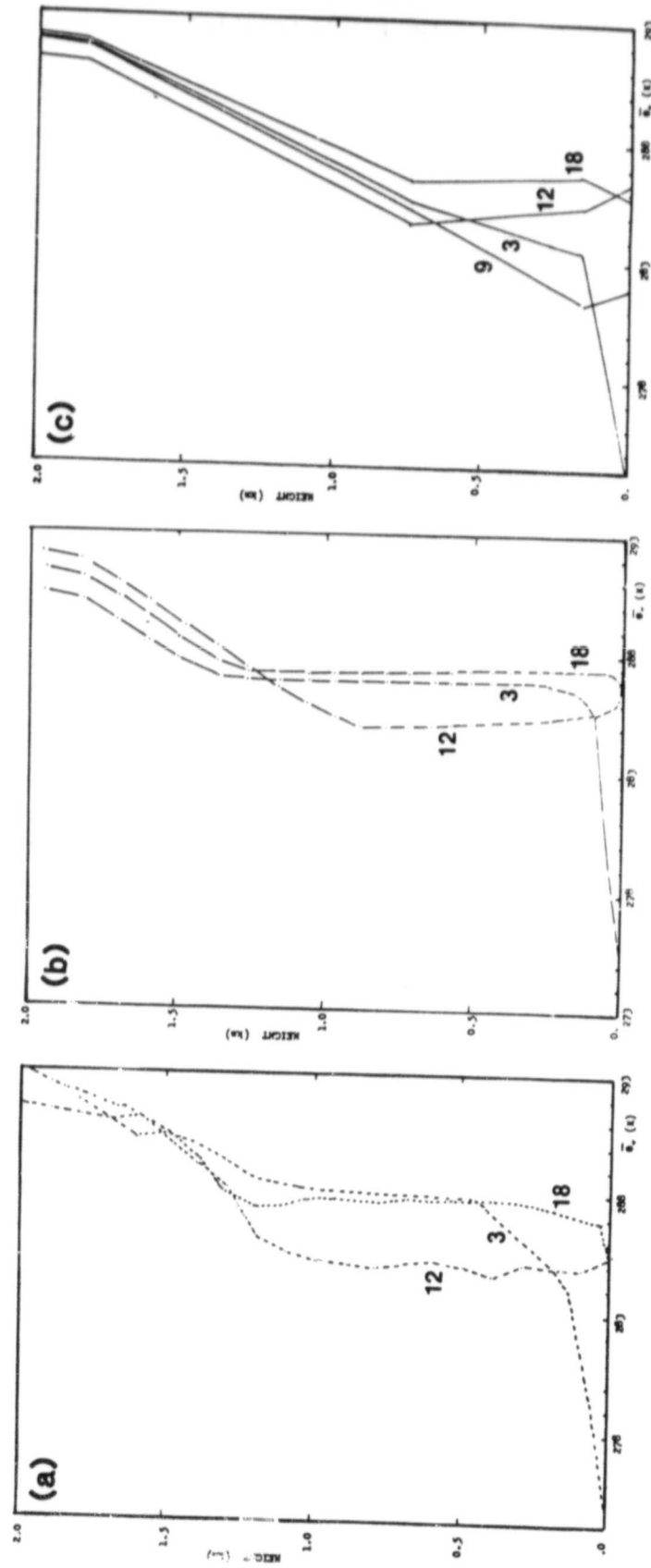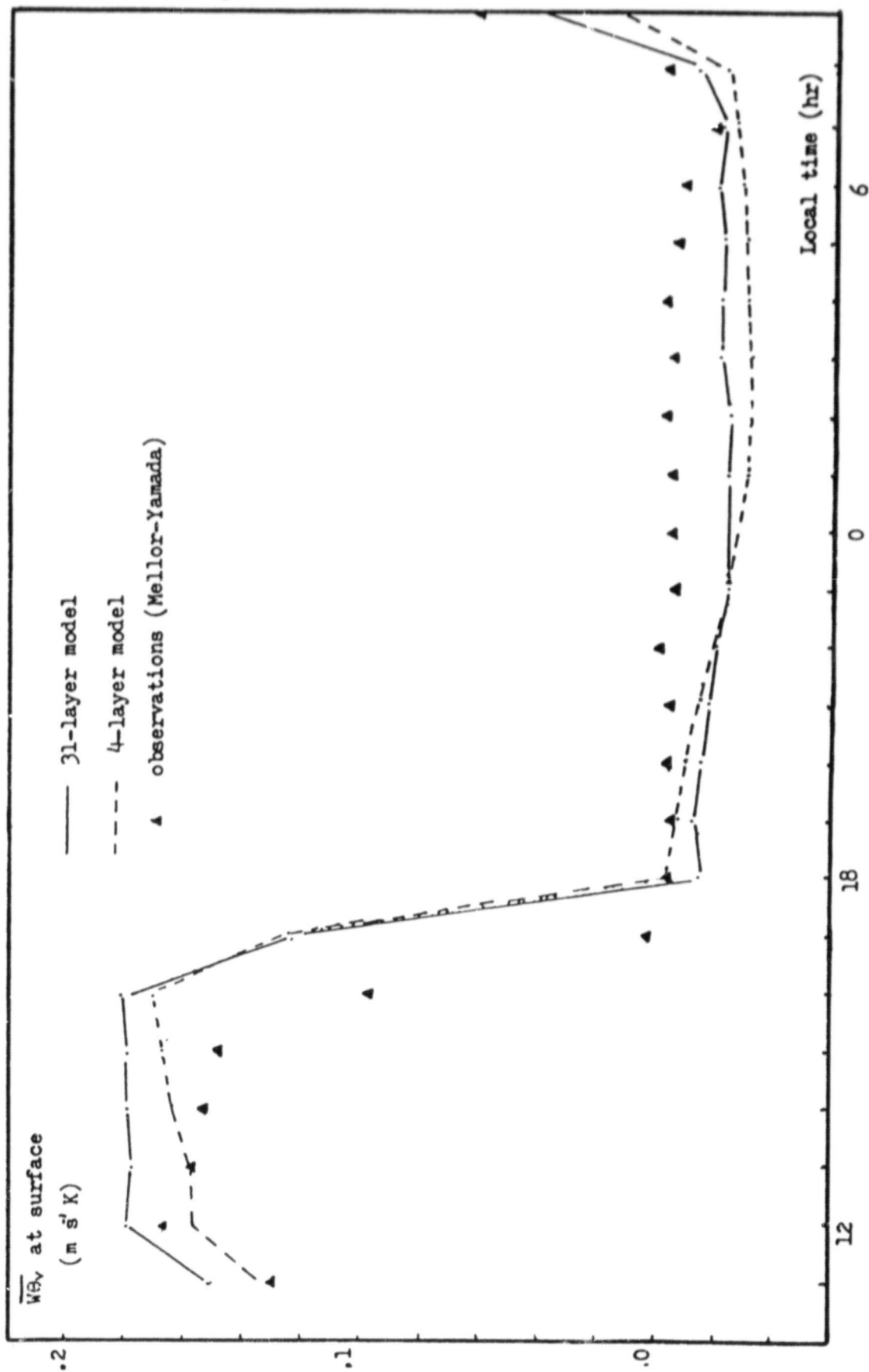
Figure 1

Figure 2

Figure 3

A STATISTICAL DYNAMICAL STUDY OF LARGE-SCALE FLOW ANOMALIES

S. D. Schubert

1. INTRODUCTION

In this study the large-scale intraseasonal variability of the winter time extratropical atmosphere is examined within the framework of a hemispheric equivalent barotropic model expanded in horizontal empirical orthogonal functions (EOFs) in the wave domain. This approach allows for a detailed observational and statistical analysis of the anomaly fields and in addition provides insights into the dynamical processes governing their behavior.

2. OBSERVATIONS

The anomaly fields are computed as deviations from a mean seasonal cycle based on a ten-year data set of the 500 mb streamfunction. A statistical test developed by Preisendorfer et al. (1981) shows that the first 12 time dependent principal components (PCs) associated with the EOF anomalies have a variability which is significantly different from that of PCs computed from spatially and temporally uncorrelated noise. The spatial patterns of the statistically significant modes of variability are examined in the context of the time mean kinetic energy spectrum and are interpreted by superimposing them on the winter mean flow.

The first EOF is dominated by zonal wave numbers 0 and 2 and has a spatial pattern resembling the Pacific/North American pattern reviewed recently by Wallace and Gutzler, 1981. When superimposed on the mean flow with large positive and negative PCs (2.5 standard deviations) this mode exhibits a behavior resembling an index cycle in the western hemisphere.

The second EOF has a large anomaly center over the North Atlantic and is dominated by zonal wave numbers 1 and 2. This mode is associated with fluctuations in the North American east coast jet and seems to be related to the North Atlantic Oscillation also reviewed recently by Wallace and Gutzler, 1981.

The third EOF pattern is primarily composed of zonal wave numbers 1 and 3. This mode has anomaly centers closely coupled to the positions of the east coast jets and when superimposed on the mean flow shows, for the positive case, a very zonal flow over the U.S. and for the negative case a high amplitude wave pattern with a strong North American east coast jet and extensive Pacific trough. This EOF also bears some resemblance to the Pacific/North American pattern.

A comparison with the occurrences of blocking in the Pacific and Atlantic as determined by Hartmann and Ghan, 1980 suggests that the fourth and ninth EOFs are related to Pacific and Atlantic blocking, respectively. The fourth EOF is primarily associated with zonal wave numbers 1 and 3 and has a large anomaly in the polar regions extending southward over the west coast of North America, Greenland and Asia. The spectral decomposition and spatial pattern

for EOF nine is shown in Figs. 1a and 1b, respectively. This mode has a large anomaly in the eastern North Atlantic with an anomaly os opposite sign to the south. It is dominated by zonal wave numbers 2 and 3 and a meridional scale corresponding to approximately 1.5 wavelengths between the equator and North Pole. Here n-m is is the number of zeros the spherical harmonic has between the poles.

3. MODELING

The equivalent barotropic model is formulated as a prognostic equation for the anomaly streamfunction PCs at the 500 mb level. The unknown constants involved in the boundary layer parameterizations are determined by regression methods. The seasonal cycle enters into the anomaly equations via the advective terms and a san additional source term due to the fact that the mean terms do not by themselves satisfy the vorticity equation.

The barotropic stability of the zonally varying winter mean flow may be tested with respect to perturbations composed of the EOF patterns. For this analysis, one PC is allowed into the model at a time to determine whether such a perturbation will grow or decay by gaining or losing energy from the mean state.

Fig. 2 shows the growth rates for the first 25 PCs without a dissipative term in the model. These results suggest that, except for the 8th PC, all the statistically significant modes have the potential to grow via kinetic energy transfers from the mean flow. The second and third PCs are the most unstable having e-folding times of a little more than two weeks. An analysis of the 500 mb winter mean flow shows that the zonally averaged state is barotropically stable. Thus the zonally asymmetric components of the mean state which account for less than 16% of the mean flow kinetic energy and are composed primarily of zonal wave numbers 1, 2 and 3 are key factors influencing the stability of the EOF patterns.

A more complete normal mode analysis shows that with 40 PCs the fastest growing mode is also fixed in space and is composed primarily of EOFs 2, 4 and 12. However, it should be noted that there is in general a strong sensitivity of the growth rates and period of the normal modes to the level of EOF truncation. These results are qualitatively very similar to the results obtained for the climatological mean January 300 mb flow by Simmons et al., 1982, in their study of barotropic wave propagation and instability. They found the fastest growing mode to have a period of about 50 days and an e-folding time of about one week. By varying the base state they also obtained some modes with infinite period.

The nonlinear model is analyzed in the context of steady state solutions employing a high degree of EOF truncation. The EOF interaction coefficients are linear combinations of the usual spectral interaction coefficients. An examination of these coefficients shows that by far, the strongest interactions involve the 9th EOF.

Multiple equilibria are found for severe truncations (less than eight modes) without including orography in the model. In this case, the advection of the winter mean flow vorticity by the anomalies plays the role of an orographic type

term. This term was found to dominate the topographic effects at the 500 mb level.

4. CONCLUSIONS

A statistical and observational analysis of the EOFs computed from a ten-year winter data set has shown that as many as the first 12 patterns may be associated with physically significant modes of variability. The first three EOFs show some relationships to index cycles and/or some of the teleconnection patterns discussed recently by Wallace and Gutzler, 1981. The fourth EOF is related to North Pacific blocking and the ninth bears a striking resemblance to the classical North Atlantic block. Details of the EOF patterns must, however, be viewed with some caution since the limited extent of the data set allows only a marginal resolution of the "true" climatological variances and covariances.

The linear normal mode analysis of the EOF model shows that all of the statistically significant EOFs except for the 8th have the potential to grow at the expense of the mean flow. This supports the recent work by Simmons et al., 1982, which also suggested that a major source of the observed variability of the large scale extratropical winter time circulation is derived through barotropic instability of the zonally varying mean flow.

Multiple equilibria have been obtained for highly truncated versions of the EOF model in which orographic effects are neglected. In these cases, the advection of mean flow vorticity plays the role of an orographic type term. An examination of the EOF interactions shows that the dominant interactions involve the North Atlantic blocking mode (EOF 9).

REFERENCES

Hartmann, D., and S. Ghan, 1980: A statistical study of the dynamics of blocking. Mon. Wea. Rev., 108, 1144-1159.

Preisendorfer, R. W., F. W. Zwiers and T. P. Barnett, 1981: Foundations of principal component selection rules. SIO Reference Series #S1-4, May 1981.

Simmons, A. J., J. M. Wallace, and G. W. Branstator, 1982: Barotropic wave propagation and instability, and atmospheric teleconnection patterns. Unpublished manuscript.

Wallace, J. M., and D. S. Gutzler, 1981: Teleconnections in the geopotential height field during the northern hemisphere winter. Mon. Wea. Rev., 109, 784-812.
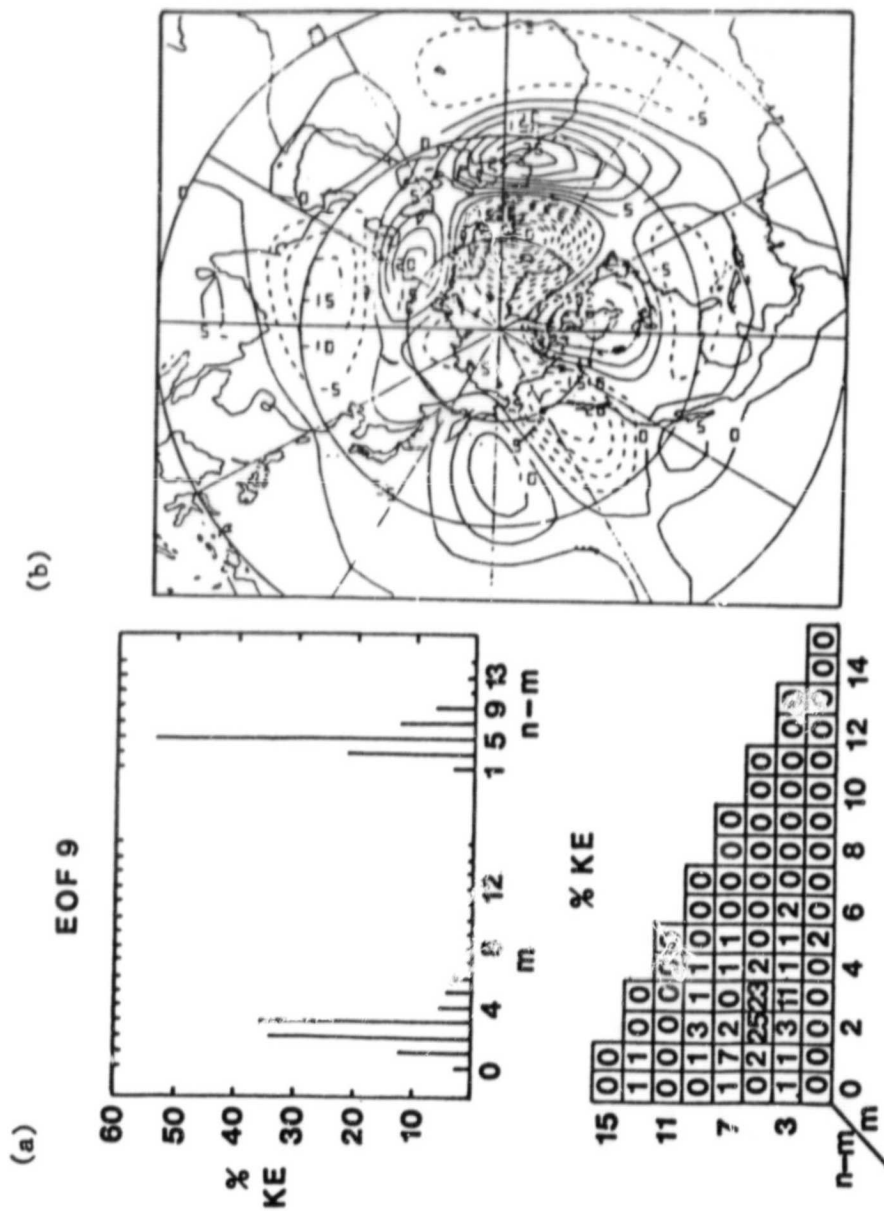
Figure 1. (a) Percent of the ninth EOF mean kinetic energy associated with each spherical harmonic where m is the zonal wave number and n is the total wave number. (b) Spatial distribution of the ninth EOF.
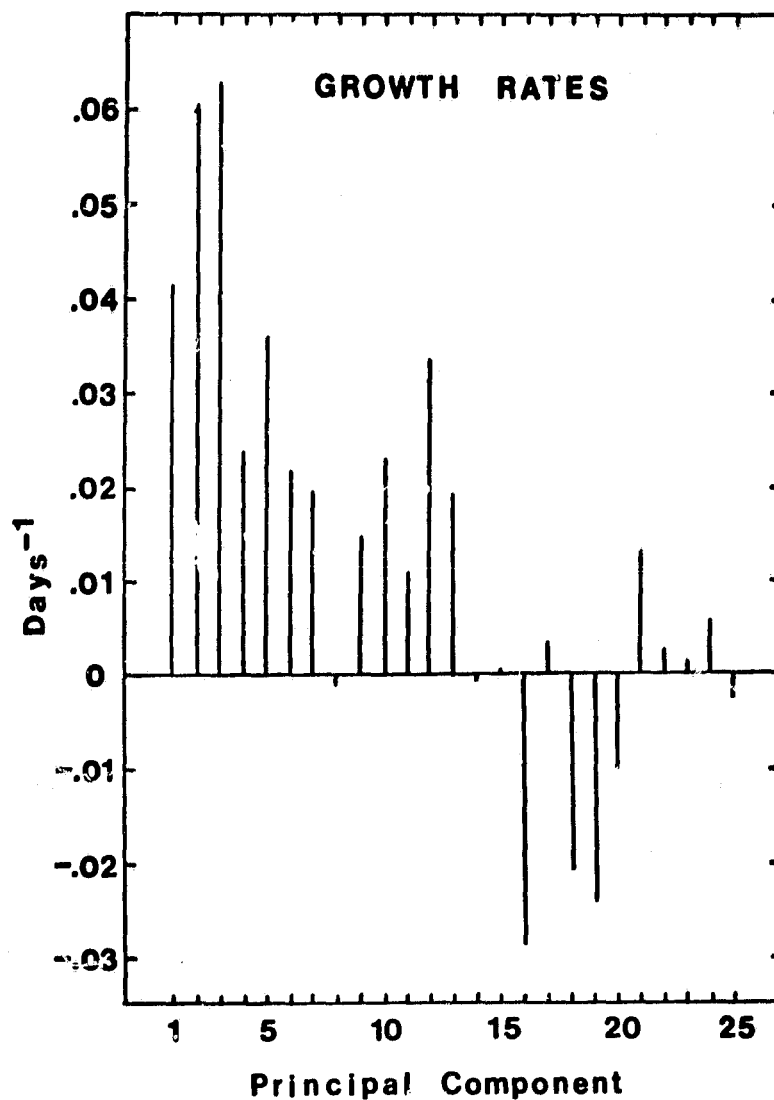
FIGURE 2. Growth rates for the first 25 principal components based on the 500 mb climatological mean winter flow for the Northern Hemisphere.

C-2

NORMAL MODES OF THE GLAS 4th ORDER MODEL

S. Bloom

1. INTRODUCTION

A recurring problem in numerical weather prediction is the initialization of primitive equation models. Recent advances in this area have involved the development of nonlinear normal mode initialization techniques (Machenauer, 1977; Temperton and Williamson, 1981; Williamson and Temperton, 1981). The computation of the normal modes of the (linearized) GLAS 4th order model is the first step in an investigation of the impact of these initialization techniques upon the full GLAS model. This note discusses some of the features of the GLAS model's normal modes.

2. GLAS MODEL MODES

a) Vertical Structure

The GLAS 4th order model equations are linearized about a basic state at rest ($\overline{u} = \overline{v} = 0$) and with an assumed average vertical temperature profile, $\overline{T}(\sigma)$, taken from the ICAO standard atmosphere. Using methods very similar to those described by Temperton and Williamson (1981), the vertical structure of the model modes is separated out. This procedure involves combining the linearized thermodynamic and hydrostatic equations in their finite differenced form. Because the vertical and horizontal structure is assumed to be uncoupled, a vertical structure problem is obtained. The solution to this vertical structure equation is an eigenvalue problem. Since the version of the model used here has nine σ levels, there are nine eigenvalues/eigenvectors, each corresponding to a particular vertical mode. When the linearized GLAS model equations are projected onto these vertical modes, they are transformed into the linear shallow water equations in spherical coordinates:

$$\frac{\partial u_\ell}{\partial t} - f v_\ell + \frac{g}{a \cos \phi} \frac{\partial h_\ell}{\partial \lambda} = 0 \tag{1a}$$

$$\frac{\partial v_\ell}{\partial t} + f u_\ell + \frac{g}{a} \frac{\partial h_\ell}{\partial \phi} = 0 \tag{1b}$$

$$\frac{\partial h_\ell}{\partial t} + \frac{D_\ell}{a \cos \phi} \left[\frac{\partial u_\ell}{\partial \lambda} + \frac{\partial}{\partial \phi} (V_\ell \cos \phi) \right] = 0 \tag{1c}$$

Here D_ℓ is the ℓth eigenvalue and (u_ℓ, v_ℓ, h_ℓ) are the variables associated with the ℓth vertical mode. Note, D_ℓ is often referred to as an "equivalent depth".

99

b) <u>Horizontal Structure</u>

Following Temperton (1977) and Dickinson and Williamson (1972), the fields are expanded in zonal Fourier harmonics, and scaled:

$$
\begin{pmatrix} u_\ell \\ v_\ell \\ h_\ell \end{pmatrix} = \begin{pmatrix} u^* \\ iv^* \\ \frac{D_\ell}{g}^{1/2} h^* \end{pmatrix} e^{is\lambda}
$$

so that eq. (1) can be written for each latitude ϕ_j:

$$(-i) \cos \phi_j \frac{\partial u^*}{\partial t}_j \quad - f_j \cos \phi_j v_j^* + \frac{S'C_\ell}{a} h_j^* = 0 \tag{2a}$$

$$(-i) \cos \phi_j \frac{\partial v^*}{\partial t}_j \quad - f_j \cos \phi_j u_j^* - \frac{C_\ell}{a} \cos \phi_j \left(\frac{\partial h^*}{\partial \phi}\right)_j = 0 \tag{2b}$$

$$(-i) \cos \phi_j \frac{\partial h^*}{\partial t}_j \quad + \frac{S'C_\ell}{a} u_j^* + \frac{C_\ell}{a} \frac{\partial}{\partial \phi} (v^* \cos \phi)_j = 0 \tag{2c}$$

with $C_\ell \equiv (gD_\ell)^{1/2}$ and $S' \equiv \frac{\sin(S\Delta\lambda)}{3\Delta\lambda} \left[4 - \cos(S\Delta\lambda)\right]$. Note, S' is the result of 4th order differencing in λ. If the modes have a harmonic time dependance (i.e., $e^{i\nu t}$), then for a sufficiently small Δt: $(-i)\frac{\partial}{\partial t} (\ )_j = -\nu (\ )_j$.

With the use of 4th order differencing in ϕ, eq. (2) can be expressed as a matrix eigenvalue problem:

$$\underset{\sim}{L}\, \underset{\sim}{u} - \nu\, \underset{\sim}{u} = 0 \tag{3}$$

where

$$
u_j = \begin{pmatrix} u_j^* \\ v_j^* \\ h_j^* \end{pmatrix} * (\cos \phi_j)^{1/2}
$$

and the matrix of coefficients $\underset{\sim}{L}$ is real and symmetric. Thus for a given zonal wavenumber s, the eignevectors of $\underset{\sim}{L}$ give the latitudinal structure of the horizontal modes (which have eigenfrequencies ν).

c) Degrees of Freedom - Influence of Poles

The number N of eigenvectors and eigenvalues in eq. (3) reflects the number of degrees of freedom in the GLAS model for a given zonal wavenumber. Since the horizontal modes can be divided into two classes (symmetric or antisymmetric across the equator), they need to be computed only in one hemisphere, 23 latitude points in a model with a meridional spacing of 4°. Eq. (2) suggests that N = 69, but consistency requirements at the pole reduce N:

$$S = 0 \; ; \quad u^*_{pole} = v^*_{pole} = 0 \text{ and } h^*_{pole} \neq 0 \qquad\qquad (N = 67)$$

$$S = 1 \; ; \quad h^*_{pole} = 0 \text{ and } u^*_{pole} = \pm\, v^*_{pole} \neq 0 \qquad\qquad (N = 68)$$

$$(+ \text{ North}, - \text{ South})$$

$$S \geq 2 \; ; \quad u^*_{pole} = v^*_{pole} = h^*_{pole} = 0 \qquad\qquad (N = 66)$$

A problem arises with the S = 1 modes, due to the use of centered differencing on a nonstaggered grid in the GLAS model. This can be seen by comparing the roles of h* and v* in eq. (2); where eq. (2b) relates v^*_{pole} to $h^*_{86°}$ and $h^*_{82°}$, but v^*_{pole} does not influence $h^*_{86°}$ or $h^*_{82°}$ in eq. (2c). Thus the matrix $\underset{\sim}{L}$ is not symmetric for S = 1. The degrees of freedom at the pole are represented by inertial oscillations (one physical, one computational) which are completely decoupled from the remaining modes.

3. COMPARISON OF GLAS MODES WITH HOUGH MODES

Longuet-Higgins (1968) and Kashara (1976) discuss alternative ways to extract the horizontal structure from eq. (1) through the use of spherical harmonic expansions. The resulting horizontal modes are called Hough modes, and they represent an analytic solution to eq. (1) to which we can compare the GLAS model modes (and eigenfrequencies). Using an algorithm similar to the one used by Kasahara (1976), Hough modes with the same D_ℓ's as the GLAS modes were computed. Both the GLAS and the Hough modes can be labeled by the number of their latitudinal nodes; i.e. a "low" mode has little structure, while a "high" mode has many oscillations. What follows are some preliminary results of the comparisons between GLAS and Hough modes.

(i) The GLAS modes consist of two types: physical and computational. The computational modes are an artifact of the finite differencing approximations and they do not represent true solutions to eq. (1). There should be roughly the same number of computational and physical modes, although identifying the higher physical GLAS modes becomes increasingly more difficult as their structure increases.

(ii) For low wavenumbers and the lowest modes, there is excellent agreement between the eigenfrequencies of the Hough and GLAS modes. The agreement deteriorates as one compares the eigenfrequencies of progressively higher modes.

(iii) An examination of the polar and near-polar structure of the lowest modes for S = 0, 1 and 2 shows the nature of the GLAS model's (linear) treatment of the pole. The best correspondance between Hough modes and GLAS modes near the pole occurs for S = 2, because no polar approximation is required for the computation of the GLAS modes for zonal wavenumbers greater than one. The greatest discrepancies near the pole occur for S = 1; this is consistent with the model's difficulty in handling the polar wind. There is much better · agreement between GLAS and Hough modes near the equator for S = 1. Finally for S = 0, the agreement near the pole lies in between those for S = 2 and S = 1. This occurs because an approximate equation for h^*_{pole} is obtained by performing polar-cap averages of eq. (2c); this approximation somewhat degrades the GLAS modes near the pole for S = 0.

4. SUMMARY

A set of normal modes for the 4th order GLAS model has been computed and compared with a corresponding set of Hough modes. The agreement between the lower GLAS (physical) and Hough modes is a useful check on the accuracy of the GLAS mode computation. Future work with the GLAS modes will involve: the diagnosis of data, linear initialization experiments, and the development of a nonlinear normal mode initialization process for the full GLAS 4th order model.

REFERENCES

Dickinson, R. E., and D. L. Williamson, 1972: Free Oscillations of a Discrete Stratified Fluid with Application to Numerical Weather Prediction. J. Atmos. Sci., 29, 623-640.

Kasahara, A., 1976: Normal Modes of Ultralong Waves in the Atmosphere. Mon. Wea. Rev., 104, 669-690.

Longuet-Higgins, M. S., 1968: The Eigenfunctions of Laplace's Tidal Equations over a Sphere. Phil. Trans. Roy. Soc. London, A262, 511-607.

Machenhauer, B., 1977: On the Dynamics of Gravity Oscillations in a Shallow Water Model, with Application to Normal Mode Initialization. Contrib. Atmos. Phys., 50, 253-271.

Temperton, C., 1977: Normal Modes of a Barotropic Version of the ECMWF Grid Point Model. ECMWF Int. Rept. No. 12, 38 pp.

Temperton, C., and D. L. Williamson, 1981: Normal Mode Initialization for a Multilevel Grid-Point Mode. Part I: Linear Aspects. Mon. Wea. Rev., 109, 729-743.

Williamson, D. L., and C. Temperton, 1981: Normal Mode Initialization for a
    Multilevel Grid-Point Model. Part II: Nonlinear Aspects. <u>Mon. Wea. Rev.</u>,
    <u>109</u>, 744-757.

LAGGED AVERAGE FORECASTING, AN ALTERNATIVE TO MONTE CARLO FORECASTING

R. N. Hoffman and E. Kalnay

In order to use the information present in past observations and simultaneously to take advantage of the benefits of stochastic dynamic prediction we formulate the lagged average forecast (LAF) method. In a LAF, just as in a Monte Carlo forecast (MCF), sample statistics are calculated from an ensemble of forecasts. Each LAF ensemble member is an ordinary dynamical forecast (ODF) started from the initial conditions observed at a time lagging the start of the forecast period by a different amount. These forecasts are averaged at their proper verification times to obtain a LAF. The LAF method is operationally feasible since the LAF ensemble members are produced during the normal operational cycle.

To test the LAF method, we use a two layer, f-plane, highly truncated spectral model, forced by asymmetric Newtonian heating of the lower layer. In the experiments a long run is generated by the primitive equation version of the model which is taken to represent nature, while forecasts are made by the quasigeostrophic version of the model. On the basis of forecast skill the LAF and MCF are superior to the ODF; this occurs principally because ensemble averaging hedges the LAF and MCF toward the climate mean. The LAF, MCF and ODF are all improved when tempered by a simple regression filter; this procedure yields different weights for the different members of the LAF ensemble. The tempered LAF is the most skillful of the forecast methods tested. The LAF and MCF can provide a priori estimates of forecast skill because there is a strong correlation between the dispersion of the ensemble and the loss of predictability. In this way the time at which individual forecasts lose their skill can be predicted (Fig. 1). This is not easy since the skill of individual forecasts, as measured by D, an RMS measure of forecast skill, breaks down suddenly anywhere from four to twenty days into the forecast (Fig. 2).

These results and the application of the LAF method to more realistic models and to monthly or seasonally averaged forecasts are discussed elsewhere in more detail (Hoffman and Kalnay, 1983).

REFERENCES

Hoffman, R. N. and E. Kalnay, 1983: Lagged averaged forecasting, an alternative to Monte forecasting. Tellus, in press.
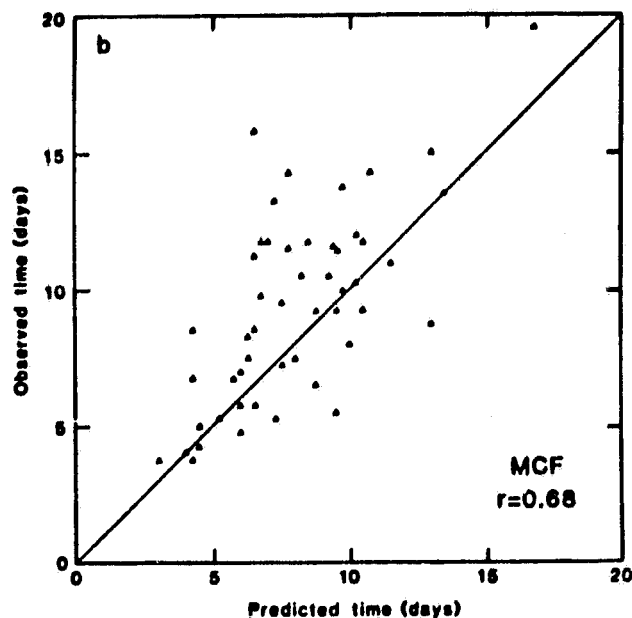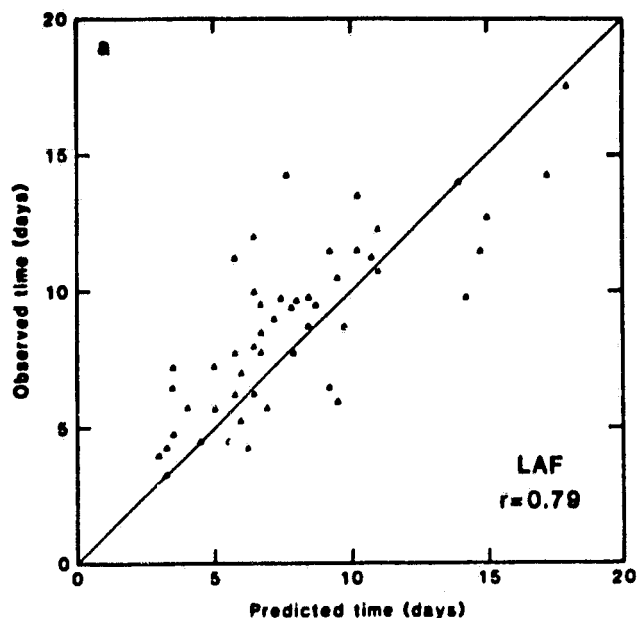
Fig. 1. Scatter plots of predicted versus observed time for $\tilde{D}$ to reach a value of 0.5 for the LAF (a) and the MCF (b). $\tilde{D}$ is the ensemble rms value of D.
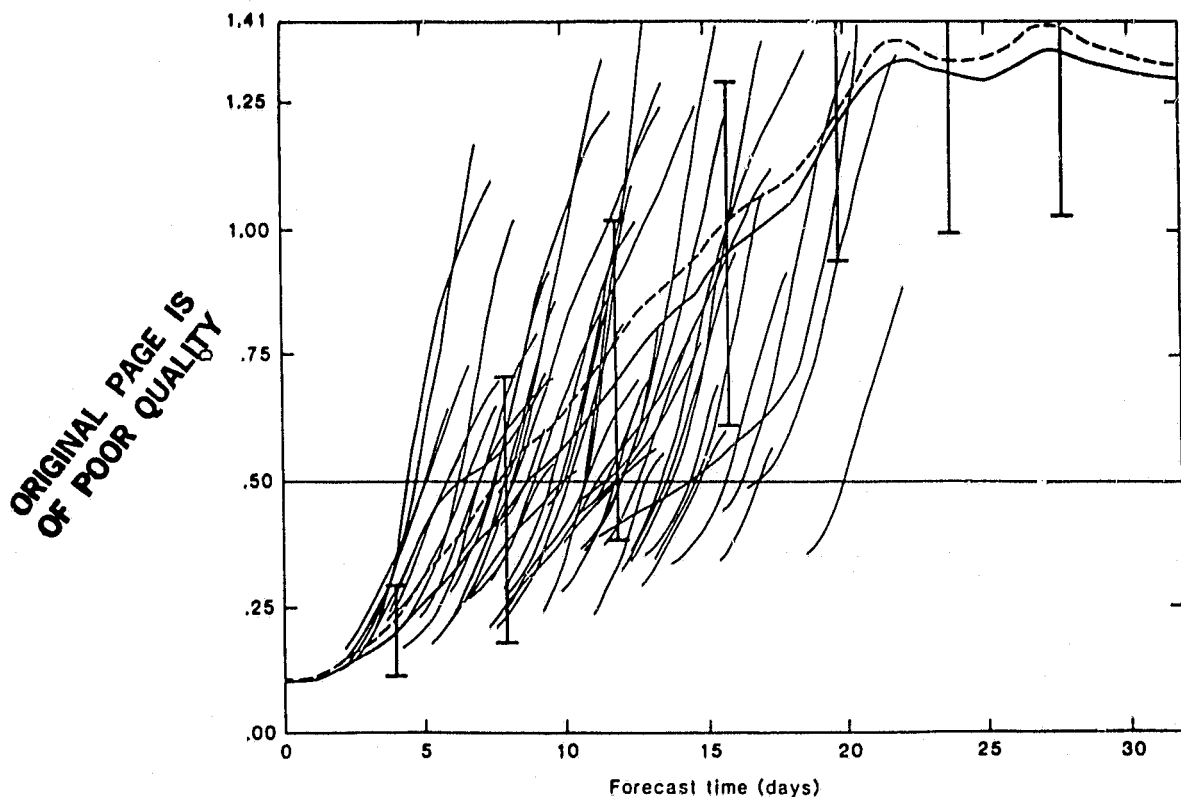
Fig. 2. Time evolution of D for the ODF experiments. Shown are selected portions of the evolution of D for each case (light ———). These curves have been smoothed to eliminate the roughness caused by the white noise observing error. Also shown are $\langle D^2 \rangle^{1/2}$ (— — —) and $\langle D \rangle$ (heavy ———). Error bars are calculated as $(\langle D^2 \rangle - \langle D \rangle^2)^{1/2}$.

A STOCHASTIC-DYNAMIC MODEL FOR THE SPATIAL STRUCTURE OF FORECAST ERROR STATISTICS

R. Balgovind, A. Dalcher, M. Ghil and E. Kalnay

A simple model that yields the spatial correlation structure of global atmospheric mass-field forecast errors is derived. The model states that the relative potential vorticity of the forecast error is forced by spatially multi-dimensional white noise. The forecast error equation contains a non-dimensional parameter c_0 which depends on the Rossby radius of deformation. From this stochastic-dynamic equation, a deterministic equation for the spatial covariance function of the 500 mb geopotential error field is obtained.

Three methods of solution are examined: 1) an analytic method based on spherical harmonics, 2) a numerical method based on stratified sampling of Monte-Carlo realizations of the stochastic-dynamic equation, and 3) a combined analytic-numerical method based on two successive applications of a fast Possion solver to the deterministic covariance equation. The three methods are compared for accuracy and efficiency, and the third, the combined method is found to be clearly superior.

The model's covariance function is compared with global correlation data of forecast-minus-observed geopotential fields for the DST-6 period February-March 1976. The data are based on the GLAS forecast-assimilation system in use at that time (Ghil et al., 1979).

The model correlations agree well with the latitude dependence of the data correlations. The fit between model and data confirms that the forecast error between 24h and 36h is largely random, rather than systematic; the value of the parameter c_0 which gives the best fit suggests that much of this error can be attributed to baroclinic, rather than barotropic effects. Deterministic influences not included in the model appear at 12h and 48h. They suggest possibilities of improving the forecast system by a better objective analysis and initialization procedure, and a better treatment of planetary-wave propagation, respectively.

An analytic formula is obtained which approximates well locally the model's global correlations. This formula is convenient to use in the calculation of weighting coefficients for analysis and assimilation schemes. It shows that Gaussian functions are a poor approximation for the forecast error correlations of the mass field. The first and second derivatives of the Gaussian functions, commonly used to model geostrophic wind error correlations, are shown to be even less accurate.
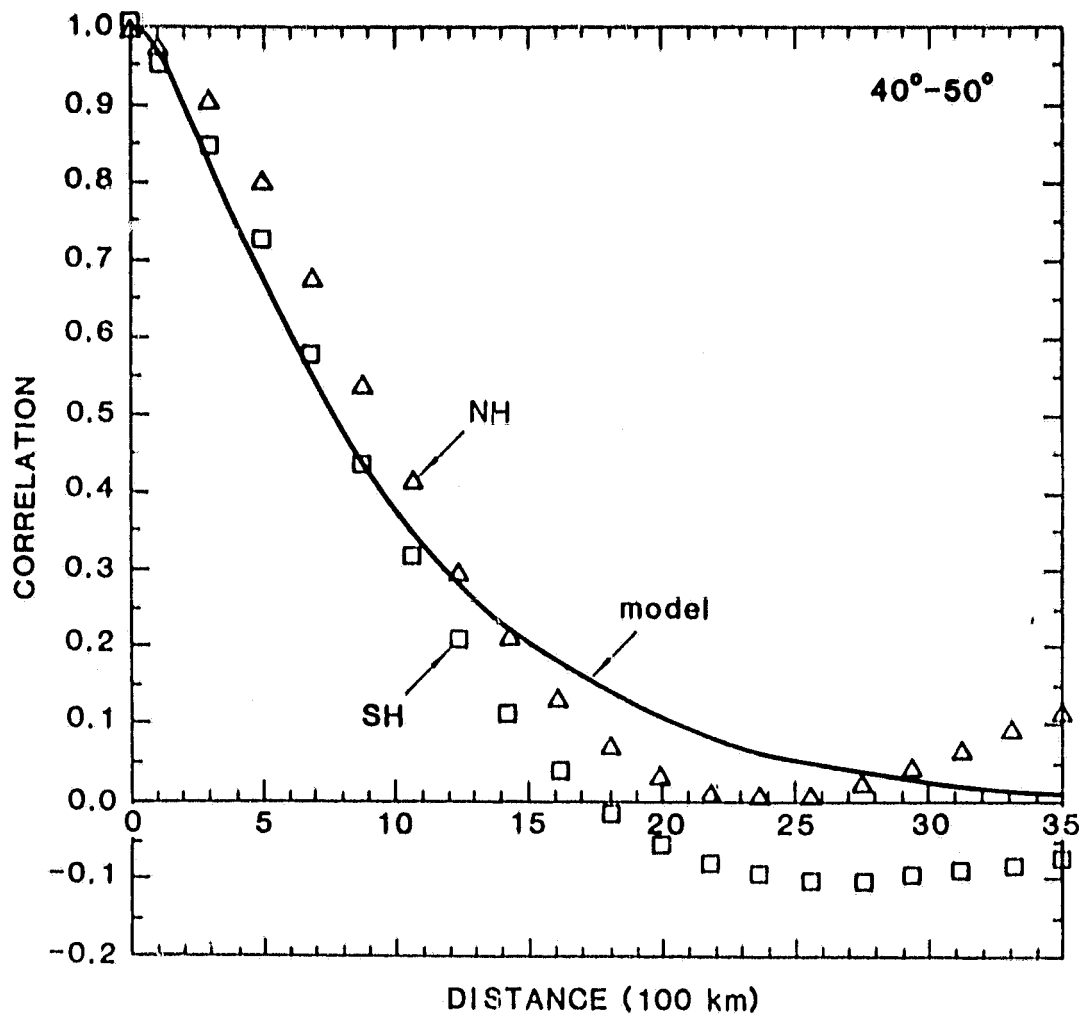
Figure 1. Comparison of model correlations with the data correlations obtained when using 48h GLAS forecasts and the corresponding NMC analyses. Model results have $c^0 = 190$; for this value of c_0, the results were almost indistinguishable from those with $c_0 = 230$.
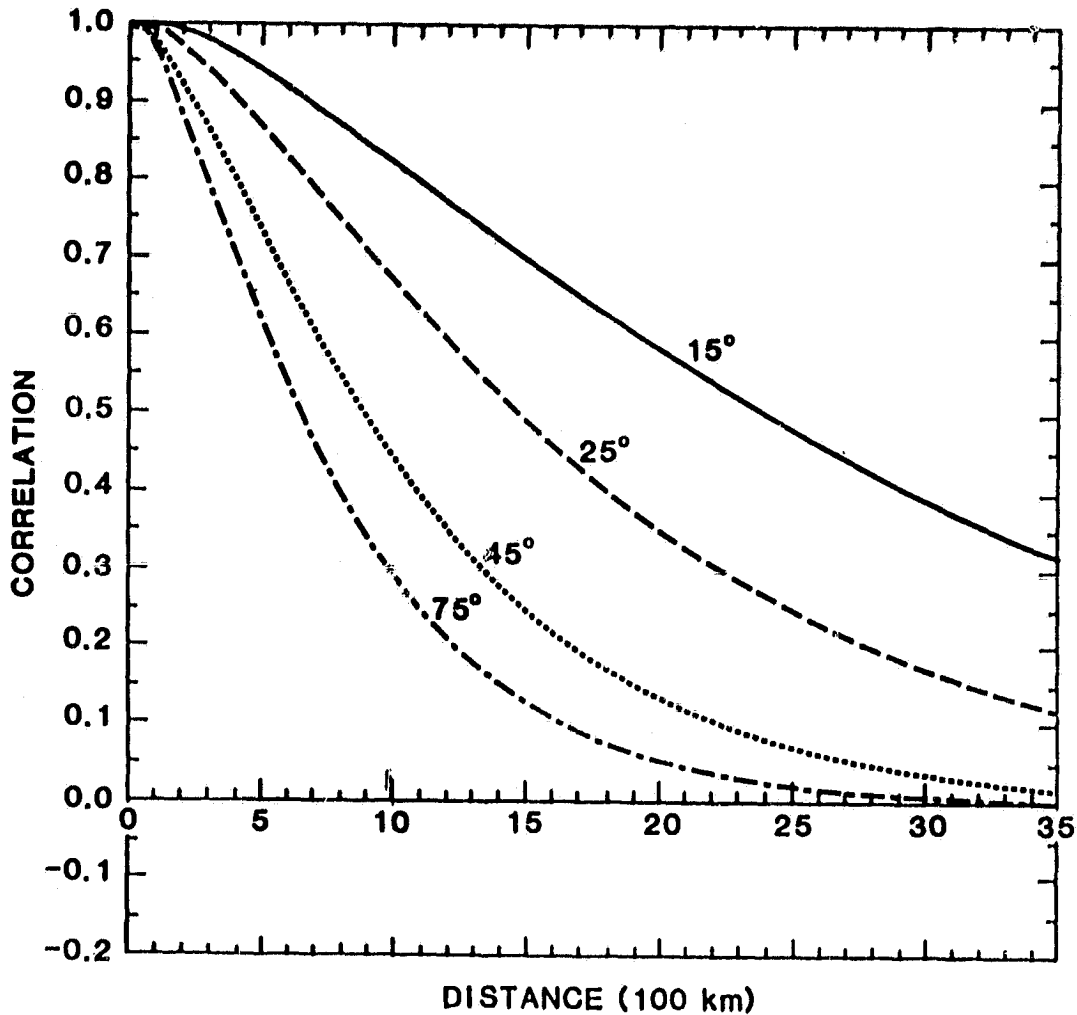
Figure 2a. Analytic approximation of global model correlations. Fig. 2a shows the shape of the Bessel-function correlations derived in this paper for different values of $\alpha = \alpha(\theta)$.
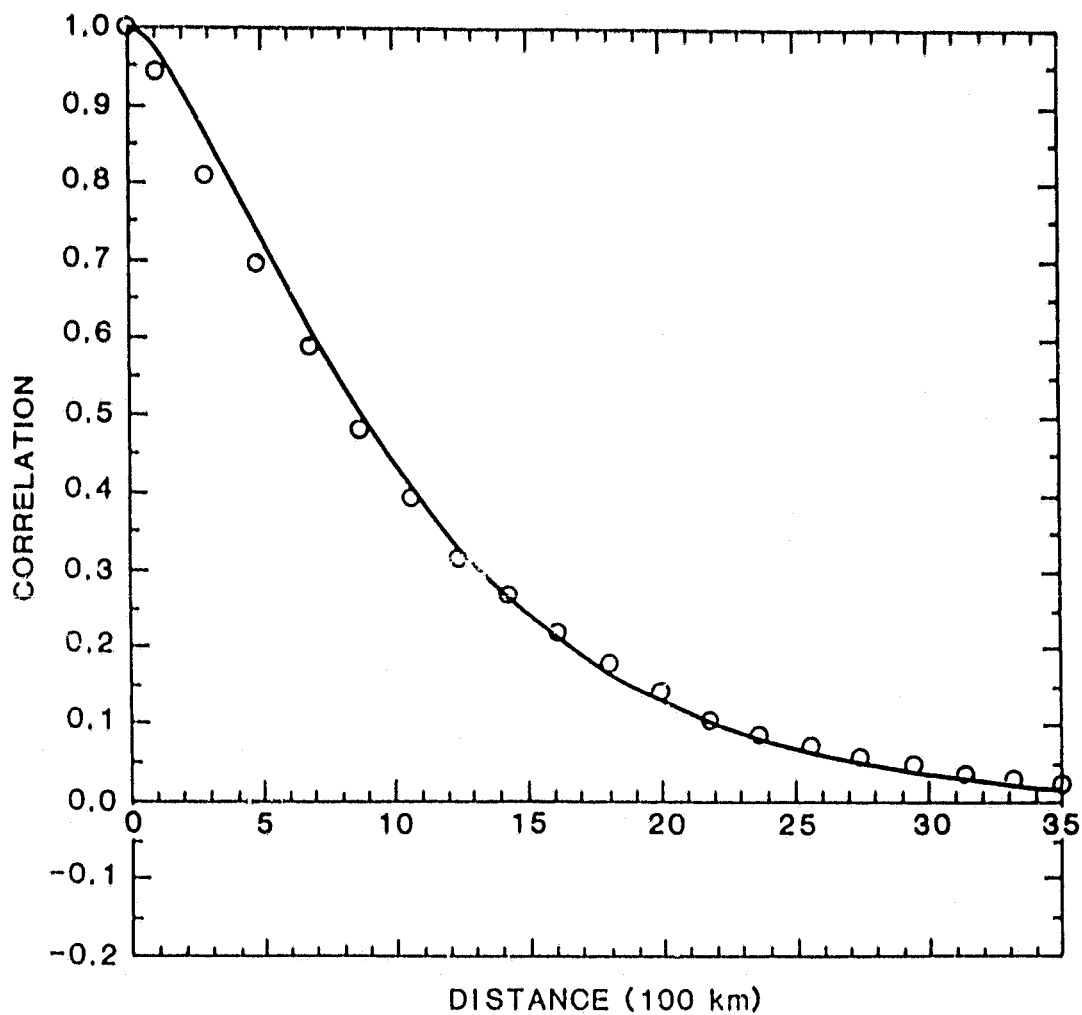
Figure 2b. Analytic approximation of global model correlations. Figure 2b compares the analytic, approximate correlation at latitude θ = 45° with the numerically computed global correlation averaged over the 40-50° latitude belt.
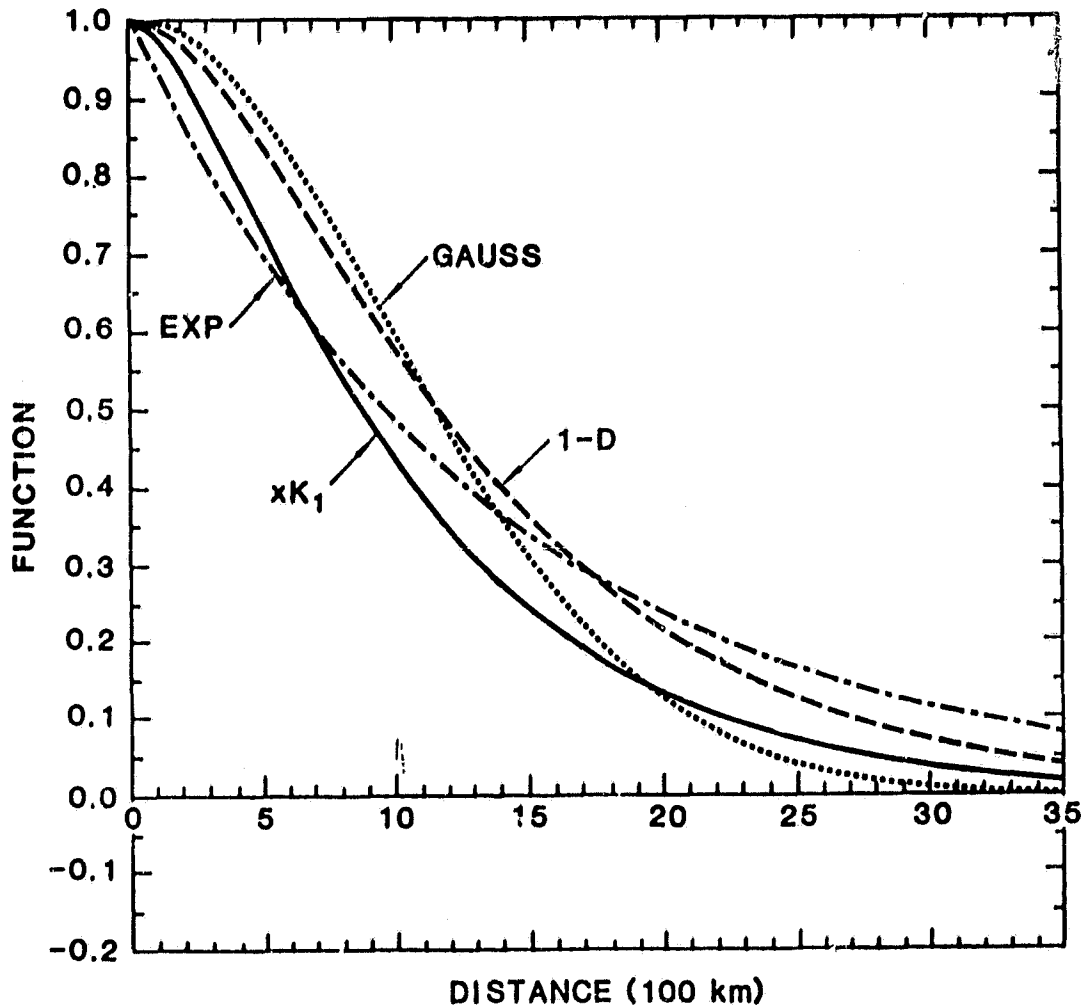
Figure 3. Comparison between analytic formulae used to approximate forecast
error correlations. The four functions compared are the Gaussian,
currently used in OI (marked Gauss in the figure), the Bessel func-
tion of Figure 2 (marked xK_1), the exponential (exp), and the one-
dimensional formula of the analytic model (1-D). Figure 3a shows
the functions themselves, Figure 3b their first derivatives, and
Figure 3c the second derivatives. According to the geostrophic
assumtpion of operational OI, if either curve in Figure 3a were
used for (ϕ-ϕ) correlations, Figure 3b would give the corresponding
(ϕ-v) correlations, and Figure 3c the (v-v) correlations, up to
a multiplicative factor. Notice large differences between the
curves in Figure 3b, c.
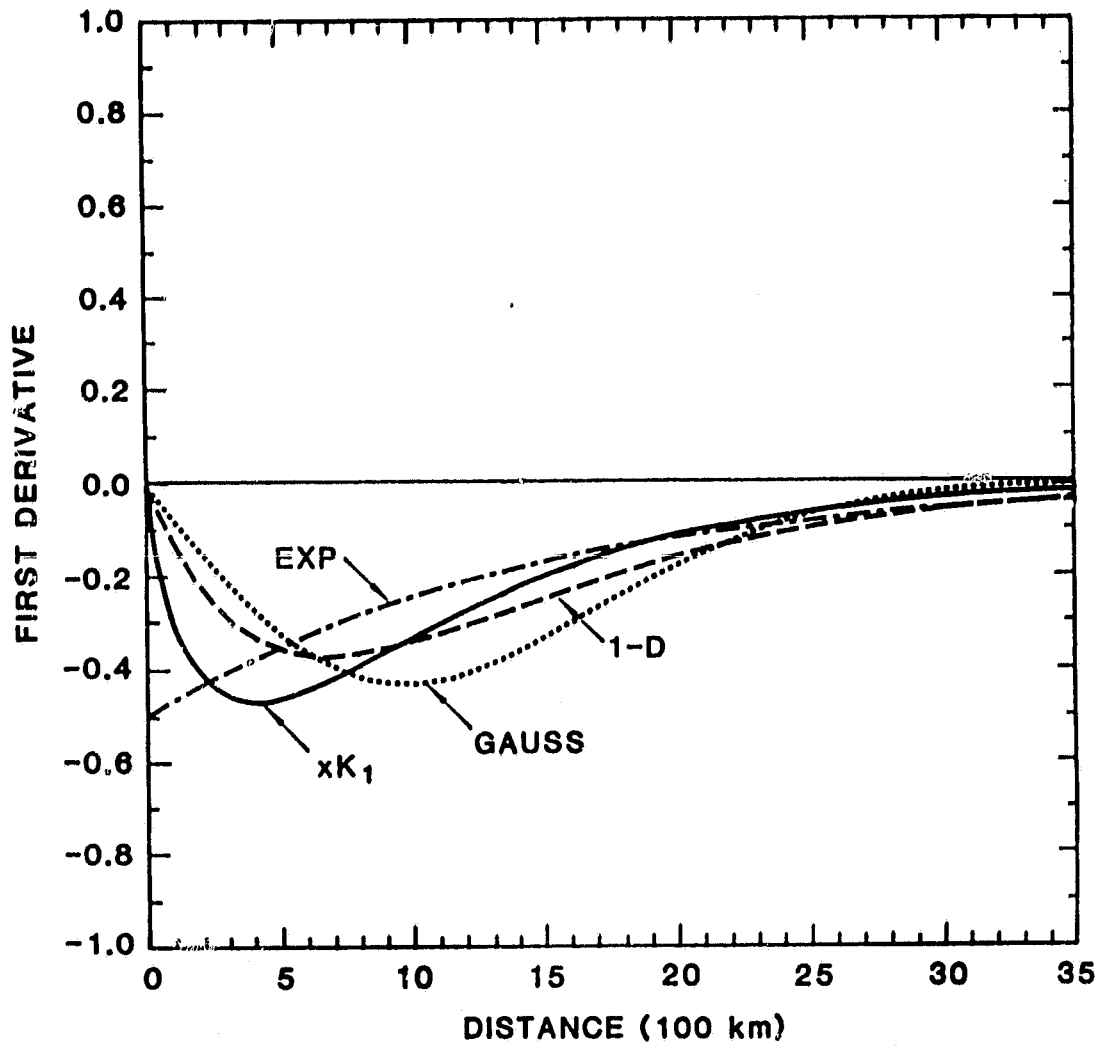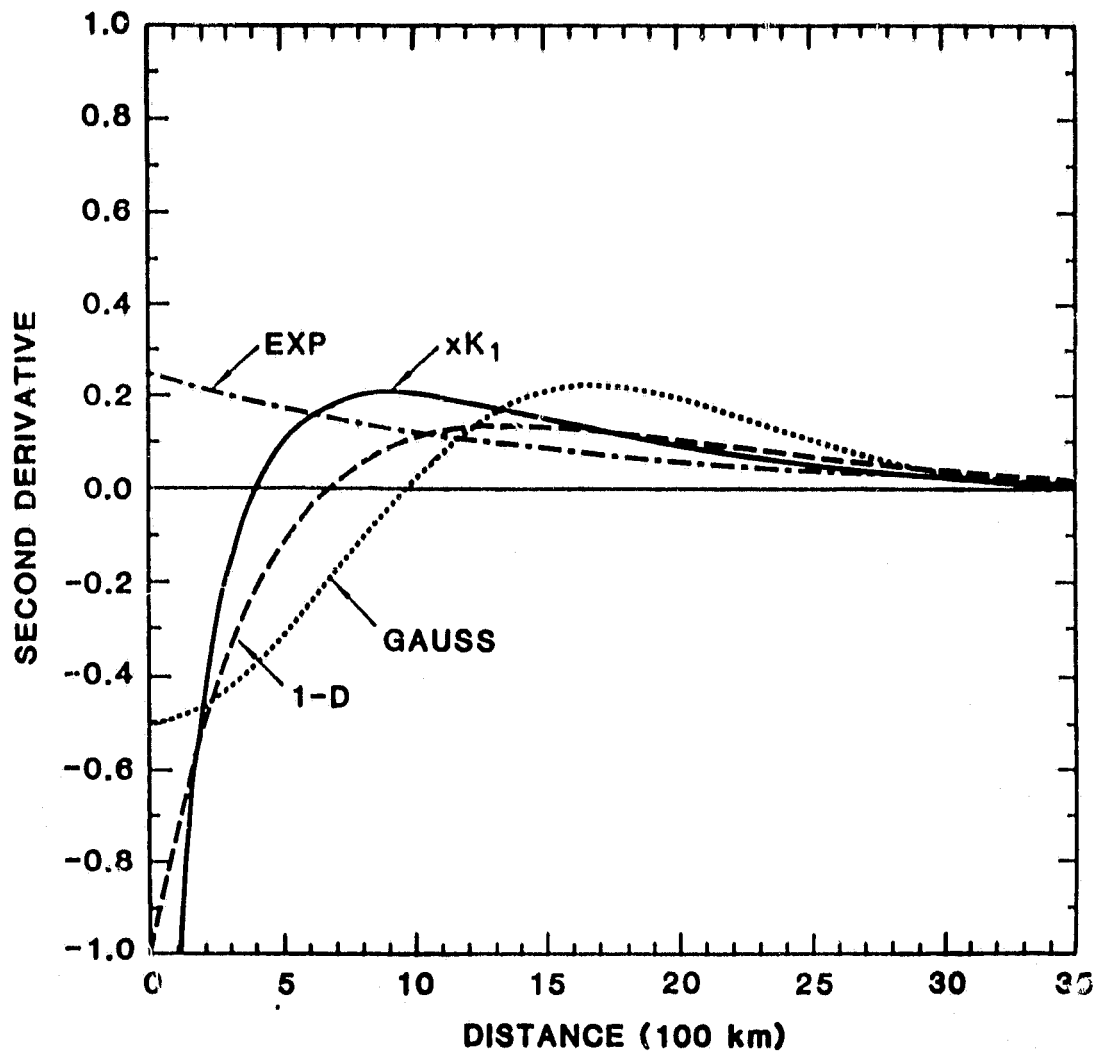
Figure 3b

Figure 3c

HIGH LATITUDE FILTERING IN GLOBAL GRID POINT MODELS

L. L. Takacs and R. C. Balgovind

1. INTRODUCTION

The process of filtering in global grid point models is fairly common in meteorological studies. High latitude filtering as described in Gates et al. (1971) is done in order to avoid the use of prohibitively short time steps required due to fast moving inertia-gravity waves near the poles. By applying filtering to certain quantities in the governing equations, the use of larger time-steps to run the model may be obtained. The specific filtering response needed to ensure stability is defined by the space and time difference schemes used, and by the type of grid structure in the model (Arakawa and Lamb, 1977).

We have found that when certain techniques are used in the application of the high-latitude filter, serious distortions of the solution occur at all latitudes, associated with spurious energy and momentum transfers. These errors are a result of the inability of the specific filtering technique used to maintain in finite-difference form the irrotationality of the gradients of the streamfunction and velocity potential.

In this paper we re-examine the effects of the distortions caused by filtering, and study its relationahip to various filtering techniques. In Section 2, a description of the model used for this study is presented, while Section 3 compares model results. Conclusions are presented in Section 4.

2. MODEL DESCRIPTION

The model used to examine the effects of filtering is based on the shallow water equations on a sphere. All variables are defined on a non-staggered 'A' grid (Arakawa, 1972) having a resolution of 10 degrees in longitude and 8.18 degrees in latitude. Spatial derivatives are approximated by energetically-conservative fourth-order differences (Kalnay-Rivas et al., 1977), while the time derivatives are approximated by the leapfrog scheme.

As the initial condition for these experiments, we followed Phillips (1959) by taking an initially non-divergent velocity field together with a height field that satisfied the balance equation, (see Fig. 1). This initial condition produces a super-rotation of the atmosphere in addition to a Rossby-Haurwitz wave which moves westward relative to the fluid. For a non-divergent barotropic atmosphere, the total solution will move from west to east without change of shape. Since we are using a free upper surface, however, some changes in the solution can be expected due to the divergent nature of our model.

For our experiments, we compare the effects of four filtering techniques. The first technique, as employed by Kalnay-Rivas et al. (1977), uses Fourier filtering of the prognostic variables u, v and h at every time-step. This technique does not conserve total energy nor does it preserve the irrotational

properties of the system. Since this filter is applied to the prognostic fields themselves, the effects of the filter are cumulative in time. This technique will be referred to as technique (b) in future reference.

The second technique used for filtering is similar to the first except that the time-changes of the prognostic flux and mass fields rather than the fields themselves are filtered, i.e., $\dot{h}u$, $\dot{h}v$, and $\dot{h}$, where (˙) refers to the time-change of the quantity. Smoothing of the time derivatives to prevent linear computaional instability has been employed by Vanderman (1972) and Temperton (1977). This technique also suffers from non-conservation of the energetics and irrotationality of the system, although the effects of the filter are non-cumulative since only time-changes are smoothed. This technique will be referred to as technique (c) in future reference.

The third technique follows that of Arakawa and Lamb (1977). In this technique, the zonal pressure gradient and zonal mass flux terms are filtered in such a way that the globally integrated total energy of the system is conserved. Although this technique was originally designed for an energy and enstrophy conserving scheme on a 'C' grid, our interest here is to study its performance in relation to our fourth-order energy conserving scheme on the 'A' grid. This technique will be referred to as technique (d) in future reference.

The last technique, which will be denoted as the P.G. (for pressure gradient) filter, is one in which the vorticity of the system is conserved in finite difference form. In a personal communication, Dr. Akio Arakawa pointed out that filtering the prognostic variables, their tendencies or the zonal pressure gradient and mass flux terms may not preserve the irrotationality of the pressure gradient in finite difference form due to the latitudinal dependence of the filter response. Because of this, a computational source of vorticity is generated near the poles which ultimately affects the solution at all latitudes. By a priori filtering of the heights used in the pressure gradient terms in the momentum equations, the irrotational properties of the system are preserved and no spurious energy or momentum transfers results. This technique will be referred to as technique (e) in future reference.

3. RESULTS

Figs. 2, 3 and 4 show the time evolution of the height field at days 4, 8 and 12. In each figure, five plots are shown corresponding to the four techniques discussed in Section 2 in addition to a non-filtered control run. The non-filtered control run is taken to be truth in these experiments, and will be referred to as technique (a) in future reference.

We can see from these figures that all techniques perform reasonable well through the first four days of integration. By day 8, however, techniques (b) and (d) show major dissimilarities compared to techniques (a), (c) and (e). It should be noted that the control run has moved approximately 90 degrees eastward as expected, with very little change in shape. In techniques (b) and (d), the amplitude of the Rossby-Haurwitz wave has decreased considerably. Also, technique (c) shows tilting east of the trough which is not apparent in the control run nor in technique (e). Finally, by day 12, only technique (e), which conserves vorticity in finite difference form, shows success in simulating the control run.

Fig. 5 shows the time evolution of the globally integrated kinetic energy due to the eddy flow. We see from the control run that the eddy kinetic energy decreases slightly from its initial value during the 12-day run. There is also a corresponding increase in the kinetic energy due to the zonal flow (not shown) which maintains total energy conservation. Techniques (b), (c) and (d) show significant deviations from the control run which are a result of the non-conservation of vorticity inherent in those techniques. Physically, the change in vorticity near the poles generates tilting of the trough-ridge lines which result in strong equatorward transports of u-momentum at mid-latitudes. This equatorward transport triggers the barotropic instability mechanism which produces a transfer of eddy kinetic energy to zonal kinetic energy. However, it can be seen that the P.G. filter, technique (e), produces almost identical results compared with the non-filtered control run.

4. CONCLUDING REMARKS

We have seen that certain high-latitude filtering techniques create spurious energy and momentum transfers, affecting the solution at all latitudes. These spurious transfers are due to a non-conservation of vorticity under the pressure gradient force, as well as to a non-vanishing curl in finite-difference form of the gradients of the streamfunction and velocity potential. By a priori filtering of the heights used in the pressure gradient terms in the momentum equations, the irrotational properties of the system are preserved and no spurious energy or momentum transfers result. This technique has shown superior results compared with filtering prognostic field variables, their tendencies or filtering with energy-conservative techniques.

REFERENCES

Arakawa, A., 1972: Design of the UCLA general circulation model. Numerical simulation of Weather and Climate, Dept. of Meteorology, Univ. of California, Los Angeles, 90024, Tech. Rept. 7, 115 pp.

Arakawa, A., and V. B. Lamb, 1977: Computational design of the basic dynamical processes of the UCLA general circulation model. Methods In Computational Physics, 17, Academic Press, 173-255.

Gates, W. L., Batten, E. S., Kahle, A. B., and Nelson, A. B., 1971: A documentation of the Mintz-Arakawa two-level atmospheric general circulation model. Advanced Research Projects Agency Rep. B-877-ARPA, Rand Corporation, Santa Monica, CA 90024.

Kalnay-Rivas, E., A. Bayliss and J. Storch, 1977: The 4th order GISS model of the global atmosphere. Contrib. Atmos. Phys., 50, 306-311.

Phillips, N. A., 1959: Numerical integration of the primitive equations on the hemisphere. Mon. Wea. Rev., 87, 333-345.

Temperton, C., 1977: Normal noise of a barotropic version of ECMF gridpoint model. Internal Report 12, Research Dept., Eutr=ropean Centre for Medium Range Weather Forecasts. Bracknell, England, 39 pp.

Vanderman, L. W., 1972: Forecasting with a global, three layer, primitive equation model. Mon. Wea. Rev., 100, 856-868.

INITIAL CONDITION
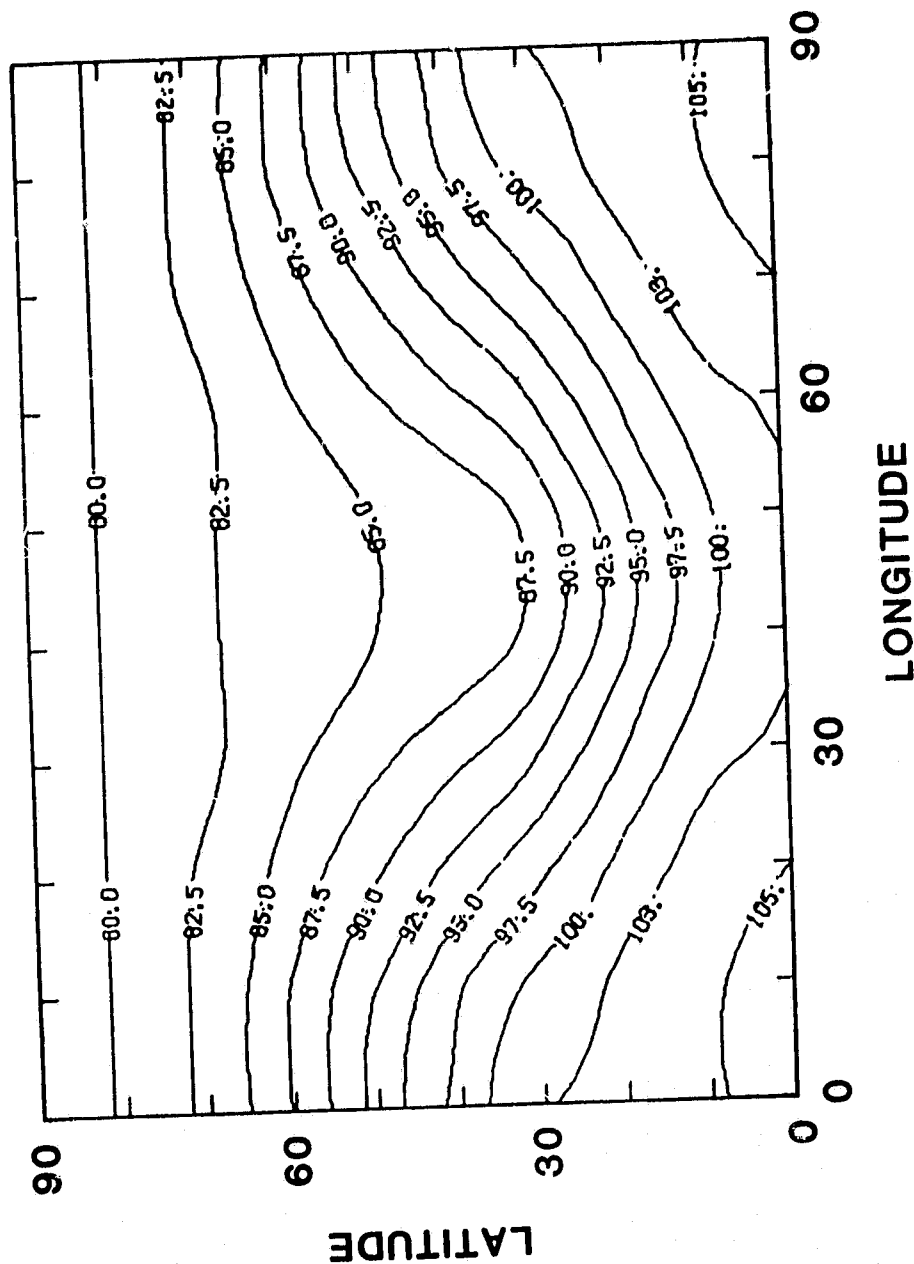
Fig. 1. Initial height field (x 100 m) over one wavelength of the Rossby-
Haurwitz wave for wavenumber 4.
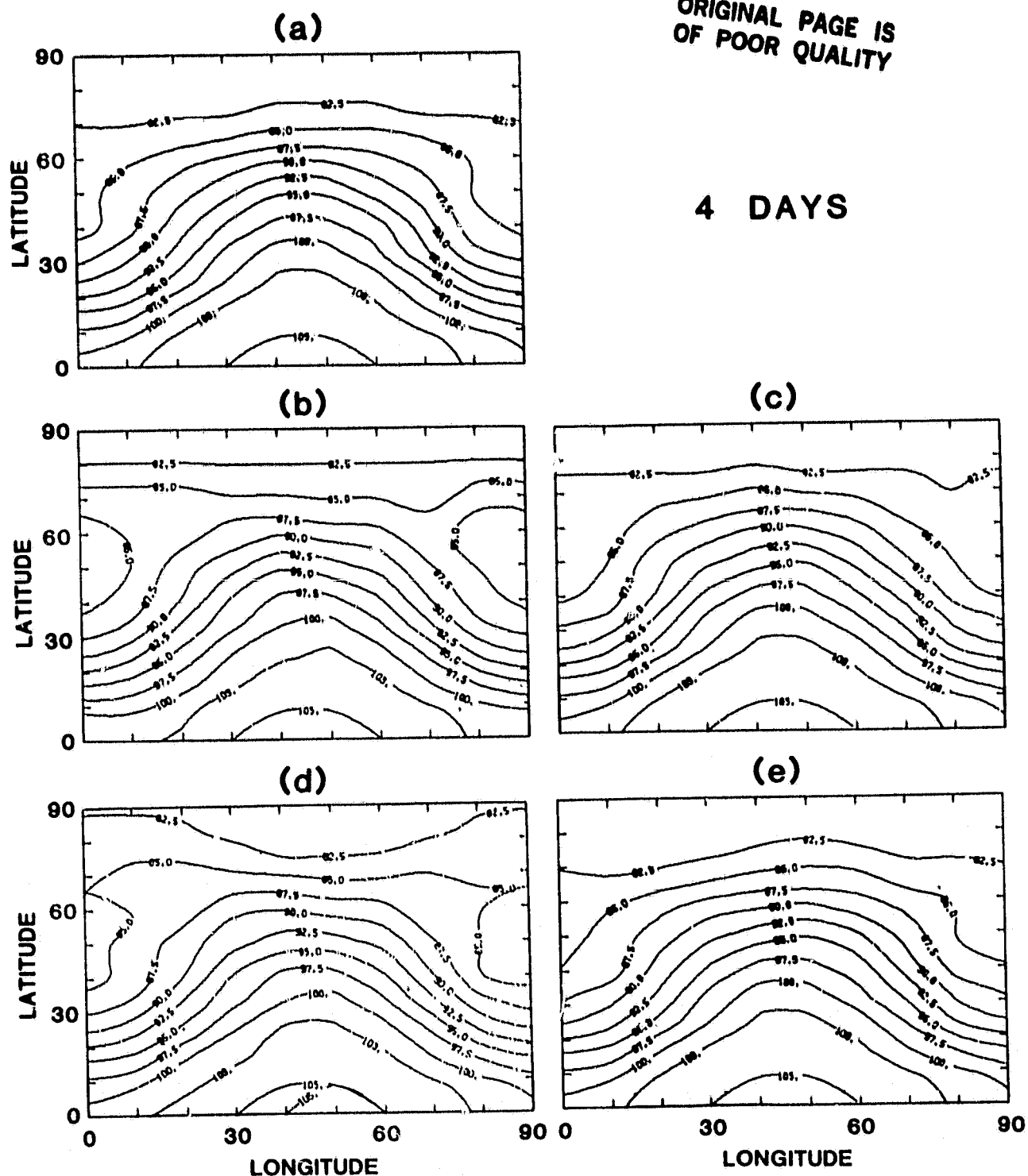
Fig. 2. Contoured height fields at day 4 using a) no filter, b) prognostic
field filter, c) tendency filter, d) energy-conserving filter, e) P.G.
filter.
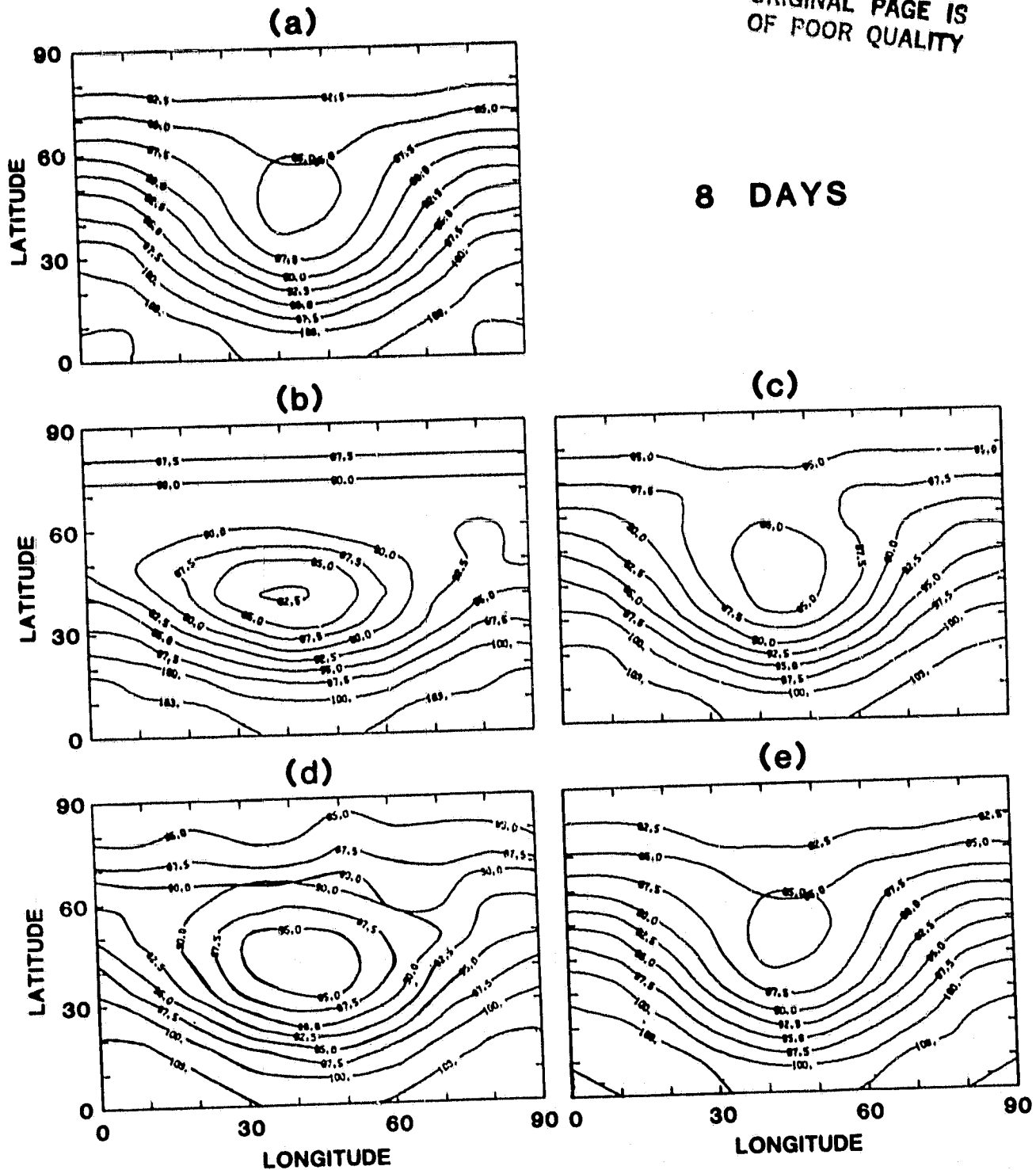
Fig. 3. As in Fig. 2 at day 8.

(a)

12 DAYS

(b)

(c)

(d)

(e)

Fig. 4.   As in Fig. 2 at day 12.

119
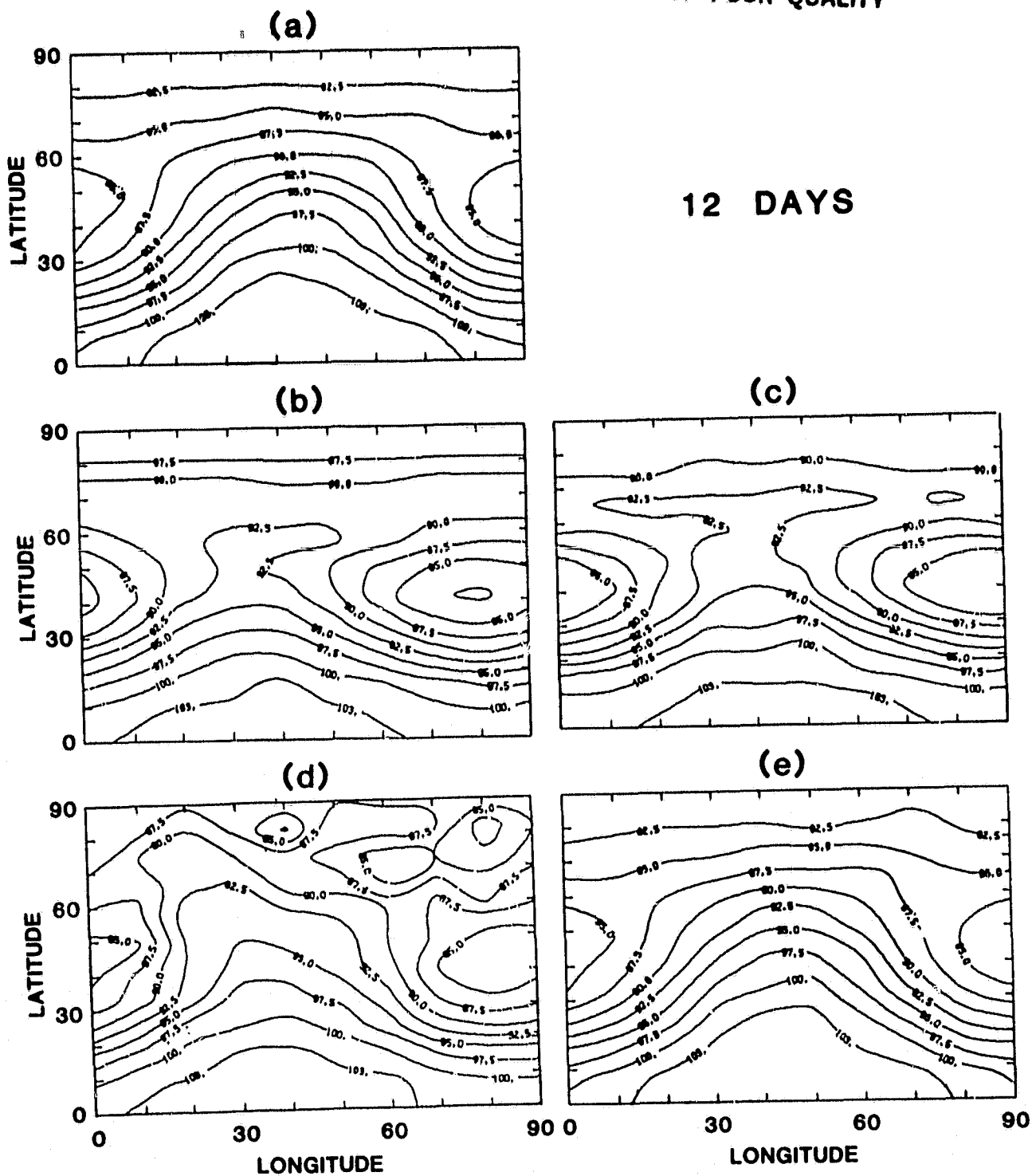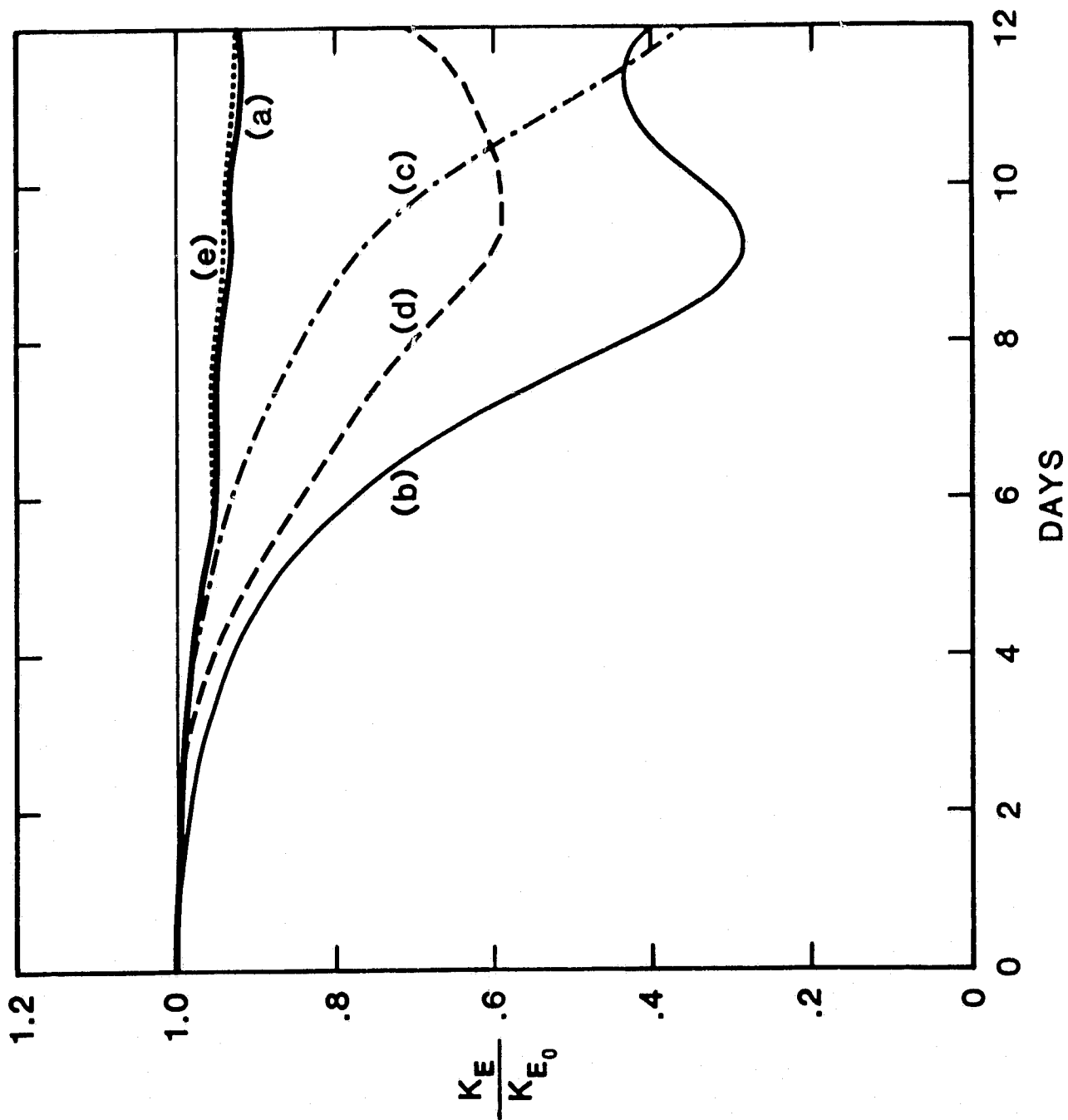
Fig. 5. Globally averaged and normalized eddy kinetic energy for the a) no filter, b) prognostic field filter, c) tendency filter, d) energy-conserving filter, e) P.G. filter.

D. ATMOSPHERIC DYNAMICS AND DIAGNOSTIC STUDIES

LARGE AMPLITUDE STATIONARY ROSSBY WAVES IN THE SOUTHERN HEMISPHERE: OBSERVATIONS AND THEORY

E. Kalnay and J. Paegle

Studies by Van Loon and Jenne (1972), Van Loon et al. (1973), Trenberth (1979) and others indicate that stationary waves in the southern hemisphere are of planetary scale, and much weaker than those in the northern hemisphere. Kalnay and Halem (1981) reported the presence of large amplitude, short stationary waves during the month of January 1979 in the lee of South America and their disappearance in February 1979. In this paper we present further observational evidence of the January waves and discuss their possible origin. The principal results are:

a) Large amplitude stationary Rossby waves with zonal wavenumber ~ 7 were present between 20°S and 40°S both in the South Pacific and east of South America during January 1979. They appear in satellite observations as enhanced bands of high clouds associated with the South Pacific convergence zone and the Amazon. Examination of satellite observations during 1974-1979 indicates some correlation between the intensity of stationary cloud bands in the two regions.

b) The stationary waves in the lee of South America are not of orographic origin since they are associated with a ridge rather than an trough east of the Andes.

c) The waves could not be produced by the CISK mechanism suggested by Kalnay and Halem (1981), because of their essentially barotropic vertical structure. SST anomalies in the South Atlantic are of the same short scale as the waves during this period. However, the fact that they are stronger at the end of January, and their phase relationship, indicated that they are a result and not a cause of the atmospheric waves.

d) Tropical heating in the Pacific and South America as diagnosed by the GLAS FGGE analysis was stronger in January than in February 1979. At the same time the easterlies were much weaker, becoming westerlies in most of the western hemisphere. The January waves appear to have been produced by the enhanced tropical heating which produced local convergence of westerly momentum and allowed (Figs. 1 and 2) energy propagation to the subtropics unimpeded by the presence of a critical line.

e) Numerical experiments with a 2-level hemispheric quasi-geostrophic model are in qualitative agreement with these conclusions.

REFERENCES

Kalnay, E., and M. Halem, 1981: Large amplitude stationary Rossby waves in the Southern Hemisphere. International Conference on Early Results of FGGE and Large-Scale Aspects of its Monsoon Experiments, Tallahassee, Fla., 12-17 Jan 1981. Condensed papers and meeting report, WMO/ICSO, Geneva, April 1981.

PRECEDING PAGE BLANK NOT FILMED

Trenberth, K. E., 1979: Interannual variability of the 500 mb zonal flow in the Southern Hemisphere. Mon. Wea. Rev., 107, 1515-1524.

van Loon, H., R. L. Jenne, 1972: The zonal harmonic standing waves in the Southern Hemisphre, J. Geoph. Res., 77, 992-1003.

van Loon, H., R. L. Jenne, and K. Labitze, 1973: Zonal harmonic standing waves. J. Geophy. Res., 78, 4463-4471.

AVERAGE ZONAL VELOCITY ($\vec{u}$ 500 mb)
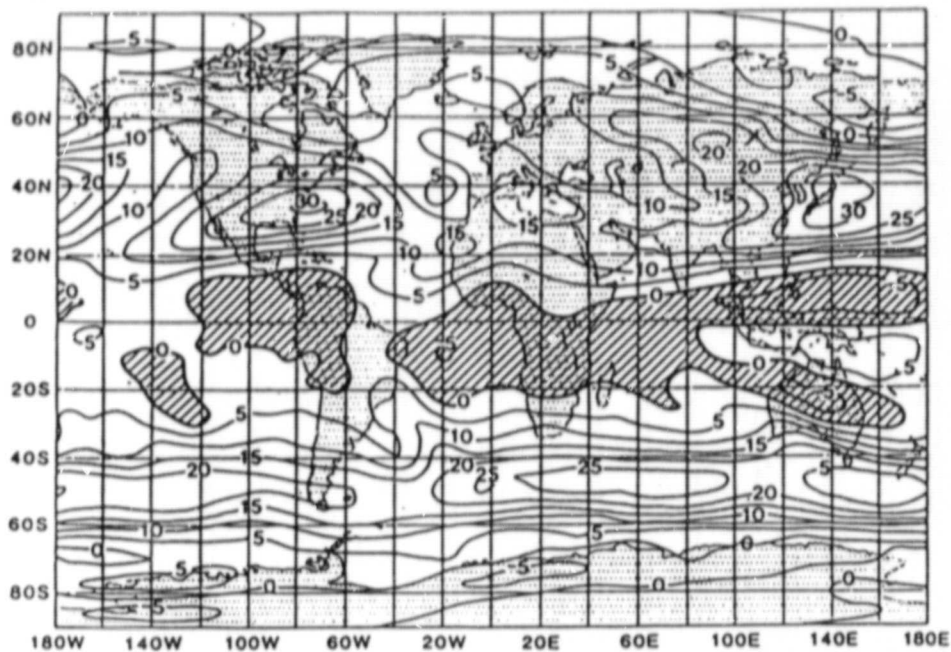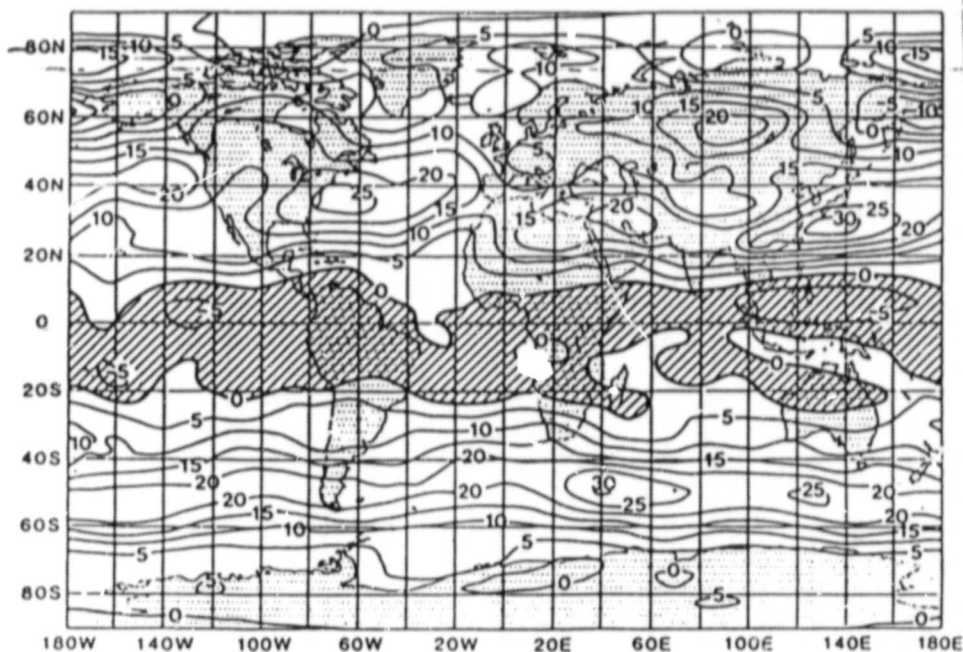
JAN 1979

FEB 1979

STATIONARY WAVES ($\overline{v}^t_{500\ mb}$)
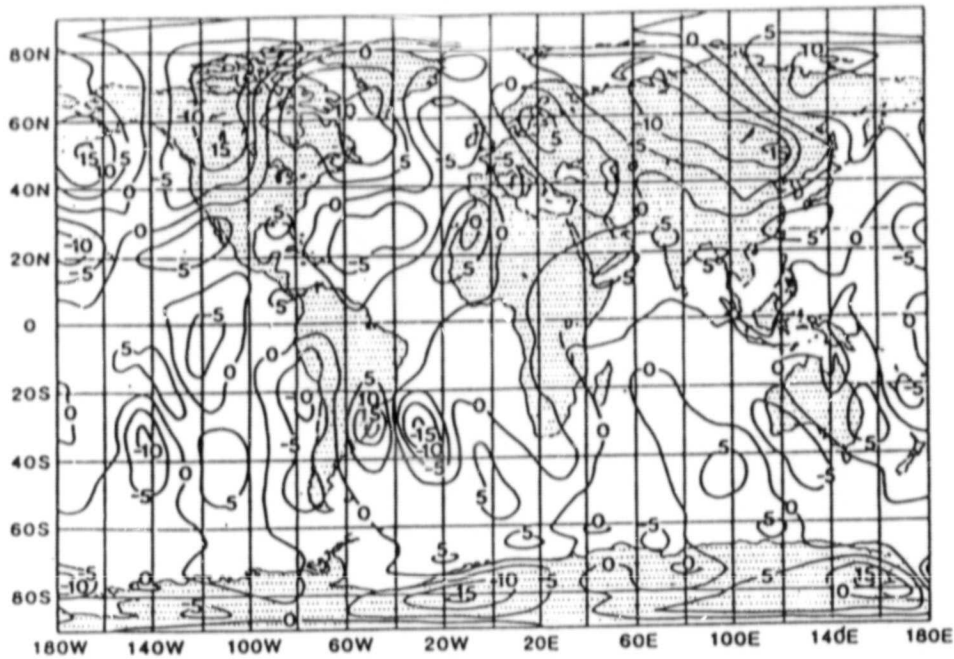
JAN 1979
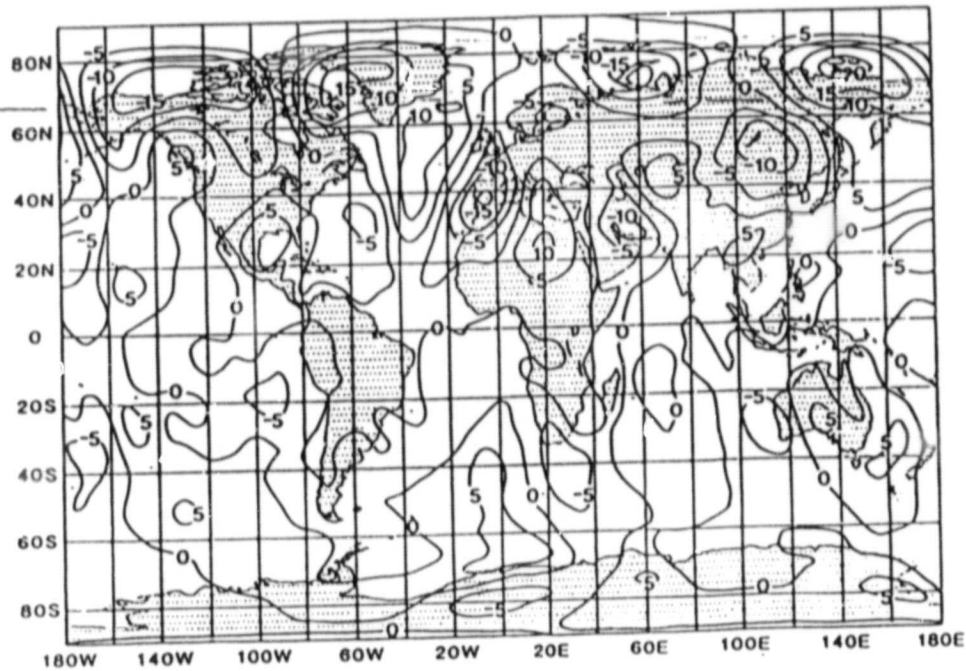
FEB 1979

A MODEL TO DETERMINE OPEN OR CLOSED CELLULAR CONVECTION

H. M. Helfand and E. Kalnay

A simple mechanism is proposed to help explain the observed presence in the atmosphere of open or closed cellular convection. If convection is produced by cooling concentrated near the top of the cloud layer, as in radiative cooling of stratus clouds, it develops strong descending currents which are compensated by weak ascent over most of the horizontal area, and closed cells result. Conversely, heating concentrated near the bottom of a layer, as when an air mass is heated by warm water, results in strong ascending currents compensated by weak descent over most of the area, or open cells. This mechanism, unlike that of Hubert (1966), does not invoke vertical variations of the eddy diffusion coefficients, and is similar to the one suggested by Stommel (1962) to explain the smallness of the oceans' sinking regions.

This mechanism is studied numerically by means of a two-dimensional, non-linear Boussinesq model. For this purpose we define open (closed) convection as a convective circulation pattern in which the majority of the fluid has a descending (ascending) motion. An internal heat source-sink destablizes a layer of fluid adding no net heating. A steady state is attained. The resulting circulation is closed, as expected, when the cooling is concentrated near the upper surface, and the heating is spread throughout the lower region. The mean lapse rate is unstable in the upper half of the fluid and stable in its lower half. Conversely, the circulation is open when heating is concentrated near the bottom. In this case, the lower half of the fluid has an unstable mean lapse rate, and the upper half of the fluid is stable.

The numerical results indicate that the width of the plume produced by the cooling in the upper part of the layer or by the heating in the lower part of the layer is largely independent of the degree of vertical asymmetry of the internal heating profile. On the other hand, the compensating motion occupies a region which becomes broader as the heating profile becomes more asymmetric. In other words, if cooling is very concentrated near the top of the layer with heating spread throughout the rest of the region or if heating is very concentrated closed or open cells have an aspect ratio much larger than 1. These results may help explain the large aspect ratios observed in atmospheric convection.

REFERENCE

Helfand, H. M., and E. Kalnay, 1983: A model to determine open or closed cellular convection. To appear in March issue of <u>J. Atmos. Sci.</u>

UNSTABLE STEADY STATES IN QUASI-GEOSTROPHIC ATMOSPHERE WITH ASYMMETRIC FORCING

E. Kalnay and K. C. Mo

Following a suggestion of Charney (1975, personal communication), Kalnay (1977) developed an iterative scheme to find an unstable stationary solution by damping time varying modes. This scheme is applied to a simple atmospheric model in order to find stationary solutions in the presence of asymmetric forcing such as orography.

The model is a two-level quasi-geostrophic on a β-plane channel with 500 km grid size and a domain of 10000 km by 10000 km. It includes simple parameterizations of long and short wave radiation, surface friction, surface fluxes of sensible and latent heat similar to those of Charney (1959). The symmetric model has no orography and the asymmetric model is forced by a Gaussian mountain located in the center of the channel (Figure 2).

Figure 1 shows the zonal velocities at the upper and lower levels of the stationary solution and the time averaged solution of the symmetric and asymmetric models. Figure 2 shows the upper and lower level streamfunctions of the stationary solution and the time averaged solution of the asymmetric model.

A linear stability analysis of the four basic states has been carried out by successive time integration of the linearized equations (Brown, 1969) until the solution can be expressed as

$$\psi(t) = \psi(0) \, e^{(\sigma_{r+i} \,\, \sigma_i)t}$$

Table 1 lists the fastest growing modes and frequencies all four cases.

Although the time averaged mean fields for both symmetric and asymmetric model are far from equilibrium; they are baroclinically much more stable. Orographic forcing stabilizes the solutions, especially the time averaged one. Wave number 2 is the fastest growing mode in the time averaged and symmetric stationary solutions. In the orographically forced stationary solution, however, the most unstable mode is a combination of wave number 1, 2 and 3, which grow at the same rate due to the interaction between the mountain and the mean flow.

REFERENCES

Brown, J. A., 1969: A numerical investigation of hydrodynamic instability and energy conversions in the quasi-geostrophic atmosphere. J. Atmos. Sci., 26, 352-365.

Charney, J. G., 1959: On the general circulation of the atmosphere. The Atmosphere and Sea in Motion. B. Bohn, ed. Rockefeller Press, N.Y. p. 178-193.

Kalnay-Rivas, E., 1977: A numerical scheme to solve unstable boundary value problems. Advances in Computer Methods for Partial Differential Equations. Vol. II, R. Vichnevefsky, Ed., IMACS, p. 264-268.

Table 1

Case	Model	Solution	Fastest Growing Mode	Growth Rate σ_r (days^{-1})	Frequency $\sigma_i/2\pi$ (day^{-1})
1	symmetric	stationary	2	0.22	0.036
2	symmetric	time avg.	2	0.10	0.083
3	asymmetric	stationary	1,2,3	0.20	0.062
4	asymmetric	time avg.	2	0.041	0.13

FIGURE CAPTIONS

Figure 1a.   Upper level zonal velocities U_1(m/s) for the four cases listed in Table 1.

Figure 1b.   Lower level zonal velocities U_3(m/s) for the four cases listed in Table 1.

Figure 2.   The streamfunctions for the asymmetric model in units of 10^5/m^2/s. (a) upper level, stationary solution, (b) lower level, stationary solution, (c) upper level, time averaged solution, (d) lower level, time averaged solution.

129
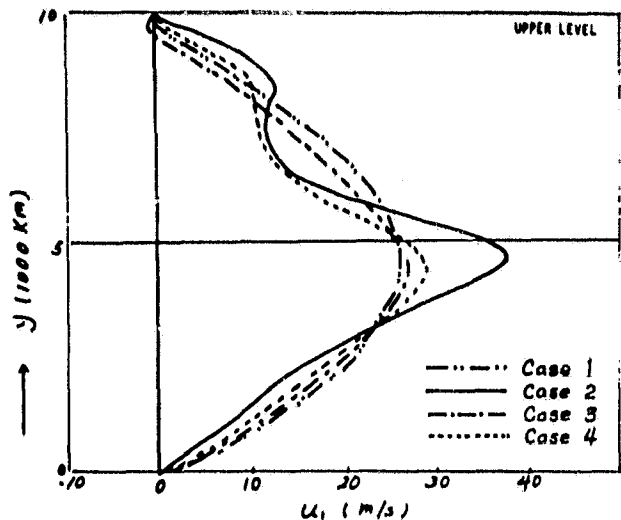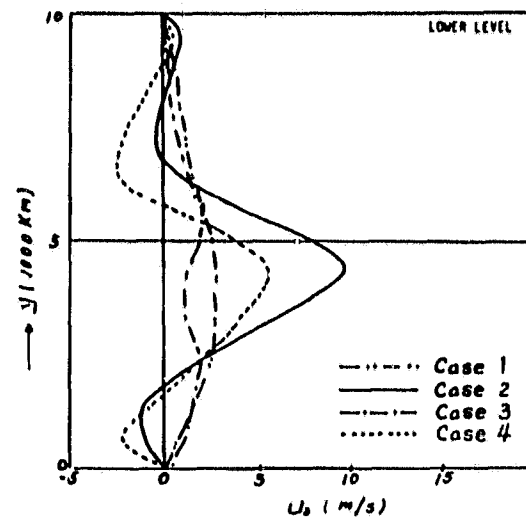
Figure 1a

Figure 1b
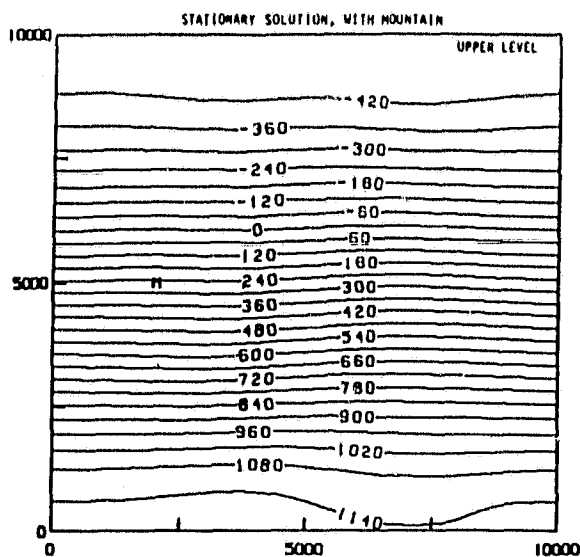
Figure 2a
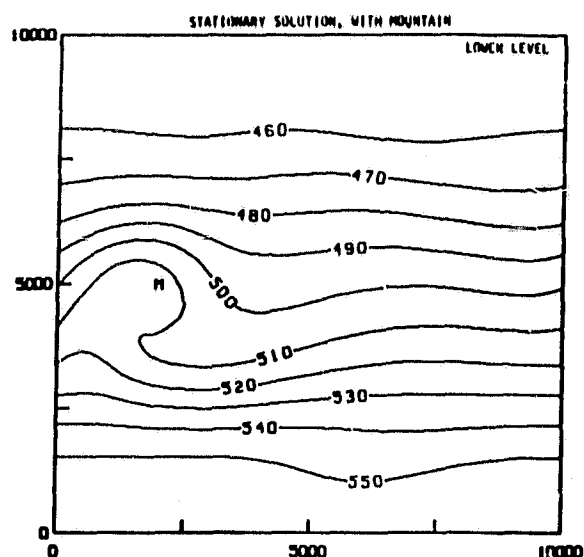
Figure 2b
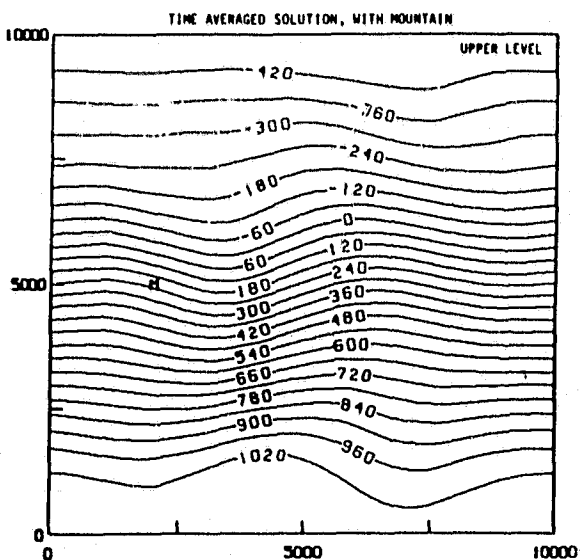
Figure 2c
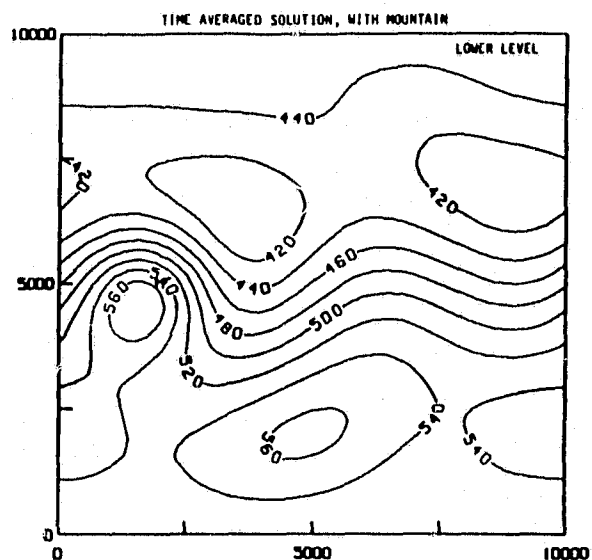
Figure 2d

BAROTROPIC INSTABILITY OF WEAKLY NON-PARALLEL ZONAL FLOWS

L.-O. Merkine* and R. C. Balgovind

Barotropic instability of weakly non-parallel zonal flows with localized intense shear regions is investigated numerically. The numerical integrations of the linear stability problem reveal the existence of unstable localized wave packets whose spatial structure and eigenfrequencies depend on two parameters which measure the degree of supercriticality and the zonal length-scale of the shear region. The results indicate that an unstable global mode solution is determined by conditions that ensure the decay of the wave packet at infinity and the transition from long to short waves across a turning point (critical layer) region which is controlled by non-parallel effects. The controlling influence exerted by the weak non-parallel effects on the evolution of the instability underlines the weakness of the parallel flow assumption which can be used locally, away from critical layers, as a diagnostic tool only.

The experiments are classified according to the nature of the basic flow, namely an intense westerly jet at the center of the channel (Figure 1) or a blocking configuration with a split westerly jet (Figure 2).

The westerly jet results showed that regardless of the type of initial conditions (random distribution or a concentrated pulse) instability developed whenever the maximum shear was in excess of the critical shear predicted by the parallel theory. It assumed the shape of a non-propagating and localized envelope modulating propagating waves. The wave-length of these waves was location dependent but the frequency of oscillation and growth rate were the same for all locations. It follows that the numerical result revealed the existence of global modes characterized by a single complex frequency which is the eigenvalue of the problem. Figure 3 depicts a structure of the instability as a function of x at the center of the channel. The complete spatial structure of the unstable wavepack is shown in Figure 4.

The results of the numerical integrations for a split westerly jet revealed again the existence of unstable global mode solutions. The modes describe propagating waves modulated by a localized stationary envelope and having a single complex frequency. Figure 5 depicts a structure of the instability as a function of x at the center of the channel. In contrast to the corresponding westerly jet case the deep downstream penetration is absent with the instability essentially confined to the supercritical region. The rapid spatial decay of the wavepacket is a consequence of the large growth rate. The complete spatial structure of the unstable wavepack is shown in Figure 6.

CONCLUSIONS

There exists one fundamental difference in the dynamics of instabilities that develop in parallel and in non-parallel flows. The parallel flow stability problem is invariant to zonal translation since the available energy is distributed evenly

---

* Dept. of Mathematics, Technion - Israel Institute of Technology, Haifa 32000, Israel.

in the zonal direction. Hence, instabilities can develop without preference at any streamwise location. The non-parallel flow stability problem is not invariant to zonal translation since the zonal distribution of the available energy is not uniform. Consequently, instabilities can develop only at certain streamwise locations which are fixed relative to the distribution of the forcing functions that drive the basic flow (Merkine, 1982).

The numerical integration revealed the existence of localized unstable global mode solutions whose spatial and temporal characteristics depend on two parameters which measure the degree of supercriticality and the length scale of the zonal variation of the basic flow. Although we considered a particular basic flow, albert with certain appealing features, the basic phenomenon and the manner by which it is controlled by these two parameters should be characteristic of a wide class of flows possessing localized intense shear regions.

The results indicate that the complex eigenfrequency of the global mode is determined by conditions that ensure the decay of the wavepacket at infinity and the transition from long to short waves across a turning point region. The dynamics of this transition region which can also be identified as a critical layer of the local parallel problem is controlled by the advection of th wave's vorticity by the weak meridional velocity of the basic state. The local structure of the wave-packet away from critical layers can be determined by parallel flow considerations applied locally provided the eigenfrequency is known. This underlines the limited usefulness of the parallel theory and demonstrates the importance of weak non-parallel effects in controlling the dynamics of the instability.

REFERENCES

Merkine, L., 1981: The stability of quasi-geostrophic fields induced by potential vorticity sources. J. Fluid Mech., 116, 315-342.
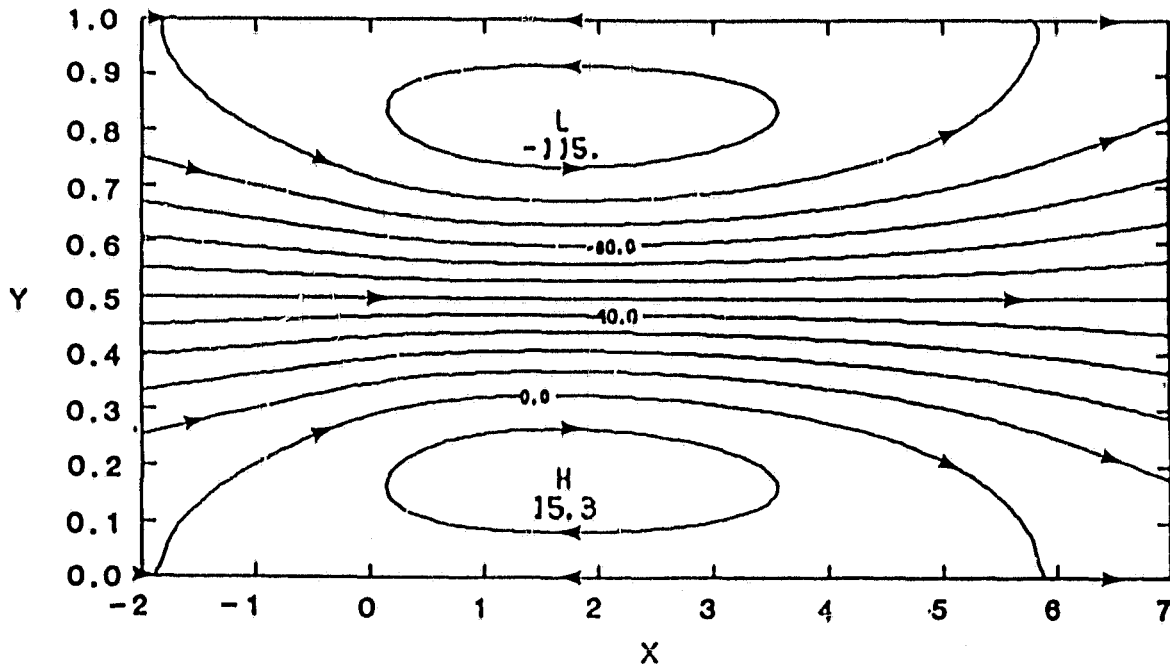
Figure 1. The basic flow for a case when vorticity source is
negative.
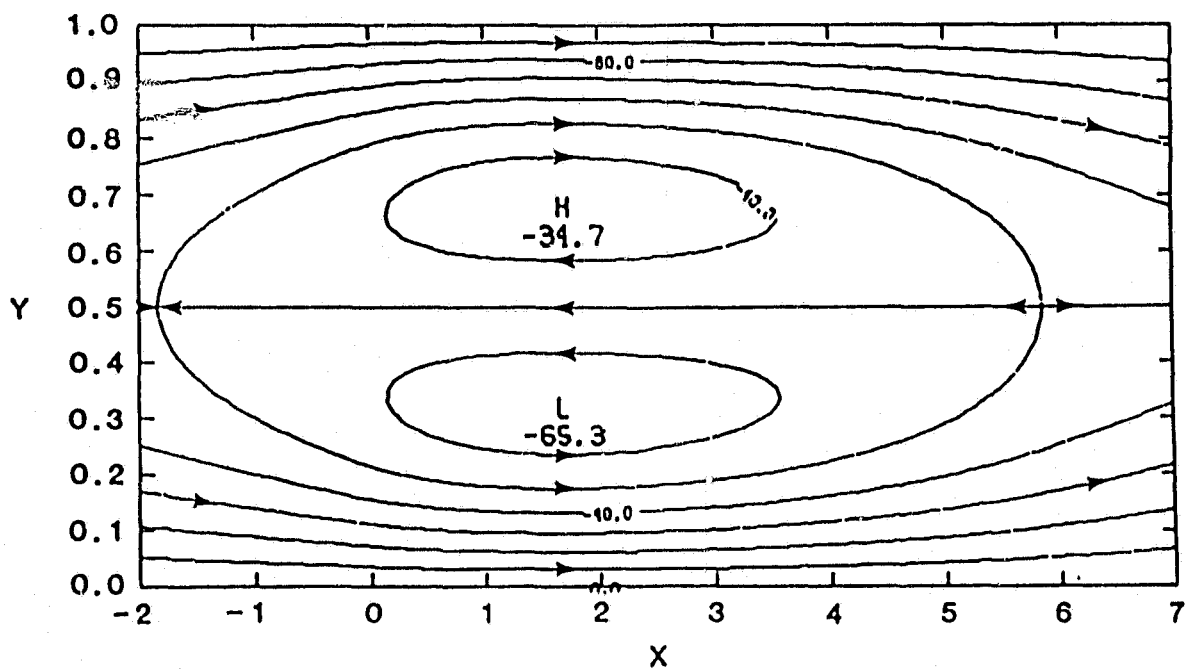
Figure 2. The basic flow for a case when vorticity source is
positive.
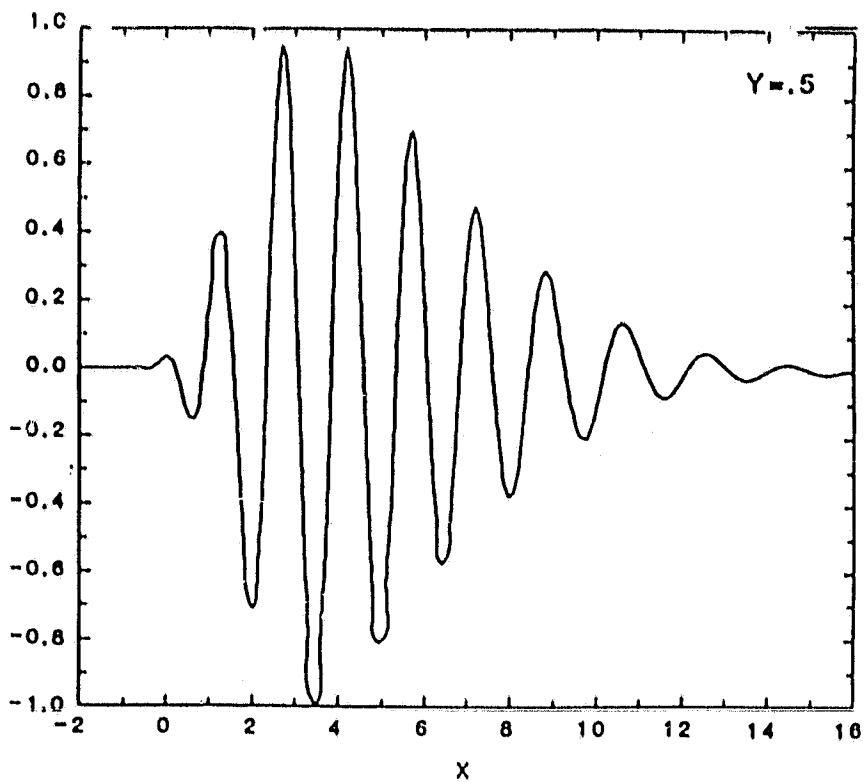
Figure 3. The structure of the instability as a function of x
at the center of the channel. The basic flow is a
westerly jet.
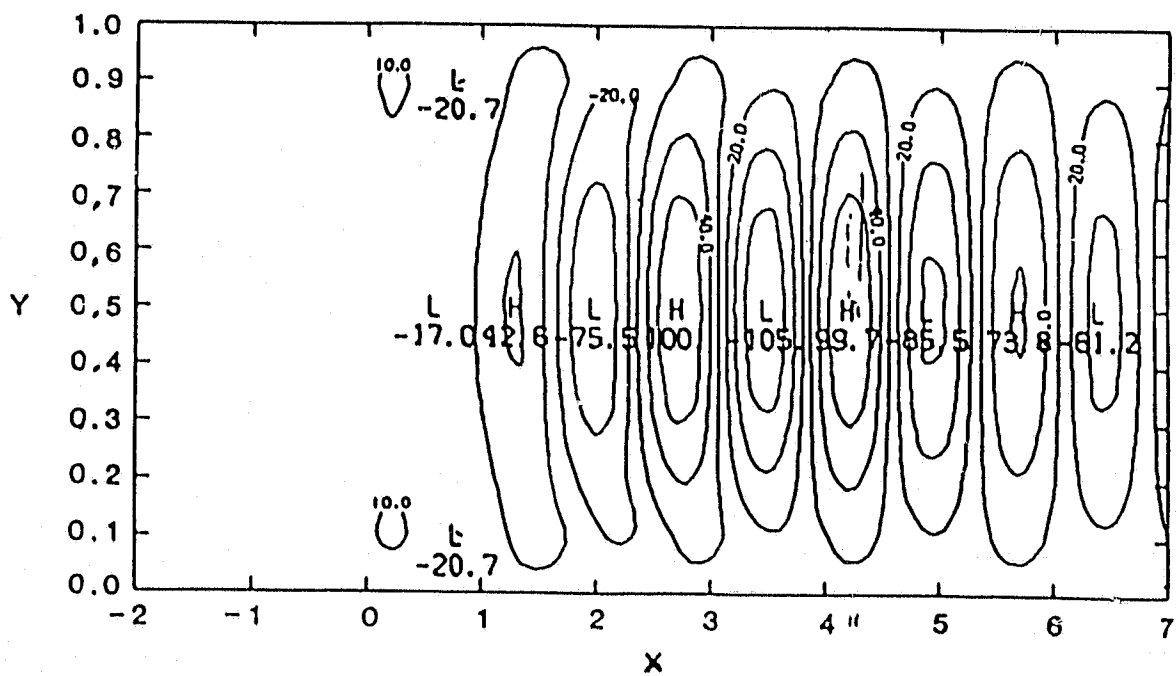
Figure 4. The streamfunction of the instability of Figure 3.
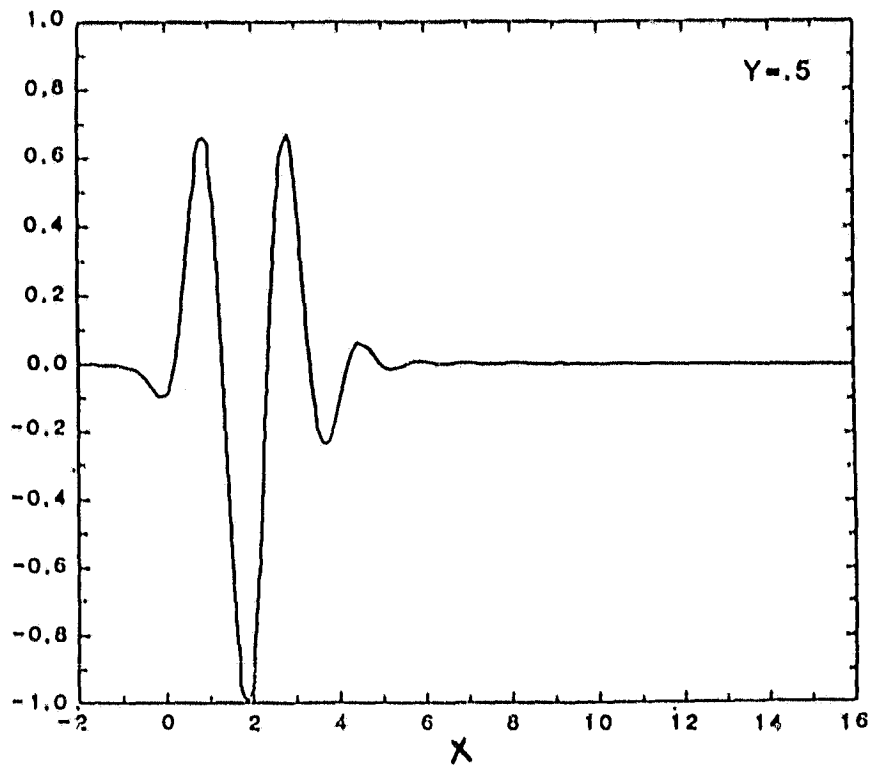
Figure 5.   The structure of the instability as a function of x
at the center of the channel.   The basic flow is a
split-westerly jet.
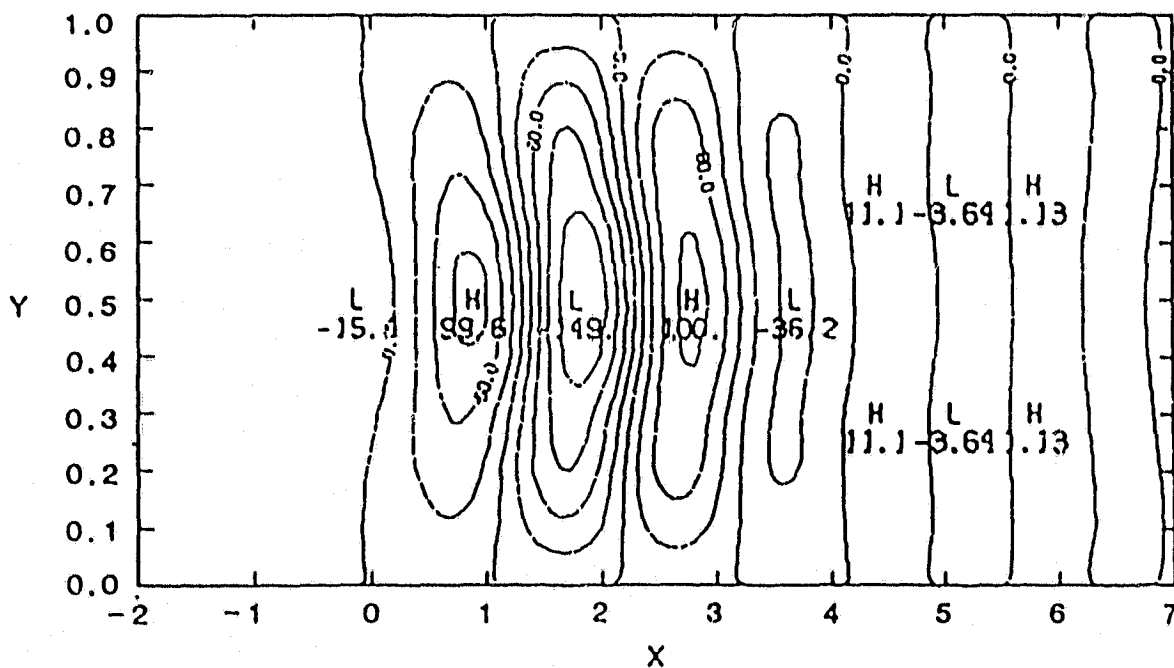
Figure 6.   The streamfunction of the instability of Figure 3.

III. CLIMATE/OCEAN-AIR INTERACTIONS

A. DATA ANALYSIS

PERSISTENT ANOMALIES OF THE SOUTHERN HEMISPHERE CIRCULATION

K. C. Mo and J. Shukla

We have examined the persistent features of large anomalies and determined the locations and structures of blocking in the Southern Hemisphere. The data set used here contains daily maps of 500 mb geopotential heights for 100 months (June 1, 1972 to Nov. 30, 1980), covering from 10S to 90S. The seasonal cycle was defined as an 8-year mean and the 8th (annual) and 16th (semiannual) Fourier components of the time series at each grid point. Anomalies were defined as the difference between the total field and the seasonal cycle for each point.

The primary conclusions of this study are:

1. Large anomalies are less persistent in the Southern Hemisphere than in the Northern Hemisphere.

We have calculated the frequency of occurrence of anomalies ($\geq$ 150 m or $\leq$ -150 m) which persisted for a certain number of days. There is no evidence of any discontinuity in either positive or negative anomaly curves. The peak near 2-3 days noted by Charney, Shukla and Mo (1980) due to synoptic scale travelling disturbances does not exist here. This indicates that most of the large anomalies do not persist more than one day at any grid point.

2. The local one day lag autocorrelation decay much faster in the Southern Hemisphere. Except in the subtropics and Australia, the red noise model fits the autocorrelation decay well.

3. The frequency of occurrence for positive anomalies satisfying the criterion (150 m, 6 days) is similar to the map of 8-64 days low pass filtered variances, and the frequency distribution for anomalies satisfying the criterion (150 m, 1-3 days) represents storm track patterns.

Figures 1a and 1b show the frequency of occurrence of persistent positive and negative anomalies satisfying the criterion (150 m, 6 days) using 100 months of data, respectively. Figure 1a is similar to that presented by Swanson and Trenberth (1982) using the criterion (100 m, 5 days). There are three maxima located in the southwest Pacific along 55S near 170W and between 140E-150E, southeast of South America (65S, 80W) and (50S, 80E) Indian Ocean.

4. The maxima of frequency of occurrence of large positive anomalies and large negative anomalies do not occur in the same region.

Comparison of Figures 1a and 1b shows that the maximum in Pacific (55S, 160W) remains in both cases. The one located in the south of southern America shifts to (66S, 45W). The maximum at the Indian Ocean does not exist in Figure 1b.

Blocking is defined as an anomaly which satisfies criterion ($\pm$ 150 m, 6 days) and associates with a pronounced ridge. According to this definition, we have identified the blocking events, ridge positions and structures of each event. There are 13 events located in the southwest Pacific, four events in the south of South America. There is not blocking at (50S, 80E), where the maximum of the frequency of occurrence of positive anomalies occurs. However, further south at 60S, there are three events in the Indian Ocean.

REFERENCES

Charney, J. G., J. Shukla and K. C. Mo, 1981: Comparison of barotropic blocking
    theory with observations. J. Atmos. Sci., 38, 762-779.

Swanson, G. S., and K. E. Trenberth, 1982: Persistent anomaly statistics in
    the Southern Hemisphere. preprint.
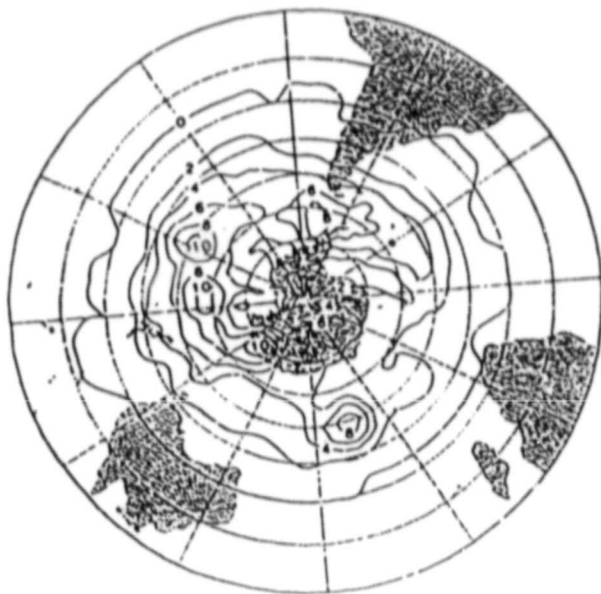
(a)
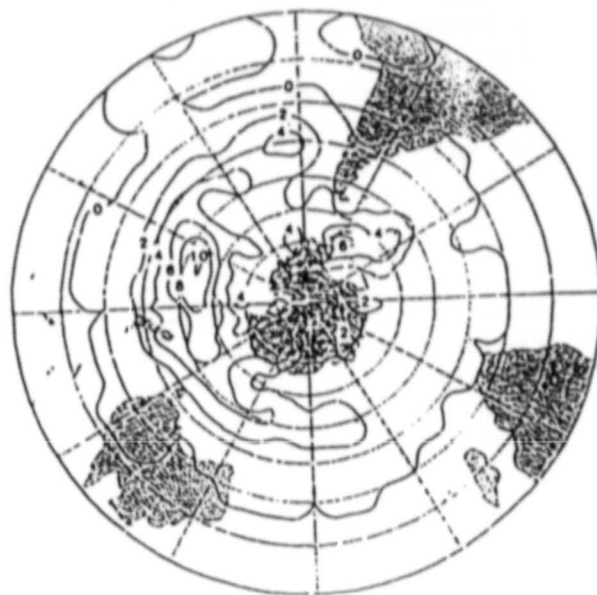
(b)

Figure 1. Number of events for anomalies satisfying the criterion: a) 150 m, 6 days, b) -150 m, 6 days. Contour interval 2.

TIME-SCALE AND ONSET CRITERIA OF AGRICULTURAL DROUGHT

Y. C. Sud and Y. G. Serafini

This work was aimed to develop a technique to establish the onset of an agricultural drought based on the time evolution of soil moisture predicted from the ground water balance. We used a criterion invoking a limiting value of 2.5% of the maximum available soil-moisture (Field Capacity - Wilting Value) to earmark the onset of an agricultural drought. The soil moisture tendency equation requires precipitation and land surface evapotranspiration as basic inputs. The former must be known a priori whereas the latter is introduced by suitable parameterizations for the potential evapotranspiration and the moisture availability parameter (Mintz and Serafini, 1982). The integrated form of the soil moisture tendency equation is found to be:

$$w(t) = w_0 + 1/\lambda \, \log_e \left[\{ 1 + R \exp(-\lambda w_0) \} \exp(E_p \lambda t / CR) - \exp(-\lambda w_0 / R) \right] \quad (1)$$

where $\lambda = \dfrac{\alpha}{w^*}$, $C = 1 - \exp(-\alpha)$, and $R = E_p / [C(P+I) - E_p]$.

Here, the time dependent soil moisture $w(t)$ is a function of the potential evapotranspiration E_p, the curvature parameter of the moisture availability formula α, the initial soil moisture w_0, the maximum available soil moisture w^* and the mean moisture source terms: precipitation rate P and irrigation rate I.

By assuming a total absence of all the moisture source terms in an agricultural drought, Eq. (1) simplifies to yield a time-scale defined as the time taken to reduce the mean monthly climatological soil moisture, $\overline{w}_c$ to the chosen wilting value, w_p. Its form is:

$$\tau = c/\lambda E_p \, \log_e \left\{ \exp(\lambda \overline{w}_c) - 1 / \exp(\lambda w_p) - 1 \right\} \quad (2)$$

The solution of Eq. (1) can be used to predict the time evolution of soil moisture to monitor a real drought situation. Furthermore, the constants α, w^* and w_p can be suitably chosen to best represent the preculiarities of the soil type and the vegetation (crops) in a region.

Alternatively Eq. (1) can be solved to determine the irrigation needs of a region. This is equal to the difference of the calculated monthly moisture source term (required to maintain a certain mean available soil moisture) and the precipitation.

Using the constructed fields of global mean monthly climatological values of soil moisture (Mintz and Serafini, 1982), the time period for the inception of an agricultural drought was obtained from Eq. (2) for each month. Sample plots for the months of January and July are shown in Figs. 1 and 2. The corresponding climatological soil moisture values are shown in Figs. 3 and 4.

REFERENCE

Mintz, Y., and Y. Serafini, 1982: Monthly normal global fields of soil moisture and land surface evapotranspiration (to be published).
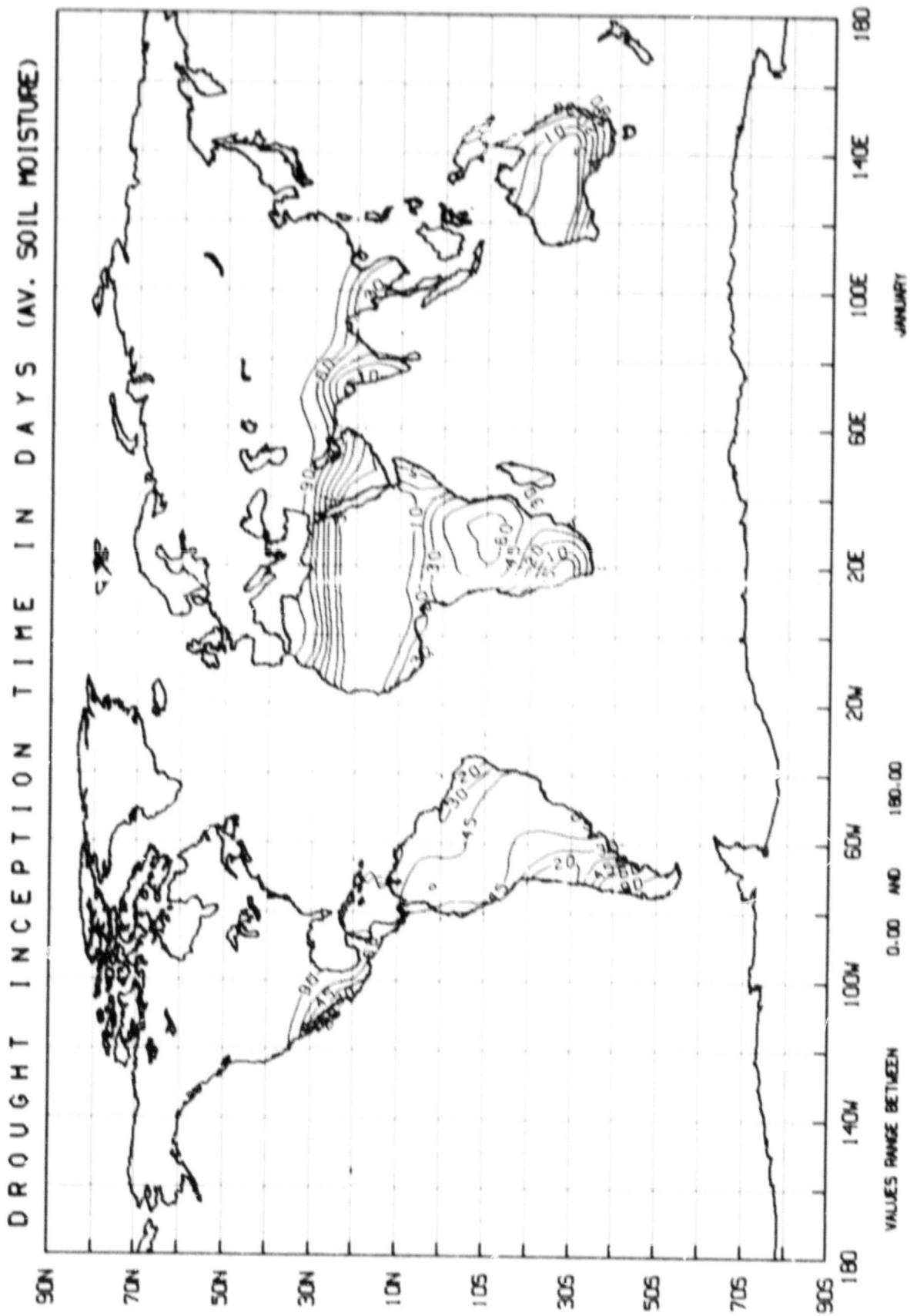
DROUGHT INCEPTION TIME IN DAYS (AV. SOIL MOISTURE)

JANUARY

VALUES RANGE BETWEEN 0.00 AND 180.00

Figure 1

DROUGHT INCEPTION TIME IN DAYS (AV. SOIL MOISTURE)

JULY

VALUES RANGE BETWEEN   0.00 AND   180.00

Figure 2

SOIL MOISTURE PERCENTAGE (FIELD CAPACITY = 150. MM)

JANUARY

VALUES RANGE BETWEEN   0.01 AND 150.00

Figure 3

767

768

SOIL MOISTURE PERCENTAGE (FIELD CAPACITY = 150. MM)

JULY

VALUES RANGE BETWEEN   0.03 AND 150.00

Figure 4

755
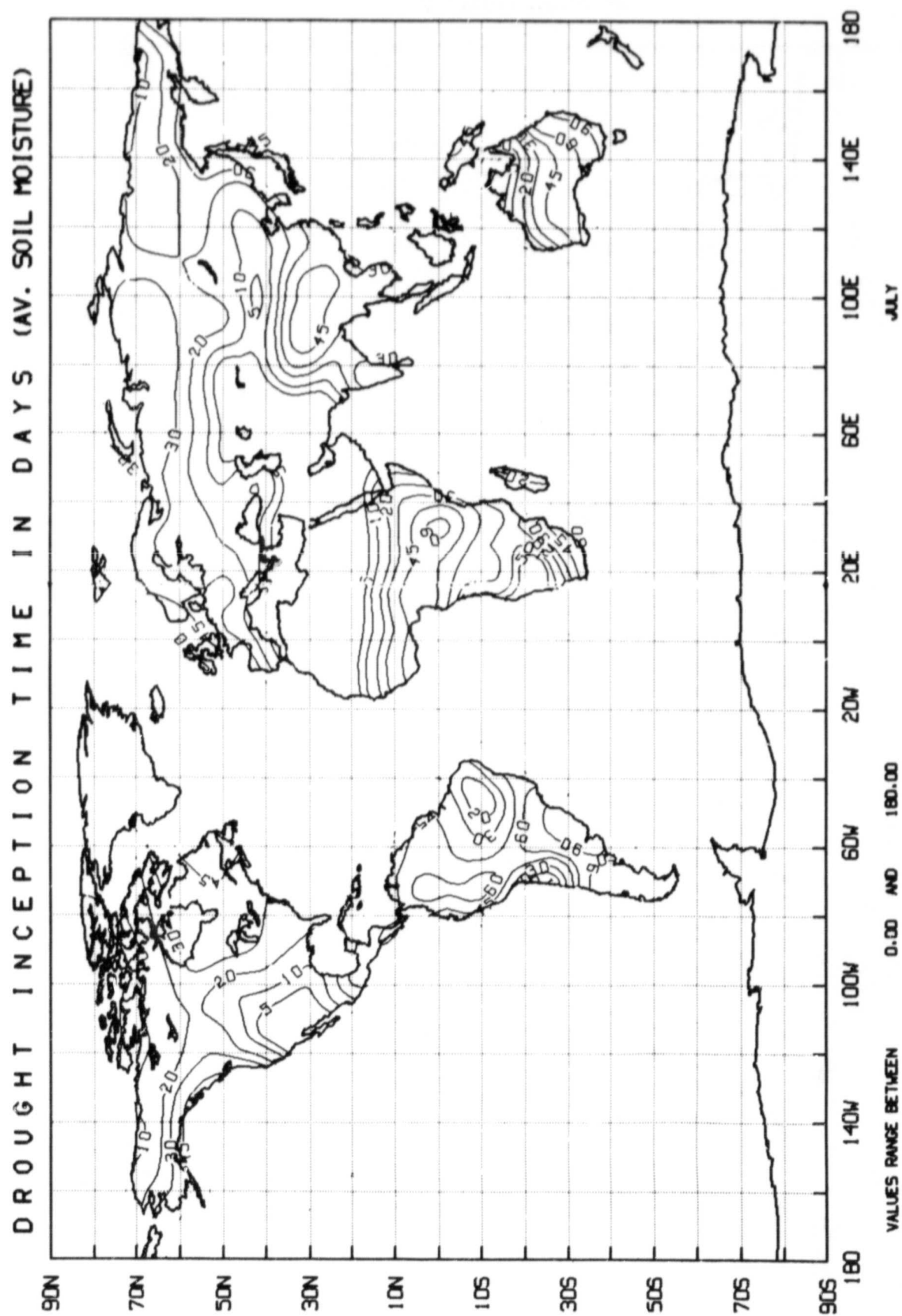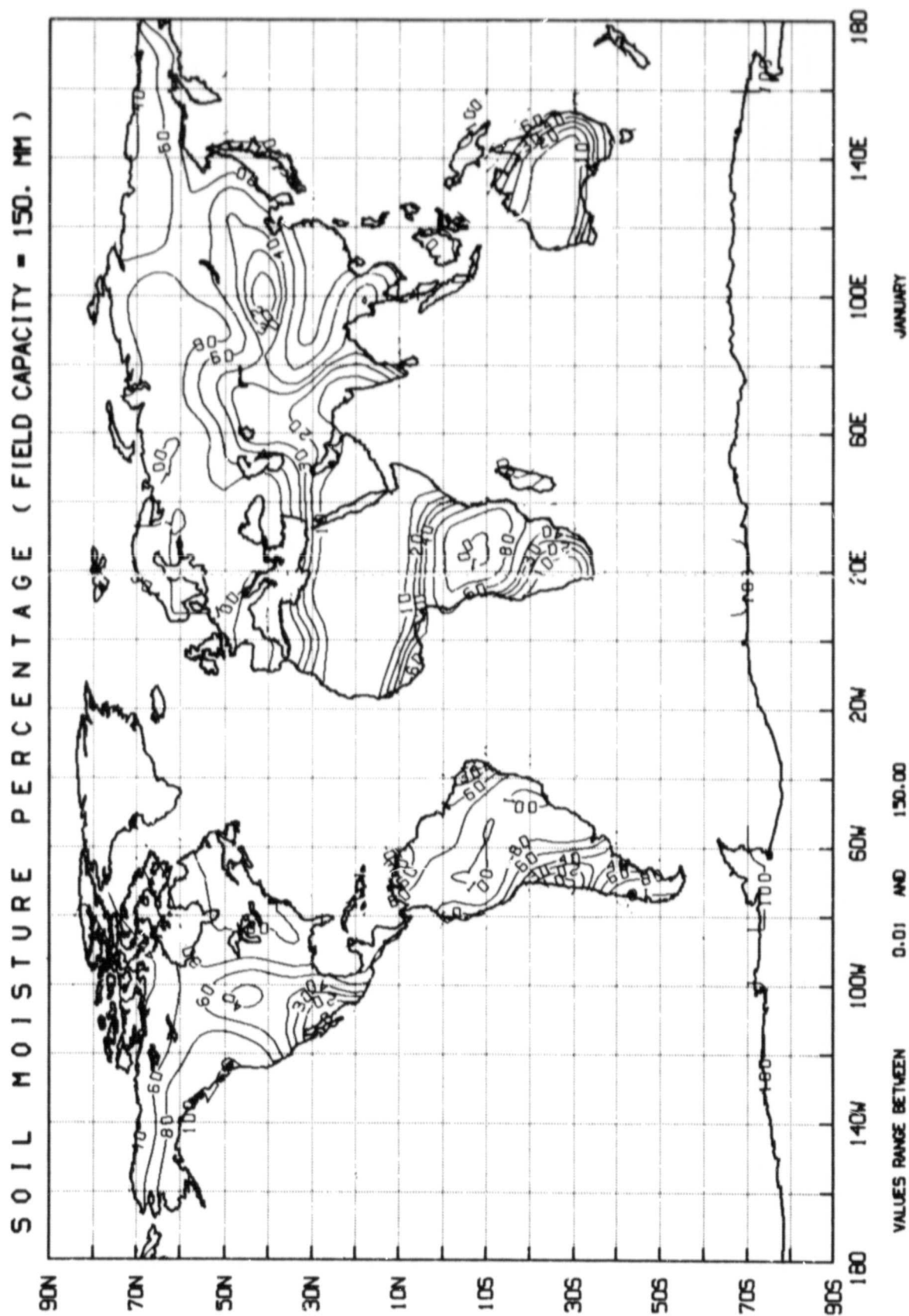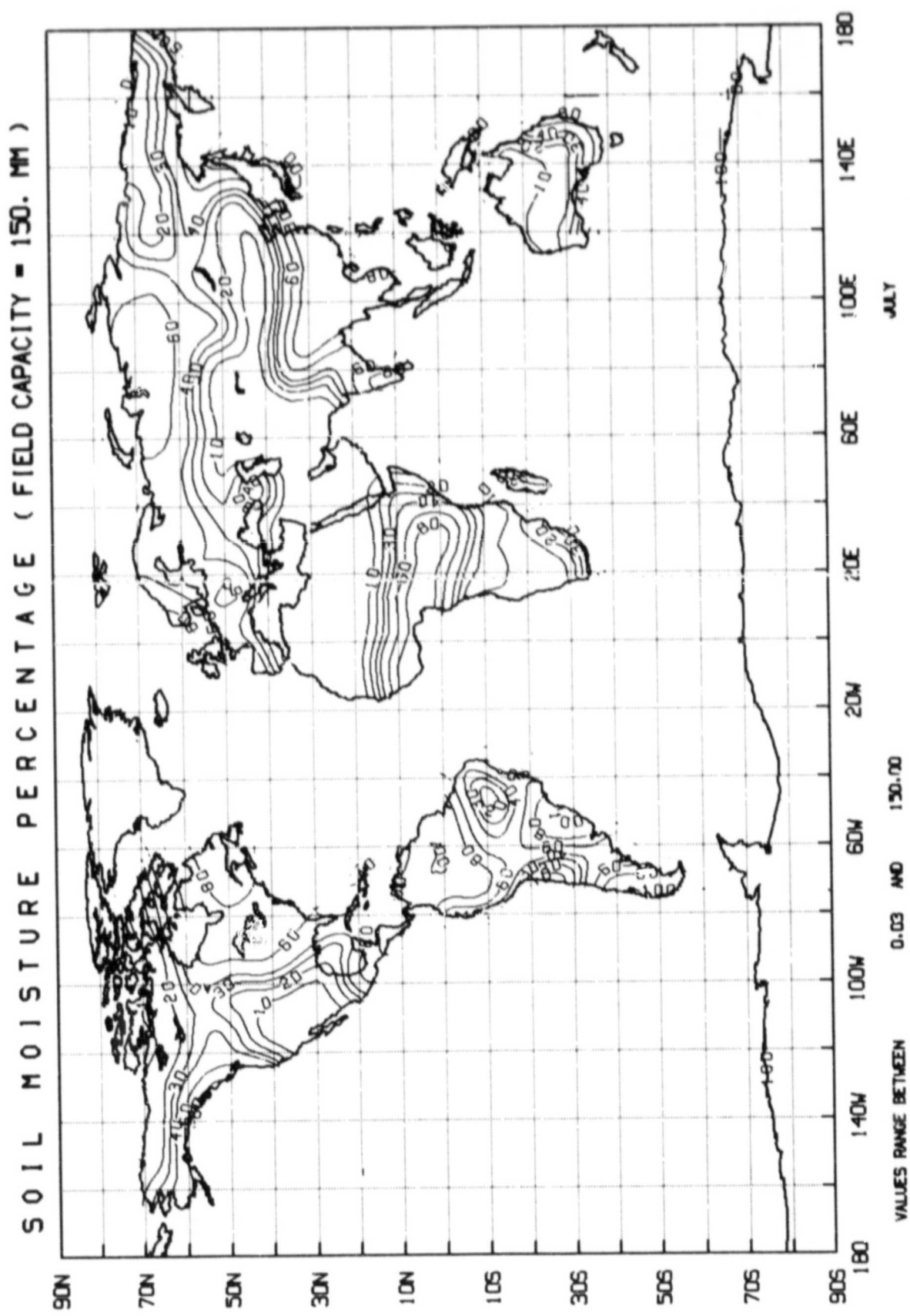
756

DEPENDENCE OF PRECIPITATION ON EVAPOTRANSPIRATION IN THE CONTINENTAL UNITED STATES

Y. C. Sud and M. Fennessy

The influence of soil mosture and its dependent evapotranspiration on mean monthly precipitation was examined by analyzing forty years of observed precipitation and surface temperature data. The data comprised of actual observations averaged over each month at 261 local climatic data (LCD) stations distributed throughout the continental United States covering the period from 1939-1980.

The actual evapotranspiration was obtained by first calculating the mean monthly potential evapotranspiration using empirical functions of Thornthwaite (1948) and Willmott (1977) and then multiplying it by the soil moisture dependent moisture availability parameter (Nappo, 1975). This evapotranspiration in conjunction with the observed precipitation provided the net surface water balance in the soil moisture tendency equation. The soil moisture tendency equation was integrated to yield the soil moisture and evapotranspiration at the beginning of each month.

The observed mean monthly precipitation was correlated with the antecedent fields of a) observed mean monthly precipitation, b) soil moisture at the beginning of the month, and c) evapotranspiration at the beginning of the month.

Statistically significant correlations were found in the drought prone western Great Plains region in September and October.

Fig. 1 shows the correlation coefficients between precipitation and antecedent soil moisture for the month of October. The Great Plains regions was then further analyzed by constructing three sets of contingency tables between the correlated fields. These statistics reaffirmed the existence of significant positive correlations between precipitation and other fields. A contingency table between soil moisture and precipitation is shown in Table 1. The strength of diagonal from top left to bottom right represents the positive correlation. CHI-square (ψ^2) values at the bottom of the table reflect the strength of the signal (s^2 = for purely random distribution).

Based on this study we conclude that in the drought prone western Great Plains region a statistically significant relationship exists between antecedent soil moisture and the precipitation, particularly in the later part of summer. This suggests the importance of soil moisture in maintaining rainfall anomalies.

REFERENCES

Nappo, C. T. Jr., 1975: Parameterization of surface moisture and evaporation rate in a planetary boundary layer model. J. Appl. Met. 14, 289-296.

Thornthwaite, C. W., 1948: An approach toward a rational classification of climate, Geog. Rev. 38, 55-94.

Willmott, C. J., 1977: A Fortra IV algorithm for calculating the climatic water budget. OWRT project No. A-040-DEL. Water Resources Center, Univ. of Delaware, Newark, Delaware.

Table 1

Normalized Contingency Table Between Antecedent Soil Moisture and Precipitation

MAY

115	156	91	58	144
78	119	100	119	58
103	106	101	98	72
97	39	108	66	156
87	39	79	176	289

CHISQ = 32.4

JUNE

173	58	106	58	87
78	52	98	119	176
106	117	98	100	85
39	105	110	79	78
87	39	97	137	173

CHISQ = 19.0

JULY

173	117	100	39	87
137	105	100	105	39
97	104	99	94	106
58	92	96	119	156
58	39	106	176	58

CHISQ = 16.2

AUGUST

58	97	115	78	29
156	105	84	119	156
103	102	96	102	121
39	92	112	119	19
115	78	121	39	0

CHISQ = 23.7

SEPTEMBER

231	97	97	58	58
215	52	92	145	58
91	112	101	90	94
19	92	98	158	117
0	58	106	78	231

CHISQ = 37.2

OCTOBER

144	156	106	19	29
156	66	110	66	39
97	102	99	100	100
58	92	98	132	117
58	78	82	176	231

CHISQ = 26.2

NOVEMBER

58	19	109	156	87
39	119	100	79	156
106	127	95	34	103
156	13	104	132	78
87	19	124	78	29

CHISQ = 30.4

JUL-OCT

152	117	104	48	50
166	82	97	109	73
97	105	99	97	105
44	92	101	132	102
57	63	104	117	130

CHISQ = 43.6
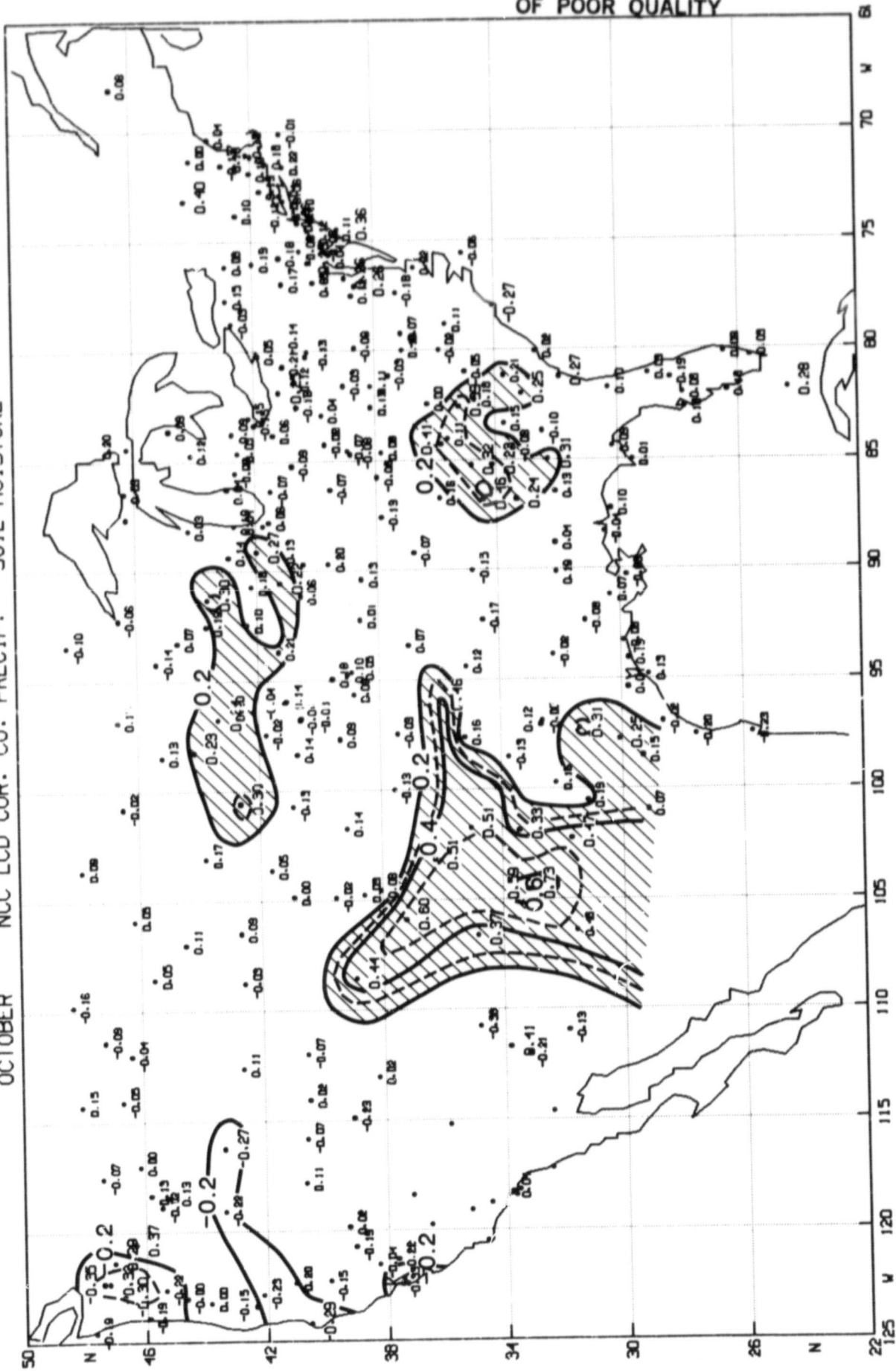
Fig. 1. Large print is for correlation coefficients having more than 80% significance for a 2-tailed T-test.

B. CLIMATE MODELING

150·

DESIGN OF AN INTERACTIVE BIOSPHERE
FOR THE GLAS GENERAL CIRCULATION MODEL

Y. Mintz, P. J. Sellers and C. J. Willmott

Research has begun on an interactive biosphere for the GLAS general circulation model, so that the calculations of the land-surface evapotranspiration and sensible heat flux will be more realistic. This is important because sensitivity experiments with general circulation models have shown that the simulated fields of rainfall, temperature and motion of the atmosphere are highly sensitive to the transfers of latent and sensible heat at the land surface.

Water and energy transfers at the land surface depend on vegetation morphology and physiology. In the model biosphere, the vegetation morphology will control these transfers through the leaf area density as a function of height, $L_D(Z)$, and through the root length density as a function of depth, $RT_D(Z)$, as expressed in a discretized form for each of the model grid areas. $L_D(Z)$ will influence (a) the aerodynamic resistance to the latent and sensible heat transfers; (b) the transmission, absorption and emission of radiation energy by the canopy and underlying ground; and (c) the interception, evaporation and throughfall of rain and snow. The vegetation physiology will control the transfers of water and energy through the stomatal resistance, the xylem resistance of the stems, and the root cortex resistance. The stomatal resistance will be a function of the leaf water potential, short-wave radiation intensity, leaf temperature, and humidity of the air.

In the initial formulation, $L_D(Z)$ and $RT_D(Z)$ are being prescribed as functions of latitude and longitude and the season of the year, as known from ecological observations in the various vegetation formations. Later, the phenological changes of $L_D(Z)$ and $RT_D(Z)$ in the deciduous forests and grasslands will be made interactive with the atmospheric variables and the soil moisture as calculated by the GCM. Finally, the vegetation formations themselves will be made interactive with the atmospheric and soil moisture conditions.

The realism of the model biosphere will be evaluated (1) through short period one-dimensional comparisons with measured values of the local atmospheric forcing and measured values of the vertical fluxes of water and energy; (2) through long period comparisons of simulated and observed catchment water budgets; and (3) through comparisons of the simulated and observed surface temperatures, surface albedos, snow cover, live biomass, and the water balances of the large river basins, when the model biosphere is forced with atmospheric variables taken from the FGGE level 3-B and 2-C data sets.

The accompanying figure illustrates (for the case of a rainforest) the procedure whereby the morphological and physiological characteristics of the vegetation are transformed into the parameters which govern the transfer of water from the root zone of the soil to the atmosphere. (For further details, see NASA Technical Memorandum XXXXX, January 1983.)

153
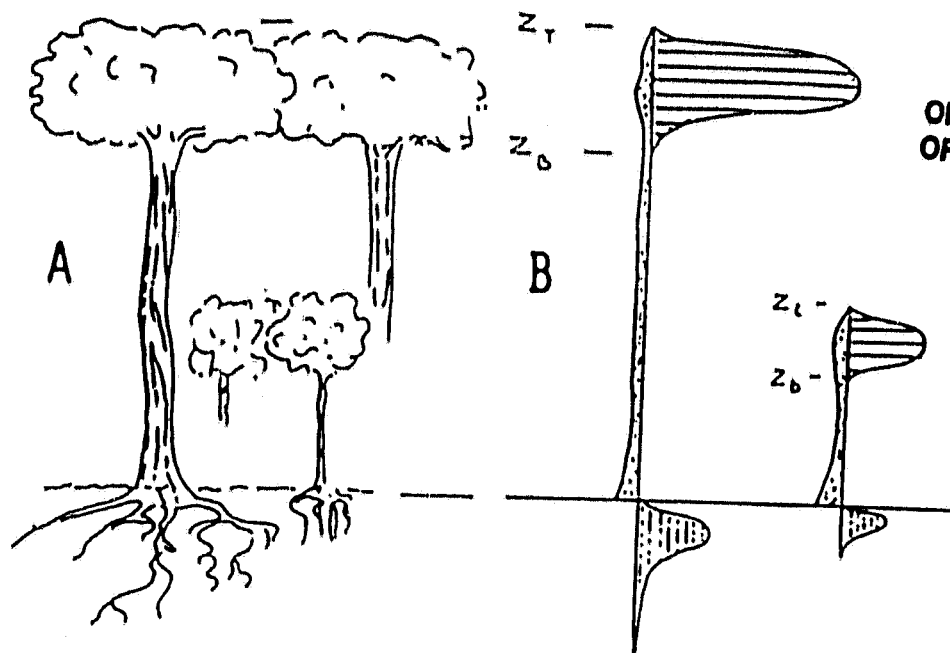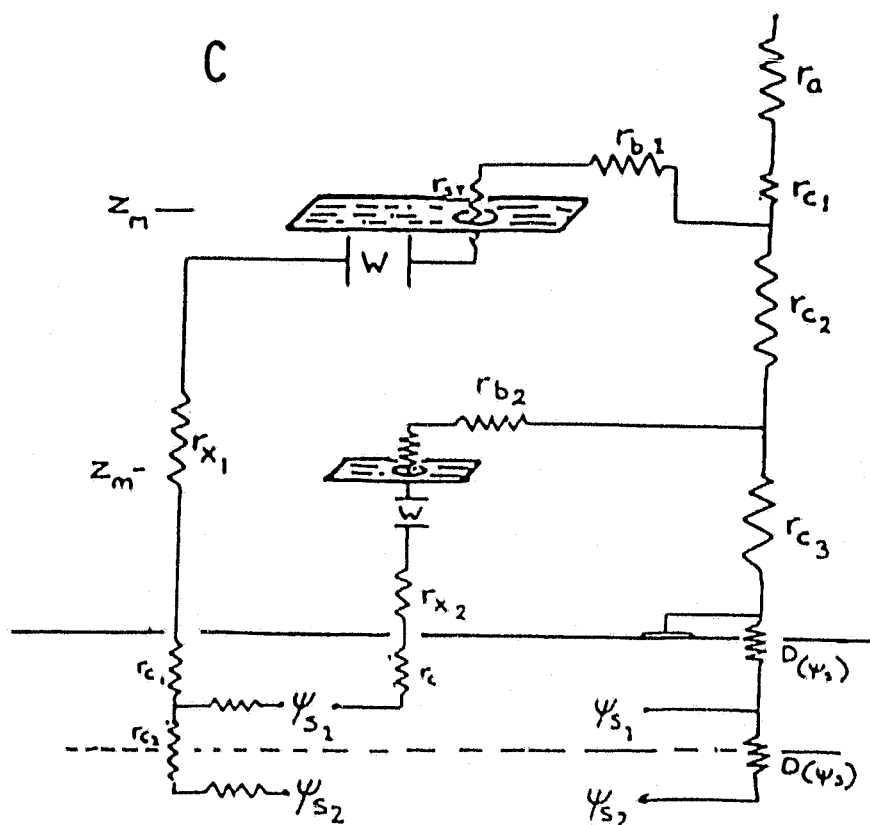
A.   Tropical rainforest vegetation; continuous canopy of tall
     trees above continuous under-storey.

B.   Leaf area density ▤ , stem area density ▨ , and
     root length density ▥ , as functions of height for the
     tropical rainforest shown in Figure A.

C.   Electrical resistance analogue of the tropical rainforest
     represented in Figure B.

INFLUENCE OF EVAPORATION ANOMALIES IN SEMI-ARID REGIONS ON JULY CIRCULATION

Y. C. Sud and M. Fennessy

In this study, two 47-day simulations were made with the general circulation model (GCM) of the Goddard Laboratory for Atmospheric Sciences (GLAS) starting from the observed initial conditions for June 15 (00Z) 1979 as produced by NMC analysis. In the first simulation, the soil moisture was normally initialized and then allowed to vary by the model generated surface water balance at each grid point. In the second simulation, the soil moisture was maintained at zero, yielding NO evaporation in each of the four chosen semi-arid regions shown in Table I. Elsewhere, the soil moisture was calculated as in the first simulation. The two runs were identical in all other respects.

The mean July precipitation in three out of four regions increased. These results are summarized in Table II. In the monsoonal regions of the Northern Hemisphere, particularly the Indian subcontinent, these results accord with a recent study by Shukla and Mintz (1982).

In each region the analysis revealed an increase in the mean monthly diabatic heating, vertical velocity and moisture convergence fields. Some increase in the moisture convergence due to an increase in the sensible heat flux (in the absence of evaporation) was to be expected. However, the overall influence of an overcompensation of the moisture deficit is truly surprising.

This study has supplemented an earlier study by Sud and Fennessy (1982) wherein the albedo was increased in the very same regions. The two studies together lead to the following conclusion. Of the two surface forcing parameters, the albedo and the soil moisture, when occurring in small semi-arid regions bordering deserts it is the influence of the albedo which tends to reduce the rainfall by producing diabatic cooling and subsidence. The evaporation anomaly influence, on the contrary, may largely compensate the moisture deficit by inducing moisture convergence caused by a corresponding increase in the sensible heat flux. It is, therefore, apparent that Charney's hypothesis which stipulated albedo increase as the primary mechanism for the feedback of a desert on itself is provided further support by this study. The role of soil moisture, though important, does not have such a positive feedback effect.

Charney et al. (1977), in their study with prescribed soil moisture, found a much larger influence of albedo changes on the precipitation as compared to Sud and Fennessy (1982). It can be argued that a part of the reason for the discrepancy between the two results is attributable to the prognostic soil moisture calculation in the latter study, which presumably had a negative feedback effect on the ensuing precipitation.

In interpreting the quantitative significance of these results, the limitations of the GCM must be recognized, particularly in parameterizations of the planetary boundary layer and convective clouds.

REFERENCES

Charney, J. G., W. J. Quirk, S. H. Chow, and J. Kornfield, 1977: A comparative study of the effects of albedo change on drought in semi-arid regions. J. Atmos. Sci., 34, 1366.

Shukla, J., and Y. Mintz, 1982: The influence of land surface evapotranspiration on earth's climate. Science, 215, 1498-1501.

Sud, Y. C., and M. Fennessy, 1982: A study of the influence of surface albedo on July circulation in semi-arid regions using the GLAS GCM. J. of Climatology, 2, 105-125.

Table I

Areal Extent of No Evaporation Anomaly Regions

#	Region	Number of Grid Points	Latitude	Longitude
1	Sahel	22	12°N-16°N 16°N-20°N	17.5°W-47.5°E 17.5°W-37.5°E
2	Thar Desert Border	4	24°N-32°N	67.5°E-77.5°E
3	Brazil	10	4°S- 8°S 4°S-20°S 4°S-24°S	32.5°W-37.5°W 37.5°W-42.5°W 42.5°W-47.5°W
4	Western Great Plains	8	32°N-48°N	97.5°W-107.5°W

Table II

Impact of Evaporation Anomaly on Simulated JULY

Regional Differences (Anomaly - Control)

REGION #	Geographical Location	Surface Balance W/m²		ΔSH Sens. Heat W/m² and %age	ΔE mm/day and w/m²	ΔP mm/day and %age	Δω ω=dp/dt µb/sec	ΔQ Diab. Heat W/m²	Δw Adiab. Heat W/m²	ΔTS/ΔTG and TS/TG (°C)
		ΔSW Shtwve. Radtn. and %age	ΔNR Net Radtn. and %age							
I	SAHEL	23.9 12.1% †	-4.4 2.2%	113.1 225%	-4.09 -113.4	0.36 6.4%	-0.241	142.7	-77.6	8.0/11.6 30.4/32.8
II	THAR DESERT	-29.0 -11.8%	-28.5 -15.3%	47.4 42.4%	-2.60 -75.3	2.67 72.2%	-0.358	148.5	-148.8	4.3/5.7 31.8/33.9
III	BRAZIL	14.3 7.2%	-9.6 6.7%	58.9 81.5%	-2.32 -67.5	-0.31 -13.9%	-0.040	65.9	-1.87	1.4/1.9 25.5/26.7
IV	GREAT PLAINS U.S.	2.6 1.0%	-8.5 4.4%	69.7 63.5%	-2.74 -78.9	0.28 9.9%	-0.156	89.6	-37.6	4.5/6.4 30.2/32.0

† Note: Percentage changes are based on the simulated values in the control run.

AN OBSERVATIONAL-DATA BASED EVAPOTRANSPIRATION FUNCTION
FOR A GENERAL CIRCULATION MODEL

Y. C. Sud and M. J. Fennessy

As described by Carson (1981), the evaporation calculation in various GCMs is of the form

$$E(Tg) = \beta(w,w^\star) \, Ep(Tg) \, , \tag{1}$$

where E is the actual evaporation, and Ep is the potential evaporation from the surface of the ground at temperature Tg and $\beta(w,w^\star)$ [hereafter β] is the evaporation coefficient and $w,w^\star$ are actual and saturation field capacities.

On the other hand, field measurements [e.g. Davies and Allen, 1973] usually give the moisture availability coefficient $M(w,w^\star)$ [hereafter M] which is defined as:

$$M = E(Tg)/Ep(Tg^\star). \tag{2}$$

Here $Tg^\star$ is the temperature of the saturated ground interacting with the atmosphere above. In order to use (1) to obtain E(Tg), a β function based on observational data, such as available in the form of the M function, is needed. Thus far, simple linear β functions have been used in various GCMs without even properly distinguishing between M and β.

For the experiment (Davies and Allen, 1973) a single relationship, $M = M(w,w^\star)$, was found by Nappo (1975) by averaging the measurements. A similar approach has been followed to derive the β function. A well known version of the GLAS GCM was modified to obtain two ground temperatures and two potential evaporations, from the naturally dry and saturated ground respectively. The β function values were derived from the daily mean evaporation fields (1). One hundred ensembles of equally spaced soil moisture between a minimum, of zero (dry), and a maximum of one (saturated), were used to calculate β from the last 31 days of simulation.

An examination of the β curve led us to a functional form of the type:

$$\beta = bw_f + cw_f^2 + aw_f^2/ (w_f^2 + \varepsilon). \tag{3}$$

The constant ε was introduced to produce a small curvature to the desired curve near the low soil moisture range of $w_f \to 0$. Values of the constants are given in Table 1. The corresponding β curve is shown in Fig. 1.

It must be noted that the β function derived in this analysis still gives a simple evapotranspiration function over global lands.

REFERENCES

Carson, D. J., 1981: Current parameterization of land surface processes in atmospheric general circulation model. JSC Study Conference on Land-Surface Processes in Atmosphere General Circulation Models, Jan. 5-10, NASA/Goddard Space Flight Center, Greenbelt, MD 20771.

Davies, J. A., and C. D. Allen, 1973: Equilibrium, potential and actual evaporation from cropped surfaces in southern Ontario. J. Appl. Meteor., 12, 649-657.

Nappo, C. J., Jr., 1975: Parameterization of surface moisture and evaporation rate in a planetary boundary layer model. J. Appl. Met., 14, 289-296.

Table 1

Text Reference	ϵ	a	b	c
Figure 2	0.075	.9333	.236	-.104
Figure 3	0.100	1.09	.087	-.078
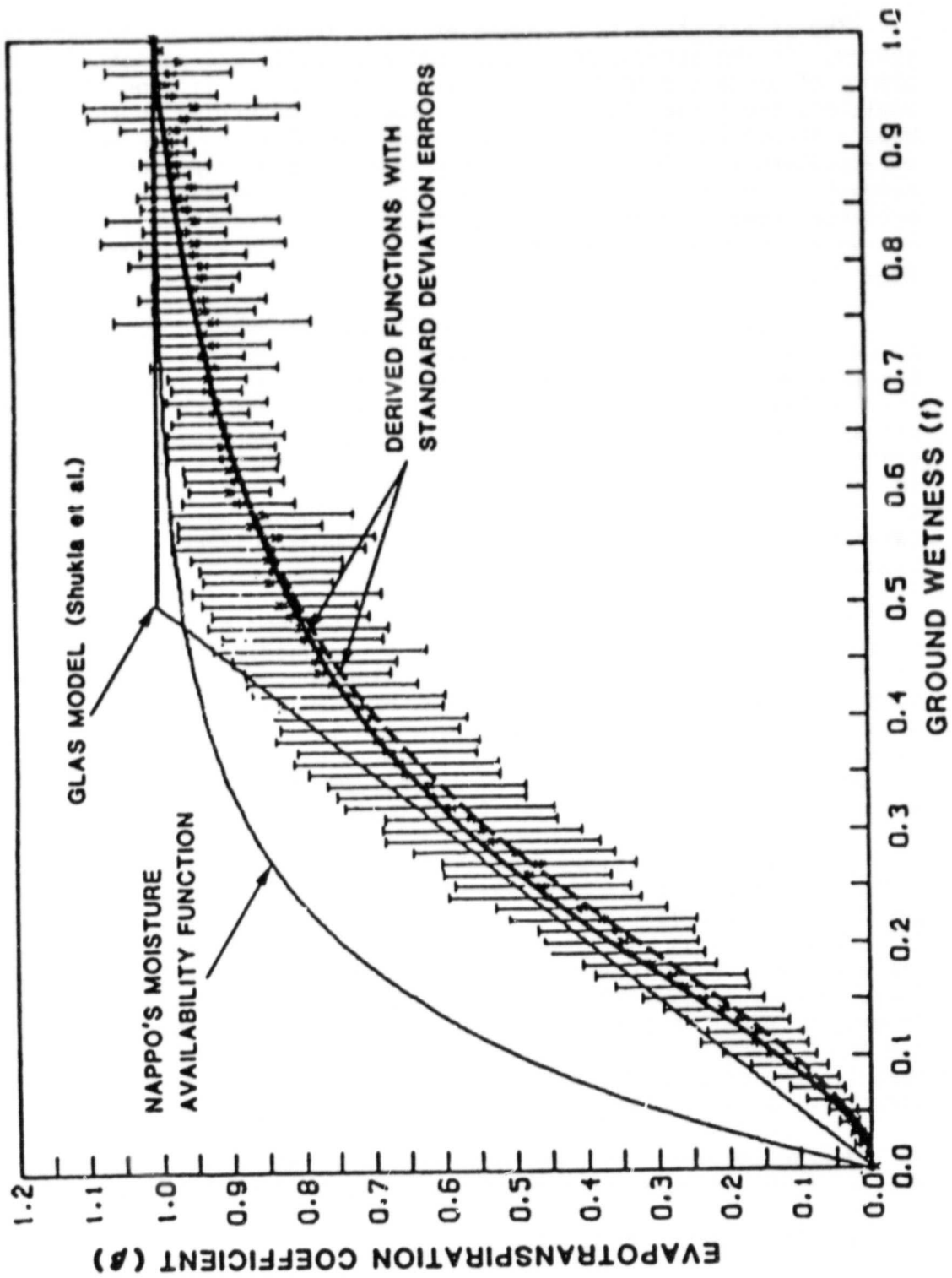
Figure 1

A STRATOSPHERIC VERSION OF THE GLAS CLIMATE MODEL

J. Abeles and D. Randall

The stratosphere is a region of great importance to the earth's climate system. In the stratosphere, the photochemically and radiatively active substance of ozone provides a shield which is vital to life on the planet. In addition, the large-scale dynamical processes occurring in the stratosphere can have a strong impact on the tropospheric circulation. The mere presence of a stratosphere is helpful in correctly modeling the troposphere, because the removal of the model top to a very high altitude where significant dissipation processes come into play mitigates false wave reflections due to the rigid top boundary condition (Lindzen et al., 1968; Kirkwood and Derome, 1977; Mechoso et al., 1982).

To successfully model the troposphere-stratosphere system, it is necessary to take full account of the tropospheric processes that significantly influence the stratosphere. These involve a very wide range of space and time scales. They include vertically propagating planetary waves, the influence of tropospheric clouds on the upwelling long-wave radiation at the tropopause, deep moisture transport by the Hadley cell, and the possible forcing of the semidiurnal tide in the lower stratosphere by cumulus heating. All of these processes are strongly influenced by the release of latent heat, which is determined by the parameterized processes of the planetary boundary layer (PBL) and cumulus convection.

We are conducting a study to examine the impact of these processes on the stratosphere by directly comparing the tropospheric forcing of the stratosphere and the simulated stratospheric circulations produced by two models whose tropospheres differ only in their treatment of diabatic heating. Although existing observational data on the stratosphere are too meager to allow a detailed comparison of model results with observations, particularly for the tropics and for seasonal variations (Hudson and Reed, 1979), gross comparisons are feasible and are an important objective of our study.

The first model is based on the potential-enstrophy-conserving GLAS Climate Model (hereafter the GLAS model). This model incorporates the tropospheric physical parameterizations of the model described by Shukla et al. (1982), including a cumulus parameterization based on the theory of Arakawa (1969), and a planetary boundary layer (PBL) parameterization based on the work of Katayama (described by Arakawa, 1972). In the past, the GLAS Climate Model has used nine layers, of equal thickness in sigma, with the model's top at 10 mb. Although the 10 mb surface is well within the stratosphere, the top model layer was so deep (on the order of 15 km) that the model could not resolve any stratospheric structure; we effectively had a tropospheric model.

During the past year, we have created a new, stratospheric version of the model. This new model differs from the old in the following respects:

1) the model's top is at 1 mb;

2) there are 15 layers, in all;

3) a pressure coordinate system is used above 100 mb;

4) the eight sigma-layers below 100 mb are of equal thickness, to accommodate certain restrictive assumptions built into the GLAS cumulus parameterization, but the seven pressure-layers above 100 mb can have arbitrary thicknesses;

5) ozone has been introduced as a prognostic variable, and the simple ozone photochemistry parameterization of Schlesinger and Mintz (1979) has been incorporated into the model;

6) the Wu-Kaplan long-wave radiation parameterization has been replaced by the Schlesinger-Mintz parameterization;

7) the solar radiation parameterization has been generalized by R. Davies, of Purdue University, to allow a general distribution of ozone, and an arbitrary number of model layers with arbitrary thicknesses.

The second model is based on the UCLA model developed by Arakawa and collaborators at UCLA, and currently running at GSFC (Abeles, Corsetti, and Randall, this volume). This model incorporates the Arakawa-Schubert-Lord-Chao cumulus parameterization and the Randall PBL parameterization.

The two models are essentially identical except for their differing parameterizations of cumulus convection and the PBL. This will allow us to study the effects of these two key tropospheric physical parameterizations on stratospheric circulations, by performing numerical experiments in which the two models are run with identical initial and boundary conditions. We will place special emphasis on comparison of the model results with respect to vertically propagating planetary waves, upwelling long-wave radiation at the tropopause, deep moisture transport by the Hadley cell, and cumulus forcing of the semidiurnal tide of the lower stratosphere.

Currently, the stratospheric GLAS model has been debugged, and a January simulation is under way. A January simulation has been completed with the 15-level UCLA GCM. Comparison of the results obtained with the two models will begin in the near future.

REFERENCES

Arakawa, A., 1969: Parameterization of cumulus convection. Proc. WMO/IUGG Symposium on Numerical Prediction in Tokyo, IV8, 1-6.

Arakawa, A., 1972: Design of the UCLA General Circulation Model. Numerical Simulation of Weather and Climate. Technical Report No. 7, Dept. Meteorology, University of California, Los Angeles, 116 pp.

Hudson, R. D., and E. I. Reed, eds., 1979: The stratosphere: Present and future. NASA RP-1049.

Kirkwood, E., and J. Derome, 1977: Some effects of the upper boundary condition and vertical resolution on modeling forced stationary planetary waves. Mon. Wea. Rev., 105, 1239-1251.

Lindzen, R. Ss., E. S. Batten, and J.-W. Kim, 1968: Oscillations in atmospheres with tops. Mon. Wea. Rev., 96, 133-140.

Mechoso, C. R., M. J. Suarez, K. Yamazaki, J. A. Spahr, and A. Arakawa, 1982: A study of the sensitivity of numerical forecasts to an upper boundary in the lower stratosphere. Mon. Wea. Rev., 110, (to appear).

Shukla, J., D. Straus, D. A. Randall, Y. Sud, and L. Marx, 1982: Winter and summer simulations with the GLAS climate model. NASA Technical Memorandum 83866, 282 pp.

SEASONAL CYCLE SIMULATION

L. Marx and D. Randall

The GLAS climate model is being used in studies of the predictability of monthly and seasonal means, and in tests of the sensitivity of the general circulation to boundary forcings such as anomalies of sea surface temperature or soil moisture. Recently, the model has been run for over two simulated years, to test its response to noninteractive annually varying boundary conditions.

The past two years have seen major improvements in model performance, as a result of several revisions of the model's numerical schemes and physical parameterizations. The principle changes to the model are:

1. New boundary layer parameterization;

2. New parameterization of evapotranspiration from land surfaces;

3. New parameterization of the interaction between clouds and radiation;

4. New scheme to maintain computational stability near the poles;

5. New vertical differencing scheme;

6. New tape format;

7. New postprocessing package.

These changes are described by Randall (1982). The model code has been completely rewritten for improved speed and readability, and we have produced a comprehensive documentation. The model is running on the new Cyber 205 computer at GSFC. It uses approximately 3 cpu minutes per simulated day.

A completely new postprocessing package has been designed to aid in the study of the model results. The synoptic records described above are written to tape in sigma coordinates. A program has been created to read one or more of these sigma-history records, interpolate to constant pressure surfaces, and write the results to tape. Another program is used to create tapes containing time-averages of these pressure history tapes. An elaborate plot package has been developed to generate plots of individual pressure history records, time averages, or differences between time averages. Finally, grid-point history records can be sorted by grid point, and plotted as simple plots against time (e.g., the record of precipitation at a grid point) or as time-height contour plots (e.g., of total diabatic heating).

Two changes were made to the boundary conditions for this run. First, the topography was revised to assign more realistic heights to Greenland. Second, the seasonally varying ground wetness data of Mintz and Serafini (1983) was included as an additional boundary condition, i.e., the ground wetness was made non-interactive.

The first 300 days of the run were carried out on the Cyber 203 at the Langley Research Center, and the remainder was completed on the Cyber 205 at GSFC. The model incidentally served as a benchmark for the newly installed Cyber 205. The running speed improved by a factor of 2.5 on the Cyber 205, as compared with the Cyber 203.

The model was initialized with the observed state of the atmosphere for 00Z, November 15, 1978. The initial ground temperatures for both the grid box and the small saturated plot were assumed to be equal to the surface air temperature. The initial snow boundaries were obtained from the climatological data of Matson (1977), and the initial snow depths were specified as functions of the surface albedo.

The results of the run, represented by monthly mean plots of several hundred prognostic and diagnostic fields, indicate realistic responses to the variations in the boundary conditions. There are realistic annual variations in the sea level pressure, geopotential height, and other fields over the two years of integration. The global and hemispheric means of potential temperature, kinetic energy, precipitation and evaporation also show realistic seasonal variations. Some results are shown in Figs. 1 and 2.

Perhaps the most serious deficiencies in the results are the familiar "cold-pole" problem, and an excess of low-level stratiform cloudiness. These problems are being addressed in ongoing research.

REFERENCES

Matson, M., 1977: Winter snow-cover maps of North America and Eurasia from satellite records, 1966-1976. NOAA Tech. Memo. NESS84, Washington, DC, 28 pp.

Mintz, Y., and V. Serafini, 1983: Monthly normal global fields of soil moisture and land-surface evapotranspiration. International Symposium on Variations in the Global Water Budget. Oxford, England, August 10-15, 1981. (Manuscript in preparation).

Randall, D. A., 1982: Monthly and seasonal simulations with the GLAS Climate Model. Proceedings of the Workshop on Intercomparison of Large-Scale Models Used for Extended Range Forecasts of the European Centre for Medium-Range Weather Forecasts, Reading, England (to appear).

SEA LEVEL PRESSURE
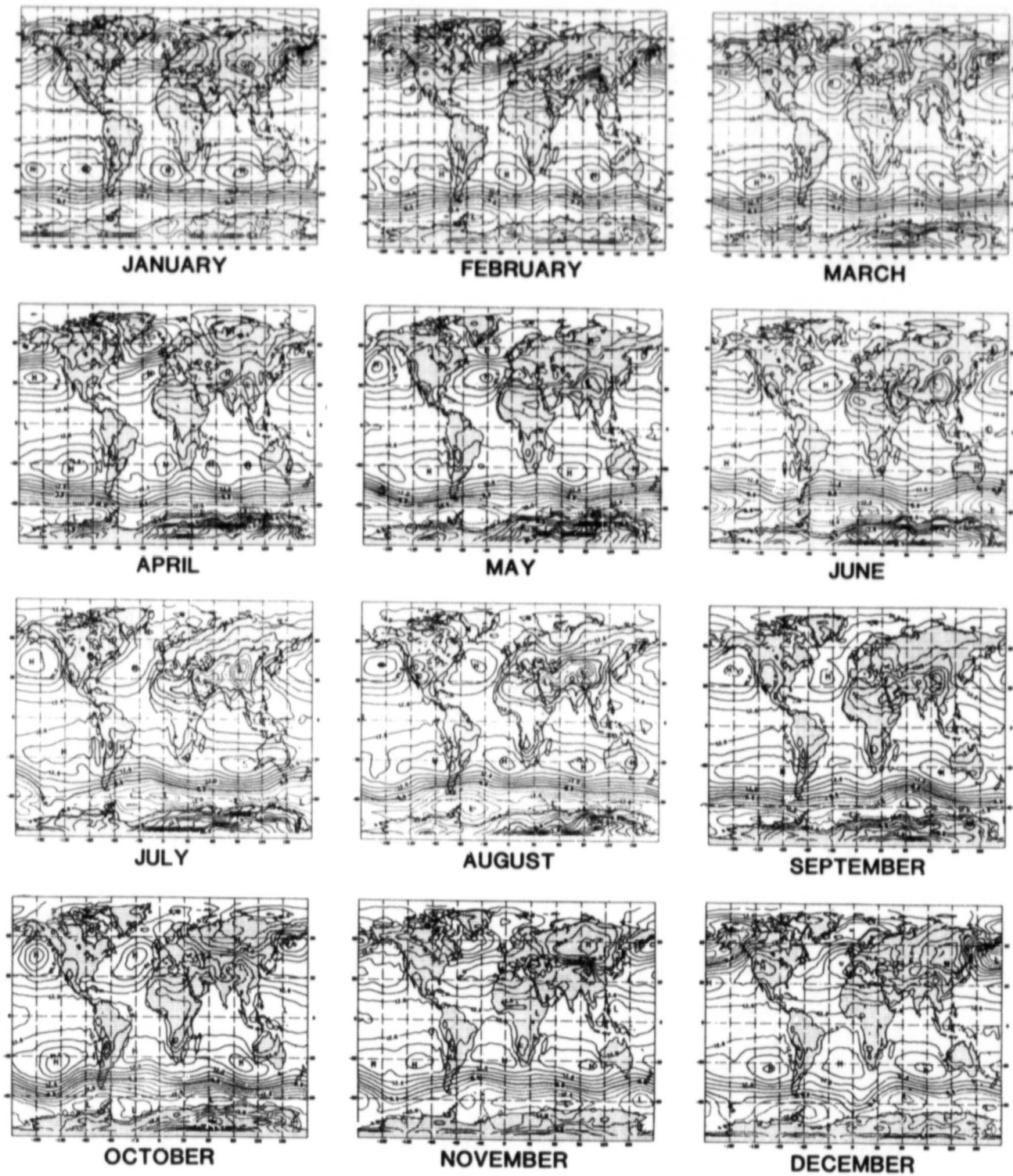
JANUARY

FEBRUARY

MARCH

APRIL

MAY

JUNE

JULY

AUGUST

SEPTEMBER

OCTOBER

NOVEMBER

DECEMBER

Figure 1

JANUARY

FEBRUARY

MARCH

APRIL

MAY

JUNE

JULY

AUGUST

SEPTEMBER

OCTOBER

NOVEMBER

DECEMBER
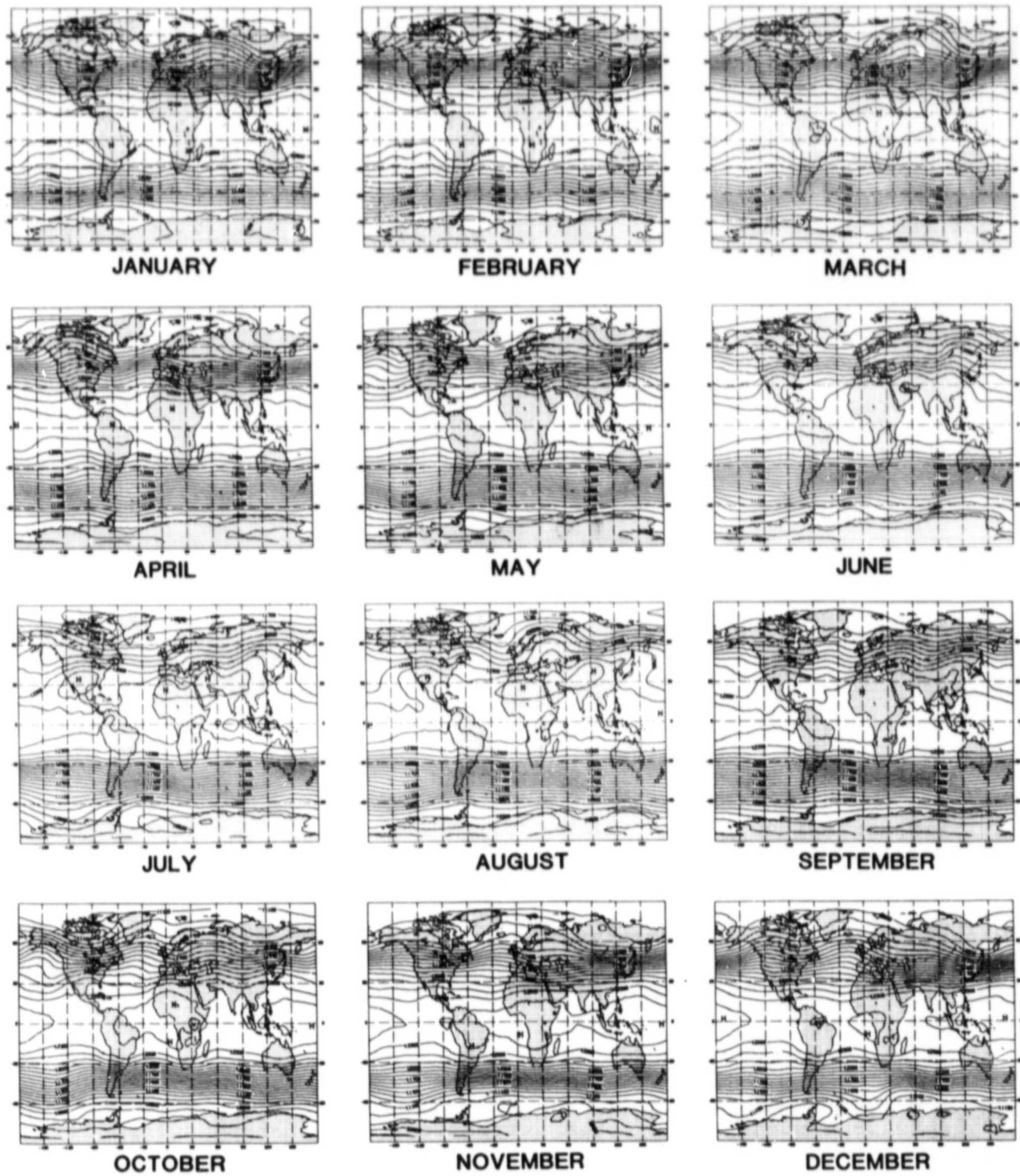
Figure 2

AN OBSERVATIONAL STUDY OF LARGE SCALE ATMOSPHERIC ROSSBY WAVES

R. S. Lindzen, D. M. Straus, and B. Katz

Analyzed global 500 mb data from the National Meteorological Center for the period 1 January 1975 to 28 February 1975 are used to determine phase and amplitude as functions of time for westward traveling Rossby waves. The methodology consisted of projecting the data (at each time) onto Hough functions, followed by band pass filtering to retain only westward propagating fluctuations in a broad period range. The first three meridional and zonal wavenumbers were studied, and in most cases Rossby waves with phase speeds close to theoretical expectations were found.

It is clear that steady phase propagation does not occur (see Figure 1 as an example). Typical intervals between breakdowns in uniform phase progression are comparable to the wave period. Such breakdowns are generally associated with minima in wave amplitudes. This picture is consistent with episodic wave generation and subsequent frictional decay. While inviscid, steadily propagating Rossby waves are not expected to interact with the mean flow (averaged over Rossby wave periods), the same is not true for damped waves. Our analysis clearly demonstrates the damped character of atmospheric Rossby waves. How important such waves are to atmospheric transport remains to be determined.
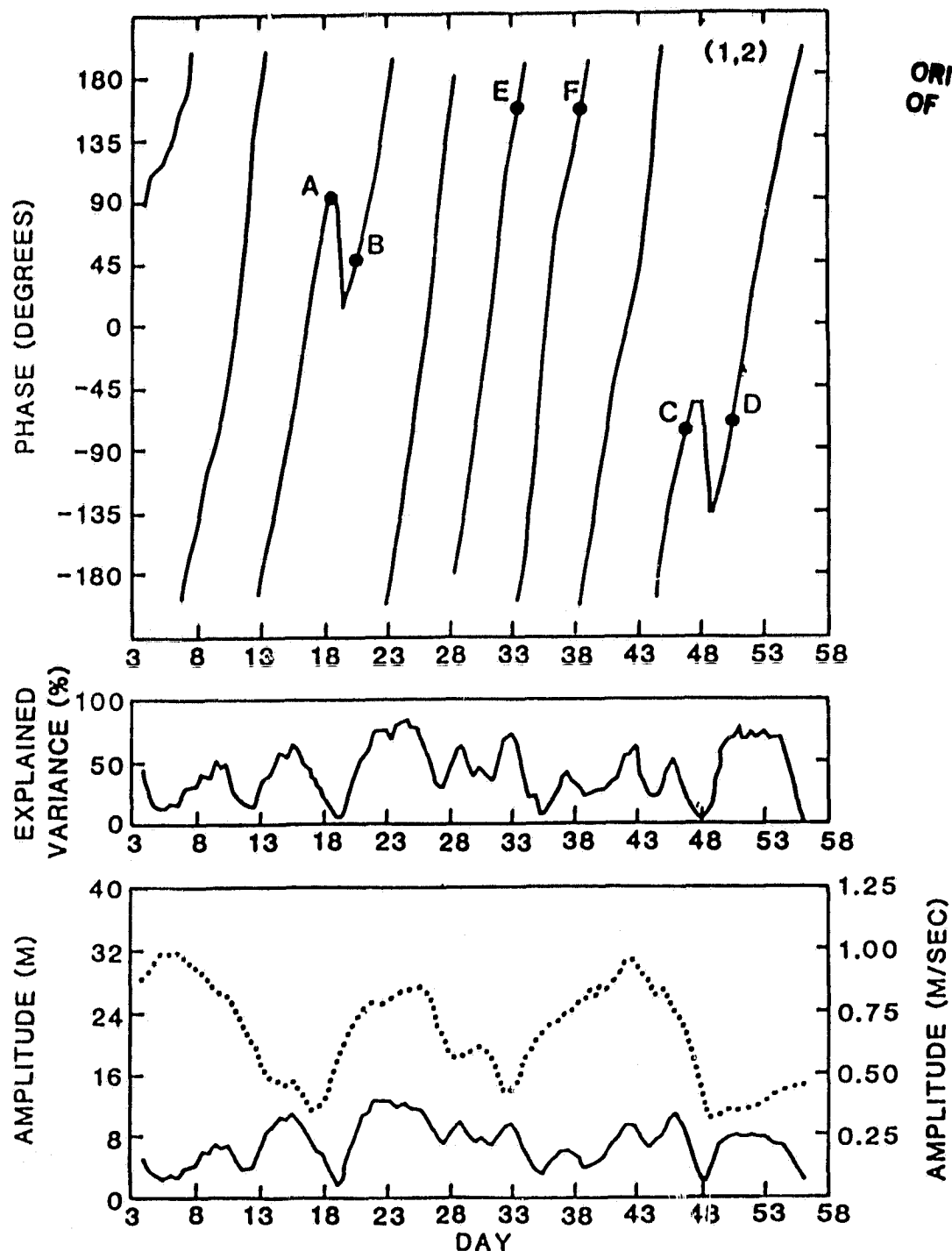
Figure 1. The behavior of the (1,2) Rossby mode (zon·l wavenumber 1, one zero crossing between the poles). The phase convention is that phase increases for westward propagation. The solid line in the lowest box is the amplitude (use the left-hand scale for the height field, the right-hand scale for the wind field). The dotted line in the lowest box is the amplitude of the average Hough mode, where the average was taken over rolling blocks of length 6.5 days. The middle box gives the percentage of the total variance of the Hough mode projection over a particular block that was explained by the Rossby wave.

ON THE ROLE OF THE SEASONAL CYCLE

D. M. Straus

The periodic change in the general circulation and local climate (i.e. the seasonal cycle) stands out as the most noticeable climate signal on time scales less than a decade or so. The resulting non-stationarity in the mean is not taken into account in the conventional statistical framework in which transients are considered to be departures from the time mean. A more natural definition of transients is the departure from the seasonal cycle.

The seasonal cycle can be defined in terms of a few orthogonal polynomials, as described in detail by Straus (1983). This is particularly useful when only short time series are available, so that ensemble averaging is not possible. The choice of polynomials depends on the length of the time series in question; the seasonal cycle is the projection of the original series onto the subspace of the chosen polynomials. This insures that the time average of any product of variables over the record length equals the sum of the time average of the product of the seasonal cycle contributions and the time average of the product of transient terms, with no cross terms. If the time average is taken over a period less than the record length, cross terms (or interaction terms) are involved and must be interpreted.

An interesting example of the importance of interaction terms is presented in Straus (1983). The 200 mb eddy momentum flux (zonally averaged) is examined from a 7-year record. The harmonic sines and cosines form a natural basis set with which to describe the seasonal cycle, which then consists of the 7-year time mean and oscillations of periods one year and 1/2 year. The remaining fluctuations are then divided up (using Fourier analysis once more) into medium frequency fluctuations (periods of 7.2 days down to the Nyquist frequency of two days) and low frequency fluctuations (involving periods of 7.2 days to 7 years, excluding the annual and semiannual cycle). The focus here is on the interannual variability of the eddy momentum flux. Winter (December through February) averages of the flux were examined for each of the 7 years. Since the time averaging period (3 months) is not identical to the record length over which the seasonal cycle is defined (7 years), interaction terms are present. Thus, for any one winter, the total eddy momentum flux is the sum of a seasonal cycle contribution, a low frequency contribution, a medium frequency contribution, and interactions between these different time scales. It turns out that the only interaction term of importance is that involving the low frequency signal and the seasonal cycle. This term explains most of the interannual variability seen in the total eddy momentum flux (see Fig. 1. This indicates that the low frequency anomalies themselves are not primarily responsible for the interannual variability of the fluxes. Rather, it is their positioning in time with respect to the seasonal cycle that is important. It is hoped that these concepts will prove useful in the study of mid-latitude blocking and the phenomenon of El Nino.

REFERENCE

Straus, D. M., 1983: On the role of the seasonal cycle. J. Atmos. Sci., 40, to be published.
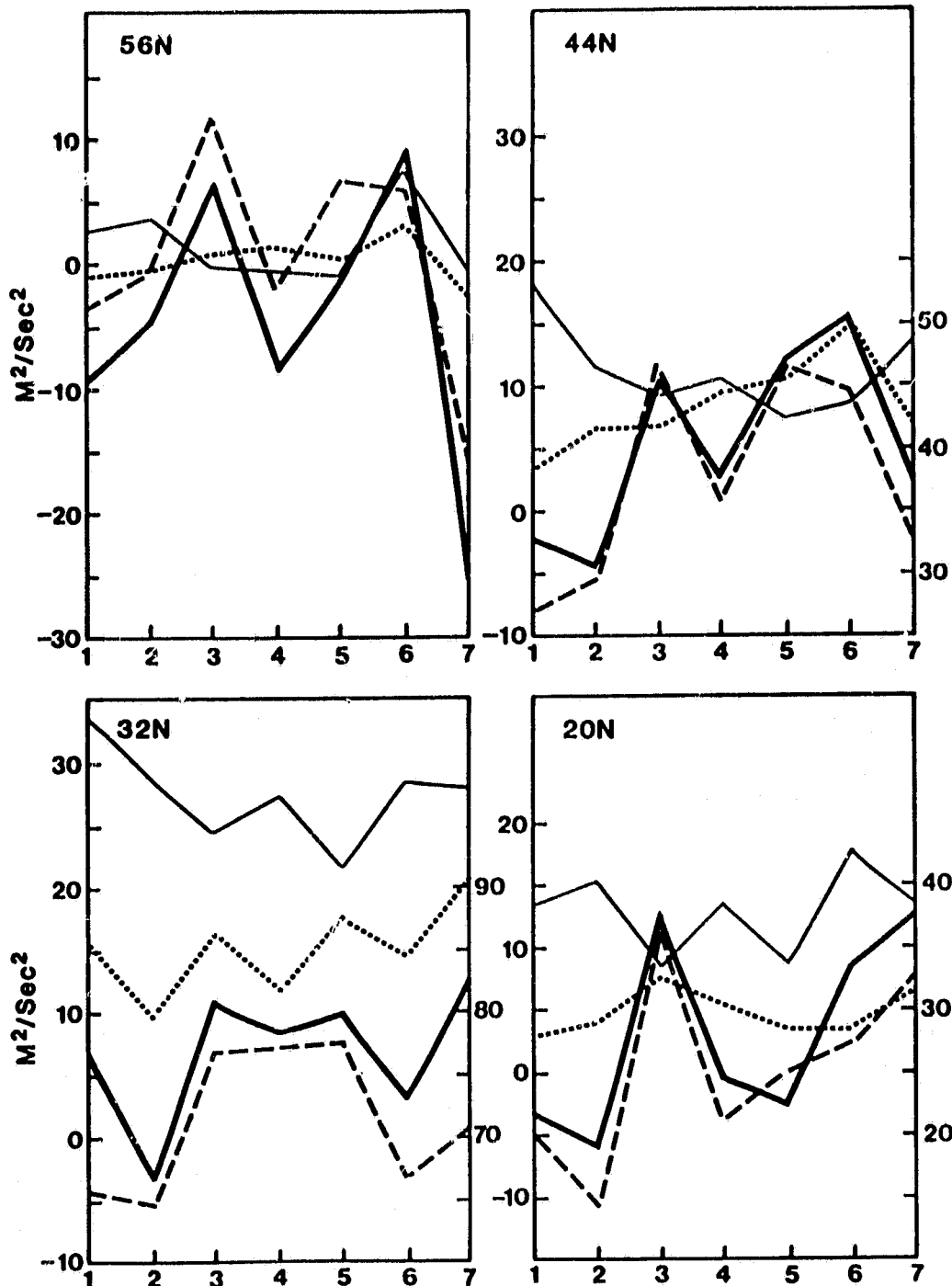
Figure 1. Winter averaged, zonally averaged eddy momentum flux
at 200 mb as a function of year (labelled 1 to 7) at
different latitudes. The heavy solid line is the
total flux, the light solid line is the flux due to
the low frequency components, the dotted line is the
flux due to the medium frequency components and the
dashed line gives the flux due to the low frequency-
seasonal cycle interactions. When a separate momentum
flux scale is given as the right side of a panel, it
refers to the total flux only.

C. SENSITIVITY EXPERIMENTS

INFLUENCE OF SOIL MOISTURE ON CLIMATE

J. Shukla and Y. Mintz

The Goddard Laboratory for Atmospheric Sciences (GLAS) Climate Model has been used to conduct a numerical experiment to determine the influence of soil moisture on climate (Shukla and Mintz, 1982). The model was run for 60 days with two assumed extreme global conditions of soil moisture, dry and saturated; for dry soil evaporation from the land surfaces in zero, and for saturated (wet) soil the evaporation equals the potential evapotranspiration. The differences in the simulated atmospheric circulations were enormous. For example, over most of North America and Europe the simulated rainfall for dry soil was about 40 percent less compared to the wet soil. The study showed that evaporation from land is an important factor in determining the rainfall over land. The results from this experiment suggest the important role of soil moisture in the inter-annual variability of climate and indicate that global observations of soil moisture can provide potential predictability for monthly and seasonal anomalies in the atmospheric circulation.

DESCRIPTION OF FIGURES

The top panel shows the annual and global mean water budget. The annual mean evaporation over land (41 cm) is about 60% of the annual mean precipitation over land (72 cm). The runoff from land to ocean is 31 cm.

The lower three panels show the results of the numerical experiment.

(a) Ground temperature: Difference [dry soil (no evaporation) - saturated soil (maximum evaporation)] for July in (°C).

   ° Positive values mean a warmer ground temperature. When land is dry, all of the solar radiation goes to heat the ground (and none to evaporate the water) and ground temperatures are very high.

(b) Sea level pressure: Difference [dry soil (no evaporation) - saturated soil (maximum evaporation)] for July in (mb).

   ° Maximum reductions of pressure occur over land for the dry soil case in the Northern Hemisphere. A compensating increase in pressure occurs over oceans.

(c) Precipitation: Difference [dry soil (no evaporation) - saturated soil (maximum evaporation)] for July in mm/day.

   ° In the case of dry soil, there is a significant decrease of precipitation over land over most of the globe except for the monsoon regions. Over the Indian monsoon region, large surface heating creates very large moisture flux convergence (moisture comes from the adjoining ocean) and leads to larger precipitation.

° Globally averaged precipitation (over land and ocean) in the dry soil
  case is reduced by about 18% of the saturated soil case. Globally
  averaged precipitation over land only is reduced by about 54% of the
  saturated soil case.

REFERENCE

Shukla, J., and Y. Mintz, 1982: Influence of land-surface evapotranspiration
    on the earth's climate. Science, 215, 1498-1501.

ANNUAL AND GLOBAL MEAN WATER BUDGET
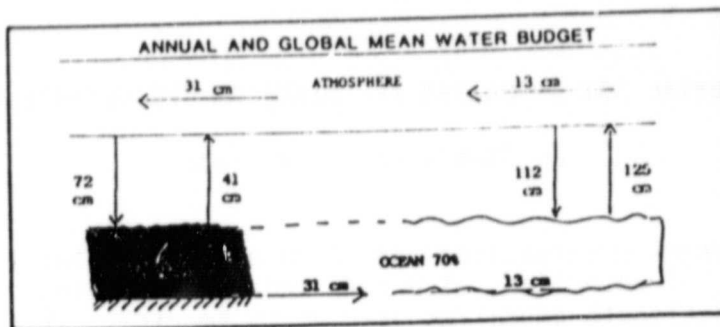
Difference between two model simulations (dry soil - wet soil)
for the month of July for (a) ground temperature (°C), (b) sea
level pressure (mb), and (c) rainfall (mm/day).
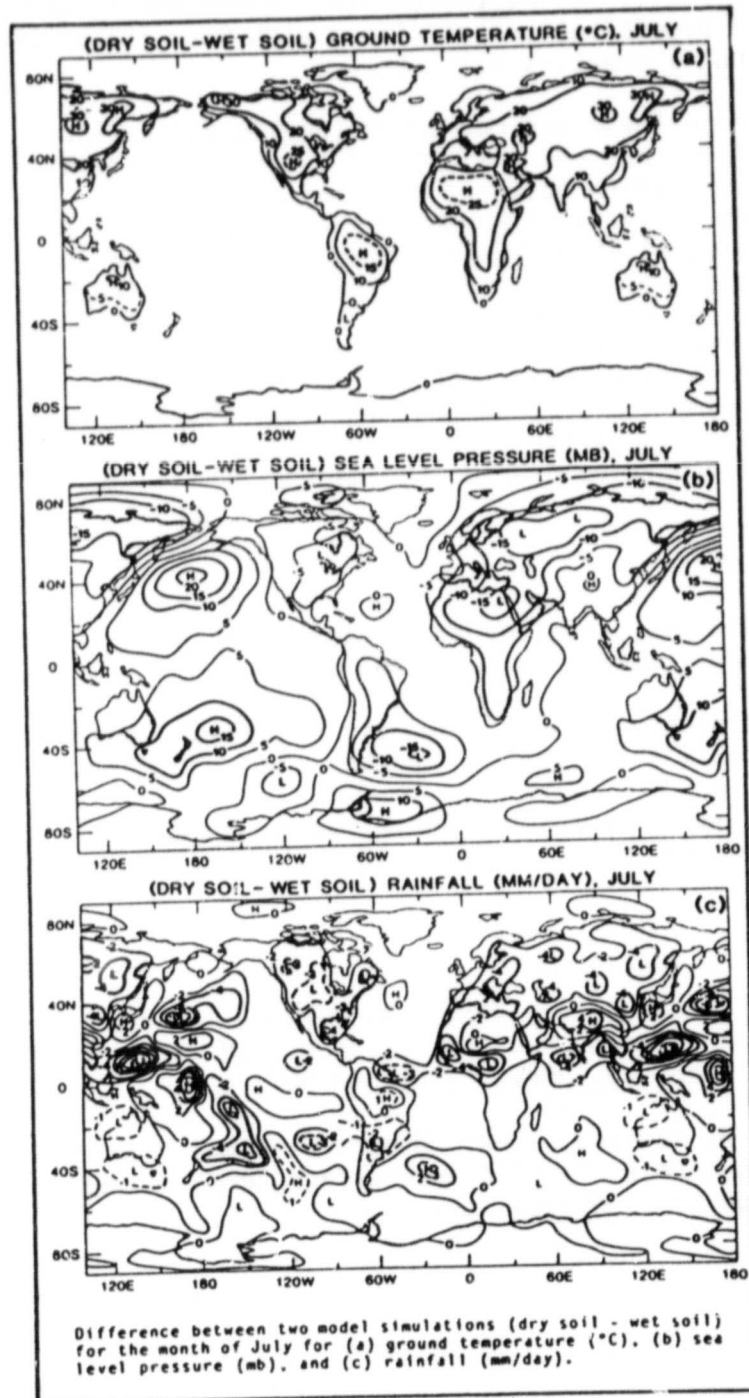
INFLUENCE OF EQUATORIAL SST ANOMALIES (EL NINO) ON THE CLIMATE OF NORTH AMERICA

J. Shukla and M. Wallace

A number of recent observational and theoretical studies indicate that the equatorial Pacific SST anomalies, also referred to as El Nino events, can produce significant climate anomalies over North America. This phenomenon is illustrated schematically in the bottom panel where the shaded area represents a zone of enhanced precipitation associated with warm SST anomalies which force a wave pattern along a great circle path.

A numerical experiment was conducted (Shukla and Wallace, 1982) with the GLAS climate model to test the validity of the above hypothesis with January initial conditions based on observed data and an equatorial Pacific SST anomaly based on the recent analysis of Rasmusson and Carpenter (1982) shown in the top panel. The middle panel shows the difference between the anomaly and control integrations averaged for days 11-30 for geopotential height at 300 mb. Positive and negative values of height differences indicate areas of warmer and colder air temperatures, respectively. It is seen that the maximum changes occur over North America. These results further confirm the earlier suggestions based on observational and simple model studies, and highlight the importance of equatorial Pacific SST anomalies in variability and predictability of monthly and seasonal mean atmospheric circulation over North America.

DESCRIPTION OF FIGURES

Top Panel: Observed SST anomalies averaged for Nov., Dec., and Jan., for four El Nino episodes (Rasmusson and Carpenter).

Middle Panel: Difference (anomaly-control) of 300 mb height averaged for days 11-30. The thick solid contour denotes the zero value.

Bottom Panel: Schematic representation of upper tropospheric teleconnection patterns associated with tropical rainfall anomaly over the shaded region.

REFERENCES

Rasmusson, E., and T. Carpenter, 1982: Variations in tropical sea surface temperature and surface wind fields associated with the Southern Oscillation/El Nino. Mon. Wea. Rev., 110, 354-384.

Shukla, J., and J. M. Wallace, 1982: Numerical simulation of the atmospheric response to equatorial Pacific sea surface temperature anomalies. Submitted for publication to J. Atmos. Sci.

OBSERVED SST ANOMALY (°C) DURING EL NINO

(a)

DIFFERENCE (ANOMALY-CONTROL) 300 MB HEIGHT (M)

(b)

SCHEMATIC PRESSURE FIELD DURING EL NINO

(c)

Influence of equatorial Pacific SST anomalies on climate over
North America. (a) Observed El Nino anomalies, (b) Difference
(anomaly - control) of two model simulations for 300 mb height
(m), (c) Schematic representation.
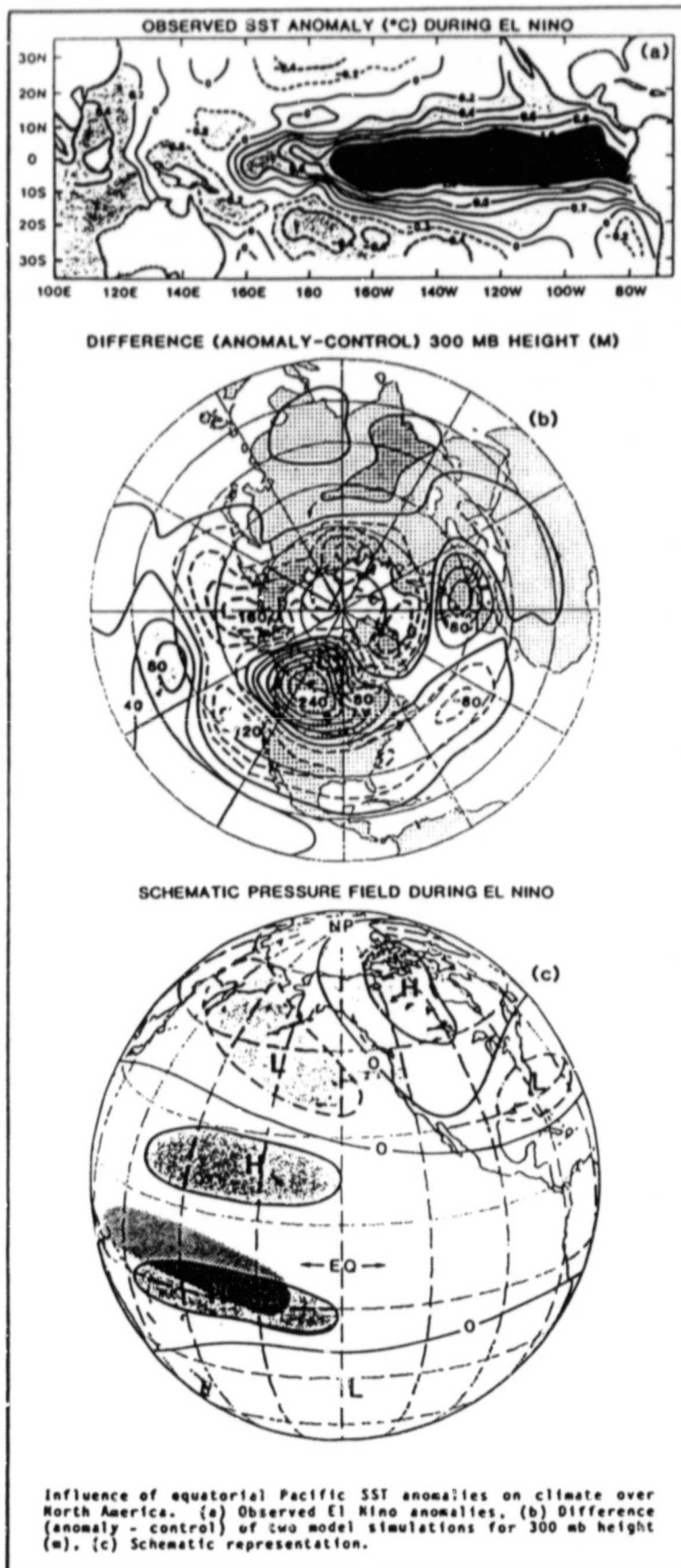
QUASI-STATIONARY STATES AND EDDY-MEAN FLOW INTERACTION IN A WIND-FORCED BAROCLINIC OCEAN MODEL

K. C. Mo, E. Kalnay and D. E. Harrison

We present results from a square basin, steadily forced non-linear two-level quasigeostrophic ocean model experiment, designed to study the effects of mesoscale motions on the mean flow. A conventional calculation of the behavior resulting from spin up from rest leads to the appearance of baroclinic eddies after about 800 days of integration, followed by a statistical equilibrium in which the eddies are prominent. The mean statistical equilibrium flow (SEQ) is similar to others which have been discussed previously, although we employ a different numerical method. We also present two quasistationary (QS) solutions to the same model ocean system, found using an iterative scheme that damps out time dependent modes, thus suppressing the appearance of eddies. The QS solutions result from convergence of the eddy-suppressing scheme started from different initial conditions. We find that the RMS value over the basin of the time derivative of the potential vorticity (R) of the QS solutions is: 1) locally minimum in the sense that small perturbations to the QS solution increase R and 2) R_{QS} is much smaller than the RMS of the other terms in the model potential vorticity equation. We find also that $R_{QS} \ll R_{SEQ}$.

When the first guess for the iterative scheme is a state of rest, the system converges to a quasistationary solution denoted QS1. From any other of our initial guess states, the scheme converges to a second quasistationary solution, QS2. QS1 resembles the state of wind driven ocean attained after about 350 days integration from rest, whereas QS2 resembles the state of the ocean after about 650 days of integration.

When QS1 is used as the initial condition in a conventional time integration, a recirculating gyre mode grows linearly with time for about 400 days, even after the mode has attained an amplitude of the same order as QS1. This linear growth ceases only when the flow becomes baroclinically unstable and eddies start to develop. Thereafter the SEQ solution is recovered. We discuss the dynamics of this resonant, linearly growing mode; it is not simply an inertial gyre. QS2 resembles QS1 plus the linearly growing mode after 400 days. When QS2 is used as initial condition, linear growth also occurs but the flow becomes baroclinically unstable much faster.

The role of the baroclinic eddies in this model ocean is studied in terms of the differences between SEQ, the statistical equilibrium solution obtained in the presence of eddies, and QS2, the second and most intense quasistationary solution. Overall, the eddies weaken the mean upper layer flow in the recirculation, and alter the mean lower layer circulation signficantly.

FIGURE CAPTIONS

Figure A: The upper level streamfunctions ψ_1 for SEQ in 100 m^2/s; contour interval 4000 m^2/s.

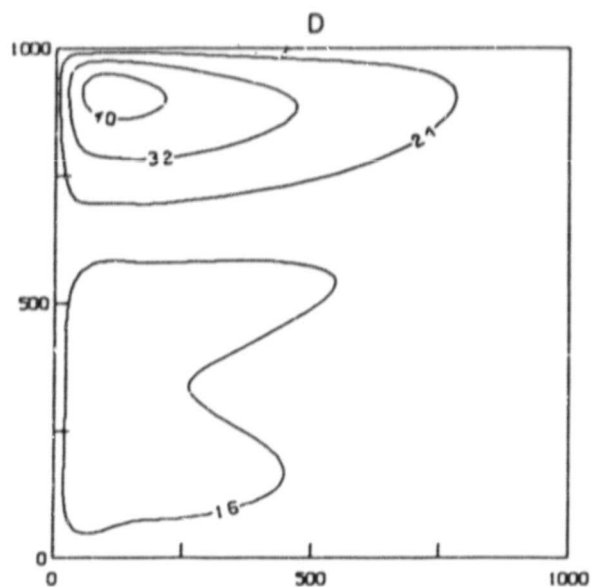Figure B: The lower level streamfunctions ψ_3 for SEQ in 100 m^2/s; contour interval 800 m^2/s.
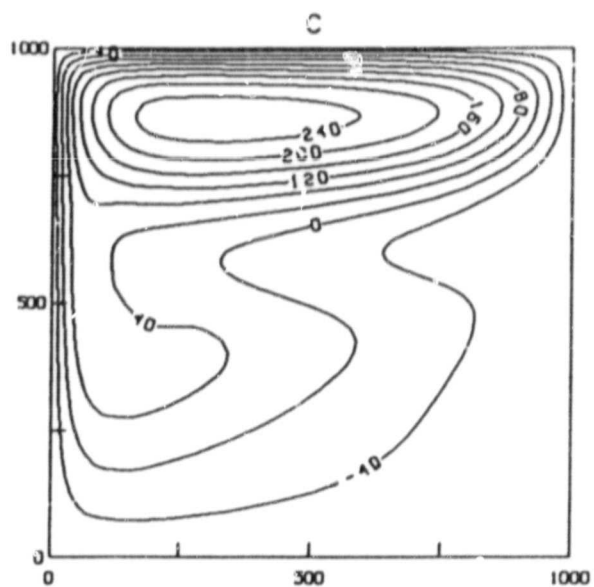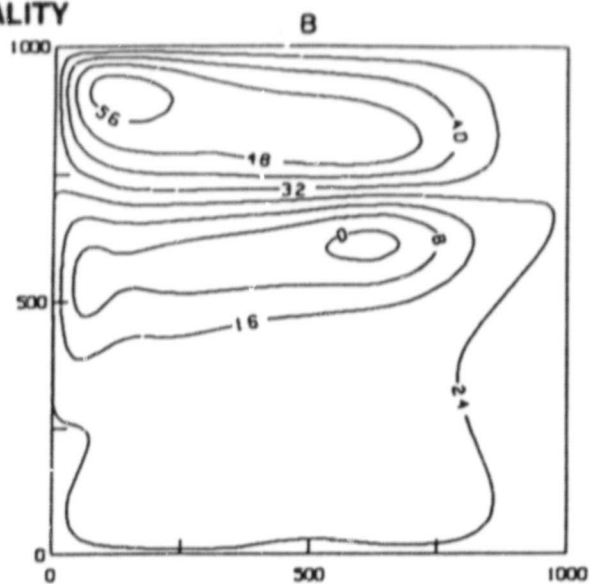
Figure C: Same as Figure 6a but for QS1.

Figure D: Same as Figure 6b but for QS1.

Figure E: Same as Figure 6a but for QS2.

Figure F: Same as Figure 6b but for QS2.
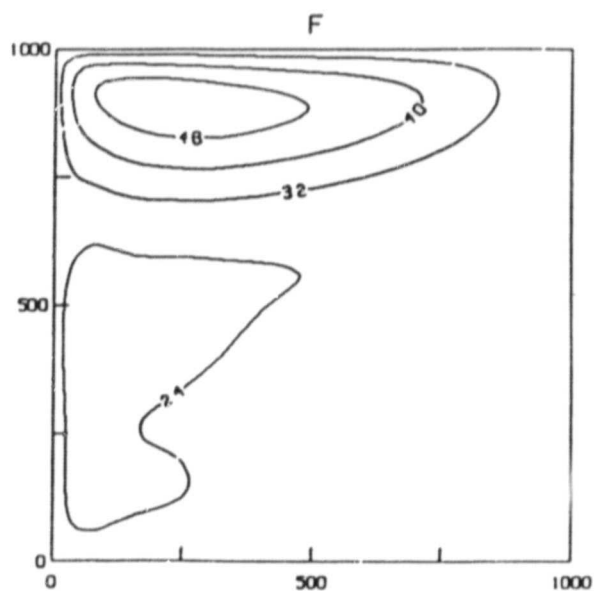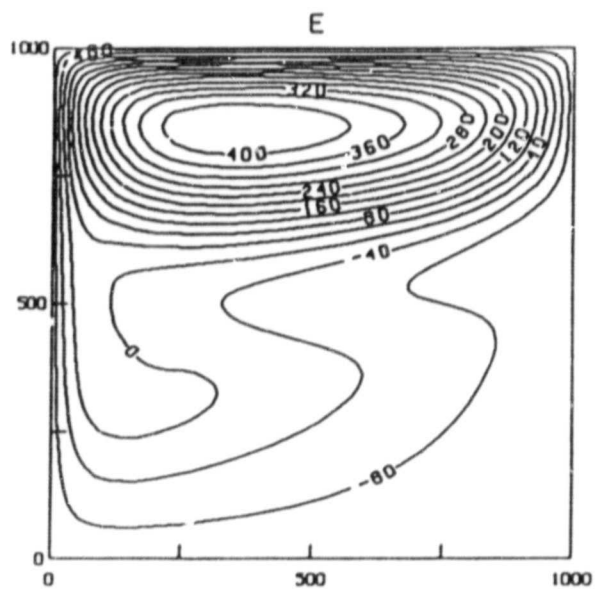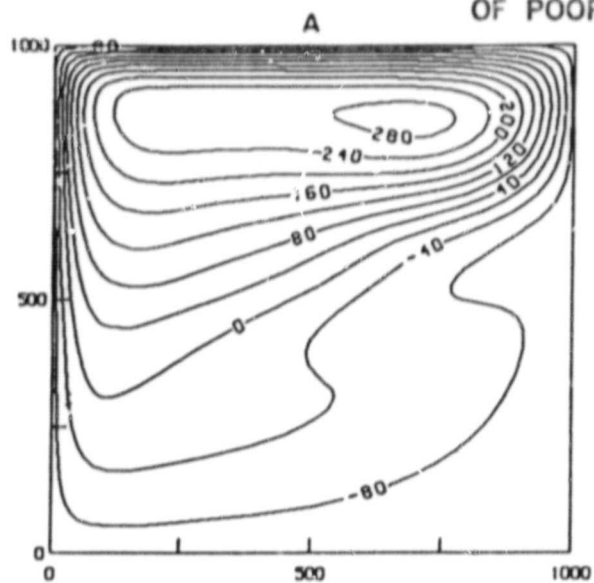
IV. CYBER CONVERSION

EXPERIMENTS WITH THE UCLA GCM

J. Abeles, T. Corsetti, and D. Randall

1. MOTIVATION

The UCLA General Circulation Model, developed over a period of two decades by A. Arakawa and collaborators at UCLA, has many features in common with the current GLAS Climate Model, yet it offers a number of significant advantages. Most importantly, it includes more realistic physical parameterizations, particularly for the planetary boundary layer and cumulus convection. It also employs improved finite-difference schemes for horizontal advection and geostrophic adjustment. It includes the mixing ratio of ozone as a prognostic variable, whose distribution is modified by advection and a simple photochemistry parameterization. Finally, the program structure is flexible as to horizontal and vertical resolution. The model description is summarized in Table 1. We are in the process of performing simulations with the model, to evaluate its ability to simulate the general circulation.

2. NUTS AND BOLTS

An effort to optimize the model on the Cyber 205 is ongoing. The original code was taken from Monterey, where limited vectorization had been accomplished on a Cyber 203. The work began on Cybernet (a commercial network) and has continued on the NACF 205. Numerous problems were encountered during the conversion effort, including compiler bugs detected during the execution of the model.

The initial goals included creating "logical unit" subroutines, making the code more readable, and creating subroutines to be shared between the physics and hydrodynamics, as well as top-down vectorization of the hydrodynamics. Table 2 shows the speed increase to date by vectorization combined with scalar optimization of various routines. Vectorization of the physics has also begun.

The model history data is interpolated to pressure surfaces, converted from full precision Cyber words (64 bits) to full precision Amdahl words (32 bits), and transferred to the front-end for further analysis. A program to process grid point history data has been completed; as a result, we will be able to put out a very detailed record of each simulation, for selected grid points.

3. RESULTS

The initial problems have been overcome, and two model simulations have begun. A 15-level model with its top at 1 mb has completed a January simulation, and a 9-level model with its top at 50 mb has completed a simulation which extends from December 31 to the end of July. Figs. 1-4 show the simulated 200 mb geopotential height, PBL depth, total cloudiness, and PBL stratus incidence, for July of the 9-level simulation. The 200 mb height field shows

strong, very realistic planetary wave activity. The PBL depth shows maxima over the warm coastal currents of the Northern Hemisphere, and minima of land where the nocturnal values are small. The total cloudiness has a realistic geographical distribution, and the globally averaged value is also realistic. The PBL stratus incidence shows subtropical maxima, in agreement with observations.

Table 1

MODEL DESCRIPTION

A. Prognostic variables: surface pressure, planetary boundary layer depth, zonal wind, meridional wind, potential temperature, specific humidity, ozone mixing ratio, ground temperature, snow depth.

B. Vertical structure:

   1. The stratosphere uses a pressure coordinate system

   2. The troposphere uses a sigma coordinate system

   3. The lowest model layer is the planetary boundary layer

   4. Arakawa-Suarez-Lamb vertical differencing.

C. The horizontal and vertical resolution are fully variable.

D. Horizontal differencing: Fourth-order potential-enstrophy-conserving momentum advection scheme developed by Kenji Takano, and fourth-order advection of potential temperature, moisture, and ozone.

E. Leapfrog-Matsuno time differencing.

F. Physical parameterizations:

   1. Arakawa-Schubert cumulus parameterization

   2. Randall planetary boundary layer parameterization

   3. Schlesinger-Katayama radiation parameterization.

Table 2

15-LEVEL MODEL TIMINGS (minutes per simulated day)

	--------- INITIAL ---------			NOW
Machine	203	205	205	205
Compiler	1.5	1.5	1.5	2.0
Compiler Options	O,U,V	O,V	NONE	MIXED
Hydrodynamics	15.6	17.2	55.2	4.0
Physics	11.5	9.5	13.2	7.0
TOTAL	27.8	27.3	69.3	11.4

GEOPOTENTIAL HEIGHT AT 200 MB
(100*GPM)
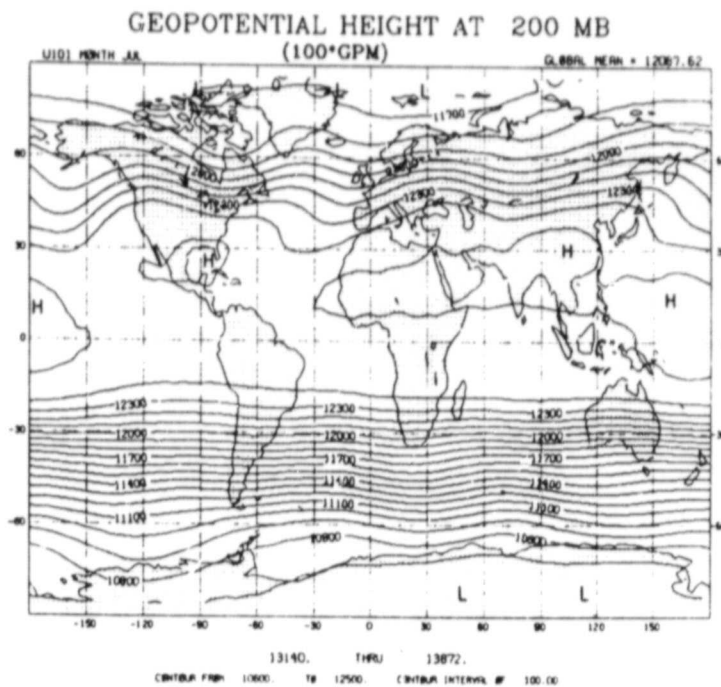
Figure 1. Simulated monthly mean 200 mb heights, for July, in m.
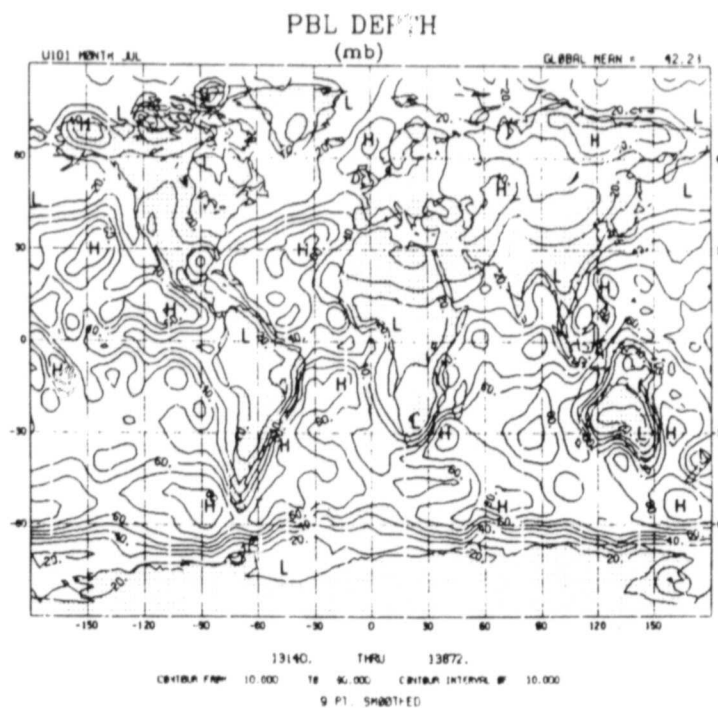
PBL DEPTH
(mb)

Figure 2. Simulated monthly mean PBL depth, for July, in mb.
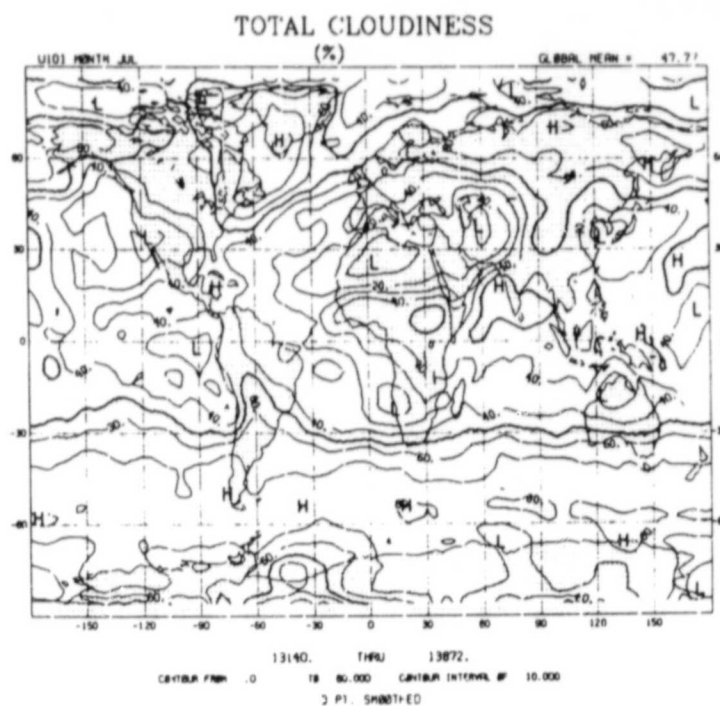
TOTAL CLOUDINESS
(%)

Figure 3. Simulated monthly mean total cloudiness, for July, in %.

PBL STRATUS INCIDENCE
(%)
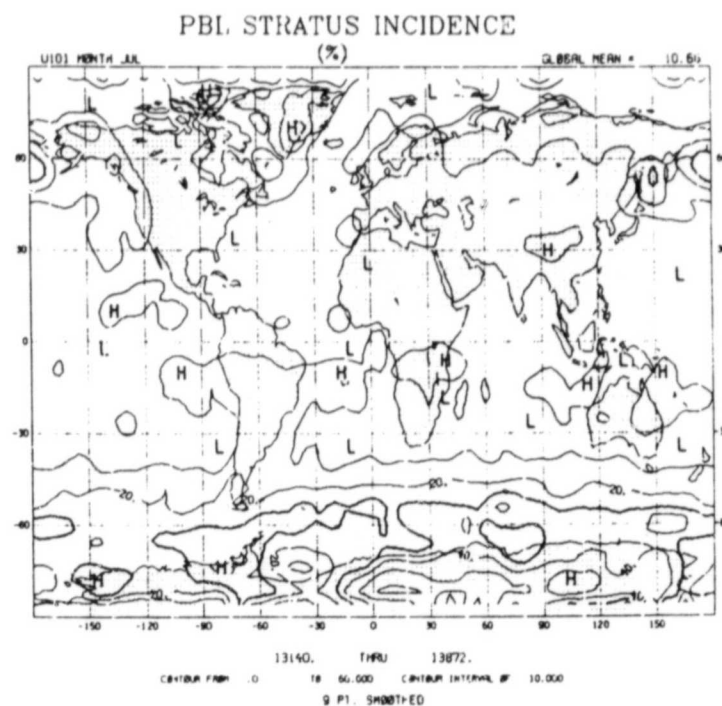
Figure 4. Simulated monthly mean PBL stratus incidence, for July, in %.

VECTORIZATION OF THE PHYSICS IN THE GWS FOURTH ORDER MODEL

Lawrence L. Takacs

In order to utilize the high-speed vector processing capability of the Cyber 205 computer, the 'physics' of the GWS fourth order general circulation model has been greatly restructured and modularized. The physics of the model consists of the determination of the ground condition, the calculation of in-coming short-wave and outgoing long-wave radiation, the effect of cumulus convection, the determination of precipation, etc., and was previously calculated one grid-point at a time with vertical integration at each grid-point where appropriate. The new version of the code streams through all longitudinal grid-points at the same time and, where appropriate, the vertical index as well. This restructuring and vectorization of the physics has produced an overall increase in speed by a factor of 7.6 over the Cyber scalar version when long-wave radiation is called, and by a factor of 3.8 otherwise.

The main body of the physics code is located in subroutine COMP3. The cumulus parameterization has been moved to a new subroutine called CUMULO, while the calls to the shortwave and longwave radiation routines are done in the new routine RADIO. The vectorization of the code is an ongoing project, and further improvements and enhancements of the model are currently being investigated.

VECTORIZATION OF THE HYDRODYNAMICS IN THE GLAS FOURTH-ORDER MODEL

Ramesh C. Balgovind

The Hydrodynamics of the GLAS Fourth-Order General Circulation Model FORTRAN code has been converted from scalar to a vector form. This in order to utilize the high-speed vector processing capabilities of the Cyber 205 computer. The Hydrodynamics part of the model consists of the advection, Fourier filterings, Shapiro filtering and the calculation of pressure to the kappa power.

In the conversion effort our major objectives were to:

1) vectorize as many DO loops as possible,

2) minimize division and the use of Q8 calls,

3) avoid descriptors whenever possible,

4) keep the variable resolution,

5) form link triads,

6) and to keep the code structure as close as possible to the scalar GCM.

This vectorization of the Hydrodynamics has produced a remarkable overall increase in speed over the scalar code. The vector code streams through all the longitudinal and the vertical grid-points at the same time and, where appropriate, the latitudinal index as well. The vector Shapiro filtering process on the CYBER 205 is over 80 times faster then the scalar version on AMDAHL. Utilizing the U.K. Meteorological Office Fast Fourier Transform code our Fourier filtering process gave us a factor of 25 over the scalar process on AMDAHL. We are also using a fast method to compute the expression, pressure to the kappa power.

The vectorization of the hydrodynamic code is now complete and further improvements and enhancements of the model are currently being investigated.

VECTORIZED SCM OBJECTIVE ANALYSIS SCHEME ON THE CYBER 205

J. Molini, W. E. Baker, D. Edelmann, and J. Woollen

The successive correction method (SCM) of objective analysis has been developed for assimilation studies with the FGGE data (Baker, 1983). In the SCM, successive modifications are made to the first guess fields provided by the fourth-order GLAS GCM (Kalnay-Rivas and Hoitsma, 1979). Eastward and northward wind components, geopotential height, and relative humidity are analyzed on mandatory pressure levels. Surface pressure and temperature are reduced to sea level and analyzed there. The assimilation procedure involves the intermittent analysis of batches of data grouped in a ± 3 h window about each synoptic time.

In order to write efficient, vectorized code for the Cyber 205, the operational code on the Amdahl V6 had to be substantially rewritten. The major internal data structures were redesigned. More of the working variables were saved in vectors. Time-consuming calculations, particularly the calculation of the gridpoint corrections, were rewritten using explicit vector syntax. The preprocessing and data checking were also modified to run as a separate program, thus simplifying the I/O on the Cyber 205. Table 1 summarizes the CPU required for one analysis cycle. As may be seen in Table 1, executing the scalar (Amdahl) code on the Cyber resulted in only a modest improvement in performance. However, redesigning the computations to take advantage of the vector architecture resulted in a significant decrease in the required CPU time.

	Amdahl	Cyber (Scalar)	Cyber (Vector)
Surface analysis	72.4	44.5	10.2
Height and moisture analysis	568.8	476.0	30.4
Wind analysis	388.9	206.3	28.4
Total	1030.1	726.8	69.0

Table 1. CPU required for one analysis cycle in sec.

V. SUMMER LECTURE SERIES

194

SECONDARY DISTURBANCES IN POLAR AIR STREAMS:
COMMA CLOUDS, TROUGHS AND POLAR LOWS

R. J. Reed/University of Washington

During the period October to April in the North Pacific comma-shaped cloud formations indicative of small synoptic-scale or large mesoscale disurbances occur frequently in polar air streams behind or poleward of major frontal bands. These systems are important to weather at sea and also at coastal localities when they come ashore. On surface weather maps they are generally marked by a trough that lies along the tail of the comma (depicted by a broken line and the symbol TROF on NMC analyses) and often by a low pressure center that lies beneath the comma head. On some occasions the trough acquires frontal characteristics and quite frequently the comma cloud excites and interacts with a wave on the polar front.

In some cases, at least, the disturbances appear to resemble polar lows, small low pressure systems that move southward from the Greenland-Iceland area and bring showery weather to the British Isles, North Sea and adjacent continent. Also in some cases they may be associated with the bent-back occlusions and secondary cold fronts that at one time were commonly analyzed on synoptic charts.

It is this host of phenomena, all characterized by development in polar air streams behind major frontal cyclones, that forms the topic of the present lecture. The main features of the systems will be reviewed and examples of several different types of developments will be shown. Finally, the origin of the systems will be discussed and pertinent theoretical and modeling studies mentioned.

194

INTENTIONALLY BLANK

A SEMI-LAGRANGIAN AND SEMI-IMPLICIT NUMERICAL INTEGRATION SCHEME
FOR THE PRIMITIVE METEOROLOGICAL EQUATIONS

A. Robert/Canadian Meteorological Center

A semi-lagrangian algorithm is associated with the semi-implicit method in the integration of the shallow water equations on a rotating sphere. The resulting model is unconditionally stable and can be integrated with rather large time steps. Truncation errors remain reasonably small with time steps 25 times as large as those used with explicit integration schemes.

An analysis of the proposed method is performed and it indicates that the scheme is stable. Also, the results of a few integrations are presented and from these we conclude that the model is not very sensitive to the size of the time step provided that it does not exceed a value of the order of two or three hours.

THE INITIAL SPECIFICATION OF THE ATMOSPHERIC STATE FOR NUMERICAL PREDICTION MODELS

A. Kasahara/National Center for Atmospheric Research

A deficiency in numerical weather prediction still exists in the gap between observational data analysis and the use of such an analysis as the initial condition for forecast models. In the traditional practice of analyzing meteorological data, one tacitly assumes that observational errors are often substantial and, therefore, observed data may be modified in the event that they don't agree with our models of the atmosphere for analysis and prediction. This practice was understandable in those days when meteorological observations were relatively primitive and scarce, but this viewpoint must change when dealing with more accurate and abundant observations than, say, ten years ago.

The problem of initial specification of the atmospheric state for numerical prediction models will be reviewed. In recent years, notable progress has been made in our understanding of initialization to set up balanced initial conditions for numerical prediction models. Discussion will be centered on the relationship between two recent approaches, called the nonlinear normal mode procedure and the bounded derivative method in relation to the classical balancing based on quasi-geostrophic theory. Since both new approaches of initialization are more general than the classical procedures, the connection of the two approaches with the quasi-geostrophic formulation will shed light on closing the gap between data analysis and the preparation of initial conditions for prediction models.

ORIGIN OF MONSOON DEPRESSION

R. Lindzen/Harvard University

The development of monsoon depressions over the Bay of Bengal is a striking phenomenon restricted largely to the month of July. It is shown that such development cannot arise from either CISK or baroclinic instability. Apart from the intrinsic weakness of baroclinic conversions, the momentum exchange associated with cumulus convection effectively inhibits both processes. This leaves barotropic instability as the likely mechanism.

Studies of barotropic instability have thus far been restricted to normal mode analyses. Normal mode instabilities, however, are at variance with observed monsoon depressions. The most rapidly growing normal modes are associated with 200 mb winds, travel far too rapidly westward and do not penetrate into the lower troposphere sufficiently to organize convection; they, morecver, display no special response for July conditions.

Instead of normal modes we examine the asymptotic response to pulse perturbations. Such asymptotics emphasize instabilities with zero group velocity. The calculation of such asymptotics is greatly facilitated by the existence of analytic expressions for stability relations (phase speed as a function of wavenumber) in the complex plane. Fortunately, we find that a very sizable class of reasonable barotropic profiles yield stability problems homomorphic to the Charney problem in baroclinic instability. Analytic solutions to the latter problem have recently been developed with WKB methods. Such methods are used to show that instability to localized perturbations emphasizes the lower troposphere and is strongest in July.

WHAT CAN SATELLITES CONTRIBUTE TO AN UNDERSTANDING OF
THE EL NINO PROBLEM?

Klaus Wyrtki/University of Hawaii

El Nino is a sporadically occurring event in the ocean-atmosphere system of the Pacific Ocean and has catastrophic consequences for the fishery off Peru, causes torrential rainfalls in the otherwise dry coastal areas of South America and has repercussions for the climate over North America in successive seasons. The last major El Nino events were in 1957-58, 1965, 1972-73, and 1976 and were apparently somewhat more frequent than in preceding decades. Research in recent years has been able to explain the oceans response by atmospheric forcing over the central equatorial Pacific and numerical models have succeeded to simulate the events for a prescribed wind forcing. Based on the dynamic theory of El Nino, which requires a build-up of warm water and higher sea level in the western Pacific caused by sustained strong southeast trade winds before the event, a prediction of the occurrence of El Nino becomes possible. Consequently, it will be possible to give advance warning of the next event, and this opportunity should be used to observe the entire sequence of atmospheric and oceanic events during the next El Nino and to obtain a set of observations never collected before. Satellites will play an important role in monitoring the next El Nino event.

Development of a strong El Nino event occurs in five phases. The build-up phase leading to El Nino is characterized by a period of sustained abnormally strong southeast trade winds lasting more than a year. As a consequence, westward flowing equatorial currents are intensified, leading to an accumulation of warm water in the western pacific and to higher sea level. At the same time upwelling along the equator and along the coast of Peru is strong and the surface waters are cool. All these effects can be easily monitored by satellite winds, XBT sections from ships of opportunity and sea level stations.

The triggering of El Nino through the collapse of the southeast trade wind field in the western and central equatorial Pacific usually occurs between December and March, during southern summer, as part of the seasonal relaxation of the wind. The extent and timing of this relaxation needs to be observed and studied, since it triggers the equatorial Kelvin wave, which travels east and causes downwelling along the coast of South America. While the deformation of the upper layer and of the discontinuity later in response to the Kelvinwave have been observed and modeled, the velocity distribution associated with it has never been measured and this would be a critical test for the validity of the model. The eastward advance of the Kelvin wave or group of Kelvin waves is apparently also accompanied by a substantial decrease of the strength of the South Equatorial Current.

About 6 to 8 weeks after its triggering, the Kelvin wave impinges on South America, accumulating surface water along the coast and depressing the thermocline. This documents itself in a rapid and virtually simultaneous rise of sea level from Ecuador to Lima. The warmer coastal temperatures can be readily explained by the suppression of upwelling and the shoreward advance of warmer offshore water, but the quantitative aspects of the process need to be checked. Much more difficult to explain are the rising

surface temperatures farther offshore in the general area between the Galapagos Islands and about 15°S. The warming of these waters can be caused either by larger heat input at the sea surface (reduced cloud cover, less evaporation) or by a weaker flow in the South Equatorial Current causing less advection of collo water from the south and a longer residence time of the surface water in the area, which would lead to in situ warming. Another aspect of El Nino during this phase is the overflow of warm low salinity water from north of the Galapagos Front towards the south between the coast and the Galapagos Islands. This overflow was observed in 1975 and is probably a feature occurring annually on a small scale and during El Nino on a very large scale.

The third phase of El Nino is characterized by a poleward spreading of the thermocline disturbance, by a westward spreading of the sea surface temperature anomaly along the equator, by a continuing draining of warm water from the western Pacific and lowering of the sea level, and by intensified eastward flow especially in the North Equatorial Countercurrent. Surface temperature anomalies appear first off the coast of Peru and spread westward reaching the Line Islands about five months later. It is not very likely that this spreading is an effect of advection, but more likely that the suppression of equatorial upwelling progresses westward as sea level in the equatorial trough rises. The time variation of equatorial upwelling and in particular the development of east-west slope of thermocline topography and sea level along the equator needs study.

The continuous draining of water from the western Pacific has been documented well by both sea level measurements and by the response of the thermal structure observed from XBT sections and the 137° hydrographic section in the western Pacific. The response of the equatorial current system in the central Pacific has been monitored by means of sea level gauges. It consists of a weakening of the westward flowing South Equatorial Current and an intensification of the eastward flowing North Equatorial Countercurrent and probably also of the South Equatorial Countercurrent. Little is known about the response of the Equatorial Undercurrent, which will require direct observation. During this phase of El Nino, which corresponds to southern winter, the sea surface temperatures off South America drop again as upwelling resumes under the influence of seasonally stronger coastal winds. A weak or moderately strong El Nino might terminate during this phase.

During the fourth phase of a strong El Nino event the eastward flowing North Equatorial Countercurrent advects much warm water into the Eastern Tropical Pacific, leading to considerable warming there. This strong flow together with a reflected wave from the western boundary may be the reason for the second peak in sea level, thermocline depression and sea surface temperature observed during strong El Nino events.

The fifth and last phase of El Nino is the unexpectedly sudden termination of the event and a rapid return to normal conditions. Sea level drops along the coast of South America, rises even more rapidly in the western Pacific, equatorial upwelling resumes, surface temperatures become cooler than normal. All happens within a rather short interval of about two months. The processes involved in this rapid return to normal have not really been investigated.

Satellites are expected to contribute significantly to the monitoring of the next El Nino event. Most important is the determination of the wind field over the ocean, which can be accomplished by either determination of cloud motion vectors or by scatterometer measurements of wind stress. Improved methods to observe sea surface temperature will allow a better determination of this important field, especially when appropriate corrections for water vapor can be applied. Water movements can be observed by the use of satellite-tracked drifting buoys, which might also relay other environmental data. Satellite observations of atmospheric circulation during and before an El Nino event are of course needed to interpret the oceanographic data and to study the interaction between the two systems.

On the other hand, measurements of subsurface thermal structure are not yet possible from satellites, and direct methods will have to be used. This applies as well for the collection of most chemical and biological data. The greatest advantage of the satellite is, however, the fact that it delivers a continous spacial coverage of global extent. This fact alone will revolutionize oceanographic research and thinking in the years to come.

VI. RECENT PUBLICATIONS

C - 3

RECENT PUBLICATIONS

Atlas, R., and R. Rosenberg, 1982: Numerical prediction of the Mid-Atlantic states cyclone of 18-19 February 1979. NASA Tech. Memo. 83992, 53 pp.

Atlas, R., M. Halem, and M. Ghil, 1982: The effect of model resolution and satellite sounding data on GLAS model forecasts. Mon. Wea. Rev., 110, 662-682.

Atlas, R., 1982: The growth of prognostic differences between GLAS model forecasts from SAT and NOSAT initial conditions. Mon. Wea. Rev., 110, 877-882.

Atlas, R. 1982: Satellite data in global scale modeling. Satellite Soundings and Their Uses, Part III, Workshop on Satellite Meteorology, July 19-23, 1982, Ft. Collins, Colorado.

Atlas, R., 1982: A numerical investigation of intense coastal cyclogenesis. Research Activities in Atmospheric and Oceanic Modelling. Report No. 3, p. 5.44.

Atlas, R., P. Woiceshyn, S. Peteherych, and M. Wurtele, 1982: Analysis of satellite scatterometer data and its impact on weather forecasting. Oceans. September 1982, 415-420.

Atlas, R., 1982: Satellite data in global scale modeling. Satellite Soundings and Their Uses, Part III, Workshop on Satellite Meteorology, July 19-23, Ft. Collins, Colorado.

Baker, W. E., and J. Paegle, 1982: The effects of tropical wind data on the prediction of ultralong waves. Research Activities in Atmospheric and Oceanic Modelling, Rep. 3, GARP Numerical Experimentation Program, pp. 1.15-1.17.

Balgovind, R., A. Dalcher, M. Ghil, and E. Kalnay, 1982: A stochastic-dynamic model for the spatial structure of forecast error statistics. Mon. Wea. Rev., in press.

Bhattacharya, K., and M. Ghil, 1982: Internal variability of an energy-balance model with delayed albedo effects. Jour. Atmos. Sci, 39.

Chahine, M. T., and J. Susskind, 1982: Determination of the horizontal and vertical distribution of clouds from infrared satellite sounding data. 1982 International Geoscience and Remote Sensing Symposium, June 1-4, Munich, Germany.

Ghil, M., S. Cohn, and A. Dalcher, 1982: Applications of sequential estimation to data assimilation. Proc. of the Joint JSC/CCCO Study Conference on Large Scale Oceanographic Experiments, May 1982, Tokyo, 67-86.

Ghil, M., and H. LeTreut, 1982: A climate model with cryodynamics and geodynamics. J. Geophys. Res., 86, 5262-5270.

Halem, M., E. Kalnay-Rivas, W. Baker, and R. Atlas, 1982: An assessment of the state of the atmosphere as inferred from the FGGE satellite observing systems during SOP-1. Bull. Amer. Soc. Meteor., 63, 407-426.

Helfand, H. M., and E. Kalnay, 1982: A model to determine open or closed convection. J. Atmos. Sci., in press.

Hoffman, R., 1982: SASS wind ambiguity removal by direct minimization. Mon. Wea. Rev., 110, 434-445.

Hoffman, R., and E. Kalnay, 1982: Lagged average forecasting, an alternative to Monte Carlo forecasting. Tellus, in press.

Kalnay, E., and J. Paegle, 1982: Large amplitude stationary Rossby waves in the southern hemisphere. Proceedings of the 14th Tech. Conf. on Hurricanes and Tropical Meteorology, June 7-12, San Diego, CA.

Kalnay, E., and J. Shukla, 1982: Numerical prediction of large scale tropical flow. Proc. of the 14th Tech. Conf. on Hurricanes and Tropical Meteorology, June 7-12, San Diego, CA.

Moeng, C.-H., and D. A. Randall, 1982: The radiative impact of cumulus cloudiness in a general circulation model. NASA Technical Memorandum 84962, 19 pp.

Munteanu, M.-J., 1982: Study of tropopause height estimate from TOMS total ozone data from NIMBUS-7 and the microwave regression temperature retrieval of simulated brightness temperatures. Paper presented at Numerical Weather Prediction and Statistics and Probability in Atmospheric Sciences, Monterey, California, Nov. 2-6, 1981.

O'Brien, J., R. Atlas, et al., 1982: Scientific Opportunities Using Satellite Wind Stress Measurements Over The Ocean. Nova University/ N.Y.I.T. Press, 152 pp.

Paegle, J., and W. E. Baker, 1982a: Planetary scale characteristics of the atmospheric circulation during January and February 1979. J. Atmos. Sci., 39, 2521-2538.

Paegle, J., W. E. Baker, 1982b: Global scale weekly and monthly energetics during January and February 1979. J. Atmos. Sci., 39, 2750-2759.

Randall, D. A., and C.-H. Moeng, 1982: Tests of alternative entrainment assumptions for cloud-topped mixed-layer models. Regional Scientific Conference on Tropical Meteorology, Tsukuba, Japan, Oct. 18-22, 181-182.

Randall, D. A., and G. J. Huffman, 1982: Entrainment and detrainment in a simple cumulus cloud model. J. Atmos. Sci., 39, 2793-2806.

Randall, D. A., 1982: Monthly and seasonal simulations with the GLAS climate model. Proceedings of the Workshop on Intercomparison of Large-Scale Models Used for Extended-Range Forecasts of the European Centre for Medium-Range Weather Forecasts, Reading, England (Invited paper; to appear)

Randall, D. A., 1982: Entrainment and clouds. <u>Conference on Cloud Physics</u>
<u>of the American Meteorological Society</u>, Chicago, IL, Nov. 15-18, 131-138.
(Invited paper)

Randall, D. A., 1982: Performance of the PBL parameterizations in the GLAS
and UCLA models. <u>Proceedings of the Workshop on the Planetary Boundary</u>
<u>Layer of the European Centre for Medium-Range Weather Forecasts</u>, Reading,
England, 81-118. (Invited paper)

Reuter, D. C., L. R. Thorne and W. D. Gwinn, 1982: Infrared and Raman spectra
and normal coordinate analysis of boranediamine ($BH(NH_2)_2$. <u>J. Phys. Chem.</u>,
<u>86</u>, 4737-4745.

Shukla, J., and Y. Mintz, 1982: The influence of land-surface evapotranspiration
on the earth's climate. <u>Science</u>, <u>215</u>, 2553-1675.

Shukla, J., 1982: Ability and limitations of general circulation models to
simulate climate and climate variability. <u>Proceedings of Study Conference</u>
<u>on the Physical Basis for Climate Prediction on Seasonal, Annual and</u>
<u>Decadal Time Scales</u>, Sept. 13-17, 1982, Leningrad, USSR (published by JSC/
WMO, Geneva).

Shukla, J., and W. Baker, 1982: Analysis and prediction of the monsoon flow
during the summer MONEX. <u>Proceedings of International Conference on</u>
<u>Scientific Results of the Monsoon Experiment</u>, October, 1981, Indonesia,
p. 4.3-4.11, (published by ICSU/WMO, Geneva).

Shukla, J., 1982: On physical basis and feasibility of monthly and seasonal
prediction with a large GCM. <u>Proceedings of WMO-CAS/JSC Expert Study</u>
<u>Conference on Long Range Forecasting</u>, Dec. 1-4, 1982, Princeton, NJ
(published by CAS/WMO, Geneva).

Shukla, J., and J. M. Wallace, 1982: GCM simulation of global effects of observed
sea surface temperature anomalies in equatorial Pacific. <u>Fourth AMS Confer-</u>
<u>ence on Ocean-Atmos. Interaction</u>, June 8-10, 1982, San Diego, CA.

Shukla, J., 1982: Influence of the oceans on the variability and
predictability of the tropical atmosphere. <u>Fourth AMS Conference</u>
<u>on Ocean-Atmos. Interaction</u>, June 8-10, San Diego, CA.

Shukla, J., and Y. Mintz, 1982: Problems and prospects for prediction of
droughts. <u>62nd Annual Meeting of Amer. Met. Soc.</u>, San Antonio, TX, Jan.
11-15, 1982.

Sud, Y., and M. Fennessy, 1982: An observational data based evapotranspiration
function for general circulation models. <u>Atmos.-Ocean</u>, <u>20</u>, 301-316.

Sud, Y., and M. Fennessy, 1982: A study of the influence of surface albedo
on July circulation in semiarid regions using the GLAS GCM. <u>J. of Clima-</u>
<u>tology</u>, <u>2</u>, 105-125.

Susskind, J., J. Rosenfield, D. Reuter, and M. T. Chahine, 1982: The GLAS
physical inversion method for analysis of HIRS2/MSU sounding data. <u>NASA</u>
<u>Tech. Memo. 84936.</u>

Susskind, J., D. Reuter, D. E. Jennings, S. D. Daunt, and G. W. Halsey, 1982: Splittings in ν_9 of ethane from diode laser spectra: torsion-vibration-rotation interactions and the barrier to internal rotation. _J. Chem. Phys._, _77_, 2728-2744.

VII. GMSB STAFF

GMSB Staff

Civil Service	RRAs	FRAs
Robert Atlas	Jeff Augenbaum	Mark Cane
Wayman Baker	Steve Bloom	Michael Ghil
Debora Boyer	Ross Hoffman	Ed Harrison
Dean Duffy	Dennis Reuter	
Milton Halem	Glenn White	
Eugenia Kalnay	Richard Wobus	
David Randall	Carl Youngblut	
Jagadish Shukla		
David Straus		
Max Suarez		
Yogesh Sud		
Joel Susskind		
Joan Wentz		

M/A-COM Sigma Data

Jim Abeles	Larry Marx
Manina Almeida	Kingtse Mo
Ramesh Balgovind	John Molini
Yevgenia Brin	Mark Nestler
Sol Broder	Dan Paolino
Alex Camerlengo	Jim Pfaendtner
Herb Carus	Bill Phillips
Tom Corsetti	Ernie Pittarelli
Amnon Dalcher	Andy Pursch
Cheryl Derrington	Bob Rosenberg
Ron Dlouhy	Joan Rosenfield
Greg Dozier	Laura Rumburg
Jim Edelmann	Kathy Schmidt
Mike Fennessy	Debbie Schwartz
Jim Firestone	Stan Scott
John Fisch	Butch Sheppard
Lena Fornito	Bill Smith
Mark Helfand	Marie Smoes
Iris Holmes	Steve Stalos
Tim Jacobs	Larry Takacs
Jane Jonker	Joe Terry
Bert Katz	Lora Thompson
Dave Lamich	Dave Wallace
Min-Nan Lee	Mary Ann Wells
Sung-Yung Lee	Barbara Worley
C.L. Lin	Jack Woolen
Mike Mandelberg	Peter Wu